

Quantum criticality and non-equilibrium dynamics in correlated electron systems



Inaugural-Dissertation
zur
Erlangung des Doktorgrades
der Mathematisch-Naturwissenschaftlichen Fakultät
der Universität zu Köln
vorgelegt von

Andreas Hackl
aus Nördlingen

Köln 2009

Berichterstatter:

Prof. Dr. M. Vojta
Prof. Dr. A. Rosch
Prof. Dr. H. Schoeller

Tag der mündlichen Prüfung:

27. November 2009

Contents

0	Introduction	1
I	Heavy-fermion systems: Kondo breakdown transitions and quantum critical transport	5
1	Introduction	7
1.1	Heavy fermions	7
1.2	Single-impurity Kondo effect	8
1.3	The Kondo lattice	10
1.4	Quantum criticality in heavy-fermion systems	13
1.5	Motivation and outline	22
2	Kondo Volume collapse transitions in heavy-fermion metals	23
2.1	Derivation of the model and large-N theory	24
2.2	Phase diagram in slave-boson mean-field theory	36
2.3	Landau theory	40
2.4	Beyond mean-field theory	46
2.5	Conclusion	47
3	Transport properties near a Kondo-breakdown transition	49
3.1	Gauge field theory	49
3.2	Quantum Boltzmann equation	55
3.3	Conclusions	67
A	Appendix to chapter 2	69
A.1	Maxwell construction for first-order phase transitions	69
A.2	Schrieffer-Wolff transformation of the periodic Anderson model	70
II	Structural and magnetic transitions in the iron arsenides	73
4	Introduction: The iron arsenides	75
4.1	General properties of iron arsenides	75

4.2	The 122 family	77
4.3	Outline	78
5	Phenomenological model for pressure driven transitions in CaFe_2As_2	81
5.1	Local moments in a correlated Anderson lattice	81
5.2	Anderson-Heisenberg lattice model	84
5.3	Elastic energy and electron-lattice coupling	85
5.4	Mean-field theory	88
6	Anderson-Heisenberg model: Phase diagrams	93
6.1	Phases and electronic phase diagram	93
6.2	Phase diagram with electron-lattice coupling	96
7	Conclusions	101
A	Formulas for fermionic mean-field theory	103
 III Non-equilibrium magnetization dynamics of ferromagnetically coupled Kondo spins		105
8	Introduction	107
8.1	Ferromagnetic Kondo model and experimental realizations	107
8.2	The flow equation method	111
8.3	Outline	115
9	Unitary perturbation theory approach to real-time evolution problems	117
9.1	Motivation: canonical perturbation theory in classical mechanics	117
9.2	Illustration for a simple oscillator model	120
9.3	Conclusions	126
10	Non-equilibrium spin dynamics in the ferromagnetic Kondo model	127
10.1	Toy model	127
10.2	Kondo model and flow equation transformation	130
10.3	Time-dependent magnetization	133
10.4	Analytical results for the magnetization	136
10.5	Conclusions	142
A	Details to part III	145
A.1	Matrix representation of the toy model	145
A.2	Flow equations for general spin S	146
A.3	Validity of tree-level approximation	148
A.4	Alternative way of calculating magnetization	149
A.5	Diagonal parameterization of isotropic couplings	150
A.6	Normal ordering	151

IV	Normal-state Nernst effect in the Cuprates	153
11	Introduction: Cuprates and the Nernst effect	155
11.1	The cuprates	155
11.2	Nernst effect and pseudogap	161
11.3	Outline	164
12	Normal-state Nernst effect in the electron-doped cuprates	165
12.1	Model	165
12.2	Semiclassical approach	167
12.3	Antiferromagnetic fluctuations	180
12.4	Conclusions	183
13	Normal-state Nernst effect in the presence of stripe order	185
13.1	Model and formalism	185
13.2	Nernst effect from stripe order for $x \geq 1/8$	187
13.3	Nernst effect below doping $x = 1/8$	196
13.4	Influence of pseudogap and local pairing	200
13.5	Summary and relation to experiments	201
	Bibliography	203
	Acknowledgements	216
	Anhänge gemäß Prüfungsordnung	218
	Kurzzusammenfassung in Deutsch und Englisch	220
	Erklärung	223
	Teilpublikationen	223
	Lebenslauf	224

Chapter 0

Introduction

“The whole is greater than the sum of its parts”. This aphorism, said to originate from Aristotle comprises why a solid containing roughly 10^{22} atoms very often shows *collective behavior* that cannot be fully understood by just naming the individual properties of the atoms a solid is built from. Any condensed matter theorist opting to understand real materials maybe grateful that solid state theory is nowadays built on two standard models: (1) The Landau theory of Fermi liquids and (2) the Ginzburg-Landau-Wilson (LGW) theory of phase transitions. The first concept might be used to predict the most ordinary properties a material can have, like its specific heat. The second standard model may be used to predict universal properties once condensed matter transforms from one phase to another. In other words, the reason why these models are standard models is that they guarantee *universality*, that is, few parameters are able to describe a large class of materials. In contrast to particle physicists, modern condensed matter physicists do not perform new experiments in order to verify *existing standard models*. Rather, they seek for new materials and phenomena that need to be described with *new theoretical concepts*. Yet, a well established class of materials has been termed that seems to be ideal to challenge any aspect of the two standard models: that are *correlated electron systems*.

In many cases, these systems refute to be described by our first standard model, Fermi-liquid theory. Typically, strongly correlated materials have incompletely filled d or f -electron shells with narrow bands. Very often then, one can no longer consider any electron in the material as being in a “sea” of the averaged motion of the others. Many, if not most, transition metal oxides belong into this class which may be subdivided according to their behavior, e.g. high- T_c superconductors, spintronic materials, Mott insulators, spin Peierls materials, heavy fermion materials, quasi low-dimensional materials and many more. The diversity of materials seems too large to be explained by a single concept beyond single particle physics. Besides providing particular examples of non-Fermi liquid physics, this thesis concentrates therefore on theoretical possibilities beyond the second standard model. We will examine two different cases of phenomena where this model is either (i) not applicable in general or even (ii) a meaningless concept.

Our field of research related to (i) shall be *quantum phase transitions*. The LGW approach

relates Landau's theory of phase transitions to the quantum mechanics of a microscopic order parameter theory. This approach leads to the prediction of universality classes of phase transition. At finite temperatures, phase transitions are described as *classical phase transitions* which fall under the well established universality classes of the LGW approach. At zero temperature, fluctuations are of quantum mechanical origin and call for the formulation of novel universality classes which cannot be described by the LGW approach. Notorious examples for the violation of the LGW approach are many heavy-fermion systems, where novel states of matter seem to emerge close to such transitions. Interestingly, also our first standard model seems to be especially violated near quantum phase transitions, which often exhibit non-Fermi liquid behavior like a divergence of the specific heat coefficient. In this thesis, we will examine theoretical models that are suitable to describe quantum phase transitions beyond the LGW paradigm.

In the second half of this thesis, we examine point (ii) mentioned above, where we will concentrate on *non-equilibrium phenomena*, which cannot be described by equilibrium statistical mechanics. A very convenient case are stationary external perturbations that are small enough to linearize the response of the system in the external perturbation. Although driving a quantum many-body system out of equilibrium, weak external perturbations probe essentially equilibrium properties of quantum many-body systems. Such experiments can be as sophisticated as measuring transverse electrical voltages in response to longitudinal thermal gradients in presence of a perpendicular magnetic field, called *Nernst effect* measurements. Measurements of the Nernst effect have recently revealed several insights about the normal state of cuprate superconductors, and a theoretical understanding of the normal state Nernst effect in the cuprates shall be one important goal of this thesis.

More complicated than stationary perturbations, a disturbance might depend on time, in which case the response of a correlated electron system is usually non-linear and depends itself on time. Importantly, analytical approaches to such problems are rare, since even if a perturbation is small, perturbation theory is usually not applicable in the limit of large times. One of the fundamental systems to discuss such effects is a single confined spin interacting with a solid state environment, as realized in quantum dots (QD). For many applications, such as those using QD spins to represent quantum information, the real-time dynamics of the interacting system after preparing a pure spin state is of great practical importance. In this thesis, we shall examine such real-time dynamics for a particular impurity spin problem in order to analytically describe the asymptotic behavior of such a non-equilibrium problem.

Since this thesis treats many different types of correlated electron systems which each come with their own theoretical developments and fundamental properties, its structure consists of four different parts with each providing its own introduction to the respective field of study.

Structure of this thesis

Part I is devoted to the unconventional behavior near quantum phase transitions in heavy fermion systems showing signatures of a localization of the local moment degrees of freedom at the QCP. After a detailed discussion of well-known theoretical concepts used to understand these materials, we discuss a scenario where the Kondo effect – being responsible for the heavy Fermi-liquid – breaks down at the quantum critical point. We derive experimental signatures of this transition by discussing the influence of electron-lattice coupling on this type of transition. Furthermore, we devise transport equations to study the transport of electrical charge in the quantum critical region, from which further characteristic signatures can be identified. The results of this part have been published in a research article (Hackl and Vojta, 2008a).

Part II applies central ideas introduced in part I to the newly discovered iron arsenic superconductors. We propose a scenario based on local-moment physics to explain the simultaneous disappearance of magnetism, reduction of the unit cell volume, and decrease in resistivity observed in CaFe_2As_2 . The quantum phase transition out of the magnetic phase is described as an orbital-selective Mott transition which is rendered first order by coupling to the lattice. These ideas are implemented by a large- N analysis of an Anderson lattice model. The results of this part have been published in a research article (Hackl and Vojta, 2009a).

Part III presents an analytical description of a non-equilibrium phenomenon in a quantum impurity system. We illustrate a recently developed extension of the flow equation method and apply it to calculate the non-equilibrium decay of the local magnetization at zero temperature. The flow equations admit analytical solutions which become exact at short and long times, in the latter case revealing that the system always retains a memory of its initial state. The results of this part have been published in a letter (Hackl et al., 2009a), a research article (Hackl and Kehrein, 2009) and a preprint (Hackl et al., 2009b).

Part IV analyzes the normal state Nernst effect in cuprate materials. This thermoelectric effect has become of intense interest as a probe for the normal state properties of the underdoped cuprates. Our focus is on the influence of various types of translational symmetry breaking on normal state quasiparticles and the Nernst effect. In the electron-doped cuprates, we show that a Fermi surface reconstruction due to spin density wave order leads to a sharp enhancement of the quasiparticle Nernst signal close to optimal doping. In the hole-doped cuprates, we discuss relations between the normal state Nernst effect and stripe order. We find that Fermi pockets caused by translational symmetry breaking lead to a strongly enhanced Nernst signal with a sign depending on the modulation period of the ordered state and details of the Fermi surface. These findings imply differences between antiferromagnetic and charge-only stripes. The results of this part have been published in form of a research article (Hackl and Sachdev, 2009) and two preprints (Hackl et al., 2009c, Hackl and Vojta, 2009b).

Part I

Heavy-fermion systems: Kondo breakdown transitions and quantum critical transport

Chapter 1

Introduction

1.1 Heavy fermions

This first part of the thesis evolves around the subject of heavy-fermion physics, with a particular focus on *quantum phase transitions* in those materials. Many references exist on this exciting field, including general reviews and books on heavy-fermion physics (Stewart, 1984, Hewson, 1997) and also on the exciting developments related to non-Fermi liquid behavior and quantum phase transitions (Stewart, 2001, Löhneysen et al., 2007, Coleman, 2007). Historically, heavy-fermion metals were discovered by Andres et al. (1975), who observed that the intermetallic compound CeAl_3 forms a metal in which the Pauli susceptibility and the linear specific heat capacity are about 1000 times larger than in conventional metals. Soon after, many materials with the same properties were discovered, and the term “heavy-fermion metal” applies today to a large and still growing list of materials. Heavy-fermion compounds have in common that their properties derive from the partially filled f -orbitals of rare earth or actinide ions. On the atomic level, the large intra-atomic Coulomb repulsion leads to a formation of localized magnetic moments in the partially filled f -orbitals. In the heavy Fermi-liquid phase, these moments are screened by the conduction electrons and lead to the formation of quasiparticles with a large effective mass below a coherence temperature T^* . The resulting phase is well described by Landau’s Fermi liquid theory (Landau, 1957a,b, 1959), albeit with tremendously renormalized Landau parameters. After the discovery of heavy-fermion materials, several different instabilities of this heavy Fermi-liquid phase were observed in subsequent experiments, starting with the discovery of superconductivity in CeCu_2Si_2 by Steglich et al. (1979). In many materials, the heavy Fermi-liquid phase lies at the brink of a magnetic instability, and it has become possible in 1995 to experimentally access a *quantum phase transition* from a heavy Fermi-liquid phase to an antiferromagnetically ordered phase (Löhneysen et al., 1994). In a finite temperature region near such a quantum phase transition, many non-Fermi liquid properties have been measured, e.g., a diverging specific heat coefficient. The current understanding of quantum phase transitions in heavy-fermion metals is based on a competition between screening of the local moments (based on the *Kondo effect*) and a competing magnetic exchange interaction between local moments (Doniach, 1977). It is

the purpose of the first part of this thesis to theoretically analyze the role of the Kondo effect near this quantum phase transition and to discuss experimental implications of one particular theoretical scenario.

1.2 Single-impurity Kondo effect

The discovery of the *Kondo effect* originated from experimental and theoretical studies of metallic systems containing a small fraction of *magnetic* impurities. It is well known that effects caused by non-magnetic impurities, like the residual resistance in metals, can be described in a single-particle framework and have been understood since the PhD thesis of Felix Bloch (1928). For magnetic alloys, the situation proved to be more complicated: In measurements by de Haas et al. (1934) on *Au* it was found that the resistivity—instead of dropping monotonically—exhibits a minimum at a finite temperature. It was only recognized later that this is an impurity effect associated with *3d* transition metal impurities such as *Fe*. Theoretical understanding of the resistance minimum was lacking until Zener (1951) introduced the fundamental *Kondo Hamiltonian* (originally referred to as *s-d Hamiltonian*).

$$H_{sd} = \sum_{\mathbf{k}\sigma} \epsilon_{\mathbf{k}} c_{\mathbf{k}\sigma}^{\dagger} c_{\mathbf{k}\sigma} + J \mathbf{S} \cdot \mathbf{s}_0 . \quad (1.1)$$

This model describes a local spin \mathbf{S} (assumed to be $S = \frac{1}{2}$ located at $\mathbf{r} = 0$) exchange coupled to the local conduction-electron spin density $\mathbf{s}_0 = \frac{1}{2} \sum_{\mathbf{k}, \mathbf{k}'} \sum_{\sigma\sigma'} c_{\mathbf{k}\sigma}^{\dagger} \boldsymbol{\tau}_{\sigma\sigma'} c_{\mathbf{k}'\sigma'}$, where $\boldsymbol{\tau}_{\sigma\sigma'}$ is the vector of Pauli matrices and $J > 0$ is the antiferromagnetic exchange coupling.¹ In a third-order perturbation theory calculation Kondo (1964) discovered that the electrical resistivity ρ due to scattering of conduction electrons off the impurity acquired a logarithmic dependence on temperature in third order in J ,

$$\rho = \rho_B [1 + N_0 J \ln(D/T) + \dots] , \quad (1.2)$$

which is proportional to the conduction electron density of states N_0 at the Fermi energy and depends also on the cutoff D of the electronic dispersion $\epsilon_{\mathbf{k}} \in [-D, D]$. Below the characteristic Kondo temperature

$$T_K = D \sqrt{N_0 J} \exp(-1/(N_0 J)) , \quad (1.3)$$

the leading order logarithmic correction exceeds the Born approximation term in the perturbative expansion of Eq. (1.2). The Kondo temperature marks a crossover temperature scale, below which a perturbative calculation of impurity observables fails. Attempts by Abrikosov (1965) to sum the leading logarithmic contributions (parquet diagrams) up to infinite order could not restore convergence of the perturbation series. New non-perturbative methods had to be developed in order to access the low-temperature regime $T < T_K$. In a first successful attempt in this direction, Anderson and Yuval (1969) demonstrated that

¹For a spin-1/2 coupled to a single band of conduction electrons in a metal, the exchange coupling is generically antiferromagnetic. In part III of this thesis, we will discuss different systems that are described by a *ferromagnetic* Kondo exchange coupling.

the thermodynamics of a magnetic impurity can be reformulated in terms of a (classical) gas of alternately charged particles with a logarithmic interaction. In a subsequent renormalization group analysis of the Coulomb gas, Anderson et al. (1970) showed that the effective coupling of the Kondo Hamiltonian increases without bound in the antiferromagnetic case. The same behavior was also obtained in a simple “poor man’s scaling approach” by Anderson (1970). Although perturbative scaling breaks down at a certain value of the coupling constant, it was nevertheless concluded that at zero temperature, the effective exchange is infinite, thus leading to perfect screening of the local moment and a non-magnetic singlet ground state. This was later confirmed by the pioneering numerical renormalization group (NRG) calculation of Wilson (1975) which may be considered as the first exact solution of the Kondo problem. After the breakthrough of Wilson, it was Nozières (1974) who finally realized that the low-energy physics of the Kondo impurity problem can be formulated as a local Fermi-liquid theory.

In real materials, the local moment degree of freedom derives from d - or f -orbitals of the impurity atom, and a more direct formulation of the appropriate impurity model is given by the Anderson impurity model (Anderson, 1961)

$$H = \sum_{\mathbf{k},\sigma} \varepsilon_{\mathbf{k}} c_{\mathbf{k}\sigma}^{\dagger} c_{\mathbf{k}\sigma} + \varepsilon_f \sum_{\sigma} f_{\sigma}^{\dagger} f_{\sigma} + U n_{f\uparrow} n_{f\downarrow} + \sum_{\mathbf{k}\sigma} V (c_{\mathbf{k}\sigma}^{\dagger} f_{\sigma} + \text{H. c.}) , \quad (1.4)$$

where f_{σ}^{\dagger} creates an electron with spin projection σ in the f orbital, $n_{f\sigma} = f_{\sigma}^{\dagger} f_{\sigma}$, and V is the hybridization matrix element. In the limit of large Coulomb repulsion U , double occupancy of the impurity level is energetically unfavorable. A necessary condition for local-moment formation clearly is that the energy of a singly (doubly) occupied f -orbital lies below (above) the chemical potential: $\varepsilon_f < 0$, $\varepsilon_f + U > 0$, such that in the *atomic limit* $V \rightarrow 0$ the atomic orbital is occupied by a single electron forming a $S = 1/2$ local moment. Dialing up a weak hybridization with $N_0 V^2 \ll U$ causes slow tunneling of the local moment between its degenerate “up” and “down” configurations,

$$e_{\downarrow}^{-} + f_{\uparrow}^{\uparrow} \rightleftharpoons e_{\uparrow}^{-} + f_{\downarrow}^{\uparrow} . \quad (1.5)$$

At a temperature scale corresponding to a thermal excitation energy $k_B T$ below the Kondo temperature, this leads to Kondo screening of the local moment, with the Kondo temperature in the symmetrical case $\varepsilon_f = -\frac{U}{2}$ given by (Wiegmann, 1980)

$$T_K = \sqrt{\frac{2U\Delta}{\pi^2}} \exp\left(-\frac{\pi U}{8\Delta}\right) , \quad (1.6)$$

where the hybridization width is $\Delta = \pi N_0 V^2$. It is also formally possible to map the symmetric Anderson impurity model onto the Kondo model by projecting out the valence fluctuation processes

$$f^0 \rightleftharpoons f^1 \rightleftharpoons f^2 \quad (1.7)$$

by a canonical transformation originally derived by Schrieffer and Wolff (1966), becoming an exact transformation in the *Kondo limit*

$$\begin{aligned} N_0 \left| \frac{V^2}{\epsilon_f} \right|, N_0 \left| \frac{V^2}{\epsilon_f + U} \right| &\ll 1 \\ \epsilon_f < 0 \text{ and } \epsilon_f + U > 0 . \end{aligned} \quad (1.8)$$

Thereby, e.g., the spin exchange processes

$$e_{\uparrow}^{-} + f_{\downarrow}^{\uparrow} \leftrightarrow f^2 \leftrightarrow e_{\downarrow}^{-} + f_{\uparrow}^{\uparrow} \quad (1.9)$$

are removed, which induce an antiferromagnetic superexchange interaction

$$\begin{aligned} H_{\text{exch}} &= -2J \left[\frac{1}{4} - \vec{S} \cdot \vec{s}(0) \right] \\ J &= \frac{4V^2}{U} \end{aligned} \quad (1.10)$$

between the local conduction electron spin density and the impurity local moment. Omitting the constant in Eq. (1.10) and adding the non-interacting conduction electrons shows that in this limit, the Anderson impurity Hamiltonian is equivalent to the s-d Hamiltonian formulated in Eq. (1.1).

1.3 The Kondo lattice

Heavy-fermion materials provide examples of systems where local moments deriving from atomic orbitals are periodically arranged on a lattice and thus not independent objects that can be considered as dilute impurities. A classic example for such a lattice of local moments is CeCu₆ (Coleman, 2007). The Cerium Ce³⁺ ions in this material are ions in a 4f¹ configuration with a localized magnetic moment with total angular momentum $J = 5/2$. The remaining three valence electrons of the partially filled Ce valence shell are not fully localized in molecular bonds with Cu atoms, but at least partially contribute to a reservoir of conduction electrons. At temperatures below a coherence temperature of order $T_{\text{coh}} \sim 10K$, the local moments form composite quasiparticles with the conduction electrons and behave as if the lattice contains periodically arranged Ce⁴⁺ ions. Above the coherence temperature T_{coh} , CeCu₆ is a Curie paramagnet which behaves like a lattice of free local moments. Such a system leads to a generalization of the single-channel Anderson impurity model to a lattice of localized orbitals, described by the *periodic Anderson model* (PAM)

$$H = \sum_{\mathbf{k}, \sigma} \epsilon_{\mathbf{k}} c_{\mathbf{k}\sigma}^{\dagger} c_{\mathbf{k}\sigma} + \epsilon_f \sum_{\sigma} f_{i\sigma}^{\dagger} f_{i\sigma} + U n_{i\uparrow}^f n_{i\downarrow}^f + \sum_{\mathbf{k}i\sigma} (V_{\mathbf{k}} e^{-i\mathbf{k}\mathbf{R}_i} c_{\mathbf{k}\sigma}^{\dagger} f_{i\sigma} + \text{h.c.}) . \quad (1.11)$$

In the Kondo limit (1.8), on each lattice site the atomic f -orbitals constitute an effective local moment coupling to the local spin density $\mathbf{s}_i = \frac{1}{2} \sum_{\sigma\sigma'} c_{i\sigma}^{\dagger} \boldsymbol{\tau}_{\sigma\sigma'} c_{i\sigma'}$, and the PAM maps then onto a Kondo lattice model,

$$H = \sum_{\mathbf{k}\sigma} \epsilon_{\mathbf{k}} c_{\mathbf{k}\sigma}^{\dagger} c_{\mathbf{k}\sigma} + \sum_{\mathbf{k}\mathbf{k}'i} J_{\mathbf{k}'\mathbf{k}} e^{-i\mathbf{k}\mathbf{R}_i} \mathbf{S}_i \cdot \mathbf{s}_{\mathbf{k}'\mathbf{k}} , \quad (1.12)$$

where the Kondo couplings $J_{\mathbf{k},\mathbf{k}'}$ are related to the parameters of the Anderson lattice model through $J_{\mathbf{k},\mathbf{k}'} = 2\frac{V_{\mathbf{k}}^*V_{\mathbf{k}'}}{2}\left[\frac{1}{U+\epsilon_f} - \frac{1}{\epsilon_f}\right]$ (Hewson, 1997). This mapping can be made rigorous by a generalization of the Schrieffer-Wolff transformation to the lattice case, as detailed in appendix A. At sufficiently low temperatures, both the Kondo lattice model and the PAM may behave as a conventional Fermi liquid. However, theoretical treatments show also non-Fermi liquid phases as well as antiferromagnetic and superconducting order, e.g., obtained by slave particle techniques (Senthil et al., 2003, 2004). These details certainly depend on microscopic parameters and on the validity of the techniques applied to these models. For small U , perturbation theory in U is a viable method and shows that the PAM leads to a description in terms of a Fermi liquid with two quasiparticle bands (Hewson, 1997). Below a coherence temperature T_{coh} , a Fermi liquid can exist also in the large- U limit, including especially the case of a Kondo lattice. In this kind of Fermi liquid, the local moments need then to be screened by a lattice version of the Kondo effect. According to *non-perturbative* arguments given by Oshikawa (2000), the quasiparticle Fermi surface volume \mathcal{V}_{FS} then counts both the conduction electron density n_c and the local moment density n_f , such that the Luttinger sum rule (Luttinger, 1960)

$$\mathcal{V}_{FL} = \mathcal{K}_d[(n_a)(\text{mod}2)] \quad (1.13)$$

is fulfilled in any spatial dimension d .² Here, $\mathcal{K}_d = (2\pi)^d/(2v_0)$ is a phase space factor, v_0 is the volume of the unit cell of the ground state, $n_a = n_f + n_c$ is the mean number of all electrons per volume v_0 and n_f (an integer) is the number of local moments per volume v_0 . Note that $n_{c,a}$ need not be integers, and the (mod 2) in (1.13) allows neglect of fully filled bands.

In the temperature limit $T \gg T_{\text{coh}}$, the Fermi volume will retain only the conduction electrons. Those are interacting weakly with a paramagnetic system of localized spins. In the crossover region $T \sim T_{\text{coh}}$, the quasiparticles successively lose their coherence and are strongly scattered. In this temperature region the resistivity is significantly enhanced, and in experiments, T_{coh} is thereby often defined by the corresponding resistivity maximum (Löhneysen et al., 2007).

The ground state properties of the Kondo lattice are more diverse than those discussed for the single impurity version of this model, since the local moments have an indirect exchange interaction mediated by the conduction electrons. This has been first shown by Ruderman and Kittel (1954), who considered the problem of nuclear spin ordering in a metal, described by the nuclear spins \mathbf{S}_i of the host atoms arranged on lattice sites indexed by i . Within second order perturbation theory, they derived the exchange interaction (Tsunegutsu et

²Originally, Luttinger's theorem was derived to all orders in perturbation theory (Luttinger, 1960). However, non-perturbative effects may violate this derivation. Oshikawa's derivation of Luttinger's theorem is based on a topological argument and non-perturbative effects in any spatial dimension d . In the Kondo lattice model, in Oshikawa's sumrule the local moments contribute whenever the system is in a Fermi-liquid phase.

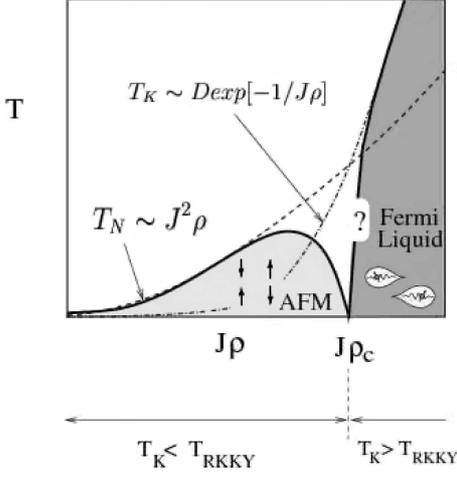


Figure 1.1: Doniach diagram, illustrating the antiferromagnetic regime with an ordering temperature $T_N \sim N_0 J^2$, where $T_K < T_{RKKY}$ and the heavy Fermi-liquid regime, where $T_K > T_{RKKY}$, with $T_{RKKY} = N_0 J^2$. The heavy Fermi-liquid is formed below a coherence temperature T_{coh} . Various experiments have revealed a quantum phase transition between these phases. The behavior of T_{coh} across the quantum phase transition is still a matter of controversy and is discussed in section 1.4. Figure from Coleman (2007).

al., 1997)

$$\begin{aligned}
 \mathcal{H}_{\text{RKKY}} &= J_{\text{RKKY}} \sum_{\langle ij \rangle} \mathbf{S}_i \cdot \mathbf{S}_j F(k_F r_{ij}) \\
 F(x) &= \frac{x \cos(x) - \sin(x)}{x^4} \\
 J_{\text{RKKY}} &= -\frac{9\pi}{8} n_c^2 \frac{J^2}{\epsilon_F}, \tag{1.14}
 \end{aligned}$$

where n_c is the conduction electron density, k_F is the Fermi wave number and J is the hyperfine coupling of the nuclear spins. Today, this form of interaction is well known as the Rudermann-Kittel-Kasuya-Yosida (RKKY) interaction. Particular magnetic structures induced by the RKKY interaction depend on the position of the maximum of the spin susceptibility $\chi(\mathbf{q})$ of the conduction electrons, leading to various possible magnetic structures, including Néel order, ferromagnetism or spiral order. Magnetic properties of rare-earth metals were discussed by Kasuya (1956) based on the RKKY interaction (1.14), and the magnetic structure of most of these materials can be understood by this mechanism. Soon after the discovery of heavy-fermion systems, Doniach (1977) made the radical proposal that the phase diagram of heavy-fermion systems is governed by the Kondo lattice model. Doniach tried to explain the competition between antiferromagnetic order and heavy Fermi-liquid behavior by the competition between two energy scales, the single ion Kondo temperature T_K and the energy scale T_{RKKY} set by the RKKY exchange, given by

$$\begin{aligned}
 T_K &= D\sqrt{N_0 J} \exp(-1/(N_0 J)) \\
 T_{\text{RKKY}} &= N_0 J^2. \tag{1.15}
 \end{aligned}$$

In this picture, T_{RKKY} dominates and gives rise to an antiferromagnetic ground state when J is small, but when J is large, the Kondo temperature is the largest scale and a Kondo-screened state with heavy Fermi-liquid behavior results.

It turns out that the single ion Kondo temperature is in general not coinciding with the coherence temperature scale T_{coh} below which the heavy Fermi-liquid phase is stabilized. Within a mean-field approach to the Kondo lattice model, Burdin et al. (2000) obtained two different energy scales that are relevant for the Kondo lattice problem. Magnetic moments are locally screened upon lowering T below T_K , while the Fermi liquid is stabilized below a coherence temperature T_{coh} which is typically smaller than the temperature scale for local Kondo screening, $T_{\text{coh}} < T_K$. In the weak-coupling limit $N_0 J \ll 1$, the ratio T_{coh}/T_K is a function of the conduction band properties only, independent of the Kondo coupling J (Burdin et al., 2000). This result contradicts Nozières *exhaustion scenario* (Nozières, 1985), proposing that $T_{\text{coh}} \propto T_K^2/D$, such that the single-ion Kondo effect would be very inefficient in stabilizing a coherent Fermi liquid since $T_K/D \ll 1$. Later on, Nozières (2005) admitted that his exhaustion scenario is too simplistic, e.g., it does not correctly account for the flow of the Kondo coupling. Beyond mean-field theory, the Anderson and Kondo lattice models have been studied using the dynamical mean-field theory (DMFT) (Pruschke et al., 2000, Si, 2001). NRG calculations by Pruschke et al. (2000) show that in the metallic regime with a conduction band filling of $n_c \lesssim 0.8$, the ratio T_{coh}/T_K depends only on n_c but not on the Kondo coupling J , contradicting also Nozières exhaustion scenario. Taken together, DMFT and mean-field studies make it plausible that the lattice version of the Kondo effect can stabilize a Fermi liquid phase with a coherence temperature T_{coh} that can be of the same order than the single ion Kondo temperature T_K .

The Doniach argument represents purely a comparison of energy scales and does not provide a detailed mechanism connecting the heavy-fermion phase to the local moment anti-ferromagnet. This issue has received especial attention since the experimental tunability of a quantum phase transition has been discovered by Löhneysen et al. (1994). In the next section, we review the rich experimental and theoretical developments that were initiated by this discovery.

1.4 Quantum criticality in heavy-fermion systems

Quantum criticality describes the collective fluctuations of matter undergoing a second-order phase transition at zero temperature. Heavy-fermion metals have in recent years emerged as prototypical systems to study quantum critical points (Löhneysen et al., 2007). There have been considerable efforts (experimental and theoretical) that use these magnetic systems to address problems that are central to the broad understanding of strongly correlated quantum matter. Here, we summarize some of the basic issues, including the extent to which the quantum criticality in heavy-fermion metals goes beyond the standard theory of order-parameter fluctuations, the nature of the Kondo effect in the quantum-critical regime and the non-Fermi-liquid phenomena that accompany quantum criticality.

General aspects

A quantum mechanical system possesses typically a ground state energy and several excited eigenenergies that altogether can be tuned by changing its coupling constants or applied external fields, denoted collectively by g . In some cases, an excited level can become the

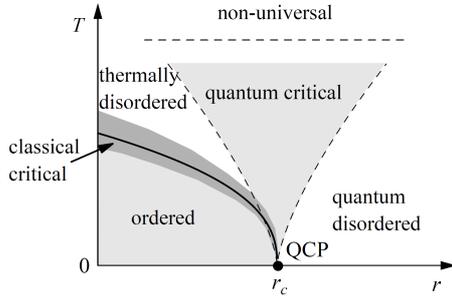


Figure 1.2: Schematic phase diagram in the vicinity of a continuous quantum phase transition as an endpoint of a line of continuous phase transitions. The horizontal axis represents the control parameter r used to tune the system through the quantum phase transition, and the vertical axis is the temperature, T . The solid line marks the finite-temperature boundary between the ordered and disordered phases. Close to this line, the critical be-

havior is classical. Dashed lines indicate the boundaries of the quantum critical region where the leading critical singularities can be observed.

new ground state at a critical value of the tuning parameter g . In other cases, such a level crossing does not occur, but an excited level can become infinitesimally close to the ground state. Both cases will lead to a non-analyticity of the ground state energy as a function of g . A common interpretation is to identify any non-analyticity of the ground state energy as a function of g as a quantum phase transition (Sachdev, 1999). In contrast to a classical phase transition which is induced by thermal fluctuations, such a transition is purely induced by quantum fluctuations. The distance to such a quantum transition is phenomenologically described by a control parameter r , with the quantum phase transition occurring at the critical value $r = 0$, which marks the quantum critical point (QCP) in parameter space. Near the QCP, the control parameter depends linearly on physically accessible parameters, which might be external pressure p , doping x , magnetic field H or some other quantity being suitable to tune the system to its QCP.

A quantum critical point is often the endpoint of a line of second order phase transitions in the parameter space of temperature (T) and control parameter (r). In this case, a generic phase diagram is given by Fig. 1.2 (Vojta, 2003).

The quantum critical point separating two different phases at zero temperature ($T = 0$) has important properties that are qualitatively different from a critical point of a classical phase transition. Although the correlation length ξ diverges as well at a quantum phase transition as at a classical phase transition, at a quantum phase transition it does so both in space and imaginary time. In contrast, classical phase transitions exhibit only a divergent correlation volume in space, ξ^d . The divergence in correlation time, $\tau_c \propto \xi^z$, is described by the dynamical critical exponent z , such that the divergent correlation volume at a quantum phase transition has an effective dimensionality $d + z$. The critical fluctuations in imaginary time are exclusively of quantum mechanical nature and have the characteristic energy scale $\hbar/\tau_c \propto \xi^{-z}$.

Even in a certain finite temperature region of the phase diagram, the existence of a quantum critical point implies important modifications which are absent if only classical phase transitions occur in the phase diagram of a physical system. Those features arise from the competition of quantum fluctuations and thermal fluctuations occurring at the thermal energy scale $k_B T$. Although the energy scale \hbar/τ_c of quantum fluctuations is finite

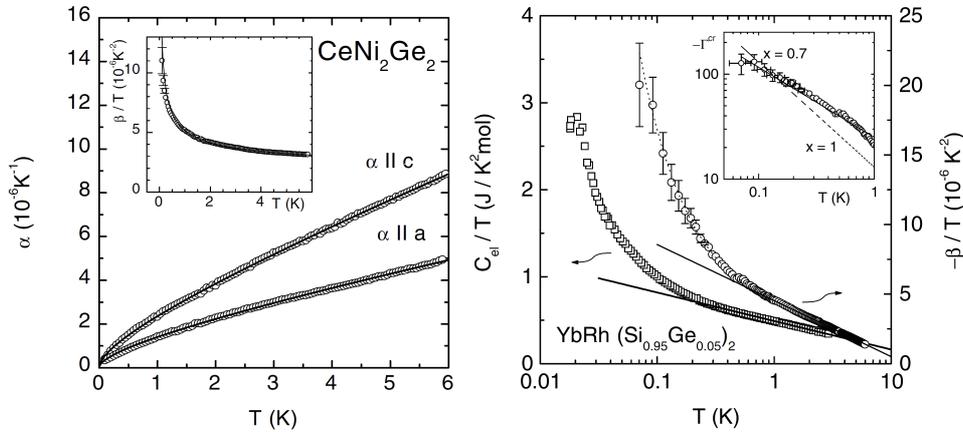


Figure 1.3: Measurements of the linear/volume thermal expansion coefficients α and β in zero field ($B = 0$) in CeNi_2Ge_2 (left) and $\text{YbRh}_2(\text{Si}_{0.95}\text{Ge}_{0.05})_2$ (right). For CeNi_2Ge_2 , $\alpha(T) = a\sqrt{T} + bT$, which fits spin-fluctuation theory. In $\text{YbRh}_2(\text{Si}_{0.95}\text{Ge}_{0.05})_2$, neither of the two regimes is explained within Hertz' theory: For $T > 1\text{K}$, $\beta/T \sim -\log(T_0/T)$ and for $T < 1\text{K}$, $\beta/T \sim a_0 + a_1/T$ (right axis, left axis shows specific heat coefficient). For definitions of α and β , see text. Figures taken from KÜchler et al. (2003).

everywhere except at the QCP, sufficiently deep in the ordered or disordered phase thermal fluctuations are strong enough to render the quantum fluctuations unimportant. The dominance of classical fluctuations is however challenged when temperature is comparable to the typical energy scale of quantum fluctuations,

$$k_B T \sim \hbar/\tau_c \propto \xi^{-z} \propto |r|^{-\nu z} . \quad (1.16)$$

This situation defines a crossover to the quantum critical regime, where

$$k_B T \lesssim \hbar/\tau_c \propto \xi^{-z} \propto |r|^{-\nu z} . \quad (1.17)$$

Finite temperature properties of the quantum critical regime are characteristic for the underlying quantum critical point, which is responsible for many unusual properties observed in real experiments at finite T , including, e.g., non-Fermi liquid behavior in metallic systems. In most cases, the quantum critical regime is separated from any classical phase transition, which is then preempted by a crossover to the classical regime. This crossover can also be understood as a dimensional crossover of a system from $d+z$ to d dimensions. A different situation occurs in dimensions below the *lower critical dimension*, where continuous symmetries cannot be broken at finite temperatures and a corresponding classical phase transition is forbidden (Mermin and Wagner, 1966). Still, a quantum phase transition might occur due to the enhanced effective dimensionality $d+z$ related to a phase transition at $T = 0$. For a more comprehensive introduction to quantum critical phenomena, we refer the reader to the texts of Sachdev (1999) and Vojta (2003).

Hertz' theory

Over 30 years ago, Hertz (1976) put forward a model that has become the standard theory for magnetic instabilities in itinerant electron systems at zero temperature. The finite temperature properties of the Hertz model describe non-Fermi liquid behavior above a zero temperature instability, and those features are widely used to describe experiments on heavy-fermion compounds. Assuming that the critical modes at a magnetic instability are described by a bosonic order parameter field only, the Hertz model introduces an effective action for a three-component order parameter field $\Phi = (\phi_1, \phi_2, \phi_3)^T$. This effective action can be formally derived by decoupling a Hubbard-type interaction with the order parameter field as an auxiliary decoupling field. After integrating out the fermionic degrees of freedom, the effective action is expanded in powers of Φ in the quantum disordered phase, and it is assumed that all terms of higher order in Φ than four are irrelevant in the RG sense. As a result, the general structure of the Hertz effective action is given by

$$\begin{aligned}
 S_{\text{Hertz}} &= S^{(2)}[\Phi] + S^{(4)}[\Phi] \\
 S^{(2)}[\Phi] &= \frac{1}{\beta V} \sum_{\mathbf{k}, \omega_n} \frac{1}{2} \Phi^T(\mathbf{k}, \omega_n) \epsilon_0 \left(\delta_0 + \xi_0^2 k^2 + \frac{|\omega_n|}{\gamma(k)} \right) \Phi(\mathbf{k}, \omega_n) \\
 S^{(4)}[\Phi] &= u_0 \int d\tau \int d^d \mathbf{r} [\Phi^T(\mathbf{r}, \tau) \Phi(\mathbf{r}, \tau)]^2, \tag{1.18}
 \end{aligned}$$

where the prefactor of the $\Phi^T \Phi$ term is identical to the inverse spin susceptibility $\chi^{-1}(\mathbf{k}, \omega_n)$. In this action, the distance to the ordered phase is controlled by the non-thermal control parameter δ_0 . The energy scale ϵ_0 and the correlation length ξ_0 are given by the Fermi energy ϵ_F and the inverse Fermi wave vector k_F^{-1} , respectively.

For an antiferromagnet we have $\gamma(k) \sim \gamma_0$, independent of k , yielding $z = 2$ for the dynamical critical exponent. In three dimensions, the order parameter theory is therefore above its upper critical dimension d_c^+ ($d_c^+ = 4$) and controlled by a Gaussian fixed point. In two dimensions, the interaction is marginal since the theory is at its upper critical dimension, and this case needs special consideration. In recent years, the applicability of the Hertz model to antiferromagnetic instabilities in two dimensions has been questioned by several authors, e.g., by Abanov and Chubukov (2004).

Starting from Eq. (1.18), various critical exponents for thermodynamic quantities can be derived and compared with experiments, as outlined in a seminal RG treatment of the Hertz model by Millis (1993). Numerous experimental results in heavy-fermion systems raise questions about the validity of the approach given by Hertz. One particular example where Hertz' theory fails is depicted in Fig. 1.3, showing the thermal volume expansion coefficient $\beta = \frac{1}{V} \frac{\partial V}{\partial T} \Big|_p$ and the linear thermal expansion coefficient $\alpha = \frac{1}{L} \frac{\partial L}{\partial T} \Big|_p$ in CeNi_2Ge_2 and $\text{YbRh}_2(\text{Si}_{0.95}\text{Ge}_{0.05})_2$ single crystals at ambient pressure and in zero magnetic field. Although both materials are close to an antiferromagnetic quantum critical point for the experimental parameter values and do not show a saturation in the quantity α/T at low temperatures as in a Fermi liquid, it turns out that only the measurements on CeNi_2Ge_2 are described by Hertz-Millis theory (with $d = 3$ and $z = 2$). In contrast, not any values of z and d fully explain the non-Fermi liquid behavior in $\text{YbRh}_2(\text{Si}_{0.95}\text{Ge}_{0.05})_2$ observed over

several decades of temperature.

Not only experimental evidence indicates a failure of Hertz' theory, but also theoretical assumptions can be violated in certain theoretical scenarios. A particular important case where a Landau-Ginzburg-Wilson approach fails occurs if additional degrees of freedom other than magnetism become critical at the transition. A drastic example for such a violation of Hertz' theory would be a breakdown of the Kondo effect at the transition, implying a jump in the Fermi volume, as detailed in the following.

Kondo breakdown

Although it is generally accepted that the zero temperature magnetic quantum phase transition in heavy-fermion metals is caused by a competition of Kondo screening and a tendency to magnetic order caused by RKKY or superexchange interaction, the nature of the phase transition has remained unclear, and at least two different types of magnetically ordered metals seem possible.

(i) Magnetism can arise from a spin-density-wave instability of the parent heavy FL state – a quantum phase transition to such a state is well described by Hertz' theory.

(ii) A different kind of magnetic metal is possible where the localized moments order due to RKKY exchange interactions and do not participate in the Fermi volume, i.e., Kondo screening is absent. We denote this state as a local-moment magnetic (LMM) metal.

The anomalous behavior close to an antiferromagnetic QCP in heavy-fermion systems like $\text{CeCu}_{6-x}\text{Au}_x$ and YbRh_2Si_2 (discussed in detail in the next subsection) is inconsistent with Hertz-Millis theory and has stimulated discussions about a different type of transition. If the ordered state is a LMM metal, the transition to be considered now involves the breakdown of Kondo screening, accompanied by an abrupt change of the Fermi surface. Several theoretical scenarios for such a transition have been put forward in recent years, all of them using the Kondo lattice model (1.12) as a microscopic starting point. For convenience, an explicit Heisenberg exchange is often added to this model, leading to the Kondo-Heisenberg lattice model

$$\mathcal{H}_{\text{KHM}} = \sum_{\mathbf{k}\sigma} \epsilon_{\mathbf{k}} c_{\mathbf{k}\sigma}^\dagger c_{\mathbf{k}\sigma} + J_K \sum_r \vec{S}_r \cdot \vec{s}_r + J_H \sum_{\langle rr' \rangle} \vec{S}_r \cdot \vec{S}_{r'}. \quad (1.19)$$

a) Local QCP within extended DMFT

It has been proposed by Si et al. (1999), Smith and Si (2000) that the breakdown of Kondo screening is a spatially local phenomenon, affecting every spin of the underlying Kondo lattice independently. This idea has been implemented using an extension to dynamical mean-field theory (Si et al., 1999, Smith and Si, 2000), which provides a self-consistent approximation of the Kondo-Heisenberg lattice model by a local impurity problem, becoming exact in the limit of infinite spatial dimensions ($d \rightarrow \infty$). While the usual DMFT maps the lattice problem to a single impurity in a fermionic bath, the extended DMFT (EDMFT) uses a mapping to a so-called Bose-Fermi Kondo model with both fermionic and bosonic baths. The Bose-Fermi Kondo model is known to have a continuous quantum phase transition (Zarand and Demler, 2002) between a phase with Kondo screening and

one with universal local-moment fluctuations, mediated by the competition between the two types of baths. The QCP of the lattice model is thus mapped—via EDMFT—onto the corresponding impurity QCP of the Bose-Fermi Kondo model, where the magnetic instability of the lattice drives the Kondo effect critical. Preliminary approximative solutions of the self-consistency equations in $d = 2$ (Si, 2003, Grepel and Si, 2003, Zhu et al., 2003) show ω/T scaling of the spin susceptibility, with a good quantitative agreement with fits to neutron scattering experiments by Schröder et al. (2000). A fully numerical solution of the self-consistency equations is an open problem, and several important aspects of the EDMFT approach remain to be clarified.

b) Fractionalized Fermi liquid and deconfined criticality

A different scenario for a breakdown of the Kondo effect at a quantum critical point has been given by Senthil et al. (2004), and we discuss the main ideas here. This theory starts with identifying the zero temperature phase that arises when Kondo screening breaks down without the simultaneous onset of magnetic order. A simple mean field theory captures many features of this scenario, and we use it to discuss the basic ideas we shall elaborate further on in chapters 2 and 3. Using a slave-fermion representation of the local moments in Eq. (1.19), $\vec{S}_r = \frac{1}{2} f_{r\alpha}^\dagger \vec{\sigma}_{\alpha\alpha'} f_{r\alpha'}$ with the vector of Pauli matrices $\vec{\sigma}_{\alpha\alpha'}$ and spinful local fermions $f_{r\alpha}$, the Kondo-Heisenberg model can be decoupled with the mean fields $2b_0 \equiv J_K \langle c_{r\alpha}^\dagger f_{r\alpha} \rangle$ and $2\chi_0 \equiv J_H \langle f_{r\alpha}^\dagger f_{r'\alpha} \rangle$. The amplitude χ_0 is always finite below a temperature $T \sim J_H$ and has only the effect of providing a dispersion to the f -fermions. The important part of the resulting mean-field Hamiltonian derived from Eq. (1.19) is therefore – besides ordinary kinetic energy terms of the c - and f -fermions – a hybridization between c and f -fermions of the form $-b_0 \sum_{\mathbf{k}\sigma} (c_{\mathbf{k}\sigma}^\dagger f_{\mathbf{k}\sigma} + h.c.)$. At zero temperature, a finite amplitude of b_0 results, e.g., in the limit $T_K \ll J_H$, and the mean-field ground state is a Fermi-liquid with two fermionic bands. Upon decreasing the ratio J_K/J_H at zero temperature to a critical value, a quantum phase transition occurs where $b_0 = 0$. This phase transition describes a breakdown of the Kondo effect due to the loss of the hybridization between c and f -fermions. The resulting phase is a paramagnet where the conduction electrons form well-defined quasiparticles on their own and the local moments are in a fractionalized spin-liquid state—this phase has been termed a *fractionalized Fermi liquid* (FL^*) (Senthil et al., 2003). This particular theory will be fundamental for the work presented in the next two chapters. Its critical properties can be described by a $U(1)$ -gauge theory that describes the fluctuations around the simple mean-field saddle points. A detailed presentation of the gauge field theory will be given in chapter 3.

c) Spin-charge separation at the QCP

A related scenario for the breakdown of Kondo screening has been proposed by Pépin (2005), using the idea of spin-charge separation as a mechanism for the breakdown of Kondo screening. Concretely, this scenario implies that the heavy fermionic quasiparticles e_σ^- fractionalize into a neutral “spinon” s_σ and a spinless charge e fermion ϕ^- , $e_\sigma^- \rightleftharpoons s_\sigma + \phi^-$ at the QCP. Formally, the Kondo interaction of the Kondo lattice model is decoupled here

with the ϕ^- -fermion as an auxiliary field, and the dynamics of this fermion is key for the critical behavior, e.g., a $T^{-1/3}$ upturn of the low-temperature specific heat derives from the dominant free energy contribution of the ϕ^- -fermions, as observed in YbRh_2Si_2 by Custers et al. (2003).

AFM QCP in experiments

The competition between on-site Kondo interaction, quenching the localized magnetic moments, and intersite RKKY interaction between these moments allows for both non-magnetic and magnetically ordered ground states in heavy-fermion systems. According to the Doniach picture (Doniach, 1977), this competition is governed by a single parameter, the Kondo exchange constant J between conduction electrons and local moments. The strength of the Kondo exchange interaction is usually tuned by composition or chemical pressure, in addition, a magnetic field can suppress Kondo screening. Owing to the extremely strong dependence of the Kondo energy scale on the interatomic distance d , which arises from the exponential dependence of T_K on J , volume changes are often the dominant effect in producing the magnetic-nonmagnetic transition if isoelectronic constituents are substituted against each other (Löhneysen et al., 2007). We will discuss here two systems that exhibit continuous quantum phase transitions that have been characterized thoroughly. These are the materials $\text{YbRh}_2(\text{Si}_{1-x}\text{Ge}_x)_2$ and $\text{CeCu}_{6-x}\text{Au}_x$, that both show non-Fermi liquid behavior that is not compatible with a standard Hertz-Millis theory. Both materials provide particular candidates for the various theories proposing a breakdown of the Kondo effect at the quantum phase transition out of the heavy Fermi-liquid phase. We add here that Hertz-Millis theory is not violated by *all* heavy-fermion materials which show magnetic quantum phase transitions. One example is CeNi_2Ge_2 , discussed already in context of Fig. 1.3, showing a thermal expansion coefficient as expected from Hertz-Millis theory for 3d antiferromagnets. In addition, the specific heat CeNi_2Ge_2 shows a $C/T = \gamma_0 - \beta\sqrt{T}$ behavior (Küchler et al., 2003), as expected for Hertz-Millis theory with $d = 3$ and $z = 2$. Thus, this material appears to follow the predictions of the Landau-Ginzburg-Wilson approach to 3d antiferromagnets.

A detailed discussion of $\text{YbRh}_2(\text{Si}_{1-x}\text{Ge}_x)_2$ and $\text{CeCu}_{6-x}\text{Au}_x$ has been given by Löhneysen et al. (2007), and further references and details that we omit in the following two paragraphs can be found there.

a) $\text{CeCu}_{6-x}\text{Au}_x$ The parent compound of $\text{CeCu}_{6-x}\text{Au}_x$, CeCu_6 , has been established as a heavy-fermion system showing no long-range magnetic order down to the range of ~ 20 mK. Upon alloying with Au the CeCu_6 lattice expands while retaining the orthorhombic (at room temperature) Pnma structure. Thereby, the hybridization between Ce $4f$ electrons and conduction electrons, and hence J , decreases, leading to the stabilization of localized magnetic moments which interact via the RKKY interaction. The result is incommensurate antiferromagnetic order in $\text{CeCu}_{6-x}\text{Au}_x$ beyond a threshold Au concentration $x_c \approx 0.1$, as has been confirmed, e.g., by neutron scattering (Chattopadhyay et al., 1990, Schröder et al., 2000). This behavior of magnetic order upon Au doping is depicted in Fig. 1.4, together with specific heat data for various pressures at the dopant concentration

$x \approx 0.2$ plotted as C/T . The specific heat coefficient C/T does not seem to saturate at low temperatures for pressures close to a pressure-induced quantum critical point, showing a violation of Fermi-liquid theory. The specific heat data can be temperature-integrated to obtain the entropy $S = \int_0^T dT' \frac{C_V}{T'}$, where the dominant low-temperature contribution arises from the Ce local moments. A characteristic temperature for the onset temperature of local Kondo screening is given by $T_{1/2}$, the temperature where the entropy per local moment reaches $0.5R \ln 2$, which is half the value given by a free local moment with effective spin $1/2$. In a doping driven quantum phase transition in $\text{CeCu}_{6-x}\text{Au}_x$, a finite value of $T_{1/2}$ was obtained at the quantum critical point (Löhneysen et al., 1996).

Interestingly, a logarithmically divergent specific heat coefficient can be obtained within a Hertz-Millis like theory of a *two-dimensional* order parameter coupled to quasiparticles with $3d$ dynamics (Rosch et al., 1997). The interpretation of inelastic neutron scattering data at the critical concentration $x_c = 0.1$ show strong spatial anisotropy of the spin fluctuations (Stockert et al., 1998). Whether the anisotropy is strong enough to qualify them as being $2d$ is still a matter of debate. Inelastic neutron scattering experiments by Schröder et al. (2000) at the quantum critical point revealed the scaling behavior

$$\chi^{-1}(\mathbf{q}, E, T) = c^{-1}[f(\mathbf{q}) + (-iE + aT)^\alpha] \quad (1.20)$$

of the dynamical spin susceptibility $\chi(\mathbf{q}, E, T)$ with an anomalous scaling exponent $\alpha = 0.74 \neq 1$. This type of scaling is incompatible with the Hertz model—there E/T scaling is only expected below the upper critical dimension, which is $d = 2$ for the metallic antiferromagnet. Altogether, these experiments prompted new theoretical concepts considering a breakdown of the Kondo effect at the quantum critical point.

b) $\text{YbRh}_2(\text{Si}_{1-x}\text{Ge}_x)_2$ The compound YbRh_2Si_2 was the first Yb compound to show pronounced non-Fermi-liquid effects near a magnetic ordering transition. Maxima in the AC susceptibility (Trovarelli et al., 2000) as well as a kink in the resistivity around 70 mK (Gegenwart, 2002) signal the onset of antiferromagnetic ordering, although to date no neutron scattering data are available to further justify this assignment. Interestingly, Gegenwart et al. (2005) reported evidence for *ferromagnetic* quantum critical fluctuations. Even the tiny critical field of 60 mT induces a sizable magnetization of almost $0.1\mu_B$ per Yb such that YbRh_2Si_2 is almost ferromagnetic (Gegenwart, 2002). Importantly, YbRh_2Si_2 is a stoichiometrically clean sample close to a quantum critical point that can be tuned by application of a weak magnetic field $H_{\perp c} \approx 0.06$ T perpendicular to the c -axis and a stronger field $H_{\perp c} \approx 0.66$ T applied along the c -axis. Well above the magnetic ordering temperature and near the magnetic field-tuned quantum critical point, the specific heat coefficient γ shows a logarithmic divergence $C_V/T \propto \ln(T_0/T)$, similar to that observed in $\text{CeCu}_{6-x}\text{Au}_x$. Below $T=0.4$ K, the specific heat becomes more singular, $C_V/T \propto T^{-\alpha}$ with $\alpha \sim 0.3$. A further interesting discovery for YbRh_2Si_2 is the observation of a divergent *Grüneisen parameter*³ $\Gamma \propto T^{-0.7}$ at lowest temperatures, which fits Hertz-Millis theory for antiferromagnetic quantum critical points neither in $2d$ nor in $3d$ (Küchler et al., 2003). One

³The Grüneisen parameter Γ is defined as the ratio of the thermal expansion coefficient α and the molar specific heat c_p .

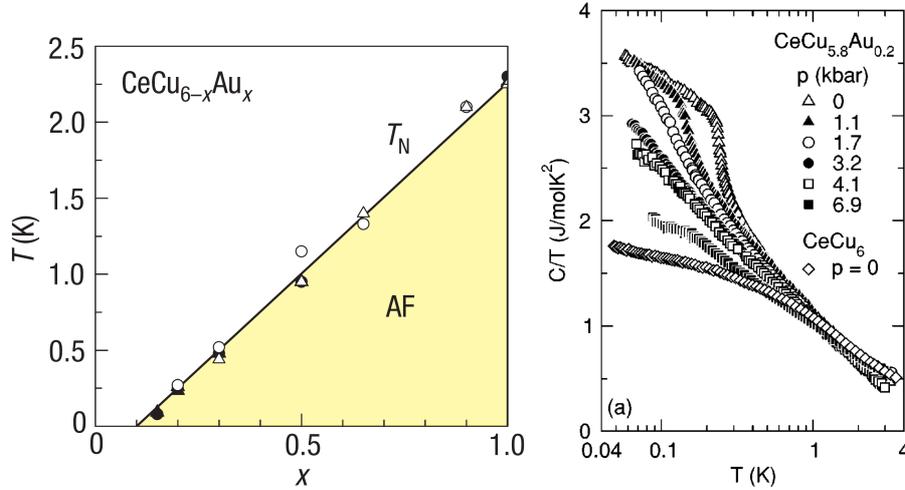


Figure 1.4: Quantum phase transition and non-Fermi liquid behavior in $\text{CeCu}_{6-x}\text{Au}_x$ induced by doping and pressure, respectively. Left: AF ordering temperature T_N versus Au concentration x for $\text{CeCu}_{6-x}\text{Au}_x$, showing a doping-induced quantum critical point. Figure from Gegenwart et al. (2008) at $x_c \simeq 0.1$. Right: Specific heat coefficient C of $\text{CeCu}_{5.8}\text{Au}_{0.2}$ plotted as C/T vs T on a logarithmic scale. Hydrostatic pressure tunes a quantum phase transition to a non-magnetic phase. At $p = 4.1$ kBar the non-Fermi liquid behavior $C/T = a \ln(T_0/T)$ is observed over two decades of temperature. Figure from Löhneysen et al. (1996, 1998).

of the central questions for quantum phase transitions out of the heavy Fermi-liquid phase is whether the Fermi volume changes abruptly at the underlying second-order transition. If the Fermi volume evolves discontinuously at a zero-temperature transition, a discontinuous evolution of the Hall constant is expected (Si et al., 1999, Coleman et al., 2001, 2005). Indeed, a rapid crossover of the Hall constant across a field driven quantum critical point in YbRh_2Si_2 has been measured, with a scaling of the half-width of the field-driven crossover with \sqrt{T} (Paschen et al., 2004). Newer data exists that confirms a scaling behavior of this half-width down to the lowest measured temperature $T = 20$ mK, but proportional to T instead of \sqrt{T} (Friedemann, 2009). An extrapolation of this crossover towards a jump of the Hall constant at zero temperature would give strong arguments for a jump of the Fermi volume at the QCP, but further measurements also at lower temperatures are needed to sufficiently justify such an extrapolation. Interestingly, the Hall-effect crossover is accompanied by changes in the slope of the isothermal magnetization and magnetostriction, see Fig. 1.4. These findings suggest the existence of an additional energy scale distinct from the Fermi liquid coherence temperature.

We close this paragraph by mentioning recent experiments by Friedemann et al. (2009) on $\text{Yb}(\text{Rh}_{2-x}\text{M}_x)\text{Si}_2$, with $\text{M}=\text{Ir}, \text{Co}$ substituting Rh , causing positive or negative chemical pressure on the unit cell. The magnetically ordered phase of YbRh_2Si_2 is shifted either to

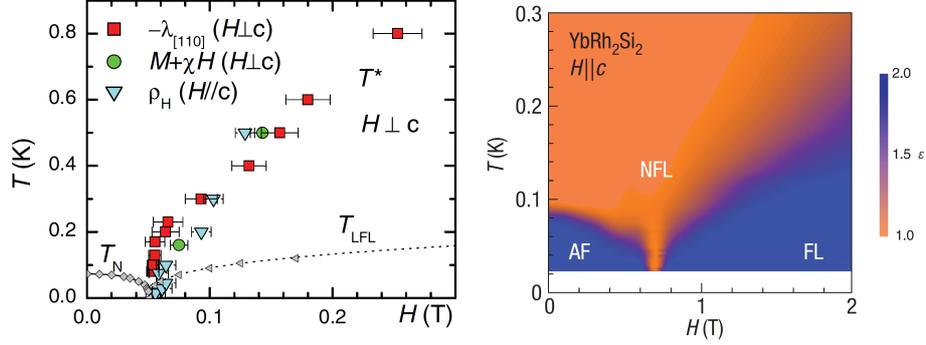


Figure 1.5: Left: The crossover temperature T^* in YbRh_2Si_2 as determined from crossovers in the field dependence of the magnetostriction $\lambda_{[110]}$, the effective magnetization $\tilde{M} = M + \chi H$ and the Hall resistivity ρ_H . The gray diamonds and triangles represent, respectively, the Néel ordering temperature (T_N) and the crossover temperature T_{LFL} , below which the electrical resistivity has the Fermi liquid form $\rho = \rho_0 + AT^2$. Right: Evolution of ε , the exponent in $\Delta\rho(T) = [\rho(T) - \rho_0] \propto T^\varepsilon$, within the temperature-field phase diagram of a YbRh_2Si_2 single crystal. The non-Fermi liquid (NFL) behavior, $\varepsilon = 1$ (yellow), is found to occur at the lowest temperatures right at the QCP, $H = H_c = 0.66 \text{ T}$ ($\mathbf{H} \parallel \mathbf{c}$). Data taken from Gegenwart et al. (2008) (left) and Custers et al. (2003) (right), where further details are provided.

overlap with the energy scale T^* in case of Co doping or away from the T^* line in case of Ir doping. In the latter case, the magnetic transition separates from the FL phase, and an additional zero temperature quantum phase emerges in between. These findings pose new questions about the nature of the quantum phase transition in YbRh_2Si_2 .

1.5 Motivation and outline

In this first part of the thesis, we will analyze one particular theoretical proposal for a breakdown of the Kondo effect at a heavy-fermion quantum critical point. Above, we introduced the scenario of Senthil et al. (2004), that proposes a primary instability to a phase without symmetry breaking in the local moment sector. In chapter 2, we analyze modifications to this transition by coupling lattice degrees of freedom to the Kondo lattice model. This analysis is in particular motivated by the observation of strong first order transitions in trivalent rare earth metals. Other important properties of a Kondo-breakdown transition might be measured in transport properties, due to the volume collapse of the Fermi surface predicted by Senthil et al. (2004). In chapter 3, we will devise transport equations describing the interplay of the several low-energy degrees of freedom in the quantum critical region of the Kondo-breakdown transition and give a preliminary interpretation of physical implications.

Chapter 2

Kondo Volume collapse transitions in heavy-fermion metals

Most theoretical approaches for heavy-fermion systems start from suitable versions of the Anderson- or Kondo lattice model. These models contain minimal physical mechanisms that can explain a heavy Fermi-liquid phase and a competing tendency to magnetic order. However, it is known from experiment that the coupling parameters of these models are difficult to be tuned directly and experiments rely mostly on changes of the unit cell dimension, which can either be induced by doping different atoms or applying external pressure. It is therefore conceivable that the coupling of electronic to lattice degrees of freedom can play a nontrivial role for the overall shape of the phase diagram, which is the main motivation of our subsequent analysis.

A well known but spectacular example are the pressure-induced volume-collapse transitions in the trivalent rare earth metals, such as the transition between α - and γ -Ce (Thalmeier and Lüthi, 1991). In this material, a line of first-order transitions in the pressure-temperature plane is found with a finite temperature critical endpoint. The first order transition has been quantitatively analyzed (Allen and Martin, 1982, Lavagna et al., 1982, 1983) by a volume dependence of the Kondo exchange coupling of a Kondo impurity Hamiltonian. In this description, the large elastic energy change across the transition is balanced by an increasing single ion Kondo temperature, a phenomenon that is often referred to as *Kondo volume-collapse* transition (Allen and Martin, 1982). Since both Kondo volume collapse transitions and quantum phase transitions in heavy-fermion materials can be tuned by external pressure, thereby strongly influencing the Kondo exchange coupling J , an intricate interplay of electronic and lattice degrees of freedom may be expected in heavy-fermion materials. It is the purpose of this chapter to derive and study a model that contains the ingredients both for the Kondo-breakdown quantum phase transition as well as for the Kondo volume collapse physics. In a detailed study of the unified phase diagram for both phenomena, of particular interest will be whether a continuous Kondo breakdown transition survives upon including a coupling to the lattice degrees of freedom.

2.1 Derivation of the model and large-N theory

The $\gamma \rightarrow \alpha$ transition in Ce metal is a very prominent example how lattice degrees of freedom can couple to the Kondo effect in a non-trivial manner. Several theoretical scenarios have been considered to explain this transition, and we will finally stick to the most realistic scenario that we will apply to derive a suitable microscopic model to describe changes by hydrostatic pressure in heavy-fermion materials later on.

Importantly, the $\gamma \rightarrow \alpha$ transition is a first order and isostructural fcc \rightarrow fcc transition, involving the loss of magnetic moments and a volume decrease of about 15% in the α -phase (Thalmeier and Lüthi, 1991). It is generally agreed that in the γ -phase there is only one localized $4f$ electron per cerium atom and that the phase transition involves some change in the state of the $4f$ electron. Explanations of the phase transition involve changes in the energy scale of either spin or charge fluctuations throughout the transition. Two scenarios for changes in the *charge fluctuations* have been proposed.

(i) In the *promotional model* (Coqblin and Blandin, 1968), the $4f$ level moves from below to above the Fermi energy in the $\gamma \rightarrow \alpha$ transition, so that the electronic configuration changes from $4f^1c^3$ to $4f^0c^4$, where c^n denotes n conduction electrons contributed per cerium.

(ii) A different interpretation has been given using a *Mott transition picture* (Johansson, 1974), in which the $4f$ electrons retain their $4f$ character in both phases, but are described by traditional band theory in the α -phase, whereas they are Mott localized in the γ -phase. Both scenarios are not confirmed by experiments, which show small changes in both the f -occupation and the Coulomb repulsion U across the transition. A successful description has been given instead in terms of a change in the spin-fluctuation energy of the $4f$ electrons. These spin fluctuations are described by the virtual processes

$$f^0c^4 \rightleftharpoons f^1c^3 \rightleftharpoons f^2c^2 \quad (2.1)$$

that mediate the superexchange interaction known as Kondo exchange (see section 1.2). Therefore, the relevant energy scale that changes across the transition is a suitably defined Kondo temperature, and this scenario has led to the so called *Kondo volume-collapse* (KVC) *model* for the $\gamma \rightarrow \alpha$ transition in cerium (Allen and Martin, 1982, Lavagna et al., 1982, 1983).

The Kondo volume collapse model

Originally, the Kondo volume collapse model has been derived using an Anderson impurity Hamiltonian with parameters obtained from electron spectroscopy (Allen and Martin, 1982). Here, we use the more realistic formulation in terms of an Anderson lattice model

$$\begin{aligned} H = & \sum_{\mathbf{k}\sigma} \epsilon_{\mathbf{k}} c_{\mathbf{k}\sigma}^\dagger c_{\mathbf{k}\sigma} + \sum_{i\sigma} \epsilon_f^0 f_{i\sigma}^\dagger f_{i\sigma} \\ & + U \sum_i n_{i\uparrow}^f n_{i\downarrow}^f + \frac{1}{\sqrt{N}} \sum_{\mathbf{k}i\sigma} (V_{\mathbf{k}} e^{-i\mathbf{k}\cdot\mathbf{R}_i} c_{\mathbf{k}\sigma}^\dagger f_{i\sigma} + H.c.) , \end{aligned} \quad (2.2)$$

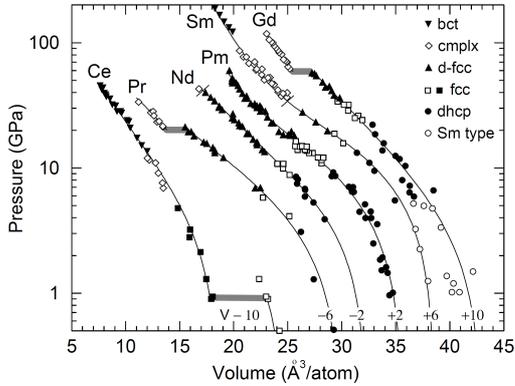


Figure 2.1: Pressure-volume data for the rare earths. Structures are identified, with “cmplx” signifying a number of complex, low-symmetry structures. The volume collapse transitions are marked by the wide hatched lines for Ce, Pr, and Gd, while lines perpendicular to the curves denote the d-fcc to hP3 symmetry change in Nd and Sm. The curves are guides to the eye. Note that the data and curves have been shifted in volume by the numbers (in $\text{\AA}^3/\text{atom}$) shown at the bottom of the figure. Figure from McMahan et al. (1998).

describing the hybridization of conduction electrons with local atomic f -orbitals located on the lattice sites. In this model, the first term describes the conduction electrons with some filling n_c of the energy band, while the f orbitals are characterized by the bare f electron energy ε_f and the Coulomb repulsion U . The hybridization matrix element $V_{\mathbf{k}} = \langle \mathbf{k} | \hat{V} | f \rangle$ describes the overlap of the conduction electron wave function $|\mathbf{k}\rangle$ with the atomic potential \hat{V} acting onto the f electron in the orbital state $|f\rangle$. In the following, we neglect any \mathbf{k} -dependence of the hybridization, setting $V_{\mathbf{k}} \equiv V$. The underlying lattice geometry might be a regular $2d$ or $3d$ lattice, the former being realized in layered materials with weak electronic interlayer coupling.

We now want to describe the influence of hydrostatic pressure onto the various model parameters of the Anderson lattice model (2.2). Our description is motivated by the Kondo volume collapse model of Dzero et al. (2006) that uses an Anderson lattice model with a strain-dependent hybridization. While in principle all parameters of the Anderson lattice model are modified by changing the unit cell dimensions, experimental data on elemental Ce shows that the f level occupation and the f electron levels are nearly unchanged during the volume collapse transition (see Allen and Martin (1982) and references therein). Similarly, the Coulomb repulsion stays close to a large value of $6 - 7$ eV during the collapse transition (Wieliczka, 1982). The most obvious change in experiment is a change in the width Γ of the imaginary part of the dynamic spin susceptibility, $\chi''(\omega, \mathbf{Q})$, fitted to a Lorentzian $\chi''(\omega, \mathbf{Q}) = C\Gamma\omega/(\Gamma^2 + \omega^2)$ in a region of weak dependence on \mathbf{Q} with a normalization constant C (Shapiro et al., 1977). Neutron scattering shows a tremendous change from $\Gamma \sim 10 - 14$ meV in the γ -phase to $\Gamma \gtrsim 70$ meV in the collapsed α -phase,¹ and this change has been interpreted as an order of magnitude change of the Kondo temperature by defining the energy width of the susceptibility as a measure of the Kondo temperature, $\Gamma \sim T_K$. Altogether, these results motivate us to neglect any volume dependence other than that of the hybridization matrix elements, which will influence the

¹The energy width Γ in the α -phase is probably even considerably higher than 70 meV, since the energy resolution of Shapiro et al. (1977) did not resolve an energy width larger than 70 meV.

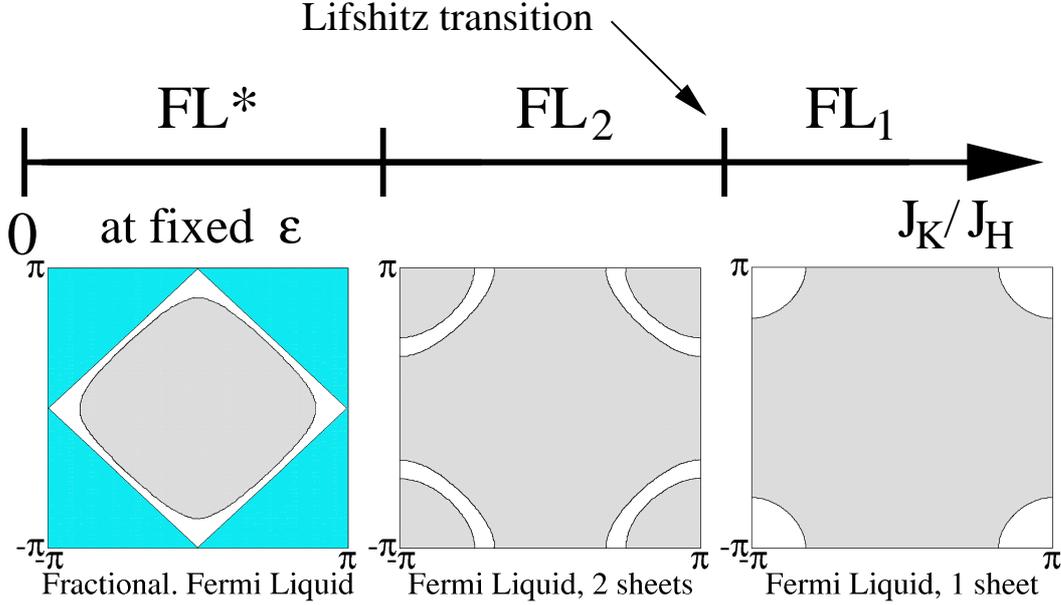


Figure 2.2: Fermi surface evolution from FL^* to FL , where shaded areas correspond to occupied states. Left: FL^* , with one spinon (dark) and one conduction electron (light) sheet. Note that the spinon band is hole-like. Middle: FL_2 , with two sheets, where the outer one represents heavy quasiparticles with primarily f character. Right: FL_1 , with one heavy-electron sheet. FL_2 and FL_1 are separated by a Lifshitz transition where the outer Fermi sheet disappears at critical value of the ratio J_H/J_K . The conduction band has a filling of $n_c = 0.8$. (The corresponding band structures are also shown in Fig. 2.7 below.)

Kondo temperature with exponential sensitivity according to Eq. (1.6) - while in principle also the conduction electron bandwidth depends on volume, both quantities will influence the Kondo temperature with exponential sensitivity since $N_0 \sim 1/D$ for a flat band, and for our qualitative considerations, taking into account the volume dependence of one is sufficient. The order parameter at a volume collapse transition is the trace

$$\epsilon \equiv \text{tr}\{\hat{\epsilon}\} \quad (2.3)$$

of the strain tensor $\hat{\epsilon}$, which describes relative volume changes of the unit cell, $\epsilon = \frac{V-V_0}{V_0}$ where V_0 is a reference volume that we will specify later on.

The entries of the strain tensor are conveniently defined as (Landau and Lifshitz, 1986)

$$\epsilon_{ik} = \frac{1}{2} \left(\frac{\partial u_i}{\partial x_k} + \frac{\partial u_k}{\partial x_i} \right) \quad (2.4)$$

with the displacement field $\mathbf{u}(\mathbf{r})$ that measures the local displacement of a differential volume element (Landau and Lifshitz, 1986). Under hydrostatic conditions, only the diagonal entries $\epsilon_i \stackrel{\text{def}}{=} \epsilon_{ii}$ are non-zero, describing a relative local length change along the axis

\hat{e}_i . Usually, the ϵ_i are referred to as mechanical strain, and we shall use the terminology “strain” in the following. In presence of acoustic phonons, e.g., the quantity ϵ is local, denoted by $\epsilon(\mathbf{r})$. For small changes of the local strain $\epsilon(\mathbf{r})$, the hybridization can be linearized in the local strain, and for *cubic symmetry* of the unit cell, the Anderson lattice Hamiltonian (2.2) obtains the additional contribution

$$\mathcal{H}_c = \gamma V \sum_{i\sigma} \epsilon(\mathbf{r}_i) (f_{i\sigma}^\dagger c_{i\sigma} + H.c.) + \frac{B V_0}{2 \mathcal{N}} \sum_i \epsilon(\mathbf{r}_i)^2, \quad (2.5)$$

where the bulk elastic energy has been parameterized using the bulk modulus $B = -V_0 \frac{\partial p}{\partial V}|_{V=V_0}$ and the coefficient γ describes the assumed linear local strain dependence of the hybridization. It is important to stress that the parameterization (2.5) in terms of lattice distortions is appropriate only for cubic systems like Ce, Yb or polycrystalline samples (Thalmeier and Lüthi, 1991). Many heavy-fermion systems have no cubically symmetric unit cell, and the parameterization (2.5) can then only lead to a qualitative description. However, it is hopeless to capture material-specific details of an exhaustive list of heavy-fermion materials within a single model calculation.

At the volume collapse transition, the elastic energy term leads to an increase in energy of the compressed solid. This energy increase is compensated by a gain in hybridization and thus a coupling constant $\gamma > 0$ (Shapiro et al., 1977, Dzero et al., 2006) with a magnitude that has to be fitted to the experimentally observed change in the energy scale T_K as obtained, e.g., from the dynamical spin susceptibility (see above). The competition of these two energy contributions as a function of lattice strain yields a non-linear equation of state $p(V) = -\frac{\partial F}{\partial V}|_T = -\frac{1}{V_0} \frac{\partial F}{\partial \epsilon}|_T$. The resulting non-linear $p - V$ isotherms are similar to the van-der-Waals theory of the liquid-gas transition (Allen and Martin, 1982), see also Fig. A.1. A mean-field theory analysis of this model has been discussed by Dzero et al. (2006), and a zero-temperature volume collapse transition in the heavy Fermi-liquid phase was found below a critical value B^* of the bulk modulus. In our subsequent analysis, we shall discuss the interplay of volume collapse transitions with a possible breakdown of the Kondo effect due to competing intermoment exchange.

Coupling heavy-fermions to lattice degrees of freedom

Across the volume collapse transition in Ce, the f -valence changes not drastically, and spin fluctuations are considered to be the most important energy scale. We will in general neglect charge fluctuations in the f -orbitals for our discussion of heavy-fermion physics in presence of electron-lattice coupling. This approximation is also motivated by our discussion of Kondo-breakdown transitions, for which it is convenient to consider the Kondo regime of the Anderson lattice model. On the formal level, this step is achieved by taking the Kondo limit $N_0 \frac{V^2}{\epsilon_f + U}, N_0 \frac{V^2}{\epsilon_f} \rightarrow 0$ (with $\epsilon_f < 0$ and $\epsilon_f + U > 0$), thereby fixing the f valence to unity. The resulting Kondo lattice model has the form

$$\begin{aligned} \mathcal{H}_{\text{KLM}} = & \sum_{\mathbf{k}} \epsilon_{\mathbf{k}} c_{\mathbf{k}\sigma}^\dagger c_{\mathbf{k}\sigma} + J_K (1 + \gamma\epsilon)^2 \sum_r \mathbf{S}_r \cdot \mathbf{s}_r \\ & - \frac{\mathcal{N}}{4} J_K (1 + \gamma\epsilon)^2 + \frac{B}{2} V_0 \epsilon^2 \end{aligned}$$

where $\mathbf{s}_{\mathbf{r}} = \frac{1}{2}c_{\mathbf{r}\sigma}^\dagger \boldsymbol{\sigma}_{\sigma\sigma'} c_{\mathbf{r}\sigma'}$ is the local spin density of the conduction electrons, coupling to spin-1/2 local moments $\mathbf{S}_{\mathbf{r}}$. The additional constant appearing in the model can be understood from a rigorous formulation of the Schrieffer-Wolff transformation for the periodic Anderson model (see appendix A.1).

It remains to discuss the influence of lattice distortions on interorbital magnetic exchange, which we will neglect due to two reasons.

(i) This exchange interaction sets an energy scale $J_{\text{RKKY}} \propto \rho_F J^2$ (Ruderman and Kittel, 1954) that is much less sensitively dependent on the Kondo exchange coupling J than the competing energy scale T_K with its exponential dependence $T_K = D\sqrt{N_0 J} \exp(-1/(N_0 J))$.

(ii) It is mainly the ratio T_K/J_{RKKY} that influences the physics, and qualitative considerations are already possible by coupling only one of these energy scales to pressure.

In order to simplify an approximative treatment of the correlated lattice problem, it is then justified to supplement our microscopic model with an explicit Heisenberg-type exchange that is not coupled to the local strain,

$$\begin{aligned} \mathcal{H}_{\text{KHM}} = & \sum_{\mathbf{k}} \epsilon_{\mathbf{k}} c_{\mathbf{k}\sigma}^\dagger c_{\mathbf{k}\sigma} + J_K (1 + \gamma\epsilon)^2 \sum_{\mathbf{r}} \mathbf{S}_{\mathbf{r}} \cdot \mathbf{s}_{\mathbf{r}} \\ & - \frac{\mathcal{N}}{4} J_K (1 + \gamma\epsilon)^2 + \frac{B}{2} V_0 \epsilon^2 + J_H \sum_{\langle \mathbf{r}\mathbf{r}' \rangle} \mathbf{S}_{\mathbf{r}} \cdot \mathbf{S}_{\mathbf{r}'} . \end{aligned} \quad (2.6)$$

In the following, we will analyze the zero-temperature phase diagram of the model \mathcal{H}_{KHM} using the slave-particle theory of Senthil et al. (2004), allowing to capture a Kondo-breakdown transition and its competition with Kondo volume collapse physics.

Large- N theory

Various approaches have been employed to analyze the phase diagram of the Kondo-Heisenberg model (2.6) at fixed ϵ , while an exact treatment is still lacking. By extending the symmetry of local moments and conduction electrons to the $SU(N)$ group, a specific saddle point of the action corresponding to Eq. (2.6) is approached in the limit $N \rightarrow \infty$, and corrections to this saddle point description arising at finite N can be analyzed by considering fluctuations around the saddle point (Burdin et al., 2002, Senthil et al., 2004). This approach has found extensive application in the analysis of Kondo lattice models, with various different implementations of a large- N limit.

A suitable language to interpret the Kondo effect is a fermionic representation of the local moments, since it allows to capture phases both with and without Kondo screening (Hewson, 1997). In order to introduce an expansion parameter for an approximate solution, we formally extend the local moment symmetry group to $SU(N)$ symmetry, such that the Heisenberg exchange is given by

$$\mathcal{H}_H = \frac{J_H}{N} \sum_{\langle ij \rangle} \hat{S}_\alpha^\beta(i) \hat{S}_\beta^\alpha(j) \quad (2.7)$$

where $\hat{S}_\alpha^\beta(\vec{r})$ are the generators of the $SU(N)$ symmetry group and repeated indices $\alpha, \beta = 1, \dots, N$ are summed over. We will represent the generators $\hat{S}_\alpha^\beta(\vec{r})$ in terms of neutral

fermions $f_{r\sigma}$ with a local constraint

$$\hat{S}_\alpha^\beta(\vec{r}) = f_{r\alpha}^\dagger f_{r\beta} - \frac{\delta_{\alpha\beta}}{2}, \quad \sum_{\sigma=1}^N f_{r\sigma}^\dagger f_{r\sigma} \equiv \frac{N}{2}. \quad (2.8)$$

This representation has been used extensively for studies of the antiferromagnetic Heisenberg model (Marston and Affleck, 1989, Georges et al., 2001) and Kondo lattice models (Burdin et al., 2002, Senthil et al., 2004). To allow for a consistent large- N treatment of the Heisenberg model, the spin degeneracy of the conduction electrons is simultaneously adjusted to N and the Kondo coupling is rescaled as $J_K \rightarrow \frac{J_K}{N}$, leading to

$$\mathcal{H}_K = \frac{J_K}{N} \sum_{\sigma\sigma'r} \hat{S}_\sigma^{\sigma'}(r) c_{r\sigma'}^\dagger c_{r\sigma}, \quad (2.9)$$

which is the Coqblin-Schrieffer form of the Kondo interaction Hamiltonian (Coqblin and Schrieffer, 1969). Note that the exchange interaction term (2.9) contains the SU(2) symmetric Kondo exchange interaction as the special case $N = 2$. Using the pseudofermion representation (2.8), the interaction terms $\mathcal{H}_\mathcal{H}$ and \mathcal{H}_K become quartic in fermions, and an exact solution is still out of reach. A convenient way to select an approximative solution is prepared by rewriting the full Hamiltonian in a path integral language, where the action is given by:

$$\begin{aligned} S &= S_c + S_{fc} + S_f \\ S_c &= \int d\tau \sum_{\mathbf{k}} \bar{c}_{\mathbf{k}\sigma} (\partial_\tau - \varepsilon_{\mathbf{k}}) c_{\mathbf{k}\sigma}, \\ S_f &= \int d\tau \frac{J_H}{N} \sum_{\langle rr' \rangle} \sum_{\sigma\sigma'} [\bar{f}_{r\sigma} f_{r\sigma'} - \frac{\delta_{\sigma\sigma'}}{2}] [\bar{f}_{r'\sigma'} f_{r'\sigma} - \frac{\delta_{\sigma\sigma'}}{2}] \\ S_{cf} &= \int d\tau \frac{J_K}{N} \sum_{\langle rr' \rangle} \sum_{\sigma\sigma'} [\bar{f}_{r\sigma} f_{r\sigma'} - \frac{\delta_{\sigma\sigma'}}{2}] c_{r\sigma'}^\dagger c_{r\sigma}. \end{aligned} \quad (2.10)$$

We note that the couplings J_K and J_H in the interaction terms have been appropriately rescaled to lead to an action that becomes extensive in the parameter N , $S \propto N$. In analogy to the classical limit $\hbar \rightarrow 0$, the limit $N \rightarrow \infty$ can therefore be used to construct a Gaussian saddle point with corrections that are controlled by the parameter $1/N$. Various saddle points can be realized by rewriting the action (2.10) using auxiliary fields, and a choice of auxiliary fields is thus necessarily guided by physical principles. We will illustrate them after presenting some fundamental definitions.

For our purpose, we introduce Hubbard-Stratonovich fields $b_r(\tau)$ conjugate to $\sum_\sigma f_{r\sigma}^\dagger c_{r\sigma}$

and $\chi_{ij}(\tau)$ conjugate to $\sum_{\sigma} f_{i\sigma}^{\dagger} f_{j\sigma}$, thus that the action has to be rewritten as

$$\begin{aligned}
S' &= S_c + S_f + S_{fc} + S_b \\
S_c &= \int d\tau \sum_{\mathbf{k}} \bar{c}_{\mathbf{k}\sigma} (\partial_{\tau} - \varepsilon_{\mathbf{k}}) c_{\mathbf{k}\sigma} \\
S_f &= \int d\tau \left[\sum_r \bar{f}_{r\sigma} (\partial_{\tau} - ia_0(r)) f_{r\sigma} - \sum_{\langle ij \rangle} \chi_{ij}^* \left(\sum_{\sigma} \bar{f}_{i\sigma} f_{j\sigma} \right) + h.c. \right] \\
&\quad + \sum_{\langle ij \rangle} \frac{4|\chi_{ij}|^2}{J_H} \\
S_{cf} &= - \int d\tau \sum_r (b_r \bar{c}_{r\sigma} f_{r\sigma} + h.c.) \\
S_b &= \int d\tau \sum_r \frac{2|b_r|^2}{J_K}
\end{aligned} \tag{2.11}$$

and the auxiliary fields $b_r(\tau)$ and $\chi_{ij}(\tau)$ have to be integrated over in order to recover the original partition function according to

$$\int \mathcal{D}\chi \mathcal{D}b \exp(-iS'[b_r(\tau), \chi_{ij}(\tau)]) = \exp(-iS) , \tag{2.12}$$

with the original action S given by Eq. (2.10). The Lagrangian multiplier $a_0(r)$ fulfills the local particle number conservation law for the spinons and we omitted a quadratic term of the spinons that will only lead to a constant shift of $a_0(r)$. It is convenient to represent the field $\chi_{ij}(\tau)$ as

$$\chi_{rr'}(\tau) = \exp(ia_{rr'}(\tau)) \chi_{0rr'}(\tau) . \tag{2.13}$$

As long as the amplitude $\chi_{0rr'}$ stays finite, its amplitude fluctuations have a mass gap and we can make use of the identity $\chi_{0rr'} \equiv \chi_0$ in the effective low energy theory (Senthil et al., 2004). In this way, the interaction between the spinons is mediated by the compact $U(1)$ gauge field $a_{rr'}(\tau)$, whose temporal component is $a_0(r)$. We note here that the transformation $a_{rr'}(\tau) \rightarrow a_{rr'}(\tau) + 2\pi$ leaves the action invariant and implies the compactness of $a_{rr'}$. Important properties of the gauge field $a_{rr'}$ can be understood by ignoring all couplings between c and f fermions for this purpose. The compactness property is important for excitations of the gauge field – in general there exist monopole excitations, which remain gapped in 3d. An important problem might occur in two dimensions, where Polyakov (1977) argued that the pure compact $U(1)$ gauge theory is always confining at zero temperature. Whether in the present problem a deconfined phase of the spinons is admitted in two dimensions and at zero temperature is an open problem. The particular choice of the decoupling field χ_{ij} has found widespread applications in the RVB theory for high-temperature superconductors (Ioffe and Larkin, 1989, Lee and Nagaosa, 1992) and the description of spin liquids (Herbut et al., 2003), and it is useful to describe phases without broken symmetry of the auxiliary f -fermions. Finally, the auxiliary boson field $b_r(\tau)$ naturally leads to the simplest mean-field approximation to the Kondo problem, e.g.,

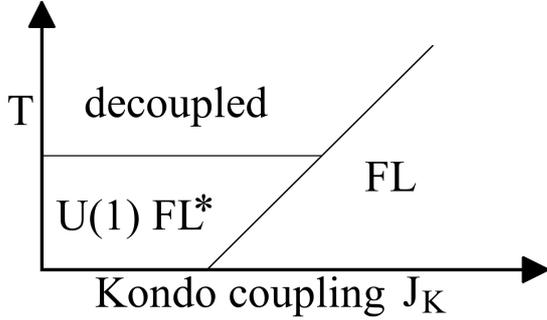


Figure 2.3: Schematic mean-field phase diagram of the Hamiltonian \mathcal{H}_{mf} from Eq. (2.15) at constant strain ϵ , as a function of Kondo coupling J_K and temperature T . The decoupled phase (corresponding to $b_0 = \chi_0 = 0$) is an artifact of mean-field theory, and the corresponding transitions will become crossovers upon including fluctuations, as will the transition between the FL and U(1) FL* phases.

The FL phase corresponds to $b_0 = 0$, the U(1) FL* phase to $b_0 = 0$ and $\chi_0 \neq 0$.

allowing to describe a breakdown of the Kondo effect in the uncondensed phase of the boson, where the mean-field amplitude $b_0 = 0$. The breakdown of the Kondo effect in the single impurity Kondo model is here understood as a vanishing of the energy scale T_K defined in Eq. (1.3). To understand this further, it is useful to consider the impurity spectral function

$$A_f(\omega) = \frac{1}{\pi} \text{Im} G_f(\omega - i\delta) \quad (2.14)$$

with the Fourier transform of the time-ordered f-Green's function,

$$G_f(\omega) = -i \int_{-\infty}^{\infty} dt \langle T f_{\sigma}(t) f_{\sigma}^{\dagger}(0) \rangle e^{i\omega t} .$$

At $\omega = 0$, $A_f(\omega)$ has a resonance which is conveniently used as an alternative definition of the Kondo temperature as the width of this resonance (Hewson, 1997). This width is $\sim b_0^2/D$, such that the Kondo temperature follows $T_K \sim b_0^2/D$ and vanishes at $b_0 = 0$ (Burdin, 2001). If $b_0 \neq 0$, the boson is condensed and the Kondo effect is therefore intact. In the Kondo lattice, the energy scale $T_K \sim b_0^2/D$ can be obtained as the temperature where the boson condenses (Burdin, 2001) ($b_0 = 0$). A vanishing amplitude $b_0 = 0$ is usually interpreted as breakdown of the Kondo effect (Paul et al., 2007), although T_K is not the only energy scale in the Kondo lattice (Burdin et al., 2000, Pruschke et al., 2000). At the mean-field level, scattering processes of the spinons and boson fields on fluctuations of the gauge field $a_{rr'}(\tau)$ are neglected, which are of particular importance for a description of electrical transport properties in the finite temperature region above the Kondo-breakdown QCP (see chapter 3). We will return to a discussion of the field theory in chapter 3 in order to discuss transport properties near the Kondo-breakdown QCP.

For the discussion of the possible low-temperature phases of the action (3.1), it is useful to consider a mean-field theory derived from this field theory. In the following, our aim is to derive the mean-field theory for the Kondo-breakdown transition that we sketched in chapter 1. Since the action (3.1) grows extensively in the parameter N , the $N \rightarrow \infty$ -limit is

equivalent to a saddle point configuration of the auxiliary fields $b_r(\tau)$ and $\chi_{ij}(\tau)$. Here, we assume a spatially homogeneous mean-field state² where b_r , $a_0(r)$, and χ_{ij} take constant values b_0 , λ , and χ_0 . Finally, we arrive at the mean-field Hamiltonian

$$\begin{aligned}
\mathcal{H}_{\text{mf}} = & \sum_{\mathbf{k}\sigma} (\varepsilon_{\mathbf{k}} - \mu_c(\epsilon)) c_{\mathbf{k}\sigma}^\dagger c_{\mathbf{k}\sigma} \\
& - \sum_{\mathbf{k}\sigma} \left(\lambda + 2\chi_0 \sum_{\mathbf{r}=\text{n.n.}} e^{i\mathbf{r}\cdot\mathbf{k}} \right) f_{\mathbf{k}\sigma}^\dagger f_{\mathbf{k}\sigma} \\
& - b_0(1 + \gamma\epsilon)^2 \sum_{\mathbf{k}} (c_{\mathbf{k}\sigma}^\dagger f_{\mathbf{k}\sigma} + h.c.) \\
& - \frac{\mathcal{N}J_K}{4} (1 + \gamma\epsilon)^2 + V_0 \frac{B}{2} \epsilon^2 \\
& + \frac{2z\mathcal{N}\chi_0^2}{J_H} + (1 + \gamma\epsilon)^2 \frac{4\mathcal{N}b_0^2}{J_K}.
\end{aligned} \tag{2.15}$$

where a shift of the one-particle energies $\varepsilon_{\mathbf{k}}$ by $-\frac{1}{2}J_K(1 + \gamma\epsilon)^2$ has been absorbed into a shift of the chemical potential μ_c , which now depends explicitly on strain. The lattice structure implicitly enters the mean-field Hamiltonian via the spinon dispersion and the coordination number z , which counts the number of nearest neighbors. The mean-field amplitudes λ , χ_0 , b_0 and the chemical potential μ_c in (2.15) have to be obtained from a minimization of the free-energy

$$\begin{aligned}
F(\epsilon, \chi_0, b_0, T) = & -2 \sum_{\alpha=\pm} \frac{V_0}{(2\pi)^d} T \int d^d\mathbf{k} \ln(1 + e^{-\beta(E_{\mathbf{k}}^\alpha(\epsilon))}) \\
& + \frac{2z\mathcal{N}\chi_0^2}{J_H} + (1 + \gamma\epsilon)^2 \frac{4\mathcal{N}b_0^2}{J_K} + \frac{1}{2}BV_0\epsilon^2 - \frac{\mathcal{N}}{4}J_K(1 + \gamma\epsilon)^2
\end{aligned} \tag{2.16}$$

with respect to the variables λ , χ_0 , b_0 , μ_c , requiring the stationary conditions

$$\frac{\partial F}{\partial b_0} \stackrel{!}{=} \frac{\partial F}{\partial \chi_0} \stackrel{!}{=} \frac{\partial F}{\partial \lambda_0} \stackrel{!}{=} \frac{\partial F}{\partial \mu_c} \stackrel{!}{=} 0 \tag{2.17}$$

to be fulfilled. The resulting saddle point equations can be written in the following compact form:

$$\left\{ \begin{array}{c} \frac{b_0(1+\gamma\epsilon)^2}{J_K} \\ \frac{\chi_0}{J_H} \\ 1 \\ n_c \end{array} \right\} = \sum_{\mathbf{k}} \left\{ \begin{array}{c} G_{fc}(\mathbf{k}, \tau = 0^-) \\ G_f(\mathbf{k}, \tau = 0^-)(\varepsilon_{f\mathbf{k}} - \lambda) \\ G_f(\mathbf{k}, \tau = 0^-) \\ G_c(\mathbf{k}, \tau = 0^-) \end{array} \right\} \tag{2.18}$$

where $\varepsilon_{f\mathbf{k}} = -2\chi_0 \sum_{\mathbf{r}=\text{n.n.}} e^{i\mathbf{r}\cdot\mathbf{k}}$ is the dispersion of the f -fermions and G_c , G_f and G_{fc} are the full conduction-electron, f -electron and mixed Green functions, respectively, obtained

²A spatially modulated solution occurs if the band masses of electrons and spinons have opposite sign (Paul et al., 2007). In this phase, b_0 is not spatially uniform which implies a charge density modulation in the heavy Fermi-liquid. To our knowledge, such a phase is not realized experimentally.

from the Matsubara Green functions:

$$\begin{aligned}
G_c(i\omega_n, \mathbf{k}) &= G_c^0(i\omega_n + \mu_c - b_0^2 G_f^0(i\omega_n, \mathbf{k}), \mathbf{k}) \\
G_f(i\omega_n, \mathbf{k}) &= G_f^0(i\omega_n - b_0^2 G_c^0(i\omega_n, \mathbf{k}), \mathbf{k}) \\
G_{fc}(i\omega_n, \mathbf{k}) &= \frac{b_0 G_f^0(i\omega_n, \mathbf{k}) G_c^0(i\omega_n, \mathbf{k})}{1 - b_0^2 G_f^0(i\omega_n, \mathbf{k}) G_c^0(i\omega_n, \mathbf{k})}
\end{aligned} \tag{2.19}$$

Here $G_c^0(i\omega_n, \mathbf{k}) = (i\omega_n - \varepsilon_{\mathbf{k}})^{-1}$ and $G_f^0(i\omega_n, \mathbf{k}) = (i\omega_n - \varepsilon_{f\mathbf{k}})^{-1}$ are the non-interacting conduction and f electron Green functions. The equilibrium lattice strain ϵ minimizes the free-enthalpy function

$$G(\epsilon) = F(\epsilon) + pV_0\epsilon \tag{2.20}$$

what leads to the additional self-consistency condition

$$\begin{aligned}
\epsilon &= \left(\frac{BV_0}{\gamma^3} - \frac{pV_0}{\gamma^2} \right) \left(\left(\frac{3}{2} - n_c \right) J_K \right. \\
&\quad \left. + \frac{8b_0^2}{J_K} + \frac{BV_0}{\gamma^2} \right)^{-1} - \gamma^{-1}
\end{aligned} \tag{2.21}$$

which completes the set of mean-field equations together with Eq. (2.18).

Zero-temperature phases

The presence of the strain parameter ϵ in the mean-field theory (2.15) leads not to additional zero temperature phases, since its effect are just renormalizations of a chemical potential and the Kondo coupling J_K . This type of mean-field model displays two qualitatively distinct zero-temperature phases that have been already discussed at length by Senthil et al. (2004) and are depicted in Fig. 2.3. First, there is the usual FL phase when b_0, χ_0, λ are all nonzero. In this phase, the f -electrons hybridize with the conduction electrons and therefore are necessarily nonlocal objects with a nonzero hopping matrix element χ_0 . This Fermi liquid phase cannot exist for a vanishing Kondo hybridization $b_0 = 0$ with $\chi_0 \neq 0$, where necessarily $\lambda = 0$. In this case, the f -electrons form a U(1) spin liquid with a Fermi surface of neutral spinons, while the conduction electrons are decoupled from the spinons and form a small Fermi surface without participation of the local moments. As has been shown by Senthil et al. (2004), the FL phase is stable with respect to fluctuations, as is FL*, provided that the U(1) gauge field is in a deconfined phase, requiring that the theory has been defined in dimension $d > 2$. This state has been dubbed fractionalized Fermi liquid (FL*). At zero temperature, it is possible to describe the transition between these two phases qualitatively correct within mean-field theory, while fluctuations about this mean-field description are essential to describe the non-Fermi liquid physics in the quantum critical regime of the Kondo-breakdown transition (Senthil et al., 2004). In chapter 3, we will formulate a critical theory for this transition including fluctuation effects and examine their influences in more detail.

Using the transformation

$$\begin{aligned} c_{\mathbf{k}\sigma} &= u_{\mathbf{k}}\gamma_{\mathbf{k}\sigma+} + v_{\mathbf{k}}\gamma_{\mathbf{k}\sigma-} , \\ f_{\mathbf{k}\sigma} &= v_{\mathbf{k}}\gamma_{\mathbf{k}\sigma+} - u_{\mathbf{k}}\gamma_{\mathbf{k}\sigma-} , \end{aligned} \quad (2.22)$$

the mean field Hamiltonian is readily rewritten in the diagonal form

$$H_{\text{mf}} = \sum_{\mathbf{k}\sigma} E_{\mathbf{k}}^+ \gamma_{\mathbf{k}\sigma+}^\dagger \gamma_{\mathbf{k}\sigma+} + E_{\mathbf{k}}^- \gamma_{\mathbf{k}\sigma-}^\dagger \gamma_{\mathbf{k}\sigma-} + E_0 , \quad (2.23)$$

with the dispersions

$$E_{\mathbf{k}}^\pm = \frac{\varepsilon_{\mathbf{k}} + \varepsilon_{f\mathbf{k}}}{2} \pm \sqrt{\left(\frac{\varepsilon_{\mathbf{k}} - \varepsilon_{f\mathbf{k}}}{2}\right)^2 + 4b_0^2} \quad (2.24)$$

and the energy E_0 given by the constants appearing in Eq. (2.15). On a d -dimensional hypercubic lattice, the spinon dispersion $\varepsilon_{f\mathbf{k}}$ is given by $\varepsilon_{f\mathbf{k}} = -2\chi_0 \sum_{a=1,\dots,d} \cos(k_a)$. The transformation coefficients $u_{\mathbf{k}}$, $v_{\mathbf{k}}$ defined above can be obtained from

$$\begin{aligned} u_{\mathbf{k}} &= -\frac{b_0 v_{\mathbf{k}}}{E_{\mathbf{k}}^+ - \varepsilon_{\mathbf{k}}} \\ u_{\mathbf{k}}^2 + v_{\mathbf{k}}^2 &= 1 . \end{aligned} \quad (2.25)$$

Within mean-field theory, many aspects of the phase transition between FL and FL^{*} can be understood from the evolution of the Fermi surface and the quasiparticle weights of conduction electrons and spinons upon tuning the amplitude b_0 . In the following, we consider a less than half-filled conduction electron band. However, the arguments can be suitably modified to apply for a more than half-filled conduction electron band. First, we consider the case of a small value b_0 with $b_0 \ll \chi_0, t$, where both bands $E_{\mathbf{k}}^\pm$ together intersect the Fermi surface at least twice. As can be seen in Fig. 2.7, for small b_0 the bands $E_{\mathbf{k}}^\pm$ retain their c and f character, with only small admixtures of f and c character, respectively. For increasing b_0 , a transition is possible where the $E_{\mathbf{k}}^+$ band is empty and the $E_{\mathbf{k}}^-$ band intersects the Fermi surface only once, see Fig. 2.2. The transition to this Fermi liquid phase with different Fermi surface topology is a Lifshitz transition (Lifshitz, 1960a,b). In the Fermi liquid phase, both c electrons and f particles participate in the Fermi volume and fulfill Luttinger's sum rule stated in Eq. (1.13). Upon decreasing b_0 , the Fermi surfaces asymptotically match that produced by the bare dispersions $\varepsilon_{\mathbf{k}}$ and $\varepsilon_{f\mathbf{k}}$. Importantly, when b_0 becomes zero, the spinons do not participate in the Fermi volume and Luttinger's sum rule does not apply (Senthil et al., 2003). As has been shown by Senthil et al. (2003), the Fermi volume is instead quantized according to the rule

$$\mathcal{V}_{\text{FL}^*} = \mathcal{K}_d [n_c \pmod{2}] , \quad (2.26)$$

which is determined by the density of conduction electrons n_c alone.³ This unusual jump of the Fermi volume at a second order quantum phase transition can be understood from

³The sum rule (2.26) is written in terms of the symbols introduced in Eq. (1.13).

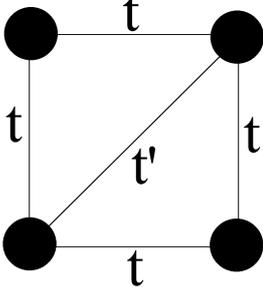


Figure 2.4: Hopping processes on a square lattice, chosen to mimic nearest-neighbor hopping on a triangular lattice. The resulting tight-binding dispersion is $\varepsilon_{\mathbf{k}} = -2t[\cos(k_x) + \cos(k_y)] + t' \cos(k_x + k_y)$.

the evolution of the quasiparticle weight upon approaching the transition, which is easy to obtain from the present mean-field theory. Using the transformation (2.22), the conduction electron Green's function is obtained as

$$G_c(\mathbf{k}, i\omega_\nu) = \frac{u_{\mathbf{k}}^2}{i\omega_\nu - E_{\mathbf{k}}^+} + \frac{v_{\mathbf{k}}^2}{i\omega_\nu - E_{\mathbf{k}}^-}. \quad (2.27)$$

As obtained by numerical solutions of the mean field equations and depicted in Fig. 2.7, both Fermi sheets derive from the $E_{\mathbf{k}}^-$ band. At the c Fermi surface and for $|b_0/t| \ll 1$ we have $E_{\mathbf{k}}^- \approx \varepsilon_{\mathbf{k}} = 0$, and from $G_c(\mathbf{k}, i\omega_\nu)$ it is seen that the quasiparticle weight is $Z = v_{\mathbf{k}}^2$. Close to this Fermi surface, we can approximate

$$E_{\mathbf{k}}^+ \approx \varepsilon_{f\mathbf{k}} + \frac{b_0^2}{\varepsilon_{\mathbf{k}} - \varepsilon_{f\mathbf{k}}}. \quad (2.28)$$

Considering a tight-binding dispersion $\varepsilon_{\mathbf{k}} = -2t \sum_i \cos k_i$, near this Fermi surface we have $|\varepsilon_{\mathbf{k}} - \varepsilon_{f\mathbf{k}}| \approx \chi_0(\mu_c/t) \sim J_H$. Using Eq. (2.25), it can be seen that $u_{\mathbf{k}} \approx -\frac{b_0}{J_H} v_{\mathbf{k}}$ near this Fermi surface, such that the quasiparticle weight at this part of the Fermi surface is $Z \approx 1$. In analogy, on the Fermi surface of the f -band with $E_{\mathbf{k}}^- \approx \varepsilon_{f\mathbf{k}} = 0$, we have

$$E_{\mathbf{k}}^+ \approx \varepsilon_{\mathbf{k}} + \frac{b_0^2}{\varepsilon_{\mathbf{k}} - \varepsilon_{f\mathbf{k}}}. \quad (2.29)$$

Since near this Fermi surface $|\varepsilon_{\mathbf{k}} - \varepsilon_{f\mathbf{k}}| \approx \mu_c \sim t$, the quasiparticle weight $Z = v_{\mathbf{k}}^2$ vanishes as

$$Z \approx \left(\frac{b_0}{\varepsilon_{\mathbf{k}} - \varepsilon_{f\mathbf{k}}} \right)^2 \sim \left(\frac{b_0}{t} \right)^2. \quad (2.30)$$

Therefore, the quasiparticle residue on the f -Fermi surface vanishes continuously throughout the transition, and the f -band becomes thus Mott-insulating. Due to the vanishing quasiparticle weight, the resulting phase is a non-Fermi liquid with fermionic excitations (Senthil et al., 2003, 2004). Note that this implies not that the effective mass of the spinons diverges, since they continue to disperse in their Mott insulating phase.

2.2 Phase diagram in slave-boson mean-field theory

In this section, we turn to the discussion of numerical solutions of the self-consistency equations (2.18) and (2.21). For this purpose, we specify different tight-binding dispersions for the c -electrons, which are defined by particular lattice geometries. Experimentally, heavy fermions often show a tetragonal unit cell, but also monoclinic or orthorhombic lattices are observed (Stewart, 1984, Löhneysen et al., 2007). While many materials show clear three dimensional properties, the puzzling example of $\text{CeCu}_{6-x}\text{Au}_x$ shows critical spin-fluctuations which have been interpreted as having two-dimensional momentum dependence (Stockert et al., 1998), although the magnetic structure in the ordered phase appears to be three-dimensional. Specifically, we perform calculations for tight-binding dispersions on square lattices, cubic lattices and triangular lattices, given by the formulas

$$\varepsilon_{\mathbf{k}} = -2t \sum_{i=1}^d \cos(k_i) \quad (2.31)$$

$$\varepsilon_{\mathbf{k}} = -2t[\cos(k_x) + \cos(k_y)] + t' \cos(k_x + k_y). \quad (2.32)$$

The latter dispersion corresponds to the hopping processes illustrated in Fig. 2.4. It is implemented in order to frustrate magnetic interaction and to reduce nesting properties of the Fermi surface, which might be responsible for various instabilities such as spin-density wave order. While we do not allow for magnetic order within our model, nesting might in principle also be of importance for Kondo volume collapse transitions. We note that within our mean-field approach, dimensionality and geometry of the lattice enter only within the electronic dispersions and the classical strain variables $\epsilon_{i=x,y,z}$. For concreteness, we assume here that the phonon degrees of freedom are three-dimensional in all cases. We illustrate the main aspects of the phase diagrams for different bulk moduli in Fig. 2.6. The tendency to first order transitions increases with decreasing bulk modulus. Below a critical bulk modulus B_c , a first order transition line occurs in the phase diagram. Interestingly, this transition occurs concomitantly with the Lifshitz transition, with the endpoint lying on the Lifshitz line within numerical accuracy. These generic numerical findings appear also within a general Landau theory analysis we will introduce in section 2.3. Decreasing the bulk modulus further leads to a stronger first order transition into the FL^* phase above a critical endpoint of the Lifshitz transition. Below a second critical bulk modulus B^* , the critical end point of the first order transition finally vanishes, leading to a pressure-induced first order transition at $J_H = 0$. This transition is the Kondo volume collapse transition discussed by Dzero et al. (2006). In determining the asymptotic zero temperature limit of the phase diagram, the temperature has to be kept sufficiently below the energy scales J_H and T_K which stabilize finite mean field amplitudes of χ_0 and b_0 at zero temperature. Our modeling defines pressure and magnetic exchange as two independent tuning parameters which lead to a rich structure of the mean-field phase diagram as a function of those two parameters.

It has been shown by Dzero et al. (2006) that the bulk modulus B can be tuned to a quantum critical end point of the Kondo volume collapse model, where the Kondo volume collapse transitions cease to exist. We implement phase diagrams for various different

values of the bulk modulus and keep the conduction electron density n_c fixed, since changes of band filling lead to no qualitative or considerable quantitative changes of our phase diagrams. The different dispersions defined above lead to the same qualitative features in the phase diagrams which we therefore discuss in detail only for the example of the 2d square lattice geometry. Particular additional features originating from variations in lattice geometry are then added in separate discussions.

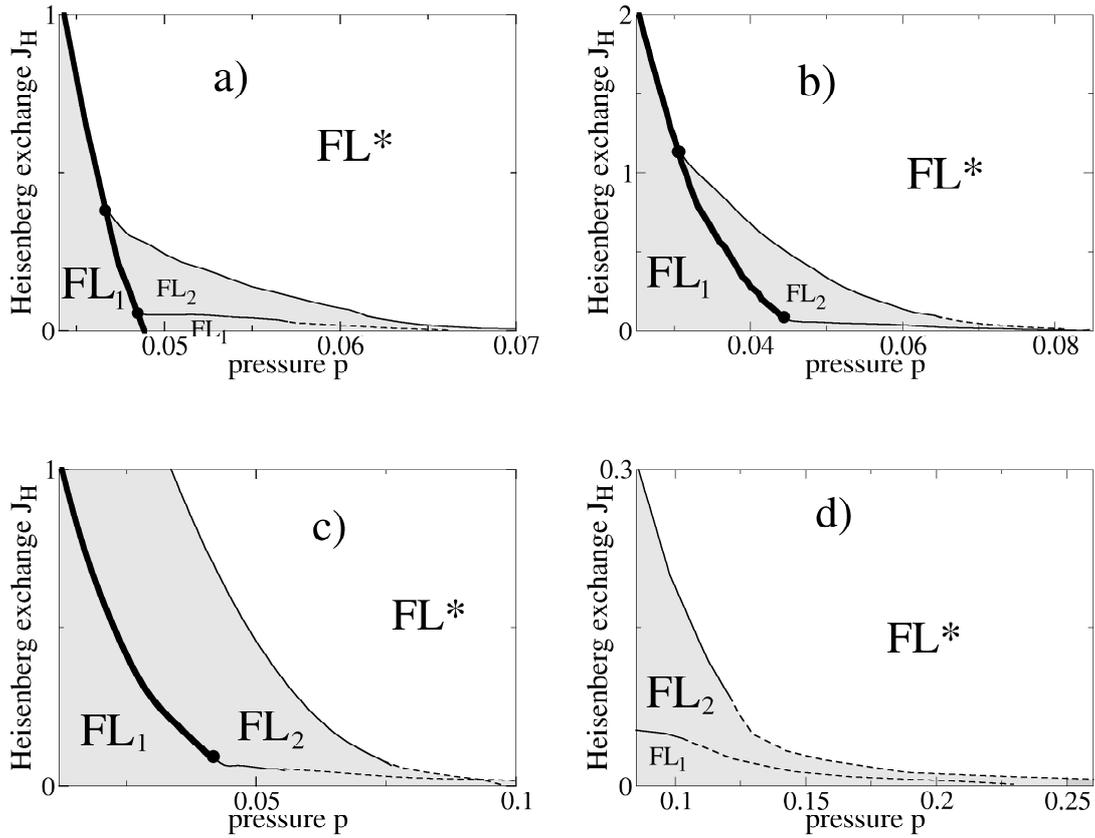


Figure 2.5: Large- N ground state phase diagrams of the Kondo-Heisenberg model on a 2d square lattice, as function of pressure p and inter-moment exchange J_H . The panels a) to d) are for bulk moduli $B=0.005, 0.0055, 0.007,$ and 0.015 ; the other parameters are $t=1, n_c = 0.8, J_K = 1.5$ and $\gamma = 0.05$. Thin (thick) lines are second (first) order transitions. The Lifshitz transition line separates FL_1 and FL_2 , the Kondo breakdown transition separates FL from FL^* , for details see text. (The calculations have been at a low $T = 0.005$, the dashed lines are extrapolations of the phase boundaries obtained from runs at lower T .)

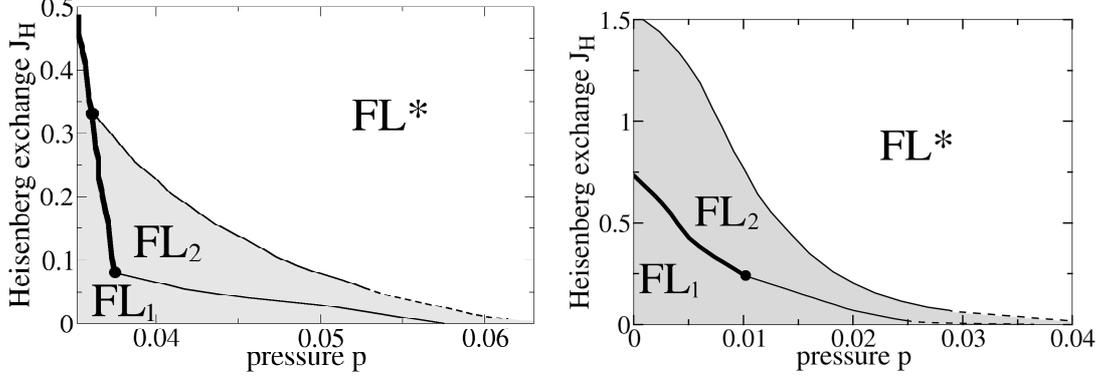


Figure 2.6: [Left panel] Phase diagram as in Fig. 2.5, but for electrons on a 3d cubic lattice, for $B = 0.005$. [Right panel] Phase diagram as in Fig. 2.5, but for electrons on a 2d triangular lattice with dispersion (2.32), for $B = 0.005$ and $t = t' = 1$. These phase diagrams qualitatively correspond to Fig. 2.5b and Fig. 2.5c, respectively. By tuning the parameter B , the other phase diagrams of Fig. 2.5 are qualitatively realized for both lattices.

Numerical results

The dashed lines in Fig. 2.5 indicate the extrapolated behavior for very small J_H obtained by successively lowering temperature below the energy scales J_H and T_K . All these features were also recovered for the triangular lattice dispersion (2.32), with one particular example shown in Fig. 2.6.

A discussion of the large- N results for 3d electrons moving on a cubic lattice shows no qualitative difference to the $d = 2$ case. Again, first order Lifshitz transitions are found, with a critical end point close to or at the Lifshitz transition, see Fig. 2.6. Due to finite numerical accuracy, this question will only be answered in the Landau theory analysis in section 2.3 where we can generically exclude that this critical end point is situated on the Lifshitz line. We recovered additional features of the 2d phase diagrams that are not shown explicitly here. Again, the $T = 0$ endpoint of the first-order transition disappears below a critical value of the bulk modulus, and a direct first order transition from FL to FL* occurs for sufficiently large values of the intermoment exchange J_H . Finally, first order transitions cease to exist above a critical value of the bulk modulus.

A more detailed understanding of the pressure-induced transitions can be obtained from changes in the band structure upon tuning pressure, see Fig. 2.7. In the parameter regime covered by our numerical solutions, χ_0 turns out to be negative, leading to a hole-like spinon dispersion, see Fig. 2.7c. At a Lifshitz transition with a change from one to two Fermi surface sheets, this kind of dispersion manifests in the formation of a hole-like pocket that splits from the Fermi surface. This behavior leads to a contribution to the density of states from the emerging hole pocket, leading to a singularity in the total density of states

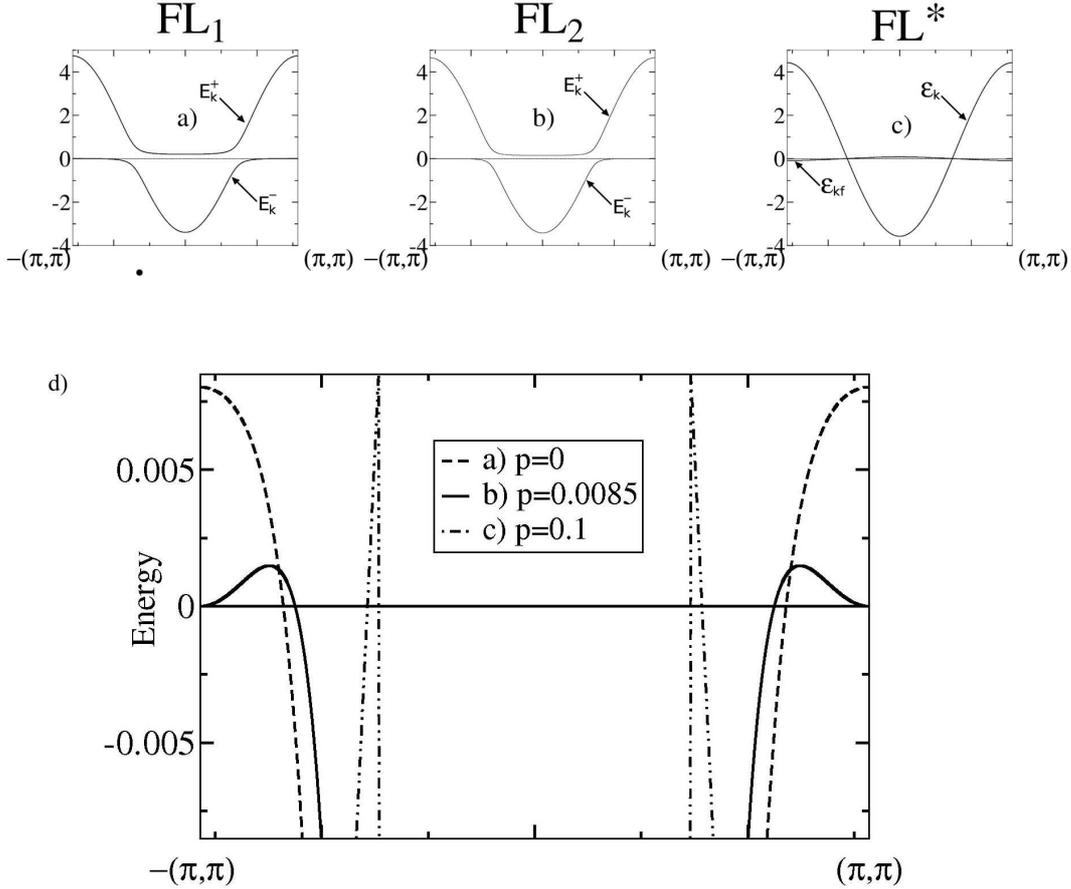


Figure 2.7: Quasiparticle dispersions for different parameters along a constant- J_H cut of the phase diagram in Fig. 2.5, for parameters $t = 1$, $n_c = 0.8$, $J_H = 0.1$, $J_K = 1.5$, $\gamma = 0.05$, $B = 0.01$ and $T = 0$. Upper panel: Bands along the $-(\pi, \pi) \rightarrow (\pi, \pi)$ direction for pressures in the a) FL_1 , b) FL_2 (close to the Lifshitz transition), and c) FL^* phases ($p = 0, 0.0085, 0.1$, respectively). Lower panel: Comparison of the low-energy part of the dispersions. Case a) has one heavy electron-like band intersecting the Fermi level. Increasing pressure lowers the energy at the zone boundary and eventually causes the emergence of a hole-like sheet, case b). At higher pressures, the two bands evolve into conduction electron and spinon bands, which each intersect the Fermi energy once - this is the FL^* phase, case c).

at the Lifshitz transition. This singularity has fundamental consequences for the behavior of the strain order parameter at the Lifshitz transition, as will be discussed within the Landau theory approach given in section 2.3.

At mean-field level, the character of the numerical phase diagrams does not change at sufficiently small but finite temperatures. A notable feature is the vanishing of the first-order lattice transition line in the $p - J_H$ plane at a finite temperature critical end-point. These endpoints terminate at the $T = 0$ endpoint described above. A proper analysis of fluctuation effects of the strain field $\epsilon_{\mathbf{r}}$ (this will be detailed in section 2.4) shows that the mean-field treatment of the phonon modes is exact at the quantum critical end-point of the Kondo volume collapse. Considering this argument, a related analysis of strain fluctuation effects onto the Kondo volume collapse by Dzero et al. (2006) has to be reinterpreted.

In the limited range of parameters covered by our numerical calculations, several non-trivial effects occurred upon inclusion of the strain order parameter: (i) The Lifshitz transition tends to become first order. (ii) The Kondo breakdown transition remains of second order, except for soft lattices where it merges with a first order Lifshitz transition. (iii) For $2d$ electrons, the quantum critical end point of the first order lattice collapse seems to be situated on the Lifshitz line of the quantum critical point, such that two critical phenomena seem to coincide without fine tuning. Although we gave detailed reasons for our choice of parameters in the Kondo-Heisenberg model (2.6), our numerical analysis treats only a limited range of the physical parameter space. In addition, finite numerical resolution restricts the ability to resolve a possible coincidence of transition lines. Especially to overcome these limitations, in the following section we formulate an effective Landau theory that leads to a more detailed interpretation of our numerical findings.

2.3 Landau theory

Landau functional

A suitable order parameter for a Landau theory description is the strain ϵ , describing isostructural volume-changing transitions of the lattice. In analogy to the textbook example of the liquid-gas transition, such transitions break no symmetries and there are no symmetry-forbidden terms in the Landau free energy functional (Chaikin and Lubensky, 1995). We will assert a constant strain value ϵ_0 to the location of the Lifshitz transition. For convenience, we chose the reference volume V_0 such that in all cases $\epsilon_0 = 0$. For an appropriate description of first order phase transitions and considering small changes in the strain, it is necessary and sufficient to expand the free energy up to fourth order in ϵ , leading to the formal Landau free energy

$$F(\epsilon) = F_0 - V_0 p^* \epsilon + \frac{m}{2} \epsilon^2 - \frac{v}{3} \epsilon^3 + \frac{u}{4} \epsilon^4. \quad (2.33)$$

Here, it is assumed that the free energy is analytic as a function of ϵ . At zero temperature, however, the Landau free energy contains a non-analytic correction from a band minimum crossing the Fermi level at the Lifshitz transition, see Fig. 2.7d. Microscopically, the lattice parameter ϵ will couple linearly to, e.g., hopping matrix elements, which in turn

moves fermionic bands relative to the chemical potential. Therefore the strain ϵ will couple linearly to the chemical potential. The non-analytic part can be derived from the additional contribution to the fermionic density of states, which is

$$D(\omega) \propto \Theta(\omega)|\omega|^{\frac{d}{2}-1} \quad (2.34)$$

close to the Lifshitz transition and in d dimensions, where $\Theta(\omega)$ is the step function. Assuming an energy distance $\Delta\mu$ of the Fermi surface to the band extremum crossing the Fermi surface that is linearized in ϵ , $\Delta\mu \propto \epsilon$, the non-analytic free energy contribution close to the Lifshitz transition is given by

$$- \int_0^{\Delta\mu} D(\omega)\omega d\omega \propto |\epsilon|^{\frac{d}{2}+1}. \quad (2.35)$$

Including the singular contribution from the Lifshitz transition, the Landau free energy function for the combined Lifshitz transition and volume collapse now reads:

$$\begin{aligned} F(\epsilon) &= F_0 - V_0 p^* \epsilon + \frac{m}{2} \epsilon^2 - \frac{v}{3} \epsilon^3 + \frac{u}{4} \epsilon^4 \\ &- \kappa \Theta(-\epsilon) |\epsilon|^{\frac{d}{2}+1}, \end{aligned} \quad (2.36)$$

with the positive coupling constant κ .

Mean-field phase diagram in $d=2$

First order lattice transitions and their properties within our effective Landau theory can be classified by the parameters m and v of the free energy function (2.36). At a first order transition, the order parameter jumps between two degenerate local minima of the free enthalpy function. By construction of our theory, Lifshitz transitions occur at $\epsilon = 0$, e.g., involve a sign change of the order parameter ϵ .

Another criterion is that a continuous Lifshitz transition necessarily requires the existence of a local minimum at $\epsilon = 0$, which can only occur at the critical pressure $p = p^*$. At this critical pressure, a local minimum at $\epsilon = 0$ is impossible if $m - 2\kappa < 0$. In the case $m < 0$, two critical values $m_{c1,2}$ of the mass m need to be discussed, with a critical endpoint m_{c2} of the first order lattice transition and the Lifshitz transition becoming discontinuous at $m_{c1} \geq m_{c2}$. The behavior of the critical masses m_{c1} and m_{c2} is special in $d = 2$, since the non-analytic part of the free energy becomes quadratic and leads to renormalization of the mass term for all $\epsilon < 0$.

In the case $m - 2\kappa < 0$, all qualitatively different cases for the position of the critical masses $m_{c1,2}$ can be accessed by tuning the parameter v while keeping κ and u fixed, since the latter parameters are constrained to positive values. In the following, we distinguish values for v that lead to qualitatively different values of $m_{c1,2}$.

(i) $v > 0$. In this case, no second minimum of $G(\epsilon)$ can occur for $\epsilon < 0$ since $v > 0$, $m - 2\kappa > 0$ and $u > 0$. However, for $\epsilon > 0$ a formation of a second minimum of $G(\epsilon)$ occurs if v becomes sufficiently large to enable a negative slope of $G(\epsilon)$ for $\epsilon > 0$. This occurs precisely if

$$\frac{dG(\epsilon)}{d\epsilon} = p - p^* + m\epsilon - v\epsilon^2 + u\epsilon^3 \stackrel{!}{=} 0 \quad (2.37)$$

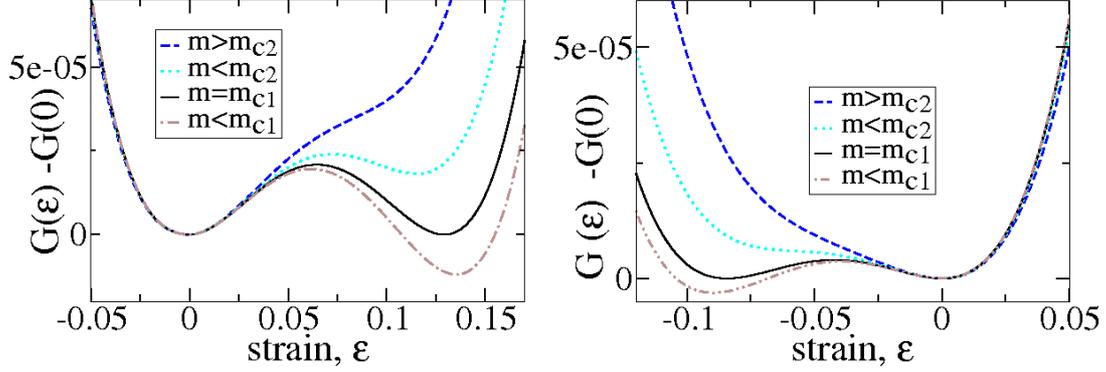


Figure 2.8: Samples of the mean-field free energy $F(\epsilon)$ (2.36), for various values of the parameter v . The left figure corresponds to $v > 0$ and $d = 2$, the right figure to $v < 0$ and $d = 3$. If m drops below m_{c2} , a second minimum evolves at some $\epsilon \neq 0$. If even $m < m_{c1}$, this minimum becomes the absolute minimum (see also Tables 2.1 and 2.2).

has at least one real solution for $\epsilon > 0$. This second minimum leads to a first order Lifshitz transition if $G(\epsilon) < F_0$ at the position of this minimum and the critical pressure p^* . Therefore, the critical mass m_{c1} has to be chosen such that

$$m\epsilon - 2\kappa\Theta(-\epsilon)\epsilon - v\epsilon^2 + u\epsilon^3 \stackrel{!}{=} 0 \quad (2.38)$$

at the position of the second minimum with $\epsilon > 0$. Besides from the trivial solution $\epsilon = 0$, possible additional solutions necessarily obey

$$\epsilon = \frac{\frac{v}{3} \pm \sqrt{\frac{v^2}{9} - \frac{1}{2}um}}{\frac{u}{2}}, \quad (2.39)$$

leading to the criterion $m < \frac{2}{9}\frac{v^2}{u}$ for the existence of a first order transition, proposing the value $m_{c1} = \frac{2}{9}\frac{v^2}{u}$ for the critical mass m_{c1} . Further conditions on the critical masses $m_{c1,2}$ are derived by analyzing the real solutions of equation (2.38) by the method of Cardano (Bronstein and Semendjajew, 1987). This method defines the discriminant

$$D = P^3 + Q^2 \quad (2.40)$$

with $P = \frac{3um - v^2}{9u^2}$ and $Q = -\frac{v^3}{27u^3} + \frac{vm}{6u^2} + \frac{p - p^*}{2u}$, which leads to the following distinctions of solutions, according to the sign of the discriminant:

- (1) $D > 0$ corresponds to a single real root and two complex roots
- (2) $D = 0$ to either one real root (a triple root) or two real roots (a single and a double

$d = 2$	$0 \leq v \leq v_{c1}$	$v_{c1} < v \leq v_{c2}$	$v_{c2} < v $
m_{c1}	$\frac{2}{9} \frac{v^2}{u} \Theta(-v) + 2\kappa$	$\frac{2}{9} \frac{v^2}{u} \Theta(-v) + 2\kappa$	$\frac{2}{9} \frac{v^2}{u} + 2\kappa \Theta(-v)$
m_{c2}	$\frac{1}{3} \frac{v^2}{u} \Theta(-v) + 2\kappa$	$\frac{1}{3} \frac{v^2}{u} + 2\kappa \Theta(-v)$	$\frac{1}{3} \frac{v^2}{u} + 2\kappa \Theta(-v)$

Table 2.1: Location of critical points from Landau theory in $d = 2$, in dependence of the cubic coefficient v . The critical values are $v_{c1} = \sqrt{6u\kappa}$ and $v_{c2} = 3\sqrt{u\kappa}$. If $m_{c1} < m_{c2}$, a critical endpoint m_{c2} away from the Lifshitz transition emerges. This is not possible if $0 \leq v \leq v_{c1}$ since always $m_{c1} = m_{c2} = 2\kappa$ then. See text for details.

root)

(3) $D < 0$ corresponds to three real roots

Independently of the parameter P , the parameter Q can always be tuned to $Q = 0$ by properly adjusting pressure. Therefore, three real solutions can be tuned by pressure if $P < 0$, and only one real solution is present if $P > 0$, independently of pressure. We conclude that two minima of the free enthalpy function cannot exist for $v^2 \leq 3um$. It follows that the first-order lattice transition line terminates at a critical endpoint with $m_{c2} = 2\kappa$ if $0 < v \leq \sqrt{6u\kappa} \stackrel{\text{def}}{=} v_{c1}$. Additional first order transitions are allowed in the opposite case $v > v_{c1}$. Then, first order transitions exist even for $m > 2\kappa$, since the free enthalpy function has an additional minimum at $\epsilon > 0$. These first order transitions can also involve Lifshitz transitions, and from the criterion (2.39), we obtain $m_{c1} = \frac{2}{9} \frac{v^2}{u}$, where the Lifshitz transition changes from first to second order. This defines the critical value $v_{c2} \stackrel{\text{def}}{=} 3\sqrt{u\kappa}$, above which the Lifshitz transition can become discontinuous even if $m - 2\kappa \geq 0$. Since the discriminant does not allow for a second minimum of $G(\epsilon)$ if $v^2 \leq 3um$, the first-order lattice transition line finally terminates at the critical endpoint m_{c2} . Importantly, this critical end point is situated on the Lifshitz line if $v \leq v_{c1} = \sqrt{6u\kappa}$, since $m_{c1} = m_{c2}$ then.

(ii) $v < 0$. This case can be treated analogous to the previous case by transforming $G(\epsilon) \rightarrow G(-\epsilon)$ in the discussion above. Since particular non-zero values of pressure do not enter the qualitative discussion of the phase diagram (see, e.g., table 2.1), this transformation has essentially only the effect of changing the mass renormalization according to $2\kappa\Theta(-\epsilon) \rightarrow 2\kappa\Theta(\epsilon)$ in our previous discussion. It is therefore readily seen that the Lifshitz transition becomes always discontinuous at $m_{c1} = \frac{2}{9} \frac{v^2}{u} + 2\kappa$, while the first-order lattice transition line always terminates at the critical endpoint $m_{c2} = \frac{1}{3} \frac{v^2}{u} + 2\kappa$. As a consequence, the phase diagram will always correspond to Fig. 2.9a.

(iii) $v = 0$. This case is trivial, with a critical endpoint $m_{c1} = m_{c2} = 2\kappa$ situated on the Lifshitz line.

A summary of all different cases in two spatial dimensions is given in table 2.1. Phase diagrams derived from Landau theory can be classified into the two qualitatively different cases depicted in Fig. 2.9. The Lifshitz line has several characteristic properties. A critical end-point located on the Lifshitz line has an effective potential $\propto |\epsilon|^2$ ($\propto |\epsilon|^3$) for positive (negative) ϵ . In consequence, the pressure-volume isotherm follows $\epsilon \propto (p - p^*)^{\frac{1}{2}}$ ($\epsilon \propto p - p^*$)

$d = 3$	$0 \leq m < m_{c1}$	$m_{c1} \leq m < m_{c2}$	$m_{c2} \leq m$
$0 \leq m < m'_{c1}$	1 st & LS	1 st & LS ¹	1 st & LS
$m'_{c1} \leq m < m'_{c2}$	1 st & LS ¹	1 st ²	1 st
$m'_{c2} \leq m$	1 st & LS	1 st	2 nd

¹an additional 1st order transition can occur

²two 1st order transitions occur

Table 2.2: Types of phase transitions from Landau theory in $d = 3$, for $m \geq 0$ and $v > 0$. We denote a first-order transition which is also a Lifshitz transition by the entry 1st & LS. If $m > 0$ and $v \leq 0$, we know from the 2d case that $m_{c1} = m_{c2} = 0$ and only the third column can be realized. The latter case leads again to the phase diagram of Fig. 2.9b. In the opposite case $v > 0$ we always obtain $m_{c2} > m_{c1} > 0$. From the above table we conclude then that in addition to Fig. 2.9b, also the phase diagrams of Fig. 2.10 can be realized.

for $p > p^*$ ($p < p^*$) in the vicinity of the endpoint. For the first-order lattice transition line near this point we conclude $|m - m_{c1,2}| \propto |p - p^*|^{\frac{1}{2}}$, such that the jump in ϵ along this line is $\Delta\epsilon \propto |m - m_{c1,2}|$. Due to the non-analytic fermionic contribution to the Landau potential, the exponents β and δ thus differ to the mean-field values, which are $\beta = 1/2$ and $\delta = 3$ (Chaikin and Lubensky, 1995).

Mean-field phase diagram in $d=3$

In three dimensions, the non-analytic contribution to the Landau free energy enters with a fractional power $\frac{5}{2}$ that is not contained in the series expansion of the regular part. This leads to a more complicated critical behavior at negative ϵ , where additional minima can occur, see Fig. 2.11. This fact motivates the definition of additional critical parameters $m'_{c1}(u, \kappa, \nu)$ and $m'_{c2}(u, \kappa, \nu)$ that mark the onset of minima of $G(\epsilon)$ at $\epsilon < 0$, see Fig. 2.10. A bifurcation of the first order lattice transition line occurs if three local minima of the free enthalpy function coexist, which is a special feature of our Landau theory occurring only in $d = 3$ (see table 2.2). By comparing the mass m to the critical values m_{c1} , m_{c2} , m'_{c1} and m'_{c2} , all qualitatively different types of pressure driven phase transitions can be classified. For $m < 0$, $G(\epsilon)$ has never a local minimum at $\epsilon = 0$, leading generically to a first-order Lifshitz transition, occurring always at $p > p^*$. It is also readily seen that $m_{c1} = m_{c2} = 0$ if $v \leq 0$, since then the non-analytic term $\kappa\Theta(-\epsilon)|\epsilon|^{\frac{d}{2}+1}$ enters with the same sign as the cubic term $-\frac{v}{3}\epsilon^3$. The remaining cases then require $m \geq 0$ and $v > 0$, and the possible phase diagrams are summarized in table 2.2. Most important, the zero-temperature endpoint of the first-order lattice transition is never located on the Lifshitz line, since always $m'_{c1} < m'_{c2}$. Still, the phase diagram of the type shown in Fig. 2.9a remains possible. Additionally, phase diagrams with bifurcations of the first order transition line occur, see Fig. 2.10.

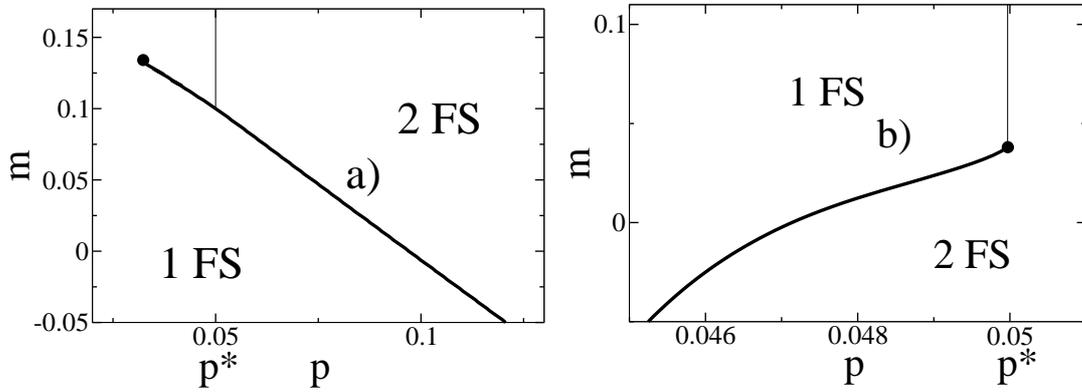


Figure 2.9: Two representative mean-field phase diagrams in two dimensions, derived from the Landau theory. Thick/thin lines represent first/second order transitions. If the parameters m_{c1} and m_{c2} coincide, the quantum critical endpoint of the lattice transition is located on the Lifshitz transition line (Fig. 2.9b). In the other case, $m_{c1} \neq m_{c2}$, the first-order lattice transition line turns away from the Lifshitz line and ends at a critical endpoint (Fig. 2.9a).

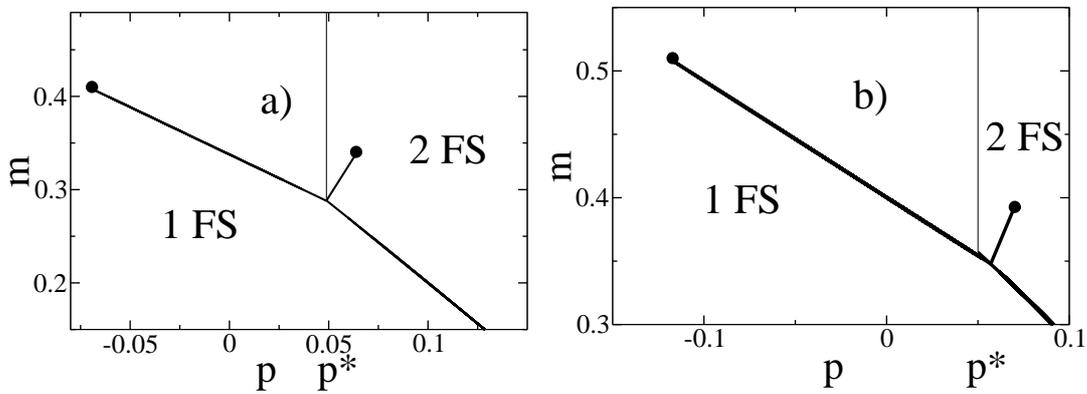


Figure 2.10: Additional cases for mean-field phase diagrams that occur in $d = 3$. In both situations the first-order lattice transition line bifurcates at a point which a) does [b) does not] coincide with the point where the Lifshitz transition changes from first to second order.

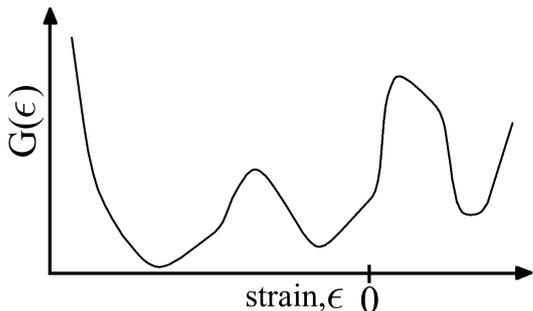


Figure 2.11: Sketch of a form of the free energy (2.36) occurring in $d = 3$. The existence of three local minima leads to two first order transitions, one of them being a first order Lifshitz transition. This situation can be realized in the phase diagrams depicted in Fig. 2.10.

Conclusions from Landau theory

Our analysis of the Landau theory helps to clarify several questions raised by numerical solutions of the large- N theory in section 2.2. We begin with a summary of observations that occurred both in $d = 2$ and $d = 3$. For an infinite range of mass parameters m , the Lifshitz transition becomes discontinuous due to coupling to the lattice, such that a first-order volume collapse coincides with the Lifshitz transition. Generically, the volume collapse transition displays a quantum critical endpoint in the $m - p$ plane. The numerical phase diagrams raised the question whether such a quantum critical end point has a tendency to be situated on the Lifshitz transition line or not. Indeed, within the $d = 2$ theory the volume-collapse endpoint is located *on* the Lifshitz transition line in a large parameter regime. Remarkably, the $d = 3$ endpoint of the volume collapse transition is always separated from the Lifshitz transition line.

2.4 Beyond mean-field theory

Near a continuous quantum phase transition, fluctuations of the order parameter compete with thermal fluctuations and lead to important modifications in a finite temperature region above the quantum critical point. These fluctuation effects are missing in our effective Landau theory as well as in the large- N approach to the Kondo-Heisenberg model. As far as mean-field theory predicts discontinuous transitions, we shall assume that those remain of first order up to a critical temperature where a finite-temperature endpoint of liquid-gas type occurs. Two of the continuous quantum phase transitions occurring in our calculations are well-understood and have properties that were already described elsewhere. **(i)** The second-order Kondo breakdown transition has been discussed at length by Senthil et al. (2004), and we will examine fluctuation effects at this transition in more detail in chapter 3. Fluctuation effects occurring at this transition have been also discussed by Senthil et al. (2004) and Paul et al. (2007). **(ii)** The Lifshitz transition is in the universality class of the dilute Fermi gas, with well known thermodynamic properties that have been discussed, e.g., in the book of Sachdev (1999).

The remaining important aspect of the phase diagram is the endpoint of the volume-collapse transition. The analysis of this endpoint is readily simplified by the fact that the critical endpoint of the volume-collapse transition has no critical fluctuations at finite

wave vectors. In order to show this property, one exploits that the strain field $\epsilon_{\mathbf{r}}$ is related to longitudinal phonons by $\epsilon_{\mathbf{r}} \sim \nabla_{\mathbf{r}} \cdot \phi$, where ϕ is the displacement field of the phonons (Landau and Lifshitz, 1986).

Close to a phase transition associated with a homogeneous deformation of the crystal the behavior will be dominated by the fluctuations of the lattice waves with the smallest velocities. An acoustic phonon mode $\omega_{\mathbf{k}}$ with a finite wave vector \mathbf{k} becomes “critical” if its velocity $\frac{1}{\hbar} \frac{\partial \omega_{\mathbf{k}}}{\partial \mathbf{k}}$ vanishes. This is forbidden in continuum elasticity theory, where all phonon velocities remain finite in presence of a finite shear modulus, even if the bulk modulus is zero (Landau and Lifshitz, 1986). In crystals, the same holds true at an isostructural volume-collapse transition, as can be shown by arguments presented by Cowley (1976). The vanishing of a phonon velocity would imply a structural transition with symmetry breaking, and therefore all homogeneous strain fluctuations remain noncritical at the isostructural volume collapse transition (Cowley, 1976). At the endpoint of the volume-collapse transition, this implies that Landau theory is exact for the lattice degrees of freedom, since only the zero-momentum mode becomes critical.

It is then easy to obtain the thermodynamics at the volume-collapse endpoint. In the particular interesting case where this endpoint is located on the Lifshitz transition line, these properties can be explained by using known results for the dilute Fermi gas. Finite temperature corrections to the mean-field parameters p^* and m originate from Fermi liquid physics and are therefore quadratic in temperature, $p^* = p^*(T = 0) + \zeta_1 T^2$ and $m_{c1} = m_{c1}(T = 0) + \zeta_2 T^2$. Furthermore, near the Lifshitz transition the singular contribution Eq. (2.35) to the free energy can be replaced by the free energy of the Fermi gas,

$$F_F(\epsilon, T) = -\kappa T^{(d/2)+1} \Phi(\epsilon/T) , \quad (2.41)$$

where a scaling function $\Phi(x)$ occurs (Sachdev, 1999). Minimization of the free enthalpy $G(\epsilon)$ now shows that the fermionic part of the free energy dominates the low temperature thermodynamics. Raising temperature at the endpoint leads to $\epsilon \propto T$ and a diverging isothermal compressibility $\kappa_T = -\frac{1}{V} \frac{\partial V}{\partial p} \propto T^{-1}$. At constant pressure, the specific heat is proportional to temperature, $C_p \propto T$.

2.5 Conclusion

Our analysis extended Kondo lattice model physics by the inclusion of volume fluctuations coupling to Kondo physics. Of particular interest in this context is the proposal of a breakdown of the Kondo effect at the quantum phase transition out of the heavy Fermi-liquid phase. We investigated one specific scenario with a transition between a Fermi liquid phase (FL) and a fractionalized phase FL* due to a continuously vanishing quasiparticle weight on the Fermi surface sheet originating from the local moment degrees of freedom. Our calculations merge former investigations on Kondo breakdown and Kondo volume collapse transitions, and we have investigated the question whether Kondo volume collapse transitions might spoil quantum criticality.

Our results show that the Kondo-breakdown transition remains continuous (except for very soft lattices), but instead the Lifshitz transition (which is a precursor of the Kondo

breakdown transition) tends to become unstable towards a first order transition. Interestingly, the zero temperature endpoint of the first order lattice transition is situated on the Lifshitz transition line for a large parameter regime in the case of $2d$ electrons. Such a coincidence of two critical phenomena cannot be explained within the Landau theory of phase transitions. However, this is not a contradiction to our mean-field approach, which lead to a non-analytic free energy near the Lifshitz transition that cannot be effectively described by an expansion in the order parameter ϵ .

The heavy-fermion metals $\text{CeCu}_{6-x}\text{Au}_x$ and YbRh_2Si_2 are particular candidates for experimental relevance of the Kondo-breakdown transition, and our findings suggest to search for first-order transitions near the unconventional quantum critical points in these materials. The non-existence of first order lattice transitions in real materials would provoke the question whether two Fermi sheets exist near the Kondo-breakdown transition. Other theoretical scenarios not necessarily imply a topological splitting of the Fermi surface near the Kondo breakdown transition and should then be analyzed in greater detail. One interesting proposal involves the idea that on moving from the heavy Fermi-liquid phase towards the QCP, the quasiparticle weight vanishes on the entire Fermi surface. This necessarily implies that the quasiparticles in the FL^* phase become singular as well, and two “hot” Fermi surface sheets will coexists at the QCP, with a “superlarge” Fermi surface of volume $1 + 2n_c$ (Senthil, 2006). Although no mean-field description of such a scenario is known, it is conceivable that a Lifshitz transition will not appear at such a type of phase transition.

Chapter 3

Transport properties near a Kondo-breakdown transition

One of the peculiar observations at the heavy fermion QCPs in $\text{CeCu}_{6-x}\text{Au}_x$ and YbRh_2Si_2 is the linear temperature dependence of the electrical resistivity over more than one decade of temperature above the QCP (Löhneysen et al., 1998, Custers et al., 2003). An additional peculiarity is the Hall coefficient in YbRh_2Si_2 , showing a rapid change across the quantum critical point (Paschen et al., 2004, Friedemann, 2009). Within the $U(1)$ gauge theory approach we briefly introduced in the previous chapter, previous work by Coleman et al. (2005) theoretically obtained a jump in the Hall and electrical conductivities at the Kondo-breakdown QCP. More difficult to analyze are the transport properties in the finite temperature region above the quantum critical point. Due to the fluctuating gauge field, bosons and spinons mutually drag each other and lead to a complicated flow of electrical charge. In addition, the conduction electrons conduct charge as well. Although these properties make a theoretical description complicated, they might hold the key to decide whether the Kondo-breakdown transition is compatible with experiment or not. In the following, we first formulate an effective low-energy theory for the quantum critical region of the Kondo-breakdown transition. Based on this description, we use the Keldysh formalism to derive transport equations and discuss approximative solutions in order to analyze the electrical conductivity.

3.1 Gauge field theory

For a description of transport properties near a Kondo breakdown transition, our mean-field description is not sufficient. Fluctuation effects are important for the transport of electrical charge, as well as for the equilibrium thermodynamics in the quantum critical region. I.e., the coupling of the spinons to the $U(1)$ gauge field leads to singular self-energy corrections for the spinons that cause non-Fermi-liquid behavior in the quantum critical region of the Kondo-breakdown transition Senthil et al. (2004). In the heavy Fermi liquid phase, fluctuations endow the f -particle with a physical electrical charge thereby making it an electron (Coleman et al., 2005).

We concentrate here on the quantum critical region, where fluctuation effects compete with thermal fluctuations. To simplify our analysis, we first derive an effective low-energy action in order to analyze transport properties in the quantum critical region. The starting point to describe fluctuation effects in the quantum critical region is the action

$$\begin{aligned}
S' &= S_c + S_f + S_{fc} + S_b \\
S_c &= \int d\tau \sum_{\mathbf{k}} \bar{c}_{\mathbf{k}\sigma} (\partial_\tau - \varepsilon_{\mathbf{k}}) c_{\mathbf{k}\sigma} \\
S_f &= \int d\tau \left[\sum_r \bar{f}_{r\sigma} (\partial_\tau - ia_0(r)) f_{r\sigma} - \sum_{\langle ij \rangle} \chi_{ij}^* \left(\sum_\sigma \bar{f}_{i\sigma} f_{j\sigma} \right) + h.c. \right] \\
&\quad + \sum_{\langle ij \rangle} \frac{4|\chi_{ij}|^2}{J_H} \\
S_{cf} &= - \int d\tau \sum_r (b_r \bar{c}_{r\sigma} f_{r\sigma} + h.c.) \\
S_b &= \int d\tau \sum_r \frac{2|b_r|^2}{J_K}
\end{aligned} \tag{3.1}$$

that we derived in form of Eq. (2.10) in chapter 2.

Derivation of effective low energy theory

In the action (3.1), the conduction electrons enter quadratically and it is easy to integrate them out exactly. This step is motivated by the observations we made in the mean-field theory in chapter 2: the important changes near the transition occur at the “hot” Fermi surface which is composed mainly out of spinons, while the “cold” Fermi surface plays a spectator role near this transition.¹ After integrating out the conduction electrons from (3.1), the action has the form $S = S_f + S_b + S_{fb}$ with the coupling S_{fb} between bosons and spinons given by

$$S_{fb} = - \int \int d\tau' d\tau \sum_{rr'} \bar{b}_r \bar{f}_r G_c(r, r', \tau, \tau') b_{r'} f_{r'} , \tag{3.2}$$

with the conduction electron propagator given by $G_c(\omega, \mathbf{k}) = \frac{1}{\omega - \varepsilon_{\mathbf{k}}}$ in frequency-momentum representation. We proceed by introducing the continuum approximation to the field variables contained in the action (3.1) by defining the vector field $\mathbf{a}(\mathbf{r})$ such that the link variable a_{ij} used in (3.1) is given by $a_{ij} = (\mathbf{r}_i - \mathbf{r}_j) \cdot \mathbf{a}[(\mathbf{r}_i + \mathbf{r}_j)/2]$. In this approximation, the lattice version of the coupling term between gauge field and spinons is then replaced

¹At the “hot” Fermi surface, near the QCP the dispersion is approximately given by the spinon dispersion, and the quasiparticle weight at this Fermi surface vanishes continuously at the transition, whereas it stays finite at the remaining “cold” parts of the Fermi surface dominated by the conduction electron dispersion, see section 2.1.

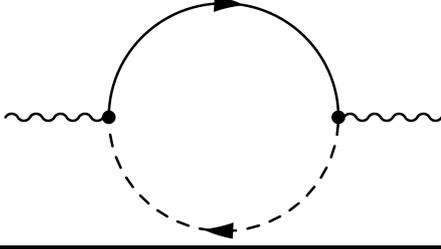


Figure 3.1: Polarization bubble that generates the dynamics of the bosons (wiggly lines). The inner lines correspond to conduction electrons (solid line) and high-energy spinons (dashed line).

by

$$-\sum_{\langle rr' \rangle} \chi_0 [e^{ia_{rr'}} \bar{f}_{r\sigma} f_{r'\sigma} + h.c.] \xrightarrow{\text{continuum}} - \int d^3\mathbf{r} \bar{f}_\sigma(\mathbf{r}) \frac{(\vec{\nabla} - i\mathbf{a})^2}{2m_F} f_\sigma(\mathbf{r}), \quad (3.3)$$

with the spinon effective mass $1/m_F \simeq J_H$ (Lee et al., 2006). In order to derive an effective low-energy theory, it is further possible to integrate out high-energy spinons far away from the spinon Fermi surface. This is formally achieved by defining two sets of variables

$$\begin{aligned} f_{\mathbf{k}}^< &= f_{\mathbf{k}}, \quad 0 < k < \Lambda \\ f_{\mathbf{k}}^> &= f_{\mathbf{k}}, \quad \Lambda \leq k, \end{aligned} \quad (3.4)$$

with some cutoff Λ of order the spinon bandwidth. The field $f_{\mathbf{k}}^>$ describes then f -excitations far away from the f -Fermi surface and can be integrated out to derive an effective low-energy theory.

This step generates the polarization loop for the bosons shown in Fig. 3.1. In this diagram, the high-energy excitations $f_{\mathbf{k}}^>$ remain gapped, and the polarization loop can therefore be safely expanded in gradients of space and time. Up to higher time and spatial gradients, this produces the additional symmetry-allowed terms

$$S_b = \int d\tau d^3\mathbf{r} \left[\bar{b}_{\mathbf{r}} (\partial_\tau - \mu_b - ia_0 - \frac{(\vec{\nabla}_{\mathbf{r}} - i\mathbf{a})^2}{2m_b}) b_{\mathbf{r}} + \frac{u}{2} |b_{\mathbf{r}}|^4 + \dots \right] \quad (3.5)$$

in the effective action for the bosons (Senthil et al., 2004). Therefore, the bosons have become a propagating mode coupling to the internal gauge field. We note that all other terms in the boson action are irrelevant in the RG sense near the Kondo-breakdown transition (Senthil et al., 2004). This includes a density-density coupling between b and f and the higher time and spatial gradients in the action S_b (Senthil et al., 2004). The total effective action for bosons and spinons at long-distance and time scales is then given by

$$S = S_b + S_f, \quad (3.6)$$

where S_f has the same form as in Eq. 3.1.

Since the external gauge field couples only to the conduction electrons and bosons, only these degrees of freedom carry a physical charge. Gauge charge (e_0) and electrical charge ($-e$) have the following assignments to the different types of particles

	gauge charge	electric charge
bosons	e_0	e
spinons	e_0	0
conduction electrons	0	$-e$

Importantly, integrating out high-energy spinons generates a vacuum contribution of the gauge field to the Lagrangian. This may be written in form of a *Maxwell term* (Herbut et al., 2003)

$$\frac{F_{\mu\nu}^2}{4g^2}, \quad (3.7)$$

with the field strength tensor defined by

$$F_{\mu\nu} = \partial_\mu a_\nu - \partial_\nu a_\mu, \quad (3.8)$$

where $\partial_0 = \partial_\tau$, $\partial_i = \partial_{x_i}$. The finite gauge-field coupling g could (in principle) be determined from the action (3.1).

Gauge field dynamics

By integrating out the matter fields of the action (3.6), an effective action for the gauge field may be obtained. In turn, fermions and bosons couple to the gauge fluctuations, which modifies the dynamics of these matter fields. At zero temperature, we are interested in the transport properties *at* the quantum critical point between the FL and FL* phase. Here, there are no bosons in the ground state, and the gauge field dynamics is entirely generated by the spinons. Integrating out the spinons from the action S_f and expanding the resulting action to quadratic order in the gauge field yields the *random phase approximation* (Lee et al., 2006)

$$S_{\text{eff}}^{\text{RPA}}(a) = \int \frac{d^{d+1}p}{(2\pi)^{d+1}} \Pi_{\mu\nu}(\mathbf{p}) a_\mu(\mathbf{p}) a_\nu(-\mathbf{p}) \quad (3.9)$$

with the $d+1$ -dimensional vector $\mathbf{p} = (\mathbf{k}, \omega)$. In this action, the current-current correlation function $\Pi_{\mu\nu}(\mathbf{p}) = \langle j_\mu(\mathbf{p}) j_\nu(-\mathbf{p}) \rangle$ enters, with the four current given by the densities and currents of gauge charge, $j_0 = c\rho$, $j_\mu = j_i$. The general low-energy form of the gauge field action $S_{\text{eff}}^{\text{RPA}}(\mathbf{a})$ obtained by expanding $\Pi_{\mu\nu}(\mathbf{p})$ in low momenta and frequencies is given by (Herbut et al., 2003)

$$S_a = \int \frac{d^d \mathbf{k} d\omega}{(2\pi)^{d+1}} \left[\frac{1}{2} a_i a_j \left(\delta_{ij} - \frac{k_i k_j}{k^2} \right) \left(\frac{|\omega| k_0}{k} + \chi_d k^2 \right) + \frac{\chi}{2} \left(1 + \frac{\gamma|\omega|}{k} \right) \left(a_0 - \frac{\omega}{k^2} k_i a_i \right)^2 \right]. \quad (3.10)$$

Here, χ_d is the spinon diamagnetic susceptibility, χ the spinon compressibility, $k_0 \simeq k_F$ and γ a damping coefficient characteristic of the spinon Fermi surface. At this stage, it is convenient to take the *transverse gauge* by imposing the gauge-fixing condition

$$\vec{\nabla} \cdot \mathbf{a} = 0. \quad (3.11)$$

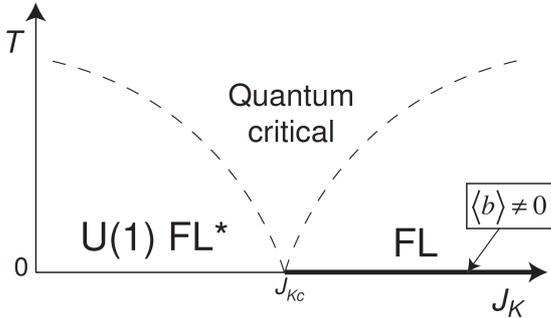


Figure 3.2: Schematic crossover phase diagram of the $d = 3$ $U(1)$ gauge theory described by (3.5) as a function of Kondo exchange J_K and temperature T . The only true phase transition above is that at the $T = 0$ quantum critical point at $J_K = J_{Kc}$ between the FL and FL* phases, described by condensation of the slave boson with $\langle b \rangle \neq 0$ in the FL phase. The crossover line between the FL and the quantum critical regime can be associated with the “coherence” temperature of the heavy Fermi liquid. For further details see main text. Figure taken from Senthil et al. (2004).

In this gauge, the scalar and vector parts a_0 and \mathbf{a} of the gauge-field dynamics are decoupled, such that in $\Pi_{\mu\nu}(\mathbf{p})$ only the components $\Pi_{00}(\mathbf{p})$ and $\Pi_{ij}(\mathbf{p})$ with $i, j \in \{1, 2, 3\}$ are nonzero. The scalar part of the gauge field action describes the density-density response function and does not show any singular behavior in the low-energy/low-momentum limit (Senthil et al., 2004, Lee et al., 2006). The long-wavelength behavior of the transverse gauge field action is in the Gaussian universality class and is therefore exactly described by $\Pi_{ij}(\mathbf{p})$ with $i, j \in \{1, 2, 3\}$ in the transverse gauge (3.11) (Gan and Wong, 1993). As can be deduced from Eq. (3.10), the propagator for the transverse gauge fluctuations takes the general form

$$D_{ij}(\mathbf{k}, i\omega_n) \equiv \langle a_i(\mathbf{k}, i\omega_n) a_j(-\mathbf{k}, -i\omega_n) \rangle = \frac{\delta_{ij} - k_i k_j / k^2}{k_0 |\omega_n| / k + \chi_d k^2}. \quad (3.12)$$

Discussion of fluctuation effects

Our mean-field theory results are modified by fluctuations in several aspects, and before turning to transport properties, we discuss their influences on the equilibrium properties. First, we briefly discuss fluctuation effects in the two phases. The heavy Fermi liquid phase is stable to fluctuations, since the gauge bosons acquire a mass by the Higgs mechanism (Senthil et al., 2004). In this phase, external and internal gauge field become effectively coupled due to the hybridization between c - and f -fermions, and the f -fermions acquire a physical charge in this way (Coleman et al., 2005).

FL* state Fluctuation effects are more interesting in the FL* state, and are described by a $U(1)$ gauge theory of a spinon Fermi surface minimally coupled to a $U(1)$ gauge field (Senthil et al., 2004). This phase may be discussed by ignoring all coupling between c and f -fermions. In three dimensions, the $U(1)$ gauge theory admits a deconfined phase where the spinons potentially survive as good excitations of the phase. Formally, this can be

justified in the same large- N limit as the one we used for the mean-field approximation (Senthil et al., 2004). In this deconfined phase, static spinons interact with each other through an emergent long range $1/r$ Coulomb interaction. A small coupling between the c - and f -particles will not change the deconfined nature of this phase (Senthil et al., 2004). An important consequence of the long-range interaction between the spinons is a $C \sim T \ln(T_0/T)$ singularity in the specific heat (Holstein et al., 1973).

Transition between FL and FL* We now turn to the most important case of our discussion, the zero temperature phase transition between the FL and $U(1)$ FL* phases. The basic properties of this transition are illustrated in Fig. 3.2. As motivated above, the properties of this transition and the quantum regime associated with it are described by the effective action (3.5). This action is similar to that in gauge theory descriptions of the normal state of optimally doped cuprates (Lee et al., 2006) but with some crucial differences that were discussed by Senthil et al. (2004). The horizontal axis in the phase diagram Fig. 3.2 is accessed by varying μ_b in the action (3.5). The Kondo-breakdown QCP between the FL and $U(1)$ FL* phases occurs precisely at $\mu_b = 0$, $T = 0$. We discuss the physical properties in the vicinity of the Kondo-breakdown QCP both at $T = 0$ and $T > 0$.

At zero temperature, it is sufficient to analyze properties in the FL* phase in order to understand the Kondo-breakdown quantum critical point, since in both cases there are no bosons in the ground state, $\langle b \rangle = 0$. We consider therefore $\mu_b < 0$ in the FL* phase in the following. The quartic coupling u contributes then no self-energy corrections due to the absence of bosons. It remains to discuss self-energy corrections related to the gauge field propagator given by Eq. (3.12). For the bosons, the imaginary part reads (Lee and Nagaosa, 1992)

$$\begin{aligned} \Sigma_b''(\mathbf{k}, \Omega) &= \int_0^\infty d\omega \int \frac{d^d \mathbf{k}'}{(2\pi)^d} [n_B(\omega) + 1][1 + n_B(\epsilon_{\mathbf{k}'})] \\ &\times (\mathbf{k} + \mathbf{k}')_\alpha (\mathbf{k} + \mathbf{k}')_\beta (2m_F)^{-2} \\ &\times (\delta_{\alpha\beta} - q_\alpha q_\beta / q^2) \text{Im} D^T(\mathbf{q}, \omega) \delta(\Omega - \epsilon_{\mathbf{k}'} - \omega) , \end{aligned} \quad (3.13)$$

where $\mathbf{q} = \mathbf{k}' - \mathbf{k}$, $\text{Im} D^T(\mathbf{k}, \omega) = (k_0 |\omega| / k + \chi_d k^2)^{-1}$ is the reduced form of Eq. (3.12) and $n_B(\omega)$ and $n_F(\omega)$ are the Bose and Fermi distribution functions, respectively. The real part $\Sigma_b'(\mathbf{k}, \Omega)$ can be obtained from the Kramers-Kronig transform

$$\Sigma_b'(\mathbf{k}, \Omega) = \frac{1}{\pi} \mathcal{P} \int_{-\infty}^{\infty} \frac{\Sigma_b''(\mathbf{k}, \Omega')}{\Omega - \Omega'} d\Omega' . \quad (3.14)$$

In three dimensions, the self-energy diagram for the bosons in Fig. 3.3 at small momenta and frequencies has the form

$$\Sigma_b(\mathbf{k}, i\epsilon) \sim k^2 (1 + c_1 |\epsilon| \ln(1/|\epsilon|) + \dots) , \quad (3.15)$$

where c_1 is some constant (Senthil et al., 2004). Apart from a renormalization of the boson mass m_b , these corrections are less relevant than the bare terms in the action (3.5). Since

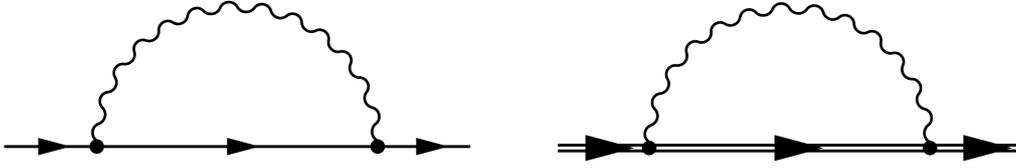


Figure 3.3: Self-energy diagrams for the spinons (left, full line) and bosons (right, double line) due to a single gauge-boson (wiggly line) exchange process.

$\Sigma_b(0,0) = 0$, also the position of the Kondo-breakdown transition remains unchanged at $\mu_b = 0$. Since the boson lifetime is clearly longer than its inverse energy,

$$\text{Im}\Sigma_b\left(\mathbf{k}, \epsilon = \frac{k^2}{2m_b}\right) \sim \text{sgn}(\epsilon)\epsilon^2 \ln(1/|\epsilon|), \quad (3.16)$$

the quasiparticle pole remains well-defined in presence of gauge fluctuations. The situation is different for the spinons, whose self-energy correction is obtained by replacing $1 + n_B(\epsilon_{\mathbf{k}'})$ with $1 - n_F(\epsilon_{\mathbf{k}'})$ in Eq. (3.13). For the imaginary part of the self-energy, this yields $\Sigma_f''(k_F, \omega) \sim |\omega|^{d/3}$ in d dimensions, implying non-Fermi-liquid behavior in $d \leq 3$ (Gan and Wong, 1993).

At *finite temperatures*, the self-energy due to the quartic coupling in (3.5) yields the contribution $\Sigma_b(0,0) = u \frac{\zeta(3/2)}{4\pi^{3/2}} (2m_b T)^{3/2}$ (Senthil et al., 2004). Both μ_b and $\Sigma_b(0,0)$ enter the b Green's function in form of mass terms, and the larger of both determines the physical properties (Senthil et al., 2004). This aspect determines the position of the crossover phase boundaries in Fig. 3.2 as $T \sim |\mu_b|^{2/3} \sim |J_K - J_{K_c}|^{2/3}$. Importantly, there is no phase transition in the FL region at $T > 0$ as wrongly predicted by mean-field theory: in three dimensions, the ‘‘Higgs’’ and ‘‘confining’’ phases of a compact $U(1)$ gauge theory are smoothly connected (Senthil et al., 2004).

We saw that the quantum critical region of the Kondo breakdown transition is influenced by four different degrees of freedom: bosons, spinons, conduction electrons and gauge field. In presence of an external electrical field, the interplay of these degrees of freedom is extraordinarily complicated. In the following section, we will first introduce the Keldysh formalism and apply it to our electrical transport problem. Afterwards, we will make use of several approximations within this formalism in order to obtain quantitative results for the electrical conductivity in the quantum critical region of the Kondo-breakdown transition.

3.2 Quantum Boltzmann equation

There are several different methods of doing transport theory. One possibility is ‘‘linear response’’ theory. One assumes that currents are proportional to weak external fields.

The proportionality constants can then be evaluated in equilibrium. This method works because one assumes that the applied fields are small, and the system is only infinitesimally disturbed from equilibrium. A complementary approach to describe transport properties is the usage of the *Keldysh formalism* for non-equilibrium Green's functions. This approach formulates an equation of motion for a non-equilibrium Green's function and constructs electrical currents etc. from the solution to this equation of motion. In the limit of small driving fields, the transport equation can be linearized in the external perturbation and this approach yields results identical to the linear response formalism. We shall use this approach in the following, since we expect that the underlying physical processes are more transparent in the transport equation formalism, in particular since several degrees of freedom (fermions, bosons, gauge bosons) participate in our low-energy effective theory. The usage of the Keldysh formalism in transport theory has been discussed in the review article of Rammer and Smith (1986) and in the book of Mahan (1990).

Keldysh formalism

In a strict sense, non-equilibrium Green's functions are used when a Hamiltonian depends explicitly on time. A very general form of such a non-equilibrium system is described by a time-dependent Hamiltonian of the form

$$\mathcal{H}(t) = H_{\text{free}} + H_{\text{int}} + V(t), \quad (3.17)$$

where $V(t) = 0$ for $t < t_0$, such that the system is influenced by the disturbance $V(t)$ only for $t \geq t_0$ and otherwise described by the time-independent interacting Hamiltonian $H = H_{\text{free}} + H_{\text{int}}$ with interaction H_{int} and the non-interacting part H_{free} . In our study of electrical transport, $V(t)$ will cause a static electrical field switched on adiabatically in the limit $t_0 \rightarrow -\infty$ and coupling to bosonic and fermionic particles. In order to evaluate a single particle Green's function ²

$$G(1, 1') = -i\langle\psi(1)\psi^\dagger(1')\rangle \quad (3.18)$$

of a Bose or Fermi field ψ , *diagrammatic perturbation theory* is a very important tool if H_{int} is complicated. We assume here and in the following that $\langle\cdot\rangle$ describes thermodynamic averaging with respect to the interacting density matrix $\frac{e^{-\beta H}}{\text{tr}(e^{-\beta H})}$, $\beta = T^{-1}$ for times $t > t_0$.

Once it is possible to assume that the system is in the non-interacting ground state of H_{free} in the limits $t \rightarrow -\infty$ and $t \rightarrow \infty$, one can use the S-matrix $S(-\infty, \infty) = \mathcal{T}e^{-i\int_{-\infty}^{\infty} dt H(t)}$ with the time ordering operator \mathcal{T} in order to formulate a diagrammatic expansion of $G(1, 1')$ using Wick's theorem. This assumption fails for a general form of perturbation $V(t)$, which can prohibit that the system returns to its initial ground state if $t \rightarrow \infty$. It is possible to introduce an extended time contour such that the equilibrium and non-equilibrium formalisms can be made *structurally* equivalent. For this purpose, a closed time path contour c is introduced that explicitly returns to the time t_0 when the time-dependent

²We introduce the abbreviation $1 \equiv (t_1, x_1)$, where t_1 denotes the temporal variable and x_1 the spatial variable that may be generalized in a straightforward manner to include spin and other degrees of freedom.

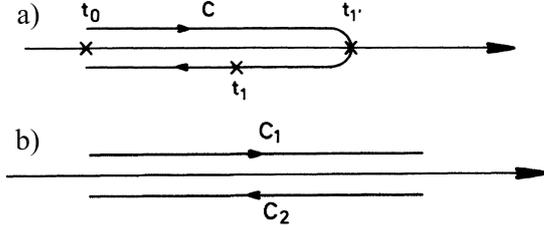


Figure 3.4: a) The “closed time path” contour c that is useful to formulate a perturbation expansion for a system that is exposed to a time-dependent perturbation at the time t_0 . b) The *Keldysh contour* c_K consists of two parts: c_1 extending from $-\infty$ to $+\infty$ and c_2 extending from $+\infty$ to $-\infty$. Figures taken from Rammer and Smith (1986).

perturbation is switched on, see Fig. 3.4a. For practical purposes, the contour c is extended beyond the largest time $\max\{t_1, t'_1\}$ by use of the unitary of the time-development operator. Furthermore, we set $t_0 \rightarrow -\infty$, such that we obtain the contour originally introduced by Keldysh and depicted in Fig. 3.4b, which allows for a formulation of diagrammatic perturbation theory in analogy to the conventional equilibrium formalism. By ordering the time argument along the Keldysh contour in Fig. 3.4b, the contour-ordered Green’s function

$$G_{c_K}(1, 1') \equiv -i \langle \mathcal{T}_{c_K}(\psi(1)\psi^\dagger(1')) \rangle \quad (3.19)$$

is defined, with the contour ordering operation \mathcal{T}_{c_K} defined by

$$\mathcal{T}_{c_K}(\psi(1)\psi^\dagger(1')) \equiv \begin{cases} \psi(1)\psi^\dagger(1') & t_1 >_{c_K} t_{1'} \\ \psi(1)\psi^\dagger(1') & t_1 <_{c_K} t_{1'} \end{cases} \quad (3.20)$$

The contour-ordered Green’s function G_{c_K} is not fully defined by its time arguments, since each real time argument has an additional contour index κ , which we set $\kappa = 1$ on the chronological part c_1 and $\kappa = 2$ on the anti-chronological part c_2 of the Keldysh contour c_K . It is convenient to map the contour-ordered function $G_{c_K}(1, 1')$ onto *Keldysh space*, where the representation is defined as a 2×2 matrix Green’s function $\hat{G}_{\kappa\kappa'}(1, 1')$ with the entries

$$\begin{aligned} G_t(1, 1') &\stackrel{\text{def}}{=} \hat{G}_{11}(1, 1') , \\ G^<(1, 1') &\stackrel{\text{def}}{=} \hat{G}_{12}(1, 1') , \\ G^>(1, 1') &\stackrel{\text{def}}{=} \hat{G}_{21}(1, 1') , \\ G_{\bar{t}}(1, 1') &\stackrel{\text{def}}{=} \hat{G}_{22}(1, 1') . \end{aligned} \quad (3.21)$$

We will call these functions the *time-ordered* Green’s function $G_t(1, 1')$,

$$G_t(1, 1') = -i \langle \mathcal{T} \psi(1)\psi^\dagger(1') \rangle , \quad (3.22)$$

the “*greater*” function $G^>$,

$$G^>(1, 1') = -i \langle \psi(1)\psi^\dagger(1') \rangle , \quad (3.23)$$

the “*lesser*” function $G^<$,

$$G^<(1, 1') = \mp i \langle \psi^\dagger(1) \psi(1') \rangle, \quad (3.24)$$

and the *antitime-ordered* Green function $G_{\bar{t}}$,

$$G_{\bar{t}}(1, 1') = -i \langle \bar{T} \psi(1) \psi^\dagger(1') \rangle. \quad (3.25)$$

We will furthermore make use of the *retarded* Green’s function

$$G_{\text{ret}}(1, 1') = -i \theta(t_1 - t'_1) \langle [\psi(1), \psi^\dagger(1')]_{\mp} \rangle. \quad (3.26)$$

In our definitions for $G^<(1, 1')$ and $G_{\text{ret}}(1, 1')$, the upper and lower signs correspond to bosons and fermions, respectively.

For the Keldysh Green’s function G_{cK} , a Dyson equation can be formulated, analogous to conventional equilibrium diagrammatic perturbation theory (Mahan, 1990),

$$\hat{G}(x_1, x_2) = \hat{G}_0(x_1 - x_2) + \int_{-\infty}^{\infty} dx_3 \int_{-\infty}^{\infty} dx_4 \hat{G}_0(x_1 - x_2) \hat{\Sigma}(x_3, x_4) \hat{G}(x_4, x_2). \quad (3.27)$$

Here \hat{G}_0 is the non-interacting equilibrium Green’s function corresponding to setting $H_{\text{int}} \equiv V(t) \equiv 0$ in Eq. (3.17). This Dyson equation is the starting point for deriving an equation of motion for the Green’s function $G^<$, which we will refer to as *quantum Boltzmann equation* (QBE) in the following. This Green’s function contains all the information to determine non-equilibrium particle and current densities.

In order to describe particle currents or densities, it is useful to introduce center of mass coordinates

$$\begin{aligned} (\mathbf{R}, T) &= \frac{1}{2}(x_1 + x_2) \\ (\mathbf{r}, t) &= x_1 - x_2 \end{aligned} \quad (3.28)$$

Using these coordinates, the lesser Green’s function is given by

$$G^<(\mathbf{r}, t; \mathbf{R}, T) = \mp i \langle \psi^\dagger(\mathbf{R} - \frac{1}{2}\mathbf{r}, T - \frac{1}{2}t) \psi(\mathbf{R} + \frac{1}{2}\mathbf{r}, T + \frac{1}{2}t) \rangle. \quad (3.29)$$

Furthermore, we introduce the Fourier transform

$$G^<(\mathbf{q}, \Omega; \mathbf{R}, T) = \int d^d \mathbf{r} e^{i\mathbf{q}\mathbf{r}} \int dt e^{i\Omega t} G^<(\mathbf{r}, t; \mathbf{R}, T) \quad (3.30)$$

The electrical current density of particles with mass m , charge $-e$ and dispersion $k^2/(2m)$ is then given by (Mahan, 1990)

$$j(\mathbf{R}, T) = \mp i e \int \frac{d^d \mathbf{k}}{(2\pi)^d} \frac{\mathbf{k}}{m} \int \frac{d\omega}{2\pi} G^<(\mathbf{k}, \omega; \mathbf{R}, T). \quad (3.31)$$

For weak electric fields, $G^<$ can be linearized in electrical field strength and the electrical conductivity can be identified from the proportionality constant between current and field strength in Eq. (3.31).³ It remains therefore to construct and solve an equation of motion for the Green’s function $G^<(\mathbf{k}, \omega; \mathbf{R}, T)$.

³However, in order to identify the DC conductivity it is necessary to assume that $G^<(\mathbf{k}, \omega; \mathbf{R}, T)$ does not depend on the center of mass coordinates (\mathbf{R}, T) , as is appropriate for a homogeneous and steady electrical field.

Quantum Boltzmann equation – formalism

We will derive the equation of motion for the function $G^<(1, 1')$ for interacting bosonic / fermionic particles with physical charge $-e$ in a weak, homogeneous and steady electrical field. We assume that the electrical field \mathbf{E} derives from both a scalar potential $H_s = -e\mathbf{E}_s\mathbf{r}$ and a vector potential $\mathbf{A} = -c\mathbf{E}_v t$, such that the system is gauge invariant and $\mathbf{E} = \mathbf{E}_s + \mathbf{E}_v$. Due to the simplicity of this external perturbation, it can be absorbed into the non-interacting part H_{free} of the Hamiltonian. Then, H_{free} of the Hamiltonian for a single particle with charge $-e$ is described by

$$H_{\text{free}}(\mathbf{r}, \mathbf{p}) = \frac{(\mathbf{p} - \frac{e\mathbf{A}}{c})^2}{2m} - e\mathbf{E}_s\mathbf{r} . \quad (3.32)$$

Next, it is possible to derive two equations of motion for the Keldysh Green's function \hat{G} by using the equation of motion for the non-interacting Keldysh Green's function $\hat{G}_0(x)$

$$\left[i\frac{\partial}{\partial t} - H_{\text{free}}(x) \right] \hat{G}_0(x) = \delta^4(x)\hat{I} , \quad (3.33)$$

where \hat{I} is the identity operator. By acting with (3.33) on the Dyson equation (3.27) both on the first and the second argument, we obtain the equations of motion (Mahan, 1990)

$$\begin{aligned} \left[i\frac{\partial}{\partial t_1} - H_{\text{free}}(\mathbf{r}_1, \mathbf{p}_1) \right] \hat{G}(x_1, x_2) &= \delta^4(x_1 - x_2)\hat{I} + \int dx_3 \hat{\Sigma}(x_1, x_3)\hat{G}(x_3, x_2) \\ \left[-i\frac{\partial}{\partial t_2} - H_{\text{free}}(\mathbf{r}_2, -\mathbf{p}_2) \right] \hat{G}(x_1, x_2) &= \delta^4(x_1 - x_2)\hat{I} + \int dx_3 \hat{G}(x_1, x_3)\hat{\Sigma}(x_3, x_2) . \end{aligned} \quad (3.34)$$

The derivation of the QBE equation involves several algebraic manipulations on the left-hand side of these equations. In order to avoid a lot of cumbersome notation, we shall not write out the right hand side of these equations during these steps.

By subtracting (first line in (3.35)) and adding (second line in (3.35)) the equations of motion (3.34) and inserting the explicit representation (3.32), the equations of motion

$$\begin{aligned} 2 \left[\Omega + e\mathbf{E}_s\mathbf{R} - \frac{1}{2m}(\mathbf{q} + e\mathbf{E}_v T)^2 + \frac{1}{8m}(\vec{\nabla}_{\mathbf{R}} + e\mathbf{E}_v \frac{\partial}{\partial \Omega})^2 \right] G(\mathbf{q}, \Omega; \mathbf{R}, T) &= \\ i \left[\frac{\partial}{\partial T} - \frac{1}{m}(\mathbf{q} + e\mathbf{E}_v T) \left(\vec{\nabla}_{\mathbf{R}} + e\mathbf{E}_v \frac{\partial}{\partial \Omega} \right) + e\mathbf{E}_s \vec{\nabla}_{\mathbf{q}} \right] G(\mathbf{q}, \Omega; \mathbf{R}, T) &= \end{aligned} \quad (3.35)$$

can be derived. In Eq. (3.35), we used the center of mass coordinates $(\mathbf{r}, t; \mathbf{R}, T)$ and employed the Fourier transform (3.30). As has been discussed by Hansch and Mahan (1983), the transport equations (3.35) have several shortcomings. (i) Since \mathbf{E}_s and \mathbf{E}_v enter the result differently, these equations are not gauge invariant. (ii) Furthermore, the center of mass time and coordinate enter the relative momentum and energy, such that the energy of the particle seems to depend on position. These deficiencies can be avoided by

the variable transform

$$\begin{aligned}
\Omega + e\mathbf{E}_s \cdot \mathbf{R} &\rightarrow \omega \\
\mathbf{q} + e\mathbf{E}_\nu T &\rightarrow \mathbf{k} \\
\vec{\nabla}_{\mathbf{R}} &\rightarrow \vec{\nabla}_{\mathbf{R}} + e\mathbf{E}_s \frac{\partial}{\partial \omega} \\
\frac{\partial}{\partial T} &\rightarrow \frac{\partial}{\partial T} + e\mathbf{E}_\nu \cdot \vec{\nabla}_{\mathbf{k}} .
\end{aligned} \tag{3.36}$$

The driving terms of the final transport equations are (Mahan, 1990)

$$\begin{aligned}
\left[\omega - \epsilon_{\mathbf{k}} + \frac{1}{8m} \left(\vec{\nabla}_{\mathbf{R}} + e\mathbf{E} \frac{\partial}{\partial \omega} \right)^2 \right] G(\mathbf{k}, \omega; \mathbf{R}, T) &= \\
i \left[\frac{\partial}{\partial T} + \mathbf{v}_{\mathbf{k}} \cdot \vec{\nabla}_{\mathbf{R}} + e\mathbf{E} \cdot \left(\vec{\nabla}_{\mathbf{k}} + \mathbf{v}_{\mathbf{k}} \frac{\partial}{\partial \omega} \right) \right] G(\mathbf{k}, \omega; \mathbf{R}, T) &=
\end{aligned} \tag{3.37}$$

It is important to note that the collision terms of these transport equations as derived by Hänsch and Mahan (1983) are not valid for a general form of the self-energy $\hat{\Sigma}(1, 1')$, since a field-dependent correction term to this self-energy arises due to the variable transformation (3.36) that has been neglected in the original formulation of Hänsch and Mahan (1983) (Chen and Su, 1987, 1990). In our case, the self energies in Fig. 3.3 are a linear functional of the full Green's function of bosons or spinons and the correction vanishes, as shown by Chen and Su (1987, 1990).

We assume a homogeneous steady system in the following, such that any dependency on the variables \mathbf{R} and T can be dropped. Then, from (3.37) the equation of motion for the retarded Green's function follows as (Mahan, 1990)

$$\left[\omega - \epsilon_{\mathbf{k}} - \Sigma_{\text{ret}} \right] G_{\text{ret}} = 1 + \mathcal{O}(E^2) \tag{3.38}$$

This equation of motion is formally identical to the equilibrium equation of motion. However, in our case the non-equilibrium form of the gauge field propagator enters the self-energy Σ_{ret} for bosons and spinons and leads to a dependence of G_{ret} on the electrical field \mathbf{E} , see also Fig. 3.3. After some formal manipulations, the quantum Boltzmann equation for the function $G^<$ to linear order in \mathbf{E} is (Mahan, 1990)

$$A(\mathbf{k}, \Omega)^2 \frac{\partial n}{\partial \omega} e\mathbf{E} \cdot [(\mathbf{v}_{\mathbf{k}} + \vec{\nabla}_{\mathbf{k}} \text{Re}\Sigma_{\text{ret}})\Gamma + \sigma \vec{\nabla}_{\mathbf{k}} \Gamma] = \Sigma^> G^< - \Sigma^< G^> . \tag{3.39}$$

Here, we employed the quantities $A = -2\text{Im}G_{\text{ret}}$, $\Gamma = -2\text{Im}\Sigma_{\text{ret}}$, $\sigma = \omega - \epsilon_{\mathbf{k}} - \text{Re}\Sigma_{\text{ret}}$ and $n(\omega)$ is the Fermi or Bose distribution function if (3.39) describes fermions or bosons, respectively. The retarded functions are obtained by the relations

$$\begin{aligned}
\text{Im}G_{\text{ret}}(k, \omega) &= G^<(k, \omega) - G^>(k, \omega) \\
\text{Im}\Sigma_{\text{ret}}(k, \omega) &= \Sigma^<(k, \omega) - \Sigma^>(k, \omega) ,
\end{aligned} \tag{3.40}$$

and it can be easily derived that the collision term $\Sigma^>G^< - \Sigma^<G^>$, is therefore identical to $i2\Gamma G^< - i\Sigma^<A$. Up to now, a solution of the transport equation (3.39) requires explicit

knowledge of both Σ_{ret} and the collision term $i2\Gamma G^< - i\Sigma^<A$. The collision term will depend on the particular degrees of freedom participating in electrical transport and on the scattering mechanisms. We will now detail these aspects for the transport properties of the Kondo-breakdown transition.

Coupled transport equations for bosons and spinons

We will assume in the following that the electrical DC conductivities (described by the current-current correlation functions of the respective types of particles) of the conduction electrons σ_c and the system of spinons and bosons (denoted by σ_{bf}) add, such that the total conductivity is given by the sum $\sigma_c + \sigma_{bf}$. This approximation is based on the assumption that the vertex between conduction electrons and bosons plus spinons is gapped (Paul et al., 2008). We will detail the justification of this aspect in our quantitative discussion of the electrical conductivity.

In the following, we analyze therefore the transport equations of the combined system of spinons and bosons, which is described by the action (3.6). For the conduction electrons, we will assume a Fermi liquid form of the electrical conductivity.

All transport properties of this system are contained in the contour-ordered Keldysh Green's functions for the bosons, fermions and gauge field, given by

$$\begin{aligned} G_b(1, 1') &= \langle T_c \bar{b}(1) b(1') \rangle \\ G_f(1, 1') &= \langle T_c \bar{f}(1) f(1') \rangle \\ D_{ij}(1, 1') &= \langle T_c a_i(1) a_j(1') \rangle . \end{aligned} \quad (3.41)$$

In absence of impurities, the whole system is translational invariant and has infinite electrical conductivity. Our main interest is to describe the temperature-dependence of the conductivity, which is easier to compare with experiment than the residual resistivity. We therefore assume that the electrical conductivity σ_{bf} of the system of spinons and bosons is dominated by collisions of the spinons and bosons on the fluctuating gauge field. This assumption is restricted to temperatures below the order of the Debye temperature, where scattering on phonons can be neglected. However, in order to obtain a finite electrical conductivity in absence of impurities we have to make a further assumption about the non-equilibrium Green's function for bosons, fermions and gauge field. We will specify this assumption after deriving the formal transport equations.

According to the diagrams (3.3), the one-loop self-energy for bosons or spinons scattered on gauge bosons is

$$\Sigma^<(\mathbf{k}, \omega) = \frac{i}{2} \frac{1}{m_b^2} \int \frac{d^d \mathbf{q}}{(2\pi)^d} \int \frac{d\Omega}{2\pi} \sum_{ij} k_i k_j (D_{ij}^<(\mathbf{q}, -\Omega) + D_{ij}^>(\mathbf{q}, \Omega)) G^<(\mathbf{k} + \mathbf{q}, \omega + \Omega) , \quad (3.42)$$

where $\Sigma^<$ and $G^<$ can equally represent spinons or bosons. Our transport theory requires up to now a formulation of transport equations for bosons, spinons and gauge field. Whether these transport equations are coupled or not depends crucially on the collision terms, which are the only objects that explicitly depend on the non-equilibrium distribution functions. Those can induce a mutual drag of bosons, spinons and gauge field. This

problem is very difficult, and our strategy will be to make assumptions about the gauge field Green's function $D_{ij}(1, 1')$ and deriving explicit transport equations only for bosons and spinons.

A first simplification is to linearize the left hand side of the transport equation (3.39) in \mathbf{E} , and the retarded functions contained in the driving term can then be replaced by their equilibrium versions. We obtain the coupled set of transport equations

$$\begin{aligned} A_b(\mathbf{k}, \omega)^2 \frac{\partial n_b}{\partial \omega} e\mathbf{E} \cdot [(\mathbf{v}_\mathbf{k} + \vec{\nabla}_\mathbf{k} R e \Sigma_{\text{ret}}) \Gamma_b + \sigma \vec{\nabla}_\mathbf{k} \Gamma_b] &= I_{\text{coll}}^b(\mathbf{k}, \omega) \\ I_{\text{coll}}^b(\mathbf{k}, \omega) &= 2i\Gamma_b(\mathbf{k}, \omega) G_b^<(\mathbf{k}, \omega) - i\Sigma_b^<(\mathbf{k}, \omega) A_b(\mathbf{k}, \omega) \end{aligned} \quad (3.43)$$

for the bosons and

$$\begin{aligned} A_f(\mathbf{k}, \omega)^2 \frac{\partial n_f}{\partial \omega} e\mathbf{E} \cdot [(\mathbf{v}_\mathbf{k} + \vec{\nabla}_\mathbf{k} R e \Sigma_{\text{ret}}) \Gamma_f + \sigma \vec{\nabla}_\mathbf{k} \Gamma_f] &= I_{\text{coll}}^f(\mathbf{k}, \omega) \\ I_{\text{coll}}^f(\mathbf{k}, \omega) &= 2i\Gamma_b(\mathbf{k}, \omega) G_f^<(\mathbf{k}, \omega) - i\Sigma_f^<(\mathbf{k}, \omega) A_f(\mathbf{k}, \omega) \end{aligned} \quad (3.44)$$

for the spinons. Importantly, the electrical field \mathbf{E} in the driving term in Eq. (3.44) has to be set $\mathbf{E} = 0$, since the electrical field does not couple to the spinons, which have no physical charge. Finally, the retarded functions in the collision terms of both transport equations depend on the electrical field \mathbf{E} through the gauge field propagator $D_{ij}(1, 1')$ which itself depends on $G_b(1, 1')$ and $G_f(1, 1')$. This fact mediates the coupling between the transport equations (3.43) and (3.44). We try to simplify these equations by a convenient approximation: setting the gauge field propagator equal to its equilibrium form, such that the transport equations (3.43) and (3.44) decouple. It is this step that renders the electrical conductivity of the system finite, since it provokes that momentum transfers to the gauge field are instantaneously equilibrated, such that momentum conservation is broken. To justify this step, it has to be assumed that other degrees of freedom, i.e. impurities, effectively equilibrate the gauge field while the propagators of fermions and bosons maintain a non-equilibrium form. We will not justify this assumption further, which is conveniently made by many authors, e.g., Ioffe and Kotliar (1990), Pépin (2008). A possible way to justify this assumption might be the *memory matrix formalism* (Forster, 1990) that allows to explicitly compare momentum relaxation rates of different degrees of freedom.

The equilibrium form of the gauge field propagator is immediately obtained as (Mahan, 1990)

$$D_{ij}^<(\mathbf{k}, \omega) = in_B(\omega) A_{ij}^D(\mathbf{k}, \omega), \quad (3.45)$$

where $A_{ij}^D(\mathbf{k}, \omega) = -2ImD_{ij}^{\text{ret}}(\mathbf{k}, \omega)$. Then, the self-energy (3.42) is approximated by

$$\Sigma^<(\mathbf{k}, \omega) = \sum_{\mathbf{q}} \int_{-\infty}^{\infty} \frac{d\nu}{\pi} \left| \frac{\mathbf{k} \times \hat{\mathbf{q}}}{m} \right|^2 ImD^T(\mathbf{q}, \nu) [n_b(\nu) + 1] G^<(\mathbf{k} + \mathbf{q}, \omega + \Omega) \quad (3.46)$$

Furthermore, the solution to the spinon transport equation (3.44) will be the equilibrium form of $G_f^<(\mathbf{k}, \omega)$, since only equilibrium quantities enter this equation. Furthermore, according to Eq. (3.38) all retarded functions can be replaced by their equilibrium versions, since field dependence enters then only to order E^2 and can be neglected in the linearized transport equations. It remains therefore to discuss the transport equation for the bosons.

Transport equation for bosons

In order to solve the transport equation (3.43), we expand the boson Green function to linear order in \mathbf{E} and make the ansatz

$$G_b^<(\mathbf{k}, \omega) = iA_b(\mathbf{k}, \omega) \left[n_B(\omega) - \left(\frac{\partial n_B(\omega)}{\partial \omega} \right) \mathbf{E} \cdot \mathbf{v}_\mathbf{k}^b \Lambda_b(\mathbf{k}, \omega) \right] \quad (3.47)$$

with the unknown function $\Lambda_b(\mathbf{k}, \omega)$ that has to be determined from a solution to the quantum Boltzmann equation. This ansatz leads to the integral equation

$$\begin{aligned} iA^2(\mathbf{k}, \omega) e\mathbf{E} \frac{dn_B}{d\omega} \vec{v}_\mathbf{k} \Gamma_b(\mathbf{k}, \omega) &= 2i\Gamma_b(\mathbf{k}, \omega) \Lambda(\mathbf{k}, \omega) A(\mathbf{k}, \omega) \frac{dn_B}{d\omega} e\mathbf{E} \cdot \mathbf{v}_\mathbf{k} \\ &+ \frac{A(\mathbf{k}, \omega)}{m_B^2} \sum_{\mathbf{q}} \int \frac{d\Omega}{2\pi} \sum_{ij} k_1^i k_1^j i n_B(\omega) A_{ij}^D(\mathbf{k}, \Omega) \\ &\times \frac{dn_B(\omega + \Omega)}{d\omega} e\mathbf{E} \mathbf{v}_{\mathbf{k}+\mathbf{q}} \Lambda(\mathbf{k} + \mathbf{q}, \omega + \Omega) \Lambda(\mathbf{k} + \mathbf{q}, \omega + \Omega) . \end{aligned} \quad (3.48)$$

This equation might be formally solved by iterating it and representing the solution as a series of recursive integrals. It seems rather formidable to evaluate this series within some controlled approximation. Therefore, we assume in the following that $G_b^<(\mathbf{k}, \omega)$ in (3.47) can be approximated by

$$G_b^<(\mathbf{k}, \omega) = iA_b(\mathbf{k}, \omega) f(\mathbf{k}) , \quad (3.49)$$

where $f(\mathbf{k})$ is a function of momentum. This approximation is justified if $A_b(\mathbf{k}, \omega)$ has sharp quasiparticle poles and can be approximated by $\text{const} \times \delta(\omega - \varepsilon_\mathbf{k})$. This is indeed the case, since (i) $A_b(\mathbf{k}, \omega)$ is equal to the equilibrium spectral function which has (ii) sharp quasiparticle poles at bosonic energies $\varepsilon_\mathbf{k}$ due to Eq. (3.16). We now use the transport equation (3.35) before the variable transform (3.36) has been performed,

$$i \left[\partial_T - \frac{1}{m_b} (\mathbf{q} + e\mathbf{E}_\nu T) (\vec{\nabla}_\mathbf{R} + e\mathbf{E}_\nu \partial_\Omega) + e\mathbf{E}_s \vec{\nabla}_\mathbf{q} \right] G^<(\mathbf{q}, \Omega, \mathbf{R}, T) = \Sigma^> G^< - \Sigma^< G^> . \quad (3.50)$$

In these variables, we have (we include an explicit dependence on the center of mass coordinates which drops out in the end for a homogeneous steady system)

$$G_b^<(\mathbf{q}, \Omega, \mathbf{R}, T) = i\delta(\varepsilon_{\mathbf{q}+e\mathbf{E}_\nu T} - \Omega - e\mathbf{E}_s \cdot \mathbf{R}) f(\mathbf{q} + e\mathbf{E}_\nu T, \mathbf{R}, T) . \quad (3.51)$$

Inserting this function into Eq. (3.50) and integrating over Ω , the result is

$$\begin{aligned} (\partial_T - e\mathbf{E}_\nu \vec{\nabla}_\mathbf{q} + \mathbf{v}_{\mathbf{q}+e\mathbf{E}_\nu T} \vec{\nabla}_\mathbf{R} + e\mathbf{E} \vec{\nabla}_\mathbf{q}) f(\mathbf{q} + e\mathbf{E}_\nu T, \mathbf{R}, T) \\ = - \int_{-\infty}^{\infty} d\Omega (\Sigma^> G^< - \Sigma^< G^>) . \end{aligned} \quad (3.52)$$

The collision term can be evaluated as

$$\begin{aligned}
& \Sigma^>(\mathbf{q} + e\mathbf{E}_\nu T, \varepsilon_{\mathbf{q}+e\mathbf{E}_\nu T})f(\mathbf{q} + e\mathbf{E}_\nu T, \mathbf{R}, T) \\
& - \Sigma^<(\mathbf{q} + e\mathbf{E}_\nu T, \varepsilon_{\mathbf{q}+e\mathbf{E}_\nu T})(1 + f(\mathbf{q} + e\mathbf{E}_\nu T, \mathbf{R}, T)) = \\
& f(\mathbf{q} + e\mathbf{E}_\nu T, \mathbf{R}, T) \frac{2}{m_B^2} \int \frac{d^d \mathbf{p}}{(2\pi)^d} \int_{-\infty}^{\infty} \frac{d\Omega}{2\pi} \sum_{ij} (\mathbf{q} + e\mathbf{E}_\nu T)_i (\mathbf{q} + e\mathbf{E}_\nu T)_j \text{Im} D_{ij}^T(\mathbf{p}, \Omega) \\
& \times n_b(\Omega) (f(\mathbf{q} + e\mathbf{E}_\nu T + \mathbf{p}) + 1) 2\pi \delta(\varepsilon_{\mathbf{q}+e\mathbf{E}_\nu T} - e\mathbf{E}_s \mathbf{R} - \varepsilon_{\mathbf{q}+e\mathbf{E}_\nu T + \mathbf{p}} + \Omega + e\mathbf{E}_s \mathbf{R}) \\
& - (f(\mathbf{q} + e\mathbf{E}_\nu T, \mathbf{R}, T) + 1) \frac{2}{m_B^2} \int \frac{d^d \mathbf{p}}{(2\pi)^d} \int_{-\infty}^{\infty} \frac{d\Omega}{2\pi} \sum_{ij} (\mathbf{q} + e\mathbf{E}_\nu T)_i (\mathbf{q} + e\mathbf{E}_\nu T)_j \\
& \times \text{Im} D_{ij}^T(\mathbf{p}, \Omega) (n_b(\Omega) + 1) (f(\mathbf{q} + e\mathbf{E}_\nu T + \mathbf{p}) + 1) \\
& \times 2\pi \delta(\varepsilon_{\mathbf{q}+e\mathbf{E}_\nu T} - e\mathbf{E}_s \mathbf{R} - \varepsilon_{\mathbf{q}+e\mathbf{E}_\nu T + \mathbf{p}} + \Omega + e\mathbf{E}_s \mathbf{R}) \tag{3.53}
\end{aligned}$$

where we made use of the identity

$$n_b(\omega) + 1 \equiv -n_b(-\omega) . \tag{3.54}$$

Now, we can invert the variable transform $\mathbf{q} + e\mathbf{E}_\nu T = \mathbf{k}$ to make the result gauge invariant, leading to the Boltzmann equation

$$\begin{aligned}
\left(\frac{\partial}{\partial T} + \mathbf{v}_\mathbf{k} \vec{\nabla}_\mathbf{R} + \mathbf{E} \vec{\nabla}_\mathbf{k} \right) f(\mathbf{k}, \mathbf{R}, T) &= \frac{4\pi}{m_B^2} \int \frac{d^d \mathbf{q}}{(2\pi)^d} \int_{-\infty}^{\infty} \frac{d\Omega}{2\pi} \sum_{ij} k_i k_j \text{Im} D_{ij}(\mathbf{q}, \Omega) \\
& \times \delta(\varepsilon_\mathbf{k} - \varepsilon_{\mathbf{k}+\mathbf{q}} - \Omega) [f(\mathbf{k}, \mathbf{R}, T)(n(\Omega) + 1)(f(\mathbf{k} + \mathbf{q}, \mathbf{R}, T) + 1) \\
& - f(\mathbf{k} + \mathbf{q}, \mathbf{R}, T)n(\Omega)(f(\mathbf{k}, \mathbf{R}, T) + 1)], \tag{3.55}
\end{aligned}$$

where we made again use of Eq. (3.54). This result coincides with the phenomenological transport equation derived by Senthil et al. (2004) if the system is homogeneous and does not depend on \mathbf{R} . In a small (as well as steady and homogeneous) electrical field, the solution to Eq. (3.55) can be approximated by the form

$$f(\mathbf{k}) = f_0(\mathbf{k}) + \mathbf{k} \cdot \mathbf{E} f_1(\mathbf{k}) , \tag{3.56}$$

with some unknown function $f_1(\mathbf{k})$ and the Bose distribution function

$$f_0(\mathbf{k}) = \frac{1}{\exp\left(\left(\frac{k^2}{2m_b} - \mu_b + \Sigma_b(0, 0)\right)/T\right) - 1} . \tag{3.57}$$

Here $\Sigma_b(0, 0) \sim T^{3/2}$, with the proportionality constant given in the end of section 3.1. From $f_1(\mathbf{k})$, the expression for the electrical current

$$\mathbf{J}_b = \int \frac{d^d \mathbf{k}}{(2\pi)^d} \frac{\mathbf{k}}{m_b} f(\mathbf{k}) , \tag{3.58}$$

and thus the boson electrical conductivity can be determined. A numerical solution to this problem has been discussed by Senthil et al. (2004), showing a $-1/\ln(T)$ -divergence of the

conductivity σ_b at low T .

Up to now, we derived the electrical DC conductivity for the bosons scattering on equilibrium gauge fluctuations. In total, we made several approximations that would lead to the conclusion that the total conductivity of the system is given by the sum of the conductivities of the bosonic particles and the conduction electrons, $\sigma_c + \sigma_b$. These approximations, especially the neglect of a drag between bosons and spinons mediated by the internal gauge field, have to be justified. As promised, we will discuss these approximations now in more detail. Fortunately, this problem is simplified by a conservation law.

Discussion of electrical conductivity

The discussion of electrical transport properties can be simplified by considering the local conservation law $f_{r\sigma}^\dagger f_{r\sigma} = 1$ associated with the fermionic representation of the local moments. This implies directly that in the full action (3.1), the total gauge current associated with the locally conserved gauge charge of the f -particles vanishes, $\mathbf{J}_f \equiv 0$. However, this conservation law is maintained also in the low-energy effective action (3.6). Since in this action also bosons couple to the internal gauge field, the conservation law for the gauge current now reads

$$\mathbf{J}_f + \mathbf{J}_b \equiv 0 . \quad (3.59)$$

From this conservation law, immediate consequences for the total electrical conductivity of the system can be derived. We note here that the DC electrical conductivities of the currents of gauge charge and physical charges are obtained from current-current correlation functions (Mahan, 1990) of the form $\Pi_{\alpha\beta}(\mathbf{k}, \omega)$ as introduced in the context of Eq. (3.9),

$$\sigma_{\alpha\beta} = - \lim_{\omega \rightarrow 0} \left(\lim_{\mathbf{q} \rightarrow 0} \frac{1}{\omega} \text{Im} [\Pi_{\alpha\beta}(\mathbf{q}, \omega)] \right) . \quad (3.60)$$

The external current associated with the external gauge field is given by the sum $\mathbf{J} = \mathbf{J}_c + \mathbf{J}_b$. Using this fact and the conservation law (3.59) for the gauge current, for the total electrical conductivity in the system the composition rule

$$\sigma = \sigma_c + [\sigma_f^{-1} + \sigma_b^{-1}]^{-1} \quad (3.61)$$

can be derived using the definition (3.60) (Pépin, 2008). It is therefore possible to discuss the three quantities σ_f , σ_b and σ_c independently in order to determine the total conductivity of the system.

The simplest contribution is the contribution of the conduction electrons. It is in general the case that there is a gap in the continuum of particle-hole excitations described by the diagram in Fig. 3.1, such that at temperatures below this gap energy scale, the conduction electrons are not affected by scattering on bosons and spinons. This can be understood from Fig. 3.5, where it is assumed that both conduction electrons and spinons have quadratic dispersion. If the conduction band is not accidentally half-filled (as the spinon band is by constraint), the Fermi wavevectors of these two bands will have a mismatch q^* leading to an energy scale E^* characteristic for particle transfer between the two bands, Fig. 3.5.

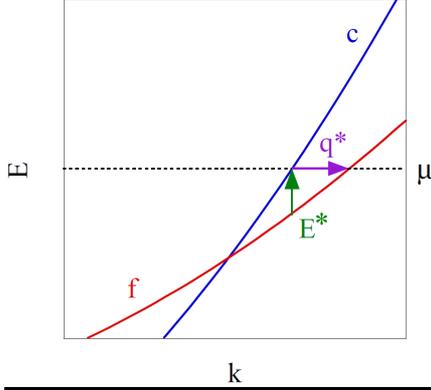


Figure 3.5: Dispersion of conduction and spinon bands, with the mismatch wavevector, q^* , and the mismatch energy, E^* . Figure taken from Paul et al. (2008).

In this case, the conduction electron resistivity is described by the standard Fermi liquid form $\rho_c \sim \rho_c^{(0)} + T^2$.⁴ The conductivity of spinons scattering on gauge fluctuations has been calculated by Ioffe and Kotliar (1990), Lee and Nagaosa (1992), with $\sigma_f \sim T^{-4/3}$ in 2d and $\sigma_f \sim T^{-5/3}$ in 3d.

Finally, the boson electrical conductivity for scattering on gauge fluctuations follows $\sigma_b \sim -1/\ln(T)$, as discussed above. However, it is realistic to assume that bosons and spinons show a saturation of their conductivities at zero temperature due to scattering on impurities. The general form of the conductivity in 3d is therefore given by

$$\sigma = \frac{1}{\rho_c^{(0)} + T^2} + \frac{1}{\rho_b^{(0)} + \rho_f^{(0)} + T^{5/3} - \frac{1}{\ln(T)}}, \quad (3.62)$$

where we assume that the combined system of bosons and spinons has a residual resistivity $\rho_b^{(0)} + \rho_f^{(0)}$ due to impurity scattering, originating either from the bosons or the spinons or both. Necessarily, the asymptotic low-temperature behavior of σ is therefore given by the $-\frac{1}{\ln(T)}$ contribution of the bosons. This result is valid also in $d = 2$, where Senthil et al. (2004) obtained the same $-\frac{1}{\ln(T)}$ dependence of σ_b , still asymptotically dominating the temperature dependence of $\sigma_f \sim T^{-4/3}$. The temperature regime of the $-\frac{1}{\ln(T)}$ -dependence of σ might be unobservable small, depending on the coefficients of the temperature-dependence of $\sigma_b, \sigma_c, \sigma_f$ and the sizes of the residual resistivities.

In order to observe the $1/\ln(T)$ dependence of the boson conductivity in experiment, this temperature dependence has to dominate that of the spinons, such that necessarily $-\ln(T) \lesssim \mathcal{O}(T^{-5/3})$. This sets an upper temperature boundary for the $1/\ln(T)$ contribution to the conductivity to be observed. On the other hand, the $-1/\ln(T)$ -contribution should be of the order of the residual resistance $\rho(T = 0) = (1/\rho_c^{(0)} + 1/(\rho_b^{(0)} + \rho_f^{(0)}))^{-1}$ in order to be observable, requiring that $T \gtrsim \exp(-1/\rho(T = 0))$. Therefore, the $1/\ln(T)$ contribution might be unobservable if $\rho(T = 0)$ is too large. Whether this is indeed the case depends on the coefficients of the $1/\ln(T)$ and $T^{-5/3}$ tails, which we did not evaluate here.

⁴For brevity, we set constants entering the temperature dependence of resistivities equal to unity here and in the following.

3.3 Conclusions

In this chapter, we discussed the electrical DC conductivity in the quantum critical region of the Kondo-breakdown transition. Our theoretical analysis started with the derivation of an effective low-energy theory for the Kondo-breakdown transition. We assumed that scattering processes of conduction electrons on bosons and spinons are gapped, leading to a Fermi-liquid-like resistivity of the conduction electrons. A more detailed analysis should also consider temperature scales above this energy gap E^* , where this assumption fails. For our effective low-energy theory, we derived a coupled set of transport equations based on the Keldysh formalism. Due to the complicated interplay between the non-equilibrium gauge field, spinon and boson propagators, we made several approximations to simplify a discussion of these transport equations. First, we assumed that the electrical conductivities of bosons and spinons are dominated by the scattering on gauge field fluctuations. Based on conservation of gauge current, we used a composition rule for the individual conductivities of spinons and bosons in order to argue that the bosons will dominate the joint conductivity of bosons and spinons. We used this argument to decouple the transport equations for bosons and spinons and derived a Boltzmann-like transport equation for a boson distribution function, agreeing with the phenomenological transport equation of Senthil et al. (2004). Finally, we discussed under which conditions the $-1/\ln(T)$ contribution of the boson conductivity might be observed in experiment.

In any case our results fail to describe the experimentally observed linear temperature dependence of the resistivity (Löhneysen et al., 1998, Custers et al., 2003). One possible reason might be that the temperature scales probed in experiment are above the energy gap E^* , beyond which our assumptions fail. From the scattering processes on excitations living above that energy scale Paul et al. (2007) find a quasilinear $T \log(T)$ behavior in $d = 3$, which still could be experimentally distinguished from a linear T resistivity. However, these authors identify the conduction electron conductivity with the quasiparticle life time, thereby neglecting vertex corrections. Finally, our approximation of an equilibrated gauge field is not justified rigorously and deserves future theoretical investigations, since this problem is of general interest for transport properties of $U(1)$ gauge theories.

Appendix A

Appendix to chapter 2

A.1 Maxwell construction for first-order phase transitions

An ideal classical gas of point-like particles with total volume V , pressure p , density n , temperature T and Loschmidt number R is described by the equation of state

$$pV = nRT . \quad (\text{A.1})$$

This equation of state cannot describe a phase transition to a liquid phase. Such a transition can be described if pV is replaced by $\left(p + a\frac{n^2}{V^2}\right)(V - nb)$ with suitable material parameters $a, b > 0$, leading to the equation of state

$$\left(p + a\frac{n^2}{V^2}\right)(V - nb) = nRT \quad (\text{A.2})$$

for the *van-der-Waals gas*. For fixed pressure p and temperature T , this equation of state has three real solutions for V if $p < p_c$, $T < T_c$ and one real solution else. This defines a critical point (p_c, V_c, T_c) , where the three real solutions are identical. Solving Eq. (A.2) for $p(V)$ at fixed $T < T_c$, it can be shown that there is always a volume region where

$$\left(\frac{\partial p}{\partial V}\right)_T > 0 , \quad (\text{A.3})$$

such that the system is mechanically unstable. Therefore, liquid and gas coexist in some finite region of volumes between V_α and V_β , where pressure ($p \equiv p_{\alpha\beta}$) is only a function of temperature. In the coexistence region, the chemical potentials of liquid and gas phase are equal, $\mu_l(T, p_{\alpha\beta}) = \mu_g(T, p_{\alpha\beta})$, and Gibbs free enthalpy is therefore equal at the points α and β , $G_\alpha(T, p_{\alpha\beta}) = G_\beta(T, p_{\alpha\beta})$, such that the difference in the free energies will be (Nolting, 2005)

$$F_\alpha - F_\beta = p_{\alpha\beta}(V_\beta - V_\alpha) . \quad (\text{A.4})$$

This difference can also be written as

$$F_\alpha - F_\beta = \int_{V_\alpha}^{V_\beta} p dV|_{T=\text{const}} , \quad (\text{A.5})$$

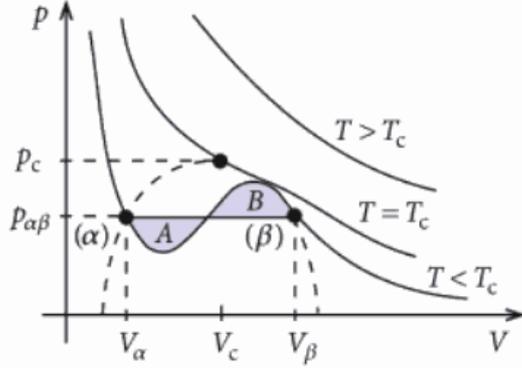


Figure A.1: Principle of the Maxwell construction for the van-der-Waals gas. Below the critical temperature T_c the pressure-volume isotherm between V_α and V_β is not given by the van-der-Waals equation of state and can be constructed as a horizontal line such that the areas A and B are equal. Figure taken from Nolting (2005).

such that we obtain the equation

$$\int_{V_\alpha}^{V_\beta} p dV|_{T=\text{const}} = p_{\alpha\beta}(T)(V_\beta - V_\alpha) , \quad (\text{A.6})$$

which has a simple geometrical meaning. In Fig. A.1, the shaded areas A and B have to be equal, and this graphical construction of the *correct* pressure-volume isotherm is called *Maxwell construction*.

A.2 Schrieffer-Wolff transformation of the periodic Anderson model

In analogy to the original work of Schrieffer and Wolff (1966) relating the single impurity Anderson model to the Kondo Hamiltonian, the periodic Anderson model (1.11) can be related to a Kondo lattice model of the type

$$H_{\text{KLM}} = \sum_{\mathbf{k}\sigma} \varepsilon_{\mathbf{k}} c_{\mathbf{k}\sigma}^\dagger c_{\mathbf{k}\sigma} + \sum_{\mathbf{k}\mathbf{k}'} J_{\mathbf{k}\mathbf{k}'} e^{-i(\mathbf{k}'-\mathbf{k})\mathbf{R}_i} \mathbf{S}_i \cdot \mathbf{s}_{\mathbf{k}'\mathbf{k}} . \quad (\text{A.7})$$

Here, we provide details of this relation which are rarely presented in the literature. The transformation we shall perform becomes valid in the *Kondo limit* of the periodic Anderson model,

$$\frac{V^2}{\varepsilon_f + U}, \frac{V^2}{\varepsilon_f} \rightarrow 0 \\ \varepsilon_f < 0, \varepsilon_f + U > 0 . \quad (\text{A.8})$$

such that fluctuations occur only in terms of virtual processes, which are described by second order perturbation theory. Since virtual processes are at least of $\mathcal{O}(V^2)$, the effective Hamiltonian can be derived by formulating a unitary transformation that eliminates all terms of linear order in V ,

$$\tilde{H} = e^S H e^{-S} , \quad (\text{A.9})$$

with $[H_0, S] = H_V$. The transformed Hamiltonian \tilde{H} has the form

$$\tilde{H} = H_0 + H_2 + \mathcal{O}(V^3). \quad (\text{A.10})$$

The generator S is easily obtained by modifying the choice of Schrieffer and Wolff (1966) by using a sum over lattice sites and multiplying each term with a phasefactor $e^{-i\mathbf{k}\cdot\mathbf{R}_i}$

$$S = \sum_{\mathbf{k}i\sigma} \left(\frac{V_{\mathbf{k}} e^{-i\mathbf{k}\cdot\mathbf{R}_i}}{\varepsilon_{\mathbf{k}} - \varepsilon_f - U} n_{i-\sigma}^f c_{\mathbf{k}\sigma}^\dagger f_{i\sigma} + \frac{V_{\mathbf{k}} e^{-i\mathbf{k}\cdot\mathbf{R}_i}}{\varepsilon_{\mathbf{k}} - \varepsilon_f} (1 - n_{i-\sigma}^f) c_{\mathbf{k}\sigma}^\dagger f_{i\sigma} \right) - \text{h.c.} \quad (\text{A.11})$$

Four terms are contained in $H_2 = \frac{1}{2}[S, H_V]$, $H_2 = H_{\text{ex}} + H_{\text{dir}} + H_{\text{hop}} + H_{\text{ch}}$, with

$$\begin{aligned} H_{\text{ex}} &= \frac{1}{2} \sum_{\mathbf{k}\mathbf{k}'i} J_{\mathbf{k}'\mathbf{k}} e^{-i(\mathbf{k}'-\mathbf{k})\mathbf{R}_i} \left(S_i^+ c_{\mathbf{k}'\downarrow}^\dagger c_{\mathbf{k}\uparrow}^\dagger + S_i^- c_{\mathbf{k}'\uparrow}^\dagger c_{\mathbf{k}\downarrow}^\dagger + S_i^z (c_{\mathbf{k}'\uparrow}^\dagger c_{\mathbf{k}\uparrow}^\dagger - c_{\mathbf{k}'\downarrow}^\dagger c_{\mathbf{k}\downarrow}^\dagger) \right) \\ H_{\text{dir}} &= \sum_{\mathbf{k}\mathbf{k}'i\sigma} \left(W_{\mathbf{k}'\mathbf{k}} - \frac{1}{4} J_{\mathbf{k}'\mathbf{k}} (n_{i\uparrow}^f + n_{i\downarrow}^f) \right) e^{-i(\mathbf{k}'-\mathbf{k})\mathbf{R}_i} c_{\mathbf{k}'\sigma}^\dagger c_{\mathbf{k}\sigma} \\ H_{\text{hop}} &= - \sum_{\mathbf{k}ij\sigma} (W_{\mathbf{k}\mathbf{k}} - \frac{1}{2} J_{\mathbf{k}\mathbf{k}} (n_{i-\sigma}^f + n_{j-\sigma}^f)) e^{-i\mathbf{k}(\mathbf{R}_i - \mathbf{R}_j)} f_{j\sigma}^\dagger f_{i\sigma} \\ H_{\text{ch}} &= -\frac{1}{2} \sum_{\mathbf{k}\mathbf{k}'i\sigma} V_{\mathbf{k}'} V_{\mathbf{k}} e^{-i(\mathbf{k}'+\mathbf{k})\mathbf{R}_i} ((\varepsilon_{\mathbf{k}'} - \varepsilon_f - U)^{-1} - (\varepsilon_{\mathbf{k}'} - \varepsilon_f)^{-1}) c_{\mathbf{k}'-\sigma}^\dagger c_{\mathbf{k}\sigma}^\dagger f_{i\sigma} f_{i-\sigma} \\ &\quad + \text{h.c.} \end{aligned} \quad (\text{A.12})$$

and coupling constants

$$\begin{aligned} J_{\mathbf{k}'\mathbf{k}} &= V_{\mathbf{k}'} V_{\mathbf{k}}^* [-(\varepsilon_{\mathbf{k}} - \varepsilon_f - U)^{-1} - (\varepsilon_{\mathbf{k}'} - \varepsilon_f - U)^{-1} + (\varepsilon_{\mathbf{k}} - \varepsilon_f)^{-1} + (\varepsilon_{\mathbf{k}'} - \varepsilon_f)^{-1}] \\ W_{\mathbf{k}'\mathbf{k}} &= \frac{1}{2} V_{\mathbf{k}'} V_{\mathbf{k}}^* [(\varepsilon_{\mathbf{k}} - \varepsilon_f)^{-1} + (\varepsilon_{\mathbf{k}'} - \varepsilon_f)^{-1}]. \end{aligned} \quad (\text{A.13})$$

In the Kondo limit (A.8), $f_{i\sigma}^\dagger f_{i\sigma} = 1$, such that H_{ch} can be neglected, since it does not connect the Hilbert space having one f electron with the remainder of Hilbert space. Furthermore, H_{dir} simplifies to

$$H_{\text{dir}} = \sum_{\mathbf{k}\mathbf{k}'i\sigma} (W_{\mathbf{k}\mathbf{k}} - \frac{1}{4} J_{\mathbf{k}\mathbf{k}}) c_{\mathbf{k}\sigma}^\dagger c_{\mathbf{k}'\sigma}. \quad (\text{A.14})$$

In contrast to the single impurity case, H_{dir} contains no scattering processes and renormalizes only one-body energies. Moreover, hopping processes in H_{hop} are suppressed, such that H_{hop} reduces to the constant $H_{\text{hop}} = -\mathcal{N} \sum_{\mathbf{k}} W_{\mathbf{k}\mathbf{k}}$. We will make the further simplification of assuming a constant hybridization, $V_{\mathbf{k}} \equiv V$. It is also possible to consider $\varepsilon_f = -\frac{U}{2}$, such that the f -band becomes particle-hole symmetric,

$$\begin{aligned} W_{\mathbf{k}'\mathbf{k}} &\equiv \frac{2V^2}{U} \\ J_{\mathbf{k}'\mathbf{k}} &\equiv \frac{8V^2}{U}. \end{aligned} \quad (\text{A.15})$$

The final Hamiltonian becomes

$$H_K = \sum_{\mathbf{k}} \epsilon_{\mathbf{k}} c_{\mathbf{k}\alpha}^\dagger c_{\mathbf{k}\alpha} + \frac{J_K}{2} \sum_r \vec{S}_r \cdot c_{r\alpha}^\dagger \vec{\sigma}_{\alpha\alpha'} c_{r\alpha'} - \frac{\mathcal{N}}{4} J_K \quad (\text{A.16})$$

Other choices than $\epsilon_f = -\frac{U}{2}$ would lead only to renormalizations of the chemical potential and the constant contribution $-\frac{\mathcal{N}}{4} J_K$. In our mean field theory derived in chapter 2 with a strain dependent $V(\epsilon) = V(1 + \gamma\epsilon)$, these changes only renormalize pressure and Bulk modulus by a small constant value $\propto V(\epsilon)^2/U$ and have only minor influence on the overall shape of the phase diagram.

Part II

Structural and magnetic transitions in the iron arsenides

Chapter 4

Introduction: The iron arsenides

The field of iron arsenic superconductors is rapidly evolving, and even during the stage this part of the thesis was written from June-July 2009, dozens of related publications appeared. In this introduction, we concentrate on the most important developments that motivated our theoretical work we shall discuss in the subsequent three chapters.

4.1 General properties of iron arsenides

Experimental discoveries

In January 2008, a preprint appeared from the group of Hideo Hosono in Japan showing the existence of superconductivity in a layered iron arsenide material with a transition temperature (T_c) of 26 K (Kamihara et al., 2008). This discovery bears some close similarities to what has been found in the cuprate materials 22 years earlier. The parent compound LaOFeAs is not superconducting, but replacing some of the oxygen by fluorine, the material becomes superconducting. Also the crystal structure is reminiscent of the cuprates, with layers of FeAs separated by spacer layers of LaO where the fluorine dopants are introduced (Fig. 4.1a). Although the parent compound orders antiferromagnetically, it is not a charge transfer insulator as the cuprate parent compounds (see also chapter 11), but is characterized as a bad metal. The doping phase diagram seems to be similar in many different iron arsenide materials, with a transition from antiferromagnetic to superconducting order induced by doping either electron or hole carriers. Among the so called *1111 compounds* REOFeAs (RE=La,Ce,Pr,Nd,Sm, ...), GdOFeAs is the record holder with $T_c \approx 55$ K. In the following, we present some important aspects on the example of the LaO_{1-x}F_xFeAs phase diagram (Luetkens et al., 2008). Where necessary, remarks on different behavior in other FeAs materials (e.g., the *122 family* AFe₂As₂, A=Ca,Sr,Ba) will follow in the next section.

Phase diagram and properties of phases

A detailed analysis of the doping phase diagram of LaO_{1-x}F_xFeAs obtained by Luetkens et al. (2008) shows that magnetism disappears abruptly at the same critical electron doping

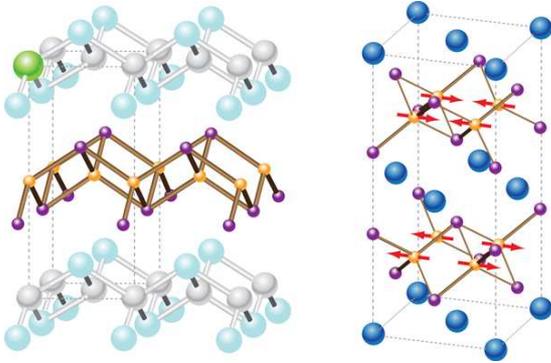


Figure 4.1: Left: Crystal structure of the 1111 FeAs material LaOFeAs . Fluorine (green) replaces oxygen (gray), donating electrons to the FeAs layers. Other atoms shown are iron (yellow), arsenic (purple), and lanthanum (light blue). Right: Crystal structure of the 122 FeAs material CaFe_2As_2 . The parent compound of both materials has iron moments (red arrows) that form a striped antiferromagnetic pattern. Calcium atoms are shown in blue. Figure from Norman (2008).

where superconductivity appears (Fig. 4.2). The magnetic phase is associated with a distortion of the crystal lattice from a tetragonal to an orthorhombic structure, and this distortion seems to be favored by iron spin order with iron spins that alternate in direction from one row of iron atoms to the next (see right panel in Fig. 4.1). Formally, this type of order is described by the ordering wavevector $(\pi, 0)$ on the Fe square lattice. The FeAs magnetism is not fully consistent with a local-moment picture, as the size of the ordered moment is unexpectedly small, in the range from $0.25\mu_B$ (Klauss et al., 2008) to $0.36\mu_B$ (Cruz et al., 2008), whereas a local moment on Fe is expected to have at least $2\mu_B$. Magnetic frustration has been invoked by Si and Abrahams (2008) to explain a reduced local moment, although a detailed microscopic theory for the magnetically ordered phase of FeAs materials is still lacking.

Measurements of the superconducting energy gap and the Fermi surface geometry are very similar among different iron arsenide materials. Angle-resolved photoemission studies have been able to map the anisotropy in momentum of the superconducting energy gap, which is important to identify the nature of the superconducting order parameter (Ding et al., 2008, Zhao et al., 2008, Kondo et al., 2008). Several cylindrical Fermi surfaces have been identified in ARPES measurements (Liu et al., 2008, Ding et al., 2008), and the gap anisotropy on each cylinder is relatively weak. In particular, no evidence for nodes – that is, points in momentum space where the energy gap vanishes – has been found. Other measurements support this interpretation, such as electron tunneling or penetration depth measurements (Chen et al., 2008, Martin et al., 2009). On the other hand, NMR studies find signatures of a gap with nodes, and controversies about a possible existence of nodes still exist. Theoretically, many different symmetries of the superconducting order parameter have been proposed, among them the particularly favored so-called s_{\pm} state (Mazin et al., 2008b). This type of superconducting order parameter takes opposite signs along the electron and hole cylinders of the multi-band FS, a type of pairing that can be understood by a spin-fluctuation mediated pairing mechanism (Kuroki et al., 2008). So far, this type of order parameter is not revealed in several experiments which find no evidence for sign changes in the order parameter, see for example Hicks et al. (2009).

Overall, a satisfactory understanding of these subtleties of the magnetic structure and symmetries of the superconducting order parameter has not been achieved yet.

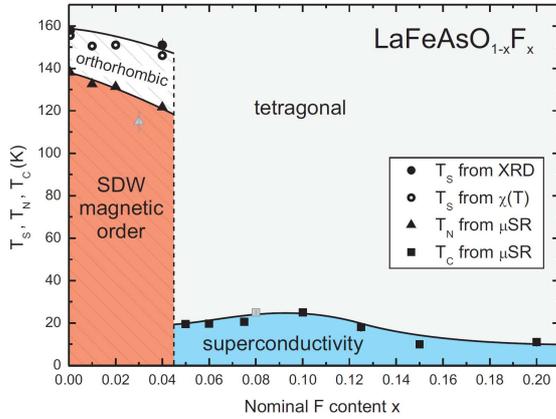


Figure 4.2: Electronic phase diagram of $\text{LaO}_{1-x}\text{F}_x\text{FeAs}$. Shown are the doping dependence of the magnetic (T_N) and superconducting transition (T_C) temperatures determined from muon-spin rotation (μSR) experiments. Also shown are the tetragonal to orthorhombic structural transition temperatures T_S determined directly from X-ray diffraction (XRD) and from susceptibility measurements which show a kink and subsequent strong reduction below T_S . Figure from Luetkens et al. (2008).

A theoretical description should certainly also consider in detail the electronic structure of the iron arsenide planes, which appears to be more complicated than that of the CuO planes in the cuprates.

Electronic structure

Both iron arsenides and cuprates are layered systems, and in both systems d -electrons play a crucial role. In cuprates, the $3d$ orbitals of Cu are non-degenerate due to the lattice structure. Nevertheless, it is often assumed that the single-band Hubbard model is sufficient to describe these materials, whereas the Fe arsenides are believed to require a multiband description. Based on LDA calculations (Singh and Du, 2008), it has been concluded that five bands are necessary to fit the Fermi surface, requiring a participation of all iron $3d$ orbitals and their hybridization with the $\text{As } 4p$ orbitals. It is also of importance to include effects of crystal field splitting and spin-orbit interaction into a description of the energy levels of the FeAs plane, which altogether have been argued to invalidate a naive Hund's rule filling of the $\text{Fe } d$ levels (Wu et al. (2008), see also Fig. 5.1). Several features of the Fermi surface as predicted from band structure calculations have been directly observed by angle resolved photoemission spectroscopy (Liu et al., 2008) and are also consistent with a quantum oscillation study of Sebastian et al. (2008), although ARPES results are in parts also controversial (Malaeb et al., 2009). These features originate mainly from the FeAs planes and apply therefore to most members of the FeAs family. Besides from the 1111 compounds, this family comprises also the so-called *122 compounds* that have become subject of intensive experimental and theoretical analysis soon after the initial discovery of superconductivity in $\text{LaO}_{1-x}\text{F}_x\text{FeAs}$.

4.2 The 122 family

The 122 family possesses the chemical composition formula AFe_2As_2 ($\text{A}=\text{Ca},\text{Ba},\text{Sr},\dots$) and can be quickly grown as single crystals. Although the superconducting transition temperatures found in these materials are somewhat lower than the values found in the

REFeAsO compounds, the salient physics appears to be similar, and more readily available single crystals, as well as potentially better and more quantifiable control over substitution, has made the AFe_2As_2 materials subject of extensive studies. The study of these materials began with the discovery of superconductivity in K-doped BaFe_2As_2 and SrFe_2As_2 by Rotter et al. (2008), with a T_c of 38 K in $\text{Ba}_{0.6}\text{K}_{0.4}\text{Fe}_2\text{As}_2$. It was soon speculated that tuning hydrostatic pressure can cause a superconducting state similar to the effect of substituting barium by potassium, and many experiments analyzed the pressure-temperature phase diagram of 122 materials subsequently (Kreyssig et al., 2008, Colombier et al., 2009, Goldman et al., 2009). Initial reports of pressure-driven superconductivity in CaFe_2As_2 by Kreyssig et al. (2008) could not be reproduced by later measurements of Goldman et al. (2009) and were caused by non-hydrostatic conditions. In contrast, later measurements by Colombier et al. (2009) on BaFe_2As_2 and SrFe_2As_2 reported pressure-induced superconductivity in these materials, see Fig. 4.3a. Although in CaFe_2As_2 superconductivity seems to be difficult to stabilize by pressure, several other salient features (Fig. 4.3b) appear in the temperature-pressure phase diagram (Kreyssig et al., 2008) of this material that will be the focus of our following study.

At ambient pressure CaFe_2As_2 has been found to undergo a first order phase transition from a high temperature, tetragonal phase to a low temperature orthorhombic/antiferromagnetic phase upon cooling through $T \approx 170$ K. With the application of pressure this phase transition is readily suppressed and by ~ 0.35 GPa, it is replaced by a first order phase transition to a low temperature collapsed tetragonal, non-magnetic phase. This transition is accompanied by a drop in the resistivity, i.e., the high-pressure phase appears to be a better conductor. Further application of pressure leads to an increase of the tetragonal to collapsed tetragonal phase transition temperature, with it crossing room temperature by ~ 1.7 GPa.

A careful reader might have recognized analogies with the Kondo volume collapse transition that was subject of chapter 2. In fact, we will elaborate further on this analogy in the next chapter.

4.3 Outline

Motivated by pressure experiments on CaFe_2As_2 , we will propose and analyze a scenario based on local moment physics to explain the simultaneous disappearance of magnetism, reduction of the unit cell volume and decrease in resistivity. In chapter 5, we will point out similarities and differences between the iron arsenides and classical heavy-fermion materials. Afterwards, we formulate an Anderson lattice model to capture the qualitative physics of the structural and collapse transitions in CaFe_2As_2 . Finally, we analyze this model in chapter 6 within a mean-field calculation and discuss implications of our results.

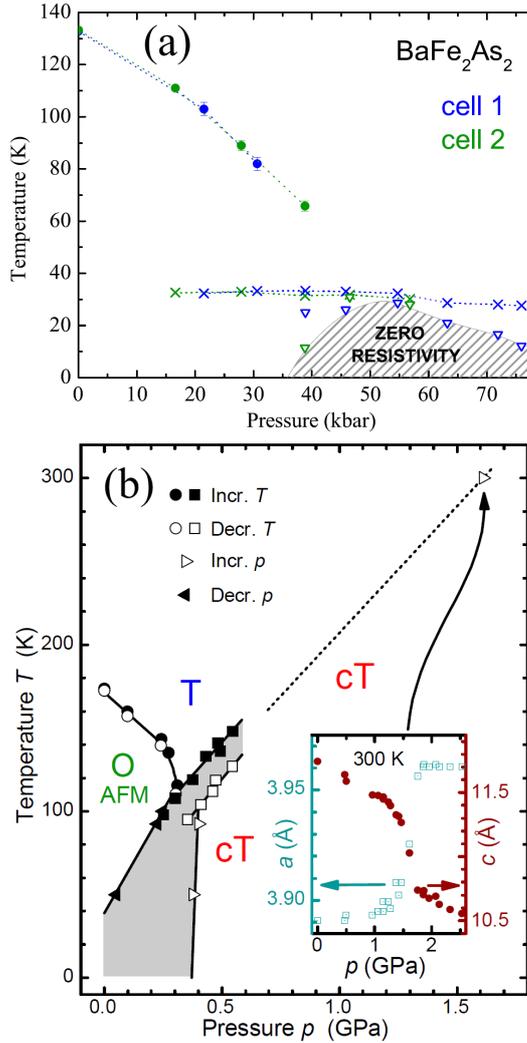


Figure 4.3: [panel a)] Phase diagram $T(P)$ of BaFe_2As_2 deduced from resistivity measurements under hydrostatic pressure by Colombier et al. (2009). Green and blue colors refer to measurements in two different pressure cells. Circles correspond to the structural transition deduced from the local maximum of the resistivity derivative. Crosses correspond to the onset of the superconducting transition. Triangles represent onset temperature of the full superconducting transition. The hatched area estimates the true zero-resistance superconducting region. Figure taken from Colombier et al. (2009). [panel b)] Pressure-temperature phase diagram of CaFe_2As_2 under hydrostatic pressure determined from neutron and high energy x-ray diffraction measurements by Goldman et al. (2009). Filled and open circles (squares) denote phase boundaries determined upon heating and cooling at a set pressure for the orthorhombic–tetragonal O-T [collapsed tetragonal–tetragonal (cT–T)] phase transition, respectively. Filled and open triangles denote phase boundaries determined upon increasing and decreasing pressure at a fixed temperature, respectively. The shaded area denotes a hysteretic region. The inset shows the change in lattice constants at the T–cT transition at 300 K as measured by high-energy x-ray diffraction. Figure taken from Goldman et al. (2009).

Chapter 5

Phenomenological model for pressure driven transitions in CaFe_2As_2

5.1 Local moments in a correlated Anderson lattice

Our starting point for a theoretical description of the iron-arsenides is a discussion of the nature of the electronic carriers in this material class. Microscopically, the electronic carriers are assumed to derive from the iron $3d$ -orbitals with a sizable admixture of As $2p$ states. The degeneracy of these hybridized orbitals is further split by spin-orbit coupling and crystal field splitting, as has been detailed by Wu et al. (2008). Combining those effects, the level scheme depicted in Fig. 5.1 has been predicted. Due to the different correlation strengths in the highest two singly occupied levels, the existence of one more itinerant and one more localized type of electrons. has been suggested (Wu et al., 2008). The mutual interaction between those degrees of freedom leads naturally to Kondo or Anderson lattice type models, which we will adopt to in the following. In this spirit, we will interpret the itinerant type of electrons as conduction electrons and the localized type of carriers as local moments, with a hybridization between both types of electrons. This microscopic picture provides a suitable basis for the iron arsenide phenomenology, and we discuss the important issues of magnetic order and electrical conductivity in relation to this scenario in the following.

Antiferromagnetic order in the iron arsenides is likely to be influenced by strong correlation effects (Si and Abrahams, 2008, Wu et al., 2008, Craco et al., 2008, Giovannetti et al., 2008). In the limit of weak correlations, antiferromagnetic order is often related to a spin-density wave like weak-coupling instability, while strong correlation effects can localize electron carriers and lead to the formation of local-moment magnetism. This discussion bears close similarities to heavy-fermion magnetism, and further details on those two types of magnetism have been discussed in chapter 2 of this thesis. Local-moment magnetism in the iron arsenides is expected to be well described by an anisotropic 3d Heisenberg model, and the elementary excitations of this model are spin-waves. Spin-wave like excitations as described by an anisotropic 3d Heisenberg model have indeed been measured in CaFe_2As_2 by McQueeney et al. (2008), at least for long wavelengths. This aspect further supports

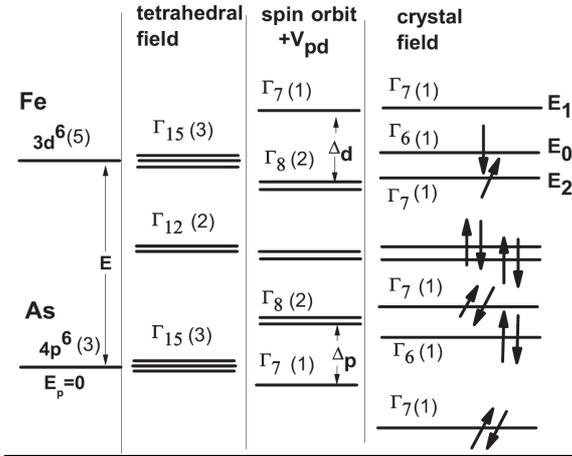


Figure 5.1: Evolution of the energy levels of the Fe $3d$ and As $4p$ levels after the inclusion of spin-orbit coupling, $p - d$ hybridization V_{pd} , and the monoclinic crystal field distortion. Figure taken from Wu et al. (2008).

the idea that local-moment physics is relevant in iron arsenides. It has to be added that itinerant and local-moment antiferromagnetism are not necessarily distinct phases, but can be adiabatically connected, e.g., in the insulating phase of a single-band Hubbard model. In contrast to cuprate materials, the antiferromagnetic phase of iron arsenides is not insulating, but neither is a good metal. Considering the coexistence of local moments and itinerant conduction electrons, the residual interaction between both degrees of freedom provides a scattering mechanism that potentially can explain bad-metal behavior. In the paramagnetic phase, the local moments are hybridized with the conduction electrons and lead to good metallic behavior, again in accordance with resistivity measurements on various types of iron arsenides. Furthermore, the scattering of itinerant electrons on local moments accounts for a reduced local moment size.

One important issue of the Anderson lattice picture is the nature of the transition between the antiferromagnetic and paramagnetic phases. Most of the groundbreaking understanding of this issue has been achieved in the context of heavy-fermion physics, with several different scenarios trying to describe the underlying quantum phase transition, see chapter 1. Our phenomenological picture of local moment-based magnetism is not compatible with the Hertz-Millis theory that is based on a standard spin-density-wave transition of a Fermi liquid. Instead, local-moment magnetism within a bad metal phase can result from an orbital selective Mott transition, where only the f -electrons localize. The existence of such a zero temperature orbital selective Mott transition occurring in the Anderson lattice model has been established by Pépin (2007). Originally, the analogous type of transition in the Kondo-Heisenberg lattice model has been considered by Senthil et al. (2004), and the main aspect of this transition is the breakdown of the Kondo effect at the quantum critical point. In the present problem, necessary theoretical modifications of such a quantum phase transition should be the structural distortions and a volume collapse observed in experiments on CaFe_2As_2 . Major efforts in describing such modifications were already laid out in chapter 2, and we shall use here an analogous description by suitably coupling lattice degrees of freedom to an Anderson lattice type model. For sufficiently strong electron-lattice coupling, the Kondo-breakdown transition became a first order transition, accompanied

by an isostructural volume collapse transition. Thereby, the antiferromagnetic quantum critical point is masked by a strong first order transition with a finite temperature critical endpoint. As a consequence of the strong first order transition, also the sharp distinction between the Kondo breakdown and spin-density-wave scenarios is removed.

So far, the analogy with heavy-fermion systems cannot be fully applied without further thoughts, since iron-arsenides are probably far from the Kondo limit. Even if correlations are not strong enough in order to apply a Kondo-breakdown scenario, the picture of an orbital-selective Mott transition in presence of valence fluctuations is still useful. This picture fits well with a non-magnetic FL phase, where the local-moment electrons become itinerant and strongly hybridized with the conduction electrons, and a magnetic phase with Mott localized local-moment electrons. Such transitions have been analyzed in several theoretical contexts, including especially two-band Hubbard models (Anisimov et al., 2002, Biermann et al., 2005). We assume that this concept provides a suitable starting point for a theoretical description of the pressure driven transitions in CaFe_2As_2 . It is straightforward to identify the low-pressure phase with a local-moment magnet due to Mott localized local-moment electrons, and the high-pressure phase with a paramagnetic Fermi liquid with strongly hybridized local-moment electrons. Due to strong electron-lattice coupling, the underlying orbital-selective Mott transition will become first order. At elevated temperatures, this first order transition becomes an isostructural lattice transition which is analogous to a Kondo volume collapse.

Overall, the sketched features of our theoretical description bear close similarities to recent theories of heavy-fermion quantum criticality, and it is important to mention some crucial differences.

(i) In most heavy-fermion materials which show magnetic quantum criticality, structural transitions at the quantum critical point are absent (Löhneysen et al., 2007). This aspect highlights the particular role of the $(\pi, 0)$ magnetic order in FeAs materials.

(ii) At present, it remains unclear whether a picture of Kondo screening applies for FeAs materials. These materials are probably far from the Kondo limit, causing sizable valence fluctuations. One of the obvious differences to heavy-fermion materials is the comparatively small quasiparticle effective mass in the high pressure phase of iron arsenides.

It is important to note that other theoretical approaches to explain magnetic order in the FeAs compounds use an itinerant spin-density wave description (For a review of these approaches, see Mazin and Schmalian (2009)). In the context of Kondo-lattice models, itinerant and local-moment magnetism can be adiabatically connected, apart from transitions that involve changes of Fermi surface topology (Vojta, 2008a). In a particular regime of intermediate electronic correlations, both types of magnetism might then be equally invoked to explain magnetic behavior.¹ In a local-moment picture, the exchange-interactions J_1 and J_2 on the square lattice of Fe atoms have been deduced to be both antiferromagnetic with $J_1 \lesssim J_2$ (Si and Abrahams, 2008, Yildirim, 2008). It is known that in this case, the ground state of the $J_1 - J_2$ square-lattice Heisenberg antiferromagnet (AFM) is of layered antiferromagnetic structure with $(\pi, 0)$ order (Chandra and Doucot, 1988, Oit-

¹Assuming adiabatic connection of both types of magnetism, intermediate correlation strength is here understood as a crossover regime where neither itinerant nor local-moment magnetism dominates.

maa and Zheng, 1996). Also an itinerant picture leads to $(\pi, 0)$ order, originating from nearly nested Fermi surfaces (Mazin and Schmalian, 2009). In any case $(\pi, 0)$ order breaks the 90° lattice rotation symmetry, inducing thereby an orthorhombic distortion inside the antiferromagnetic phase (Qi and Xu, 2008).

Experimental measurements show small valence fluctuations during Kondo volume collapse transitions (e.g., in Ce), and it is therefore advantageous to use a local moment picture to capture also the physics of the Kondo volume collapse.

It remains to discuss the issue of superconductivity, being clearly not a generic feature of the pressure-temperature phase diagram of the 122 iron arsenides (Goldman et al., 2009). From theory side, the Kondo breakdown scenario of Senthil et al. (2004) provides a generic instability of the FL phase towards superconductivity by magnetically mediated pairing. This instability becomes fragile in presence of valence fluctuations and coupling to lattice degrees of freedom. Then, the superconducting T_c will be sensitive to band structure details, and nesting properties of the Fermi surface can be essential for superconducting instabilities. In conclusion, superconductivity is a much less robust feature of the proposed scenario than volume collapse transitions and magnetic instabilities.

5.2 Anderson-Heisenberg lattice model

In the most general definition, an Anderson lattice model describes delocalized conduction (c) electrons on a lattice which hybridize with correlated and more localized f electrons on the same lattice. In principle, RKKY-like exchange interactions are already contained in this model, as discussed in part I of this thesis. The approximate treatment of magnetism can be considerably simplified by adding an explicit Heisenberg interaction between the local moments, leading to the Hamiltonian

$$\begin{aligned}
 \mathcal{H} &= \sum_{\mathbf{k}\sigma} \varepsilon_{\mathbf{k}} c_{\mathbf{k}\sigma}^\dagger c_{\mathbf{k}\sigma} + \sum_{i\sigma} \epsilon_f^0 f_{i\sigma}^\dagger f_{i\sigma} + U \sum_i n_{i\uparrow}^f n_{i\downarrow}^f \\
 &+ \frac{1}{\sqrt{\mathcal{N}}} \sum_{\mathbf{k}i\sigma} (V_{\mathbf{k}} e^{-i\mathbf{k}\mathbf{R}_i} c_{\mathbf{k}\sigma}^\dagger f_{i\sigma} + h.c.) \\
 &+ \sum_{ij} J_H(i, j) \mathbf{S}_i \cdot \mathbf{S}_j .
 \end{aligned} \tag{5.1}$$

We refrain from explaining the meaning of the different terms and definitions used in this model, since we already did so in section 2.1. Besides from specific parameter values multiplying the local terms of the model, the non-local terms have to be supplemented by a proper spatial dependence of their coupling parameters. Although the ratio of inter-plane and in-plane magnetic exchange interactions is considerably larger than in the cuprates (McQueeney et al., 2008), we assume a layered system which we model by a $2d$ square lattice. Further, we shall consider only the s-wave component of the hybridization between localized and itinerant electrons by setting $V_{\mathbf{k}} \equiv V_0$. As has been discussed by several authors (Si and Abrahams, 2008, Yildirim, 2008), including nearest and next nearest Heisenberg exchange is a suitable model to understand the structure of the antiferromagnetic ground state, which is restricted to the layers (Cruz et al., 2008). Within this model, in

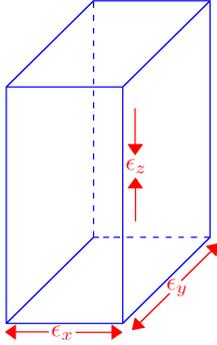


Figure 5.2: Unit cell and parametrization of the distortions. In experiment (Kreyssig et al., 2008), the perpendicular distortion is negative and large, while the horizontal axes expand slightly but with different values, leading to volume reduction and orthorhombic symmetry of the unit cell.

the Heisenberg interaction $J_H(i, j)$ only nearest (J_1) and next-nearest exchange couplings (J_2) remain nonzero, with values that obey $J_1 < J_2$. In order to introduce a mean-field treatment of the Coulomb interaction, usually an occupation constraint for the f electrons is set by taking the limit of infinite Coulomb repulsion. By taking this limit, fluctuations of the f -electron occupation are still possible and we will not consider the Kondo limit, which would fully eliminate the possibility of valence fluctuations, see also chapter 2.

5.3 Elastic energy and electron-lattice coupling

In order to understand the influence of external hydrostatic pressure within our model, it has to be clarified how the various parameters in our phenomenological model will change under application of hydrostatic pressure. A general concept how to couple the Anderson-Heisenberg lattice model to hydrostatic external pressure has been already described in chapter 2. In order to describe the complex structural transitions occurring, e.g., in CaFe_2As_2 , some modifications to this previous approach are in order.

Hydrostatic pressure leads to spatially homogeneous distortions of the lattice, and it is useful to parametrize elastic energy changes by changes of the lattice constants. We assume that these changes are small enough and treat them within the harmonic approximation, although we shall allow the symmetry of the unit cell to change from tetragonal to orthorhombic as a function of pressure. The harmonic approximation is understood as an expansion of the elastic energy contribution to the free energy up to second order in the strain variables $\epsilon_{x,y,z}$ introduced in section 2.1.

It is a matter of convenience to position the saddle point of the harmonic approximation into a phase with the highest occurring symmetry of the unit cell in order to minimize the number of expansion parameters. For tetragonal symmetry of the unit cell, the general form of the elastic energy contribution to the free enthalpy is (Landau and Lifshitz, 1986)

$$\begin{aligned}
G_{\text{lat}}(\epsilon_x, \epsilon_y, \epsilon_z) &= \frac{1}{2}v_0c_3\epsilon_z^2 + \frac{1}{2}v_0c_1(\epsilon_x^2 + \epsilon_y^2) + c_{12}\epsilon_x\epsilon_y \\
&+ v_0c_{13}\epsilon_z(\epsilon_x + \epsilon_y) + pv_0(\epsilon_x + \epsilon_y + \epsilon_z). \quad (5.2)
\end{aligned}$$

The thermodynamic variables of the elastic energy contributions are the dimensionless variables $\epsilon_{x,y,z}$, which are the relative changes of the lattice parameters of the tetragonal unit cell with predefined reference parameters, see Fig. 5.2. Within the theory of elasticity, the $\epsilon_{x,y,z}$ are obtained from the diagonal entries of the strain tensor, see section 2.1. The elastic constants c_i, c_{ij} depend on material specific properties, e.g., volume collapse transitions of the combined electron-lattice system are not expected to occur if the diagonal constants c_i exceed a critical range of values, as has been discussed for a concrete example in chapter 2. For numerical computations, we shall chose values for the elastic constants c_i, c_{ij} such that the experimentally observed lattice distortions of CaFe_2As_2 (Kreyssig et al., 2008) are approximately reproduced.

In addition to elastic energy changes, also coupling parameters of the electronic degrees of freedom depend sensitively on the lattice constants. In general, a detailed microscopic calculation how pressure affects coupling parameters of a strongly correlated electron system is beyond the scope of available methods. In iron arsenic materials, most theoretical progress along this line resulted from ab initio calculations based on the local density approximation (LDA) (Singh and Du, 2008, Singh, 2008, Subedi et al., 2008, Mazin et al., 2008a), which misses important correlation effects. In order to arrive at a plausible model for the electron-lattice couplings, we combine simple theoretical arguments with experimental results and theoretical predictions from ab initio calculations and other theoretical approaches.

In experiment, an orthorhombic distortion of the unit cell occurs nearby or at a transition to magnetic order at wave vector $(\pi, 0)$ or $(0, \pi)$ (Kreyssig et al., 2008). An additional volume collapse of the unit cell exists only in the low-temperature part of the phase diagram. Within a $J_1 - J_2$ model, an orthorhombic distortion typically stabilizes antiferromagnetic order at wave vector $(\pi, 0)$ by reducing frustration induced by the competition between the couplings J_1 and J_2 (Qi and Xu, 2008). As also observed in experiment by Kreyssig et al. (2008), this kind of distortion is not necessarily related to a collapse of the unit cell, and we shall assume an additional mechanism that drives the volume collapse. In many experiments in systems with both localized and itinerant electrons, it is revealed that external pressure can induce large changes in the hybridization of these electrons (Löhneysen et al., 2007). We will assume that the volume collapse in CaFe_2As_2 is driven by a gain in hybridization energy, as has successfully explained the Kondo volume collapse in cerium and other materials (Allen and Martin, 1982).

We start with the strain dependence of the magnetic couplings J_1 and J_2 . In experiments by Kreyssig et al. (2008) as well as first principles calculations by Yildirim (2008), anti-

²Note that this form of the elastic energy neglects effects of shear strain, which can in principle occur if pressure is not hydrostatic.

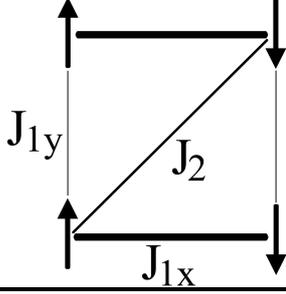


Figure 5.3: Sketch of the mechanism that leads to a stabilization of magnetic order. Vertical bonds are reduced by lowering the frustrating coupling $J_{1y} > 0$, while $J_{1x} > 0$ is enhanced and leads to a stabilization of in-plane magnetic order at wave vector $(\pi, 0)$. The distortion of the unit cell has no influence on J_2 in linear order of the strain, since to this order J_2 will only depend on the sum $\epsilon_x + \epsilon_y$.

ferromagnetic order at wave vector $(\pi, 0)$ is energetically stabilized by an orthorhombic distortion with $\epsilon_x > \epsilon_y$. Although our model is quasi two-dimensional, band structure calculations by Belashchenko and Antropov (2008) show a strong dependence of J_1 and J_2 on the strain ϵ_z . Independently of ab initio calculations, theoretical considerations showed that changes in the Fe-As bond angle stabilize antiferromagnetic ordering at wave vector $(\pi, 0)$, providing additional hints that all strain directions influence the stability of magnetic ordering. We therefore parameterize the linearized strain dependence $J_{ij}(\vec{\epsilon})$ of the exchange couplings as

$$\begin{aligned}
 J_{1x} &= J_1^0(1 + \gamma_1^\perp \epsilon_x + \gamma_1^z \epsilon_z), \\
 J_{1y} &= J_1^0(1 + \gamma_1^\perp \epsilon_y + \gamma_1^z \epsilon_z), \\
 J_2 &= J_2^0 \left[1 + \gamma_2^\perp (\epsilon_x + \epsilon_y) + \gamma_2^z \epsilon_z \right].
 \end{aligned} \tag{5.3}$$

The sign and size of the important coefficient γ_1^\perp can be estimated from LDA calculations and neutron scattering experiments by McQueeney et al. (2008), which fit J_1 and J_2 to spin wave dispersions. For local moments with $S = 1/2$, we plug the LDA values $J_{1x} = 82$ meV and $J_{1y} = 20$ meV from McQueeney et al. (2008) into the parameterization of Eq. (5.3) and set $\epsilon_x - \epsilon_y = 0.01$, as observed in the orthorhombic phase of CaFe_2As_2 . This calculation yields the estimate $\gamma_1^\perp \approx 70$. The sign and magnitude of γ_1^\perp is appropriate to stabilize magnetic order at wave vector $(\pi, 0)$, since $J_1^0 \gamma_1^\perp (\epsilon_x + \epsilon_y) \approx J_1^0$. Also ab initio calculations by Yildirim (2008) lead to the conclusion that stabilization of magnetic order at wave vector $(\pi, 0)$ can be explained by the experimentally observed orthorhombic distortion. Band structure calculations on LiFeAs by Belashchenko and Antropov (2008) yield the dependence of J_1 and J_2 on the inter-plane distance, suggesting that γ_1^z and γ_2^z are numbers of $\mathcal{O}(10)$, whereas the sign of those coefficients has been predicted to depend on pressure. At high pressures above the transition pressure to the tetragonal phase, the distortions ϵ_x and ϵ_y stay nearly constant in experiment (Kreyssig et al., 2008), whereas ϵ_z still decreases considerably. This suggests that γ_1^z and γ_2^z dominate the changes of J_1 and J_2 at high pressures, and to account for a vanishing of superconductivity at large pressures motivates us to use positive values for both γ_1^z and γ_2^z . The remaining parameter γ_2^\perp is not expected to be considerably larger than γ_1^z and γ_2^z , since the bond angles between Fe and As atoms are likely dominating the strain induced changes of J_1 and J_2 (Yildirim, 2008). Therefore, we expect that γ_2^\perp will be of $\mathcal{O}(10)$ and therefore of subleading influence within

our calculation.

Of additional importance in our model is the strain dependence of the hybridization. We will assume that this strain dependence causes the volume collapse transition observed in CaFe_2As_2 similar to a Kondo volume collapse transition as observed in cerium and other materials (Thalmeier and Lüthi, 1991). The Kondo volume collapse transition induces a gain in hybridization energy via a structural or isostructural deformation of the unit cell (McMahan et al., 1998). A plausible parameterization of the hybridization with in-plane isotropy of the strain-dependence is

$$V(\vec{\epsilon}) = V^0 \left[1 + \gamma^\perp(\epsilon_x + \epsilon_y) + \gamma^z \epsilon_z \right]. \quad (5.4)$$

Since at least five electron bands are involved in the electronic band structure of the Fe-As planes, it is difficult to relate band structure calculations or experimental results to the parameters in Eq. (5.4), which enter into our phenomenological two-band model. The situation is different in the Kondo volume collapse model for cerium, where it is known that γ^\perp and γ^z should be chosen of $\mathcal{O}(1)$ to reproduce volume collapses of $\mathcal{O}(10\%)$ (Allen and Martin, 1982, Dzero et al., 2006). In order to induce an increase in hybridization with increasing pressure, $\gamma^z < 0$ is crucial, while $\gamma^\perp > 0$ is consistent with the increase of the in-plane lattice constants throughout the collapse transition in CaFe_2As_2 . Within our calculation, the coupling $\gamma^\perp > 0$ will be of subleading influence on lattice distortions, since in-plane lattice distortions are by assumption dominated by the strain dependencies of the Heisenberg exchange couplings.

We neglect dependencies of the conduction electron dispersion $\epsilon_{\mathbf{k}}$ and the f -energy ϵ_f^0 on lattice strain. Such dependencies certainly exist, but will not change the qualitative effects of our theory, which are dominated by the strain effects parameterized in Eqs. (5.3) and (5.4). In addition, it is possible to absorb a pressure dependence of the band width into a pressure dependence of the reference energy scale.

5.4 Mean-field theory

Many explicit calculations for periodic Anderson models use the so called *slave boson approach* which is usually simplified by a mean-field approximation. This approach is capable to describe the phase transition between a local moment phase and a phase where the local moments hybridize with the conduction electrons (Hewson, 1997). Recently, it has been clarified by Pépin (2007) that this transition is indeed an orbital-selective Mott transition, where the f -electrons become Mott insulating while the c -electron band remains conducting. This approximation therefore is adequate to implement the physics that we motivated in section 5.1. In order to properly describe the competition between magnetic order and hybridization of the f -electrons, it is straightforward to introduce appropriate decoupling fields of the Heisenberg interaction that cause broken symmetries on top of the slave boson mean-field theory. We now turn to a detailed description of our mean-field theory.

We start with the explicit implementation of this strategy by taking the limit of infinite Coulomb repulsion U , which prohibits double occupation of the f -electron orbitals and imposes the local constraint $n_f(i) = \langle f_{i\sigma}^\dagger f_{i\sigma} \rangle \leq 1$, where $\langle \cdot \rangle = \text{tr}(\cdot e^{-\beta H_{ALM}}) / \text{tr} e^{-\beta H_{ALM}}$

denotes averaging with respect to the interacting density matrix in thermal equilibrium. In this case, the physical electron can be represented by a spinless boson r_i and an auxiliary fermion $\bar{f}_{i\sigma}$, $f_{i\sigma} = r_i^\dagger \bar{f}_{i\sigma}$ which carries the spin of the physical electron, obeying the constraint (Hewson, 1997)

$$r_i^\dagger r_i + \bar{f}_{i\sigma}^\dagger \bar{f}_{i\sigma} = 1. \quad (5.5)$$

The auxiliary boson is created by processes in which electrons hop from singly occupied f -orbitals, such that occupation of auxiliary boson states signals the presence of valence fluctuations. By considering only a spatially homogeneous mean-field amplitude $\langle r_i \rangle = r_0$ of the slave boson, the problem becomes considerably simplified, but still not exactly solvable. In the slave-boson mean-field approximation, the Anderson-Heisenberg lattice model reads:

$$\begin{aligned} H_{ALM} = & \sum_{\mathbf{k}\sigma} \varepsilon_{\mathbf{k}} c_{\mathbf{k}\sigma}^\dagger c_{\mathbf{k}\sigma} + \sum_{\mathbf{k}\sigma} \varepsilon_f \bar{f}_{\mathbf{k}\sigma}^\dagger \bar{f}_{\mathbf{k}\sigma} \\ & + \sum_{\mathbf{k}\sigma} r_0 V(\vec{\epsilon}) (\bar{f}_{\mathbf{k}\sigma}^\dagger c_{\mathbf{k}\sigma} + h.c.) \\ & - \lambda [\sum_{\mathbf{k}\sigma} \bar{f}_{\mathbf{k}\sigma}^\dagger \bar{f}_{\mathbf{k}\sigma} + \mathcal{N}(r^2 - 1)] \\ & - \mu [\sum_{\mathbf{k}\sigma} c_{\mathbf{k}\sigma}^\dagger c_{\mathbf{k}\sigma} - \mathcal{N}n_c] \\ & + \sum_{\langle ij \rangle} J_H^{ij}(\vec{\epsilon}) \vec{S}_i \vec{S}_j \\ & + \frac{1}{2} v_0 c_3 \epsilon_z^2 + \frac{1}{2} v_0 c_1 (\epsilon_x^2 + \epsilon_y^2) + v_0 c_{12} \epsilon_x \epsilon_y \\ & + v_0 c_{13} \epsilon_z (\epsilon_x + \epsilon_y) \end{aligned} \quad (5.6)$$

where the constraint (5.5) is now fulfilled only in the mean by introducing the spatially homogeneous Lagrangian multiplier λ . In order to decouple also the Heisenberg interaction, it is convenient to represent the local moments by the same pseudo-fermions $\bar{f}_{i\sigma}$ used for the slave-boson decoupling, such that the local spin operator becomes $\vec{S}_i = \bar{f}_{i\sigma}^\dagger \vec{\tau}_{\sigma\sigma'} \bar{f}_{i\sigma'}/2$ for local moments with $SU(2)$ symmetry group. Magnetic order or superconductivity caused by spin-fluctuations will lead to finite pairing amplitudes in the particle-hole or particle-particle channel. In order to describe such broken symmetries, we introduce the decoupling fields

$$\begin{aligned} \vec{M}_r &= \frac{1}{2} \langle \bar{f}_{r\sigma}^\dagger \vec{\tau}_{\sigma\sigma'} f_{r\sigma} \rangle \\ \Delta_{ij} &= -\langle \bar{f}_{i\uparrow} \bar{f}_{j\downarrow} - \bar{f}_{i\downarrow} \bar{f}_{j\uparrow} \rangle. \end{aligned} \quad (5.7)$$

The amplitude \vec{M}_i has the interpretation of a magnetization of the f -orbital at site i , while the field Δ_{ij} measures the pairing amplitude between a singlet of two auxiliary f -fermions located at sites i and j , respectively. A competition of magnetic and superconducting phases is achieved by mixing both decoupling channels by weighting them with

an additional decoupling parameter $x \in (0, 1)$. In decoupled form, the quartic Heisenberg interaction then takes the form:

$$\begin{aligned} \vec{S}_i \cdot \vec{S}_j &= x \left[\frac{1}{2} \vec{M}_i \cdot \vec{f}_{j\sigma}^\dagger \vec{\tau}_{\sigma\sigma'} \vec{f}_{j\sigma'} + (i \leftrightarrow j) - \vec{M}_i \cdot \vec{M}_j \right] \\ &+ (1-x) \left[\frac{1}{2} \Delta_{ij} (f_{i\uparrow}^\dagger f_{j\downarrow}^\dagger - f_{i\downarrow}^\dagger f_{j\uparrow}^\dagger) + h.c. + \frac{|\Delta_{ij}|^2}{2} \right]. \end{aligned} \quad (5.8)$$

It is not useful to use the suggestive parameter value $x = 1/2$ corresponding to an unrestricted Hartree-Fock treatment, since numerical tests within the parameter ranges discussed below show that superconducting pairing exists only for $x < 1/2$. Instead, the parameter x can be used to adjust the balance of ordered magnetism and superconductivity, and we shall discuss the values $x = 0.3$ and $x = 0.4$ below. It remains to specify the spatial dependence of the mean-field parameters Δ_{ij} and \vec{M}_i . No exact procedure exists to obtain the mean-field solutions with the lowest free energy, and our choice of solutions is guided by symmetry requirements. Obviously the magnetic structure as resolved by neutron scattering (Cruz et al., 2008) can be parameterized by the magnetization field $\vec{M}_r = m_s \exp(i\vec{Q}\vec{r})$ with $\vec{Q} = (\pi, 0)$. Contradictory symmetries of the superconducting order parameter are identified with different experimental probes (Norman, 2008). In our case we focus on saddle points with d -wave symmetry of the pairing field Δ_{ij} . This symmetry is suggested to result from doping the $J_1 - J_2$ model with electrons (Sachdev, 2002). First $d_{x^2-y^2} + id_{xy}$ pairing-symmetry emerges for a limited range of small ratios J_2/J_1 . For large J_2/J_1 , only d_{xy} pairing remains which originates from the strong vertical bonds. Assuming that electron doping is mimicked by applying hydrostatic pressure, we seek saddle points with Δ_x on horizontal bonds, $-\Delta_y$ on vertical bonds, and alternating $\pm\Delta_{xy}$ on diagonal bonds respectively, such that Δ_x and Δ_y have the same phase and are allowed to have different amplitudes in the case of orthorhombic symmetry of the unit cell. The momentum-dependent pairing term then reads

$$\Delta_{\mathbf{k}} = \Delta_x \cos k_x - \Delta_y \cos k_y + 2\Delta_{xy} \sin k_x \sin k_y. \quad (5.9)$$

We compare the free energy of saddle points with $(\pi, 0)/\pi, \pi$ magnetic order and d -wave pairing (Eq. (5.9))/ extended s -wave pairing ($\Delta_{\mathbf{k}} \sim \Delta(\cos k_x + \cos k_y)$) in Fig. 5.4. For realistic values of the strain, $(\pi, 0)$ is energetically favored. In the superconducting phase, the different pairing symmetries are energetically closeby and very difficult to resolve numerically. We stick therefore to the pairing symmetry from Eq. (5.9) that is compatible with a theoretical analysis of the electron-doped $J_1 - J_2$ model (Sachdev, 2002). For the parameter regimes discussed below, it will turn out that superconductivity exists only in absence of magnetism, where the unit cell is tetragonal, and therefore the pairing symmetry in the superconducting phase will in general be a superposition of $d_{x^2-y^2}$ and d_{xy} symmetry. In order to obtain the self-consistency equations, we define the free enthalpy function

$$G(\epsilon) = \ln \left[\text{tr}(e^{-\beta H}) \right] + p\epsilon. \quad (5.10)$$

Numerical values for the mean field parameters are obtained by solving the stationary conditions $\frac{\partial G}{\partial \Delta_{x,y,xy}} = \frac{\partial G}{\partial m_s} = \frac{\partial G}{\partial \lambda} = \frac{\partial G}{\partial \epsilon_{x,y,z}} = \frac{\partial G}{\partial \mu} = \frac{\partial G}{\partial r_0} \stackrel{!}{=} 0$ of the free enthalpy, leading to

the self-consistency equations

$$\begin{aligned}
\bar{\Delta}_x &= \frac{2}{\mathcal{N}} \sum_{\mathbf{k}} \langle \bar{f}_{\mathbf{k}\uparrow}^\dagger \bar{f}_{-\mathbf{k}\downarrow}^\dagger \rangle \cos k_x \\
\bar{\Delta}_y &= -\frac{2}{\mathcal{N}} \sum_{\mathbf{k}} \langle \bar{f}_{\mathbf{k}\uparrow}^\dagger \bar{f}_{-\mathbf{k}\downarrow}^\dagger \rangle \cos k_y \\
\bar{\Delta}_{xy} &= \frac{1}{\mathcal{N}} \sum_{\mathbf{k}} \langle \bar{f}_{\mathbf{k}\uparrow}^\dagger \bar{f}_{-\mathbf{k}\downarrow}^\dagger \rangle 2 \sin k_x \sin k_y \\
m_s &= \frac{1}{4\mathcal{N}} \sum_{\mathbf{k}} \langle \bar{f}_{\mathbf{k}\uparrow}^\dagger \bar{f}_{\mathbf{k}+\mathbf{Q}\uparrow} - \bar{f}_{\mathbf{k}\downarrow}^\dagger \bar{f}_{\mathbf{k}+\mathbf{Q}\downarrow} + h.c. \rangle \\
1 - r_0^2 &= \frac{1}{\mathcal{N}} \sum_{\mathbf{k}\sigma} \langle \bar{f}_{\mathbf{k}\sigma}^\dagger \bar{f}_{\mathbf{k}\sigma} \rangle \\
2\lambda r_0 &= \frac{1}{\mathcal{N}} \sum_{\mathbf{k}\sigma} V_0 (1 + \gamma_z \varepsilon_z + \gamma_\perp (\varepsilon_x + \varepsilon_y)) \langle \bar{f}_{\mathbf{k}\sigma}^\dagger c_{\mathbf{k}\sigma} + h.c. \rangle \\
n_c &= \frac{1}{\mathcal{N}} \sum_{\mathbf{k}\sigma} \langle c_{\mathbf{k}\sigma}^\dagger c_{\mathbf{k}\sigma} \rangle \\
0 &= pv_0 + v_0 c_{13} \varepsilon_z + v_0 (c_{11} \varepsilon_x + c_{12} \varepsilon_y) + \frac{r_0^2 \gamma_\perp 2\mathcal{N} \lambda}{(1 + \gamma_z \varepsilon_z + \gamma_\perp (\varepsilon_x + \varepsilon_y))} \\
&\quad - \frac{1}{2} (1-x) J_H^{(1)} \gamma \mathcal{N} |\Delta_x|^2 + (1-x) J_H^{(2)} \gamma [-\mathcal{N} |\Delta_2|^2] - x \left(-\frac{1}{2} J_H^{(1)} \gamma + \gamma J_H^{(2)} \right) 2\mathcal{N} m_s^2 \\
0 &= pv_0 + v_0 c_{13} \varepsilon_z + v_0 (c_{11} \varepsilon_y + c_{12} \varepsilon_x) + \frac{r_0^2 \gamma_\perp 2\mathcal{N} \lambda}{(1 + \gamma_z \varepsilon_z + \gamma_\perp (\varepsilon_x + \varepsilon_y))} \\
&\quad - \frac{1}{2} (1-x) J_H^{(1)} \gamma \mathcal{N} |\Delta_y|^2 + (1-x) J_H^{(2)} \gamma [-\mathcal{N} |\Delta_2|^2] - x \left(\frac{1}{2} J_H^{(1)} \gamma + \gamma J_H^{(2)} \right) 2\mathcal{N} m_s^2 \\
0 &= pv_0 + 0.5(1-x) J_H^{(1)} \gamma_1^z [|\Delta_x|^2 + |\Delta_y|^2] + v_0 c_{33} \varepsilon_z + v_0 c_{13} (\varepsilon_x + \varepsilon_y) \\
&\quad + \frac{r_0^2 \gamma_z \lambda 2\mathcal{N}}{1 + \gamma_z \varepsilon_z + \gamma_\perp (\varepsilon_x + \varepsilon_y)}, \tag{5.11}
\end{aligned}$$

where $\bar{\Delta}$ denotes the complex conjugate of Δ . Here, we have used the Fourier transform $\bar{f}_{\mathbf{k}\sigma} = \frac{1}{\sqrt{\mathcal{N}}} \sum_{i\sigma} \exp(i\mathbf{k} \cdot \mathbf{r}_i) \bar{f}_{i\sigma}$. The various fermionic propagators defined on the right-hand side are obtained from a straightforward numerical diagonalization of the Hamiltonian matrix in momentum space. In the magnetically ordered state, the size of the unit cell is doubled according to Fig. 5.5, and the commensurate wave vectors of the resulting eigenstates will be defined in a reduced Brillouin zone. It is therefore convenient to replace the real-space operators $c_{i\sigma}$ and $\bar{f}_{i\sigma}$ by the new operators $c_{\nu,r\sigma}$ and $\bar{f}_{\nu,r\sigma}$ defined on the sublattices shown in Fig. 5.5, where $\nu = A, B$ is the sublattice index and r_ν refers to the position of the unit cell. The Fourier transformed

$$c_{\nu,\mathbf{k}} = \sqrt{\frac{2}{\mathcal{N}}} \sum_r e^{i\mathbf{k}(\mathbf{R}_r + r_\nu)} c_{\nu,r} \tag{5.12}$$

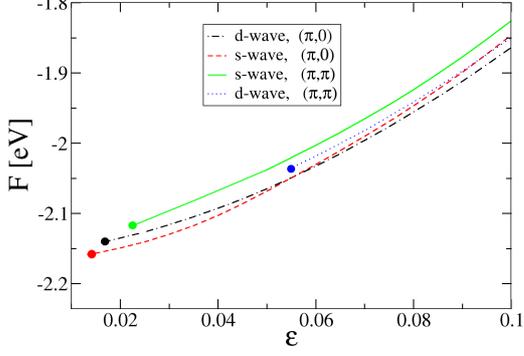


Figure 5.4: We give a comparison of the free energy $F = F_{\text{el}} + F_{\text{latt}}$ (defined in appendix A) at zero temperature for different symmetries of the pairing field and magnetic order described in the main text. The free energy is plotted in the magnetic phase in dependency of the strain ϵ , with the magnetic transition point marked by a dot. For reasonable values of ϵ (compare Fig. 6.3), magnetic order at wavevector $(\pi, 0)$ is preferred over (π, π) -order. The symmetry of the superconducting order parameter remains inconclusive since s -wave and d -wave pairing are energetically close by in the superconducting phase (not shown). Parameters are identically to Fig. 6.2, left panel.

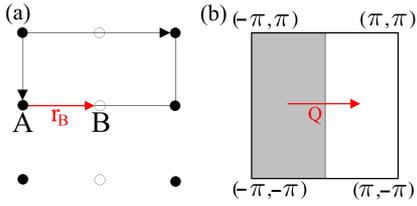


Figure 5.5: The lattice is divided into two sublattices A (black points) and B (white points). The reference point for each unit cell is chosen to be the left corner leading to $\mathbf{r}_A = (0, 0)$ and $\mathbf{r}_B = (1, 0)$. The gray shaded region shows the unit cell. (b) The Brillouin zone corresponding to the enlarged unit cell (colored in gray) is obtained from the original BZ by backfolding with the vector \mathbf{Q} .

are defined for \mathbf{k} lying in the new, reduced Brillouin zone $\mathbf{k} \in [-\pi, 0] \times [-\pi, \pi]$.

In appendix A, we provide further details of the momentum space representation of the Hamiltonian (5.6) and the numerical solution of the saddle point equations (5.11). In the next section, we proceed to discuss various phase diagrams obtained from numerical solutions of the self consistency equations (5.11).

Chapter 6

Anderson-Heisenberg model: Phase diagrams

6.1 Phases and electronic phase diagram

Within an Anderson lattice without explicit magnetic exchange, at zero temperature a finite slave boson amplitude $r_0 \neq 0$ marks a heavy Fermi-liquid phase. In the presence of pairing ($\Delta_{ij} \neq 0$) and magnetic order ($m_s \neq 0$) of the f -electrons, the slave boson amplitude obtains in addition a crucial role to distinct between magnetic and superconducting phases. Since the f -electrons are dispersionless for vanishing slave boson amplitude $r_0 = 0$, a finite pairing amplitude $\Delta_{ij} \neq 0$ leads only to pairing of localized fermions but not to a superconducting state. In the full parameter space of the mean-field parameters defined in the previous chapter, a plethora of phases can be realized:

- Decoupled, with $r_0 = 0$, $m_s = 0$, $\Delta_{ij} = 0$, describing a paramagnetic high-temperature regime with localized f -electrons.
- Fractionalized Fermi liquid (FL*), with $r_0 = 0$, $m_s = 0$, $\Delta_{ij} \neq 0$. This is a paramagnetic phase, where conduction electrons alone form a “small” Fermi surface (FS) and are decoupled from a fractionalized spin liquid of paired spinons. This phase was introduced by Senthil et al. (2003), but will not play a role here.
- Local-moment antiferromagnet (AFM), with $r_0 = 0$, $m_s \neq 0$. Here, Δ_{ij} may be zero or finite, the latter case reflecting residual spinon pairing.
- Paramagnetic Fermi liquid (FL), with $r_0 \neq 0$, $m_s = 0$, $\Delta_{ij} = 0$ with itinerant f -electrons and a “large” Fermi surface.
- Antiferromagnetic Fermi liquid, with $r_0 \neq 0$, $m_s \neq 0$, $\Delta_{ij} = 0$ with itinerant f -electrons.
- Paramagnetic superconductor (SC), with $r_0 \neq 0$, $m_s = 0$, $\Delta_{ij} \neq 0$, obtained from pairing in the large-FS Fermi liquid.

- Antiferromagnetic superconductor, with $r_0 \neq 0$, $m_s \neq 0$, $\Delta_{ij} \neq 0$.

In a self-consistent calculation, the equations (5.11) restrict the mean-field parameters and lead only to a realization of a few of these phases. A very specific feature of our approach is the zero-temperature transition from a phase with $r_0 \neq 0$ to a phase with $r_0 = 0$. Since this transition leads to a Mott localization of the f -electrons, it is an orbital selective Mott transition (Pépin, 2007). While for a paramagnetic system, this transition survives as a continuous zero temperature transition upon including fluctuations (Senthil et al., 2003, 2004), the mean-field transition from a phase with $r_0 \neq 0$ to an antiferromagnetic state is more subtle. As has been shown by Vojta (2008a), a mean-field transition into a local moment antiferromagnetic phase at $T = 0$ can become a crossover upon including fluctuation corrections, since itinerant and local moment magnetism can be adiabatically connected.

In our numerical calculations, we shall use a simple c electron dispersion resulting from nearest neighbor hopping, $\epsilon_{\mathbf{k}} = -2t(\cos k_x + \cos k_y)$. The explicit parameters of this band structure cannot be extracted from ab initio calculations, since these result in complicated band structures with at least five different bands intersecting the Fermi surface (Singh and Du, 2008). Instead, we chose $t = 0.5$ eV and filling $n_c = 0.8$, such that the band width is comparable to the energy range where sizable spectral weight of the Fe orbitals is obtained in LDA calculations (Shim et al., 2008). The f -level position ϵ_f controls the tendency of the f -electrons to show local moment like behavior, and we set it slightly below the lower band edge in order to allow for moderate valence fluctuations, $\epsilon_f = -2.3$ eV. We shall argue that magnetic and volume collapse transitions within our mean-field theory are qualitatively independent of specific details of the c -electron band structure, based on two arguments: (i) while nesting properties of the Fermi surface might be relevant for itinerant magnetism, in our local moment based picture magnetism is favored when the f -electrons become localized and completely decouple from the c -electron system. (ii) Kondo volume collapse transitions are a robust feature of our mean field approach which occurred very similarly both on frustrated and different hypercubic lattices in our analysis of chapter 2.1. In the $J_1 - J_2$ model assumed to describe magnetic exchange in the iron arsenides, the classically stable ground state occurs if $2J_2 > J_1$. This ground state manifold has a degeneracy with two sublattice Néel vectors \vec{n}_1 and \vec{n}_2 with the ground state energy being independent of the relative orientation of \vec{n}_1 and \vec{n}_2 . This ground state degeneracy is lifted by quantum or thermal fluctuations (Henley, 1989) leading to parallel or antiparallel alignment of \vec{n}_1 and \vec{n}_2 (Chandra et al., 1990), with the parallel alignment corresponding to the magnetic structure observed experimentally at ambient pressure (Cruz et al., 2008).

From ab initio calculations of Ma et al. (2008), it has been obtained that $J_2 \sim 2J_1$, with both couplings being large and antiferromagnetic. In our theory, these exchange couplings correspond to the effective couplings xJ_1 and xJ_2 , for which we chose the ratio $J_2/J_1 = 1.5$, being in qualitative agreement with the ratio obtained by Ma et al. (2008). In order to discuss the sensitivity of our approach to changes in the decoupling parameter x , we employ the two parameter sets $x = 0.3$, $J_1^0 = 200$ meV, $J_2^0 = 300$ meV and $x = 0.4$, $J_1^0 = 150$ meV, $J_2^0 = 225$ meV. The effective couplings xJ_1^0 and xJ_2^0 coincide with theoretical values from Yaresko et al. (2009) calculated for BaFe₂As₂. From neutron scattering experiments and spin wave theory, the exchange couplings for the orthorhombic phase of CaFe₂As₂ have

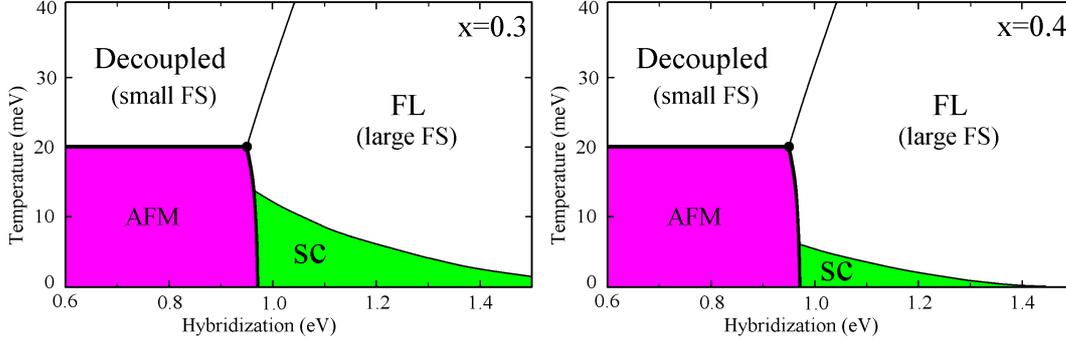


Figure 6.1: Electronic mean-field phase diagram in the temperature–hybridization plane, for fixed lattice parameters $\epsilon_{x,y,z} = 0$. Top: Mean-field decoupling parameter $x = 0.3$. Bottom: $x = 0.4$. Thick (thin) lines denote first-order (continuous) phase transitions. For small hybridization, the f -electrons are localized, and magnetism dominates at low T , whereas large hybridization leads to itinerant f -electrons and superconductivity. For details and parameters see text.

been obtained by McQueeney et al. (2008). If these results are adjusted in accordance with our $S = 1/2$ model, they yield $J_1 \approx (J_{1x} + J_{1y})/2 \approx 40$ meV and $J_2 \approx 50$ meV, agreeing in order of magnitude with our own results. It is important to note that a quantitative agreement of the microscopic exchange couplings with those used in our mean-field theory should not be overstressed, since quantum and thermal fluctuations will renormalize the mean-field ordering temperature.

Using the constraint $\epsilon_{x,y,z} = 0$, we depict the electronic phase diagram as a function of temperature T and hybridization V in Fig. 6.1 for two different decoupling parameters, $x = 0.3$ and $x = 0.4$. At elevated temperatures, the mean field phases are only distinct by the condensation of the slave boson, leading to a non-zero value $r_0 \neq 0$ in the Fermi liquid phase which contains both c - and f -electrons in the Fermi volume. An orbital selective Mott transition to a phase with localized f -electrons upon decreasing V leads to a decoupled phase with a small Fermi surface, containing only the conduction electrons. This transition will be smeared out into a crossover by fluctuations around the mean-field saddle point. All other transitions involve physical symmetry breaking and survive. In addition, we find a thermal magnetic transition which is weakly first order in our numerical calculation, but due to finite numerical resolution we cannot exclude it to be continuous. The existence of magnetic order and valence fluctuations of the f -electrons given by $r_0 \neq 0$ are mutually exclusive in all parts of the phase diagrams, and therefore superconductivity and magnetism do not coexist in the phase diagrams. Instead, they are separated by a first-order transition, where m_s and r_0 jump. Although not superconducting, the antiferromagnetic phase has paired spinons with $\Delta_{ij} \neq 0$ coexisting with local-moment antiferromagnetism at low T . The spinon pairing is restricted to d_{xy} symmetry, since magnetic order is dominated by the coupling J_2 . The d_{xy} pairing symmetry dominates also in the superconducting phase, with a small $id_{x^2-y^2}$ admixture occurring only for $x = 0.3$ and not for $x = 0.4$.

Only the superconducting part of the mean-field phase diagram appears to be significantly influenced by the variation of the decoupling parameter x from $x = 0.4$ to $x = 0.3$, with the maximum T_c dropping from $50K$ to about $5K$. The observation of a strong influence of the decoupling parameter x on the superconducting transition temperature holds more general for a variation of x in the range $x \in (0.25, 0.45)$ while keeping $xJ_{1,2}^0$ fixed, as we checked numerically. Decreasing x below $x \approx 0.25$ leads to the disappearance of the antiferromagnetic phase, which becomes replaced by a paramagnetic FL* phase. On the other hand, increasing x above $x \approx 0.45$ leads to the disappearance of superconductivity. Finally, for large $x \geq 0.5$, antiferromagnetism extends even into the large Fermi surface Fermi liquid phase. In summary, our findings show that the stability of a superconducting phase is sensitively influenced by the decoupling parameter x . The sensitivity of the superconducting phase is further enhanced by band structure details and nesting conditions which we did not discuss here, since a detailed quantitative discussion of the superconducting transition temperature T_c would require to extend our approach beyond mean-field theory.

6.2 Phase diagram with electron-lattice coupling

After discussing the general structure of the mean field phases at constant pressure, we now determine the phase diagram in dependence of temperature and pressure. In order to obtain this central result of the present chapter, the combined free enthalpy $F_{\text{el}} + G_{\text{lat}}$ of electrons and lattice defined by Eqs (5.2,A.7) has to be minimized, leading to the full set of mean field equations (5.11). Numerically, this procedure is complicated in presence of volume collapse transitions, since then at least two minima of the free enthalpy coexist near the first order transition, corresponding to different solutions of the saddle point equations. The thermodynamically stable saddle points can be obtained by analyzing the pressure-volume isotherms, in analogy to the procedure for the Kondo volume collapse transition discussed in part I of this thesis. For this purpose, one determines pressure as a function of volume at fixed temperature and performs a Maxwell construction (Nolting, 2005) to determine the critical pressure, see Fig. A.1.

From this procedure, we obtained the phase diagrams shown in Fig. 6.2. Following the discussion from chapter 2.1, we employed the electron lattice couplings $\gamma^\perp = 3.1$, $\gamma^z = -5.2$, $\gamma_1^\perp = 35$, $\gamma_1^z = 1.0$, $\gamma_2^\perp = 8.0$, and $\gamma_2^z = 5.0$. While the couplings γ_1^z , γ_2^\perp and γ_2^z had little influence on the lattice distortions, the couplings γ^\perp , γ^z and γ_1^\perp together with the values for c_i, c_{ij} were adjusted to quantitatively reproduce the lattice distortions observed in CaFe_2As_2 . Since experimental data for the elastic constants was not available to us, we chose the values $c_1 = 441$ kBar, $c_3 = 198$ kBar, and $c_{12} = c_{13} = 66$ kBar, which are approximately of the same order than the lattice constants of Ce (Thalmeier and Lüthi, 1991). The couplings γ_1^z , γ_2^\perp and γ_2^z can be chosen such that the superconducting order parameters decrease rapidly as a function of pressure in order to account for the experimentally observed phase boundaries in CaFe_2As_2 (Kreyssig et al., 2008)¹ and SrFe_2As_2 , BaFe_2As_2 (Colombier et al., 2009). The resulting phase diagrams shown in Fig. 6.2 look similar to

¹These phase boundaries are likely related to strain induced superconductivity and were not reproduced by Goldman et al. (2009), who used a He gas pressure cell.

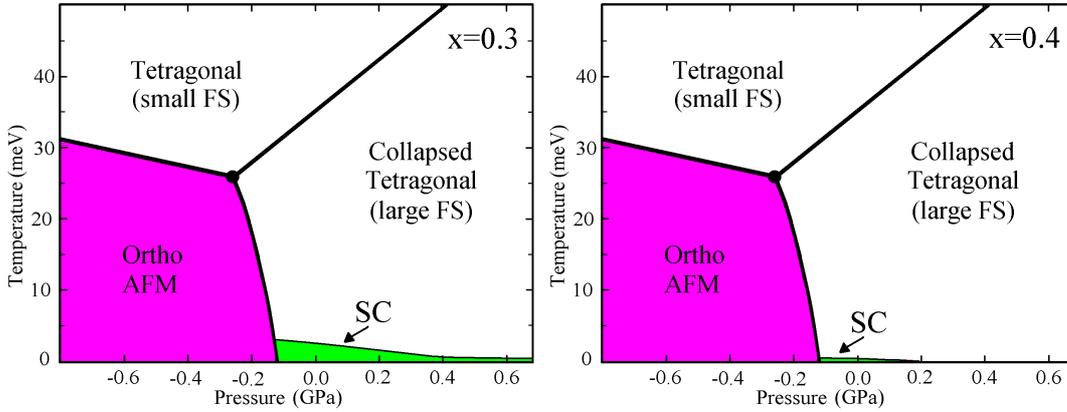


Figure 6.2: Mean-field phase diagram including electron–lattice coupling in the temperature–pressure plane. Top: Mean-field decoupling parameter $x = 0.3$. Bottom: $x = 0.4$. Thick (thin) lines denote first-order (continuous) phase transitions. The isostructural volume-collapse transition displays a critical end point at a temperature of roughly 200 meV. See text for details.

that obtained as a function of hybridization at constant pressure (Fig. 6.1). This similarity is essentially caused by our choice of electron-lattice couplings: the hybridization increases as a function of pressure, while the exchange couplings decrease somewhat, as is demonstrated in Fig. 6.3. The main changes to the phase diagram of Fig. 6.1 induced by coupling to lattice degrees of freedom are due to structural transitions or isostructural collapses that all enhance the first order character of the respective transitions of the mean-field theory. Now, the orbital selective Mott transition becomes strongly first order, both at low and at high temperatures. In addition, the antiferromagnetic phase is now allowed to reduce frustration by an orthorhombic distortion of the unit cell, and the thermal phase transition to the non-magnetic tetragonal phase becomes now a clear first order transition. In principle, an additional nematic order parameter could be included in our theory in order to separate the nematic from the magnetic transition, as observed in experiments on $\text{LaO}_{1-x}\text{F}_x\text{FeAs}$ by McGuire et al. (2008). Such a modification would have no significant influence on other features of the phase diagram. On the other hand, experiments on SrFe_2As_2 (Krellner et al., 2008), BaFe_2As_2 (Huang et al., 2008) and CaFe_2As_2 (Goldman et al., 2009) yield a coincidence of a first order structural and magnetic transition, in agreement with our findings. Finally, our pressure-dependent theory reproduces the physics of the Kondo volume collapse transition, which at all temperatures occurs concomitantly with the orbital selective Mott transition in our numerical calculations. At elevated T , the volume collapse transition becomes an isostructural transition with a tetragonal unit cell on both sides of the transition. In contrast, at temperatures below the magnetic ordering temperature, the volume collapse transition involves an orthorhombic \leftrightarrow tetragonal structural transition.

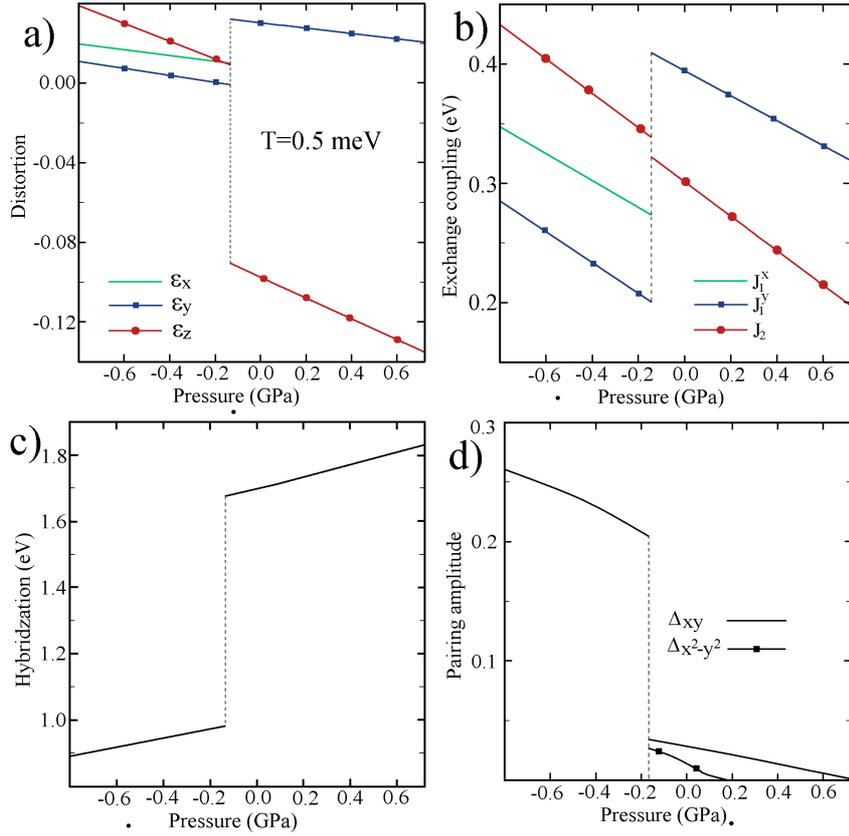


Figure 6.3: Pressure dependence of several microscopic parameters for low $T = 0.5$ meV and decoupling parameter $x = 0.3$. a) Lattice parameters $\epsilon_{x,y,z}$. Below temperatures of 30 meV, the $\epsilon_{x,y,z}$ depend only weakly on temperature, therefore this plot is representative for most parts of the phase diagram. b) Magnetic exchange constants $J_{1,2}$. c) Hybridization V . d) Pairing fields Δ_{ij} . Note that Δ_{ij} reflects superconductivity only in the Fermi-liquid regime occurring at large pressures, whereas it describes only spinon pairing in the orbital-selective Mott phase occurring at small pressures.

Comparison to experiment

In experiments on CaFe_2As_2 , a large hysteresis region extending both into the orthorhombic antiferromagnetic phase and the collapsed tetragonal phase has been observed, leading to discrepancies in reports of magnetic order, electronic properties and superconductivity (Kreyssig et al., 2008, Goldman et al., 2009). Within this area of the phase diagram, the structure and physical properties measured at a particular pressure and temperature depend strongly upon the path taken to that point. Besides from such hysteretic effects, our results reproduce most salient features observed in experiment. In particular, these are:

(i) An isostructural collapse transition from a tetragonal to tetragonal phase with the transition temperature increasing with pressure (ii) A structural transition from an orthorhombic antiferromagnetic phase to a tetragonal phase accompanied by an additional volume collapse (iii) A thermal first order structural transition from orthorhombic to tetragonal structure occurring at high temperatures, with increasing transition temperature by lowering pressure.

Including also the reported superconducting phase (see, however, footnote 1), our phase diagram looks very similar to the experimental phase diagram of Fig. 3 in the work published by Kreyssig et al. (2008). The quantitative agreement of our mean-field transition temperatures with that reported by Kreyssig et al. (2008) could be improved by suitably adjusting exchange couplings J_{ij}^H , the decoupling parameter x , etc. . However, significant corrections to the mean-field transition temperatures are expected in any case, both due to inter-plane coupling and fluctuation effects. In addition, superconductivity appears to be fragile and requires particular balance between magnetic and superconducting decoupling of our theory. Although within our theory a superconducting phase turns out to be quite stable in absence of lattice distortions, the strong volume collapse transition leads to a jump over large parts of the stability region of superconductivity upon including electron-lattice coupling into our description. For $x = 0.45$, T_c is already below 0.1 meV and is compatible with more recent experiments that find no pressure-driven superconductivity in CaFe_2As_2 (Goldman et al., 2009) down to the lowest measured temperatures of 2 K. Remarkably, all other parameters of our mean-field phase diagram are identically for $x = 0.3$ and $x = 0.4$, such that volume collapse transitions and the orbital selective Mott transition are robust features of our model.

Our theoretical results reproduce especially well quantitative experimental values for the lattice distortions close to the volume collapse transition (Kreyssig et al., 2008), with a volume collapse of 5%, a large shrinkage of the c -axis by 11% and small enlargements of the a and b axes with an appropriate orthorhombic distortion at low temperatures, see Fig. 6.3. These changes of the lattice parameters are accompanied by relatively large changes of the exchange couplings J_1 and J_2 (see Fig. 6.3), which are required to model the pressure dependences of the Néel temperature (Kreyssig et al., 2008, Goldman et al., 2009) and the superconducting T_c in SrFe_2As_2 and BaFe_2As_2 (Colombier et al., 2009) that have been observed in experiment. The mechanism that enables the large change in the c -axis length and the volume collapse is a large increase of the hybridization across the collapse transition. Physically, this mechanism is analogous to the Kondo volume collapse transition and is required to balance the large increase of elastic energy throughout the

volume collapse. The strongly increasing hybridization at the collapse leads to an itinerant character of the f -electrons in the collapsed phase, with the f occupation decreasing from 1 to ≈ 0.80 across the transition for all temperatures below 60 meV. It turns out that the pairing symmetry depends sensitively on pressure. For $x = 0.3$, the pairing is dominantly of d_{xy} -type, with a small $id_{x^2-y^2}$ admixture occurring only in a limited range of pressures in the superconducting phase. Importantly, the orthorhombic lattice distortion significantly enhances the pairing amplitude Δ_{xy} with its d_{xy} -symmetry, while the pairing amplitudes Δ_x and Δ_y on the horizontal and vertical links vanish even at the lowest temperatures accessed by our numerical calculations, see Fig. 6.3. An $id_{x^2-y^2}$ admixture vanishes at all if the decoupling parameter is set $x = 0.4$.

Chapter 7

Conclusions

In this part of the thesis, we proposed a theoretical description of the pressure-induced phase transitions in CaFe_2As_2 . We introduced an effective description in form of an Anderson lattice model, based on the idea of localized electrons hybridizing with more itinerant electrons. We introduced these two types of carriers based on phenomenological arguments and additional theoretical considerations. These conceptual ideas are not contradictory to a spin-density wave description of the FeAs magnetism, since both descriptions can potentially be used to qualitatively account for the FeAs magnetism.

Coupling microscopic parameters to the lattice degrees of freedom in our theory accounts for the orthorhombic distortion in the magnetic phase and the volume collapse transition. At low temperatures and ambient pressure, the system orders antiferromagnetically in an orthorhombically distorted lattice, and the itinerant electrons can account for weak metallic behavior. Physically, the weak metallic behavior relies on residual scattering of itinerant electrons on the local moments – an effect not captured by our mean-field approach but present in the Anderson lattice model. The high pressure phase of our theory is a paramagnetic Fermi liquid, and the first order collapse transition is driven by a strong increase in hybridization strength, with close analogies to a Kondo volume collapse. Also in absence of electron-lattice coupling, the magnetic transition is first order, and the experimentally observed phase separation (Goko et al., 2008) is by tendency implied by this theoretical observation.

The ideas described so far hold also an explanation for the coincidence of volume-collapse and magnetic-non-magnetic transition, which is also indicated by first-principles approaches (Samolyuk et al., 2009). Within our approach, superconductivity mediated by residual spin fluctuations emerges at high pressure and low temperatures, with a strong sensitivity of T_c on microscopic parameters, accounting possibly for the conflicting experimental reports on superconductivity in CaFe_2As_2 (Yu et al., 2008).

So far, the strong volume collapse transition has only been observed in CaFe_2As_2 , and a proper theoretical description needs to discriminate this diverse behavior of the 122 family. The current status of both theory and experiment suggests that CaFe_2As_2 is a particularly soft material with a small c -axis lattice constant, displays a large electron-phonon coupling and is located in close vicinity to a magnetic-non-magnetic transition. It is known that a

soft lattice is essential for the observation of a first-order volume-collapse transition, see also chapter 2.

From first-principles calculations, a giant coupling of the Fe spin state with the lattice has been reported, with the iron moment coupled strongly to the c -axis lattice constant. This effect turned out to be particularly strong in $CaFe_2As_2$ as compared to $BaFe_2As_2$ or 1111 compounds.

In contrast to a Mott transition, an orbital selective Mott transition requires not a particular filling of the conduction band. Therefore, an interesting realization of a *continuous* orbital selective Mott transition might be doping-driven magnetic transitions in iron arsenides.

Appendix A

Formulas for fermionic mean-field theory

In order to determine the eigenvalues and eigenstates of the mean-field Hamiltonian (5.6) with the decoupling (5.8), it is convenient to rewrite this Hamiltonian using the new fermionic operators according to (5.12), defined in the reduced Brillouin zone corresponding to antiferromagnetic order at wave vector $\mathbf{Q} = (\pi, 0)$. For a numerical determination of the spectrum of the mean-field Hamiltonian, the Hamiltonian for the electronic degrees of freedom (without elastic energy contributions) can be represented as

$$\mathcal{H}_{MF} = \frac{1}{2} \sum_{\mathbf{k}} \psi_{\mathbf{k}}^{\dagger} \hat{A}_{\mathbf{k}} \psi_{\mathbf{k}} + E_{\text{const}} , \quad (\text{A.1})$$

where the Hermitian matrix $\hat{A}_{\mathbf{k}}$ has the block diagonal structure

$$\hat{A}_{\mathbf{k}} = \begin{pmatrix} \hat{h}_{11}(\mathbf{k}) & 0 \\ 0 & \hat{h}_{22}(\mathbf{k}) \end{pmatrix} \quad (\text{A.2})$$

with $\hat{h}_{11}(\mathbf{k})$ and $\hat{h}_{22}(\mathbf{k})$ given below, and the momentum \mathbf{k} is summed over the reduced Brillouin zone $[0, \pi] \times [-\pi, \pi]$. In addition, we introduced the constant

$$\begin{aligned} E_{\text{const}} &= \lambda \mathcal{N}(1 - r^2) + \mu_c \mathcal{N} n_c + \frac{1}{2} (1 - x) \mathcal{N} (J_{1x}(\vec{\epsilon}) |\Delta_x|^2 + J_{1y}(\vec{\epsilon}) |\Delta_y|^2) \\ &+ (1 - x) J_2(\vec{\epsilon}) \mathcal{N} |\Delta_{xy}|^2 + 2x [J_2(\vec{\epsilon}) + \frac{1}{2} (J_{1x}(\vec{\epsilon}) - J_{1y}(\vec{\epsilon}))] \mathcal{N} m_s^2 \\ &+ \sum_{\mathbf{k}} [\bar{\epsilon}_{\mathbf{k}} + \bar{\epsilon}_{\mathbf{k}+\mathbf{Q}} + 2\bar{\epsilon}_f] \end{aligned} \quad (\text{A.3})$$

and the 16-component spinor $\psi_{\mathbf{k}}^{\dagger} = (\phi_{1,\mathbf{k}}^{\dagger}, \phi_{2,\mathbf{k}}^{\dagger})$, where

$$\phi_{1,\mathbf{k}}^{\dagger} = (c_{\mathbf{k}\uparrow}^{\dagger}, f_{\mathbf{k}\uparrow}^{\dagger}, c_{-\mathbf{k}\downarrow}, f_{-\mathbf{k}\downarrow}, c_{\mathbf{k}+\mathbf{Q}\uparrow}^{\dagger}, f_{\mathbf{k}+\mathbf{Q}\uparrow}^{\dagger}, c_{-(\mathbf{k}+\mathbf{Q})\downarrow}, f_{-(\mathbf{k}+\mathbf{Q})\downarrow}) . \quad (\text{A.4})$$

The spinor $\phi_{2,\mathbf{k}}^\dagger$ is obtained from $\phi_{1,\mathbf{k}}^\dagger$ by flipping the spin projection indices ($\uparrow \rightarrow \downarrow$ and $\downarrow \rightarrow \uparrow$). The 8×8 matrix $\hat{h}_{11}(\mathbf{k})$ is given by

$$\begin{bmatrix} \varepsilon_{\mathbf{k}} & rV & 0 & 0 & 0 & 0 & 0 & 0 \\ rV & \varepsilon_{\mathbf{k}}^f & 0 & \Delta_{\mathbf{k}} & 0 & -2xJ_H m_s & 0 & 0 \\ 0 & 0 & -\varepsilon_{-\mathbf{k}} & -rV & 0 & 0 & 0 & 0 \\ 0 & \Delta_{\mathbf{k}}^* & -rV & -\varepsilon_{-\mathbf{k}}^f & 0 & 0 & 0 & -2xJ_H m_s \\ 0 & 0 & 0 & 0 & \varepsilon_{\mathbf{k}+\mathbf{Q}} & rV & 0 & 0 \\ 0 & -2xJ_H m_s & 0 & 0 & rV & \varepsilon_{\mathbf{k}+\mathbf{Q}}^f & 0 & \Delta_{\mathbf{k}+\mathbf{Q}} \\ 0 & 0 & 0 & 0 & 0 & 0 & -\varepsilon_{-(\mathbf{k}+\mathbf{Q})} & -rV \\ 0 & 0 & 0 & -2xJ_H m_s & 0 & \Delta_{\mathbf{k}+\mathbf{Q}}^* & -rV & -\varepsilon_{-(\mathbf{k}+\mathbf{Q})}^f \end{bmatrix}, \quad (\text{A.5})$$

while \hat{h}_{22} is obtained from $\hat{h}_{11}(\mathbf{k})$ by flipping the spin projection indices in the definitions of \vec{M}_i and Δ_{ij} , which is equivalent to making the replacements $\Delta_{\mathbf{k}} \rightarrow -\Delta_{\mathbf{k}}$ and $m_s \rightarrow -m_s$. We obtained the 16 eigenvalues $E_{\mathbf{k}}^n$ and eigenvectors of the matrix $\hat{A}_{\mathbf{k}}$ by a numerical diagonalization using the LAPACK routine `zgeev`, implemented with the commonly used language ‘‘C’’.

a) Free energy From the numerically obtained eigenvalues, the free energy is obtained as

$$F = F_{\text{el}} + F_{\text{latt}}, \quad (\text{A.6})$$

with the electronic contribution

$$F_{\text{el}} = -k_B T \sum_{\mathbf{k} \in \text{RBZ}, n} \ln(1 + \exp(-\beta E_{\mathbf{k}}^n)) + E_{\text{const}} \quad (\text{A.7})$$

and the lattice contribution

$$F_{\text{latt}} = \frac{1}{2} v_0 c_3 \varepsilon_z^2 + \frac{1}{2} v_0 c_1 (\varepsilon_x^2 + \varepsilon_y^2) + v_0 c_{13} \varepsilon_z (\varepsilon_x + \varepsilon_y) + v_0 c_{12} \varepsilon_x \varepsilon_y \quad (\text{A.8})$$

defined in the context of Eq. (5.2).

b) Fermionic propagators We reexpress the Hamiltonian (A.1) by using the fermionic eigenmodes $\varphi_{\mathbf{k}} \stackrel{\text{def}}{=} \hat{U}_{\mathbf{k}}^\dagger \psi_{\mathbf{k}}$, defined such that $\hat{U}_{\mathbf{k}}^\dagger \hat{A}_{\mathbf{k}} \hat{U}_{\mathbf{k}}$ is diagonal. Any fermionic propagator $\langle \psi_{\mathbf{k},i}^\dagger \psi_{\mathbf{k},j} \rangle$ can then be reexpressed by using the eigenmodes $\varphi_{\mathbf{k},j}$,

$$\langle \psi_{\mathbf{k},i}^\dagger \psi_{\mathbf{k},j} \rangle = \sum_m U_{mj} U_{mi} \langle \varphi_{\mathbf{k},m}^\dagger \varphi_{\mathbf{k},m} \rangle \quad (\text{A.9})$$

with the expectation values $\langle \varphi_{\mathbf{k},m}^\dagger \varphi_{\mathbf{k},m} \rangle$ given by the Fermi distribution function $f(E_{\mathbf{k}}^m) = 1/(1 + \exp(\beta E_{\mathbf{k}}^m))$. The expression (A.9) can be directly calculated from the eigenvectors and eigenvalues of the matrix $\hat{A}_{\mathbf{k}}$ in order to use it in the self-consistency equations (5.11).

Part III

Non-equilibrium magnetization dynamics of ferromagnetically coupled Kondo spins

Chapter 8

Introduction

In this chapter, we formulate a non-equilibrium problem described by the ferromagnetic Kondo model subject to a non-equilibrium initial state. We discuss possible experimental realizations of such a problem and introduce the flow equation technique as an analytical approach to this problem. We start with a discussion of the ferromagnetic Kondo model and its equilibrium properties.

8.1 Ferromagnetic Kondo model and experimental realizations

Kondo Hamiltonian

The Kondo Hamiltonian – introduced already in section 1.2 – is given in a more general form by

$$H = \sum_{\mathbf{k}\sigma} \varepsilon_{\mathbf{k}} c_{\mathbf{k}\sigma}^\dagger c_{\mathbf{k}\sigma} + \sum_{\mathbf{k},\mathbf{k}'} J_{\mathbf{k}'\mathbf{k}}^\parallel S^z s_{\mathbf{k}'\mathbf{k}}^z + \sum_{\mathbf{k},\mathbf{k}'} J_{\mathbf{k}'\mathbf{k}}^\perp (S^+ s_{\mathbf{k}'\mathbf{k}}^- + S^- s_{\mathbf{k}'\mathbf{k}}^+) . \quad (8.1)$$

Here, an arbitrary impurity spin with the spin raising and lowering operators $S^\pm = S^x \pm iS^y$ couples to the conduction electron spin density given by

$$s_{\mathbf{k}'\mathbf{k}}^{z,\pm} = \frac{1}{2} \sum_{\alpha,\beta} c_{\mathbf{k}'\alpha}^\dagger \sigma_{\alpha\beta}^{z,\pm} c_{\mathbf{k}\beta} , \quad (8.2)$$

where $\sigma^\pm = \frac{1}{2}(\sigma^x \pm i\sigma^y)$ derive from the Pauli matrices. For explicit calculations, we will use the convenient momentum independent forms ($J_{\mathbf{k}\mathbf{k}'}^\perp = J^\perp$, $J_{\mathbf{k}\mathbf{k}'}^\parallel = J^\parallel$) of the exchange couplings, which may however still obtain momentum dependence during a renormalization procedure applied to H . So far, the impurity spin is allowed to have a general quantum number S and the Kondo exchange couplings shall be in the ferromagnetic regime $J^\parallel < 0$ with $|J^\perp| < -J^\parallel$. For the following calculations, it is useful to introduce the dimensionless couplings $j^\parallel \stackrel{\text{def}}{=} \rho_F J^\parallel$ and $j^\perp \stackrel{\text{def}}{=} \rho_F J^\perp$. Here and in the following, we use a constant density of states $\frac{1}{N} \sum_{\mathbf{q}} \delta(\epsilon - \epsilon_{\mathbf{q}}) \equiv \rho_F$ and a conduction band width $2D$ ($\epsilon_{\mathbf{q}} \in [-D, D]$).

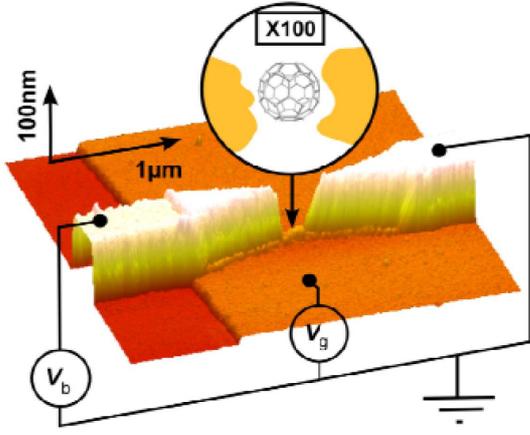


Figure 8.1: Atomic-force-micrograph of the device used to tune the spin state of a C_{60} molecule from a singlet to a triplet configuration in the experiments of Roch et al. (2008). A gold nanowire is deposited over an Al/Al₂O₃ gate, with a C_{60} molecule trapped in a nanogap of the gold wire. The gate voltage V_g is used to tune the spin state of the C_{60} molecule, while the bias voltage V_b is used to measure the differential conductance $\partial I/\partial V$, which has been used to analyze several variants of the Kondo effect. Figure from Roch et al. (2008).

Experimental realizations

a) C_{60} molecule in a nanogap Recent experiments succeeded in trapping a single C_{60} molecule in a nanogap of a gold wire, forming two leads which contact the molecule (Roch et al., 2008). Tuning the spin state of the C_{60} molecule is possible by a gate voltage applied to the substrate, and thus an even number of electrons can be realized on the dot, enabling a spin-triplet state with a total spin $S = 1$ of the C_{60} molecule.

Considering the predominant observation of a single screening channel in this experimental setup (Roch et al., 2008), such a device provides the basis for the observation of the underscreened spin $S = 1$ Kondo effect that Roch et al. (2008) report having measured in a C_{60} molecule quantum dot. As has been explained by Nozières and Blandin (1980), an impurity spin-1 is partially screened by a single conduction electron channel, and the resulting situation can be described by an effective spin-1/2 that is coupled ferromagnetically to the conduction electrons. This situation therefore leads to a ferromagnetic Kondo model as described by Eq. (8.1) for $J^{\parallel} < 0$.

b) Single-molecule magnets Single-molecule magnets (SMMs) such as Mn_{12} have become the subject of intense research. These molecules are characterized by a large total spin, a large magnetic anisotropy barrier, and a weak in-plane anisotropy which allows the spin to tunnel through the barrier (Roosen et al. (2008) and references therein). Electronic transport through SMMs offers several unique features with potentially large impact on applications such as high-density magnetic storage as well as quantum computing (Leuenberger and Loss, 2001). A very interesting approach to the study of SMMs opened up recently with the observation of quantized electronic transport through an *isolated Mn_{12} molecule* (Heersche et al., 2006). The typical experimental constellation used to observe these processes is a field-effect transistor with a SMM as medium, as sketched in the right panel of Fig. 8.2. The gate voltage V_g can be used to control the number q of excess electrons on the molecule, such that the gate contribution to the Hamiltonian becomes $U \frac{q^2}{2} - qeV_g$, where the charging energy is denoted by U . The total Hamiltonian of such

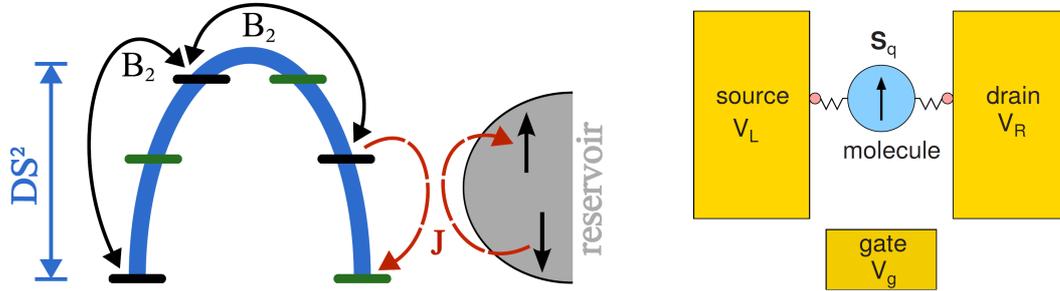


Figure 8.2: *Left:* Sketch of the energy diagram of a SMM described by the impurity Hamiltonian $H_{\text{imp}} = -DS_z^2 - \frac{1}{2}B_2(S_+^2 + S_-^2)$. The levels indicate spin eigenstates $|S, M\rangle$ which are split in energy by the uniaxial anisotropy (D). Two types of spin fluctuations occur: processes due to the intrinsic transverse anisotropy (B_2), and exchange processes involving the conduction band electrons, described by the Kondo exchange coupling J . Figure from Roosen et al. (2008). *Right:* Sketch of a field-effect transistor formed by a SMM attached to two metallic leads (source and drain) and controlled by a back gate voltage. Under suitable conditions, this device might realize a ferromagnetic Kondo Hamiltonian. Figure from Leuenberger and Loss (2001).

an arrangement is of Anderson type, and it has been shown by Gonzalez et al. (2008) that it can be mapped onto a spin- $1/2$ anisotropic Kondo Hamiltonian in two different ways. Say $S_{q=0}$ is the total of the uncharged single-molecule magnet.

(i) Denoting the total spin of the positively ($q = 1$) and negatively ($q = -1$) charged single-molecule magnet by $S_{q=\pm 1}$, the corresponding anisotropic Kondo Hamiltonian exhibits an *antiferromagnetic exchange coupling* if $S_{q=\pm 1} = S_{q=0} - 1/2$. This case corresponds to the Kondo problem for spin- $1/2$ impurities. (ii) The resulting anisotropic Kondo Hamiltonian exhibits a *ferromagnetic exchange coupling* with $J^{\parallel} < 0$ if $S_{q=\pm 1} = S_{q=0} + 1/2$. After having discussed experimental realizations of the ferromagnetic Kondo model, we mention some important equilibrium properties of this model.

Equilibrium properties of the ferromagnetic Kondo model

a) Poor man's scaling The important difference between the ferromagnetic ($J^{\parallel} < 0$) and the antiferromagnetic ($J^{\parallel} > 0$) regime of the Kondo model can be understood from Anderson's poor man's scaling analysis (Anderson, 1970). This approach divides the conduction band into states $0 < |\epsilon_{\mathbf{k}}| < D - |\delta D|$ which are retained, and states within $|\delta D|$ of the band edge which are to be eliminated. The eliminated states are accounted for in form of renormalized interactions of H due to virtual scattering of conduction electrons into the band edge. Technically, this procedure can be described by introducing a flowing cutoff energy Λ defining the reduced bandwidth and formulating differential equations for

the renormalized couplings J^{\parallel} and J^{\perp} , leading to the scaling equations (Hewson, 1997)

$$\begin{aligned}\frac{dJ^{\parallel}}{d\ln(\Lambda)} &= -\rho_F J^{\perp 2} \\ \frac{dJ^{\perp}}{d\ln(\Lambda)} &= -\rho_F J^{\perp} J^{\parallel} .\end{aligned}\tag{8.3}$$

The behavior of these scaling equations is depicted in the flow diagram Fig. 8.3. Antiferromagnetic couplings drive the scaling flow to strong coupling, such that $|J^{\parallel}| \rightarrow \infty$ and $|J^{\perp}| \rightarrow \infty$, and the scaling equations have no low-energy fixed point at finite coupling.

In contrast, a perturbative renormalization is controlled in the ferromagnetic regime with $|J^{\perp}| < -J^{\parallel}$ even if $\Lambda \ll T$, since J^{\parallel} will renormalize to a finite value in the limit $\Lambda \rightarrow 0$. For anisotropic couplings and at $T = 0$, the longitudinal coupling remains finite and the transverse coupling decays asymptotically according to the power law

$$J^{\perp}(\Lambda) \propto \Lambda^{\rho_F} \sqrt{J_{\parallel}^2 - J_{\perp}^2}\tag{8.4}$$

with the scaling trajectory given by the conserved quantity $J^{\parallel 2} - J^{\perp 2} = \text{const.}$ Once the couplings J^{\perp} and J^{\parallel} become isotropic ($J^{\perp} = J^{\parallel}$), both couplings renormalize to zero and the impurity becomes asymptotically free at low energies with the scaling behavior

$$J(\Lambda) = J/(1 + \rho_F J \ln(\Lambda/D)) .\tag{8.5}$$

b) Impurity magnetization Next, we consider the impurity magnetization $M = g_i \mu_B \langle S^z \rangle$ caused by a Zeeman term $H_{\text{Zeeman}} = -g_i \mu_B S^z B$, $B > 0$ coupling to the impurity, with the gyromagnetic ratio g_i of the impurity and the Bohr magneton μ_B . For isotropic ferromagnetic coupling J , this result has been derived by Abrikosov (1965) by a summation over parquet diagrams, leading to the result

$$M = g_i \mu_B S \left(1 - \frac{x(J\rho_F)^2/2}{1 + (J\rho_F)x} \right),\tag{8.6}$$

where we introduced $x = \ln(\epsilon_F/(g_i \mu_B B))$ with the Fermi energy ϵ_F . Consequently, in this case the impurity spin is screened as $B \rightarrow 0$ only by a small quantity of the order $(J\rho_F)/2$.

Non-equilibrium problem

Molecular nanostructures are very often not prepared in thermal equilibrium, but rather under non-equilibrium conditions. Such a situation naturally arises after non-adiabatically imposing a constraint to the system, used to prepare or read out a certain quantum state of the system. It is of great practical relevance how such pure quantum states are destroyed by their environment, e.g. for computational operations. The purpose of this part of the thesis is to analyze the real-time dynamics of a pure spin state that is instantaneously coupled to its environment, described by a ferromagnetic Kondo model. Preparing and measuring

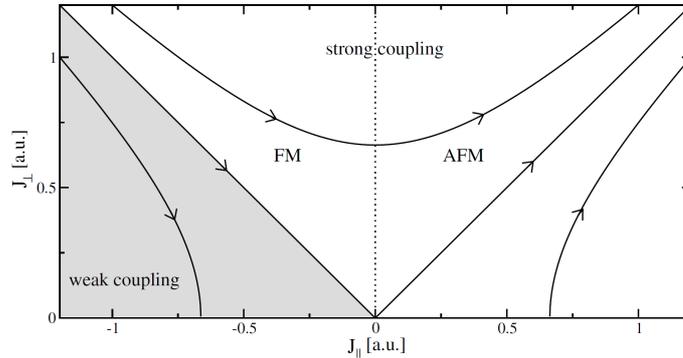


Figure 8.3: Phase portrait of Anderson's poor man's scaling equations for the anisotropic Kondo model. We distinguish two important regimes, the strong coupling regime (white) where the running coupling flows to infinity and the weak coupling regime where J_{\perp} flows to zero (grey). In addition, we call the parameter regime $J_{\parallel} > 0$ antiferromagnetic (AFM) regime, and $J_{\parallel} < 0$ the ferromagnetic (FM) regime. Figure from Fritsch (2009).

such a pure spin state can nowadays be achieved with ultrafast electrical or optical field pulses (Nowack et al., 2007, Braun et al., 2005, Atature et al., 2007), albeit experimental challenges in applying these techniques to molecular quantum dots still remain. In detail, we specify the following non-equilibrium problem:

We start with a quantum system that is described by the Kondo Hamiltonian (8.1) with *time-dependent* ferromagnetic couplings $J^{\perp}(t)$ and $J^{\parallel}(t)$. For all times $t < 0$, we assume that the impurity spin is completely decoupled from the bath degrees of freedom, such that $J^{\perp}(t) \equiv J^{\parallel}(t) \equiv 0$ for $t < 0$. Furthermore, we assume a projected spin state with $\langle S^z(t \leq 0) \rangle = S$ for a spin S , which is realized by an infinitesimally small magnetic field. The bath itself is described by the non-interacting conduction electrons $\sum_{\mathbf{k}\sigma} \varepsilon_{\mathbf{k}} c_{\mathbf{k}\sigma}^{\dagger} c_{\mathbf{k}\sigma}$, prepared in a canonical ensemble with some temperature T . For analytical calculations, we will chose $T = 0$ in order to realize a pure quantum state. We represent this initial state by

$$|\psi\rangle = |\uparrow\rangle \otimes |FS\rangle, \quad (8.7)$$

where $|FS\rangle$ is the non-interacting Fermi sea in thermal equilibrium.

At time $t = 0$ the couplings are switched on to some finite ferromagnetic values $J^{\perp} < 0$ and $J^{\parallel} < 0$ and are time-independent for $t > 0$. The observable we will be interested in is the magnetization $\langle \psi | S^z(t > 0) | \psi \rangle$. In the following, we introduce the approach that we will use to calculate this quantity.

8.2 The flow equation method

The flow equation method was originally introduced by Wegner (1994) as a new way of diagonalizing quantum many-particle Hamiltonians. Simultaneously Głazek and Wilson (1993, 1994) developed the closely related *similarity renormalization group* in the con-

text of high energy physics. Several successful ideas of theoretical physics were combined in the flow equation method. In the famous Numerical Renormalization Group (NRG) method invented by Wilson (1975), the energy spectrum of a Hamiltonian is discretized logarithmically in order to transform a Hamiltonian iteratively into an effective low-energy Hamiltonian. This aspect of *energy scale separation* is one of the main ingredients of the flow equation method. It applies a sequence of infinitesimal unitary transformations and thus opens a controlled way to construct effective Hamiltonians. An application to very different problems of condensed matter physics is possible since this method establishes a unitary transformation that preserves information, e.g., about high energy scales of the original Hamiltonian. A comprehensive review of this method and a survey of its applications can be found in the book of Kehrein (2006).

In the following, we outline the basic ideas of Wegner's approach, before discussing its advantages for the application to real-time evolution problems.

General approach

Any application of the flow equation approach starts with a transformation of a model Hamiltonian. The aim is always to decouple interaction terms in order to make the Hamiltonian more diagonal in its energy representation. This important property of the transformed Hamiltonian is especially suitable to calculate time-dependent observables, as we will show afterwards.

Central to the flow equation approach is the construction of a one-parameter family of unitarily equivalent Hamiltonians $H(B)$,

$$H(B) = U(B)HU^\dagger(B), \quad (8.8)$$

with $H(B = 0) = H$ being the initial Hamiltonian and $H(B = \infty)$ the final diagonal Hamiltonian. In the following, we denote parameters and operators **in this basis by a tilde**, e.g., $\tilde{H} = H(B = \infty)$. Here $U(B)$ is a unitary operator, $U^\dagger(B) = U^{-1}(B)$. This unitary equivalent sequence is most conveniently constructed by setting up the flow in differential formulation

$$\frac{dH(B)}{dB} = [\eta(B), H(B)] \quad (8.9)$$

with an anti-hermitian generator $\eta(B) = -\eta^\dagger(B)$. For a generic many-particle problem an exact diagonalization is in practice not possible due to the generation of higher and higher order interaction terms in (8.9). One therefore attempts to find a final Hamiltonian $H(B = \infty)$ that is approximately unitary equivalent to the initial Hamiltonian. In the spirit of Wilson's *numerical renormalization group* (Wilson, 1975), a stable sequence of approximations treats large energy differences first before proceeding to smaller energy differences. According to the differential formulation given in Eq. (8.9), such a principle of energy scale separation is naturally implemented if B is given the meaning of $|\Delta E|^{-2}$, where ΔE denotes the energy difference: $\eta(B)$ is then constructed such that it eliminates interaction matrix elements coupling states with an energy difference $|\Delta E| \sim B^{-1/2}$. Whether a generator achieves this property requires some constructive principle: it was

Wegner who proposed the generic ansatz

$$\eta(B) = [H_0(B), H_{\text{int}}(B)] , \quad (8.10)$$

where H_0 corresponds to the energy-diagonal part and $H_{\text{int}}(B)$ to the non-diagonal interaction part of the Hamiltonian. The crucial property of this choice is

$$\frac{d}{dB} \text{Tr}\{H_{\text{int}}^2(B)\} \leq 0 , \quad (8.11)$$

causing a monotonously decreasing trace of the squared interaction $H_{\text{int}}^2(B)$ during the flow towards $B \rightarrow \infty$ (Kehrein, 2006). Based on this property, it can be shown that interaction matrix elements of $H_{\text{int}}(B)$ are eliminated according to the desired correspondence $|\Delta E| \sim B^{-1/2}$.

While it is in most cases not possible to solve Eq. (8.9) exactly, it is in many applications possible to apply perturbative approximations to it, e.g., if the generator is proportional to a small expansion parameter λ . The flowing Hamiltonian can then be formally arranged as a perturbation series in the expansion parameter λ ,

$$H(B) = H^{(0)}(B) + \lambda H^{(1)}(B) + \lambda^2 H^{(2)}(B) + \dots = \sum_{n=0}^{\infty} \lambda^n H^{(n)}(B) . \quad (8.12)$$

In many cases, the expansion parameter λ is chosen as the prefactor of the dominating interaction term $H^{(1)}(B)$ in the model Hamiltonian, while the operator $H^{(0)}(B)$ is the interaction-free part of the Hamiltonian $H(B)$, and $H^{(n)}(B)$, $n > 1$ correspond to newly generated interaction terms in H . Usually, the series Eq. (8.12) contains an infinite number of terms that have to be truncated at some finite order in λ . Then, the convergence properties of the truncated expansion (8.12) can be much improved by using a normal ordering scheme.

Normal ordering and truncation scheme

Once trying to truncate the series of interactions generated during the flow, it becomes decisive to distinguish the different interaction terms occurring in the expansion (8.12). Such an interpretation can be made in a way similar to diagrammatic expansion of a quantum many-body problem by considering only *irreducible parts* of the interaction terms, which contain all the elementary interaction processes. The proper way to decompose products of fermionic operators into irreducible interactions is the normal-ordering procedure introduced by Wick (1950). We refrain from explaining the formalism of normal ordering in explicit detail here (for this purpose see, e.g., (Kehrein, 2006)), but provide a particular example that will be useful for essentially all of our subsequent applications of normal ordering.

Typical example: Fermions For fermionic operators $c_{\mathbf{k}\sigma}^\dagger$ and $c_{\mathbf{k}\sigma}$ creating/annihilating fermions in momentum state \mathbf{k} , we define the *contraction* $\langle c_{\mathbf{k}\sigma}^\dagger c_{\mathbf{k}\sigma} \rangle = n(\mathbf{k})$, which amounts

in our example to the expectation value with respect to the density matrix of the Fermi gas in thermal equilibrium $\text{Tr}\{\rho_{eq}c_{\mathbf{k}\sigma}^\dagger c_{\mathbf{k}\sigma}\}$, such that $n(\mathbf{k})$ is the Fermi distribution function $n_{\mathbf{k}} = \frac{1}{\exp(\beta\epsilon_{\mathbf{k}})+1}$. In this simple application, normal ordering of two typical products of fermionic operators is given by the operation

$$\begin{aligned} :c_1^\dagger c_1: &= c_1^\dagger c_1 - \delta_{1'1} n(1) \\ :c_1^\dagger c_2^\dagger c_2 c_1: &= :c_1^\dagger c_1: :c_2^\dagger c_2: - \delta_{1'2'} (1 - n(1)) :c_1^\dagger c_2: \\ &+ \delta_{1'2} n(1') :c_2^\dagger c_1: - \delta_{1'2} \delta_{1'2'} (n(1')(1 - n(1))) . \end{aligned} \quad (8.13)$$

where normal ordered operators have been denoted by $: \ :$ and momenta have been labeled by the numbers $1, 1', 2, 2'$. Normal ordering thus separates products of fermionic operators into one-, two- and many-particle contributions. Without normal-ordering of the series expansion (8.12), there is no feedback from higher orders in the coupling constant to lower orders, which leads to worse convergence properties of a non-normal ordered expansion since it cannot describe non-perturbative energy scales (Kehrein, 2006).

Evaluation of observables

The evaluation of observables in the flow equation framework requires some further technical steps. Let \hat{A} be a Hermitian observable and we are interested in its ground state expectation value

$$\langle \hat{A} \rangle_{\text{gs}} = \langle \psi_{\text{gs}} | \hat{A} | \psi_{\text{gs}} \rangle , \quad (8.14)$$

where $|\psi_{\text{gs}}\rangle$ is the ground state of the full interacting Hamiltonian,

$$H|\psi_{\text{gs}}\rangle = E_{\text{gs}}|\psi_{\text{gs}}\rangle , \quad (8.15)$$

with the ground state energy E_{gs} . The evaluation of (8.14) becomes much simpler if (8.15) is rewritten in the basis representation corresponding to the diagonal form of the Hamiltonian, where

$$H(B = \infty)|\tilde{\psi}_{\text{gs}}\rangle = E_{\text{gs}}|\tilde{\psi}_{\text{gs}}\rangle . \quad (8.16)$$

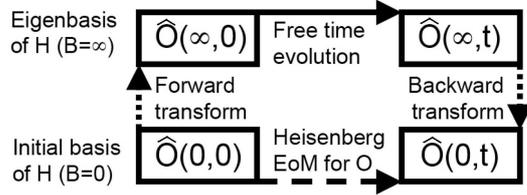
Using this representation, Eq. (8.14) reads

$$\langle \hat{A} \rangle_{\text{gs}} = \langle \tilde{\psi}_{\text{gs}} | \tilde{\hat{A}} | \tilde{\psi}_{\text{gs}} \rangle , \quad (8.17)$$

and the observable $\tilde{\hat{A}}$ is constructed from a solution to the differential equation

$$\frac{d\hat{A}}{dB} = [\eta(B), \hat{A}(B)] \quad (8.18)$$

in the limit $B \rightarrow \infty$, with the initial condition $\hat{A}(B = 0) = \hat{A}$. This solution is constructed in analogy to the procedure discussed for the diagonalization of H , e.g., it makes use of the same normal-ordering prescription. This transformation of an observable \hat{A} is part of a procedure to effectively solve the Heisenberg equation of motion $\frac{d\hat{A}}{dt} = i[H, \hat{A}]$ (see Fig. 8.4) which is the main application we are interested in.



introduces phase shifts, and therefore the form of the observable in the initial basis $B = 0$ (after a backward transformation) changes as a function of time. Figure from Moeckel and Kehrein (2008).

Figure 8.4: The Heisenberg equation of motion for an observable \hat{O} is solved by transforming to the $B = \infty$ eigenbasis of the interacting Hamiltonian H (forward transformation), where the time evolution can be computed easily. Time evolution in this basis introduces phase shifts, and therefore the form of the observable in the initial basis $B = 0$ (after a backward transformation) changes as a function of time. Figure from Moeckel and Kehrein (2008).

Motivation: Real-time evolution

It has been shown by Hackl and Kehrein (2008) that basic features of the flow equation approach are suitable to implement an analogue of *canonical perturbation theory* in classical mechanics to quantum many-body systems. We shall illustrate the method further by elaborating on this analogy and explaining the concept of canonical perturbation theory in chapter 9, while illustrating just fundamental aspects of the approach of Hackl and Kehrein (2008) in this introduction. The general setup is described by the diagram in Fig. 8.4, where in addition, some initial non-thermal state $|\Psi_i\rangle$ that one is interested in might be considered. However, instead of following its full time evolution it is usually more convenient to study the real time evolution of a given observable \hat{O} that one is interested in. This is done by transforming the observable into the diagonal basis in Fig. (8.4) (*forward transformation*), using Eq. (8.18) with the initial condition $\hat{A}(B = 0) = \hat{O}$. The key observation is that can now solve the real time evolution with respect to the energy-diagonal \tilde{H} exactly, thereby avoiding any errors that grow proportional to time (i.e., secular terms): this yields $\tilde{\hat{O}}(t)$. Now since the initial quantum state is given in the $B = 0$ basis, one undoes the basis change by integrating (8.18) from $B = \infty$ to $B = 0$ (*backward transformation*) with the initial condition $\hat{A}(B = \infty) = \tilde{\hat{O}}(t)$. One therefore effectively generates a new non-perturbative scheme for solving the Heisenberg equation of motion for an operator, $\hat{O}(t) = e^{iHt}\hat{O}(0)e^{-iHt}$ (Hackl and Kehrein, 2008). It is then possible to evaluate the observable $\langle\psi_i|\hat{O}(t)|\psi_i\rangle$ without further approximations.

8.3 Outline

In the following chapter, we will first summarize the advantage of canonical perturbation theory in classical mechanics, before illustrating the implementation of the quantum analogue of canonical perturbation theory on the example of a simple toy model. Afterwards, we investigate the non-equilibrium dynamics of the ferromagnetic Kondo model, where we will be able to extract analytical results from the flow equations in this non-trivial real-time evolution problem.

Chapter 9

Unitary perturbation theory approach to real-time evolution problems

9.1 Motivation: canonical perturbation theory in classical mechanics

Classical mechanics provides a canonical example how to improve upon the validity of classical perturbation theory in the limit of asymptotically large times. We shall illustrate this statement in the remaining part of this section, briefly mentioning the basic idea now. In a first step, a canonical transformation is applied to change to new coordinates which are closer to the eigenmodes of the Hamilton function. The remaining interaction terms are then treated perturbatively in terms of the new degrees of freedom. As a result, the perturbation expansion of the transformed equation of motion appears merely as a renormalization of model parameters, and secular terms can be avoided in this way.

A useful model to illustrate the advantages of canonical perturbation theory is given by a classical harmonic oscillator with a weak quartic perturbation, represented by the Hamilton function

$$H = \frac{1}{2}p^2 + \frac{1}{2}q^2 + \frac{g}{4}q^4, \quad (9.1)$$

where the quartic anharmonic term perturbs the periodic motion with a coupling $g \ll 1$. We will chose the initial conditions $q(t=0) = 0$ for the position q and $p(t=0) = v + \frac{3}{8}gv^3$ for the momentum p in the following.

Direct application of perturbation theory The usefulness of the sophisticated canonical perturbation theory is only justified if a direct perturbative expansion of the equations of motion for p and q leads to uncontrolled errors, although the quartic perturbation is small. Such an expansion is formally prepared by writing the perturbed solution $q(t)$ as a power series in the coupling g ,

$$q(t) = q^{(0)}(t) + gq^{(1)}(t) + \mathcal{O}(g^2). \quad (9.2)$$

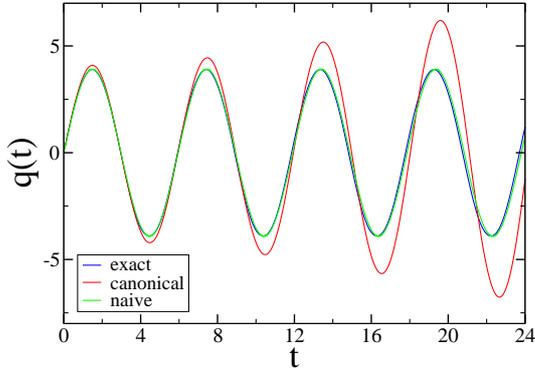


Figure 9.1: We compare the different approaches to solve the equations of motion for the anharmonic oscillator from Eq. (9.1). The difference between the numerically exact solution and canonical perturbation theory according to Eq. (9.12) can hardly be noticed. Naive perturbation theory yields large errors already after a few oscillations, with an error that grows linear in time t . Our parameters are $v = 4$ and coupling strength $g = 0.01$.

Setting $g = 0$, one recovers the trajectory $q^{(0)}(t)$ of the unperturbed solution, given by

$$q^{(0)}(t) = v \sin(t) . \quad (9.3)$$

The equation of motion for $q^{(1)}(t)$ is obtained from Hamilton's equations

$$\frac{\partial H}{\partial p} = \dot{q}; \quad \frac{\partial H}{\partial q} = -\dot{p} , \quad (9.4)$$

in which the terms in an expansion to first order in g are related by

$$\ddot{q}^{(1)}(t) = -q^{(1)}(t) - v^3 \sin^3(t) . \quad (9.5)$$

This equation of motion can be integrated in closed form, with the result

$$q^{(1)}(t) = \frac{3}{8}v^3 \sin(t) - \frac{v^3}{8}(\sin(t) \cos^2(t) + 2 \sin(t) - 3t \cos(t)) . \quad (9.6)$$

Already from this simple example, it is seen why naive perturbation theory remains uncontrolled once the parameter t becomes of order $1/g$: the *secular term* $3t \cos(t)$ grows unboundedly in time and invalidates perturbation theory.

Canonical perturbation theory A canonical way to avoid such errors is treated in many textbooks on classical mechanics, see, e.g., Goldstein et al. (2002). One first looks for a canonical transformation of variables

$$(q, p) \rightarrow (Q, P) , \quad (9.7)$$

such that Hamilton's function obtains the following normal form

$$\tilde{H} = H_0 + g\alpha H_0^2 + \mathcal{O}(g^2) \quad \text{with} \quad H_0 = \frac{1}{2}P^2 + \frac{1}{2}Q^2 . \quad (9.8)$$

The usefulness of this type of normal form is motivated by the vanishing Poisson bracket $\{H_0, H_0^2\}$, hence the equations of motion for Q and P are fully described by the non-interacting Hamilton function H_0 ,

$$\begin{aligned}\dot{Q}(t) &= \frac{\partial H(Q, P)}{\partial P} = \left(1 - 2g\alpha H_0(P, Q)\right)P \\ \dot{P}(t) &= -\frac{\partial H(Q, P)}{\partial Q} = -\left(1 - 2g\alpha H_0(P, Q)\right)Q ,\end{aligned}\tag{9.9}$$

where $H_0(P, Q)$ is a conserved quantity since the Poisson bracket $\{H_0, \tilde{H}\}$ vanishes. To zeroth order in g , we can set $H_0(P, Q) = E_0 + \mathcal{O}(g)$, with $E_0 = v^2(0)/2$. Thus, the equations of motion for P and Q are those of a harmonic oscillator with a renormalized frequency $\omega = 1 + \frac{3}{4}gE_0$, for which we chose the initial condition $Q(t=0) = 0$. The transformation that brings $H(q, p)$ to the normal form \tilde{H} is given by (Kehrein, 2008)

$$\begin{aligned}q(t) &= Q(t) - \frac{3}{32}g\left(3P^2(t)Q(t) + \frac{5}{3}Q^3(t)\right) \\ &\quad + \mathcal{O}(g^2), \\ p(t) &= P(t) + \frac{3}{32}g\left(5P(t)Q^2(t) + P^3(t)\right) \\ &\quad + \mathcal{O}(g^2) ,\end{aligned}\tag{9.10}$$

what can be proven by explicitly substituting (9.10) into $H(q, p)$ given by Eq. (9.1). Integrating Eq. (9.9) and inserting the solutions $Q(t) = v \sin(\omega t) + \mathcal{O}(g^2)$ and $P(t) = v \cos(\omega t) + \mathcal{O}(g^2)$ into Eq. (9.10) yields the result

$$\begin{aligned}q(t) &= v \sin(\omega t) \\ &\quad - \frac{3}{32}gv^3\left(3 \cos^2(\omega t) \sin(\omega t) + \frac{5}{3} \sin^3(\omega t)\right) \\ &\quad + \mathcal{O}(g^2),\end{aligned}\tag{9.11}$$

$$\begin{aligned}p(t) &= v \cos(\omega t) + \frac{3}{32}gv^3\left(5 \sin^2(\omega t) \cos(\omega t) + \cos^3(\omega t)\right) \\ &\quad + \mathcal{O}(g^2) .\end{aligned}\tag{9.12}$$

The systematic improvement of canonical perturbation theory over naive perturbation theory is best illustrated by expanding the solution (9.12) in the coupling g :

$$\begin{aligned}\sin(\omega t) &= \sin\left(\left(1 + \frac{3}{4}gE_0\right)t\right) \\ &= \sin(t) + \frac{3}{4}gE_0 t \cos(t) + \mathcal{O}(g^2) .\end{aligned}\tag{9.13}$$

This expansion automatically generates the secular term from Eq. 9.6, while in the original solution, a whole perturbation series is resummed that eliminates errors growing as powers of t .

9.2 Illustration for a simple oscillator model

A quantum many-body analogue of a perturbed harmonic oscillator is given by the *dissipative harmonic oscillator*, describing a quantum oscillator of frequency Δ coupled linearly to a heat bath consisting of bosonic normal modes b_k ,

$$\begin{aligned}
 H &= \Delta b^\dagger b + \sum_k \omega_k b_k^\dagger b_k + E_0 \\
 &+ \sum_k \lambda_k (b + b^\dagger)(b_k + b_k^\dagger) ,
 \end{aligned} \tag{9.14}$$

with the bosonic operators fulfilling canonical commutation relations

$$[b_k, b_{k'}^\dagger] = \delta_{kk'} . \tag{9.15}$$

The influence of the dissipative environment is fully described by the spectral function

$$J(\omega) \stackrel{\text{def}}{=} \sum_k \lambda_k^2 \delta(\omega - \omega_k) . \tag{9.16}$$

This model is widely used in the field of quantum optics and several other contexts, and we shall use it here as an illustration of our quantum analogue of canonical perturbation theory.

We seek to formulate an initial state causing a finite initial displacement of the expectation value $\langle \hat{x} \rangle = \frac{1}{\sqrt{2}} \langle (b + b^\dagger) \rangle$ such that the effects of coupling to the reservoir will manifest themselves in the real-time evolution of the observable $\langle \hat{x}(t) \rangle$. Although the flow equation approach is not restricted to a specific type of initial state, in the following we shall choose the convenient product initial state

$$|\psi_i\rangle = |a\rangle \otimes |\Omega\rangle , \tag{9.17}$$

with the quantum oscillator in a *coherent state*

$$|a\rangle = e^{-\frac{a^2}{2}} \sum_{n=0}^{\infty} \frac{a^n}{\sqrt{n!}} |n\rangle , a \in \mathbb{R} \tag{9.18}$$

and the heat bath in the bosonic vacuum state $|\Omega\rangle$.

Flow equation approach

The flow equation approach now follows essentially the steps given in Fig. 8.4, with the aim to solve the Heisenberg equation of motion for the transformed operator \tilde{b} . One first transforms the operator b into the eigenbasis of the diagonalized Hamiltonian \tilde{H} formulated in Eq. (9.22). Then one solves the Heisenberg equation of motion $\frac{d\tilde{b}}{dt} = i[\tilde{H}, \tilde{b}]$ for the transformed operator \tilde{b} with respect to the diagonalized Hamiltonian \tilde{H} . Finally, this time-evolved operator will be transformed into the initial basis by reverting the unitary transformation used to diagonalize H . These various steps will be implemented by solving a coupled set of differential equations.

a) Diagonalization The formal steps for the flow-equation diagonalization of the dissipative harmonic oscillator have been detailed by Kehrein and Mielke (1997). We just sketch the main steps here in order to illustrate the formal approach. We chose the generator

$$\begin{aligned}\eta(B) &= \sum_k \eta_k^{(1)} (b - b^\dagger)(b_k + b_k^\dagger) \\ &+ \sum_{k,q} \omega_k \lambda_k (b + b^\dagger)(b_k - b_k^\dagger) \\ &+ \sum_{k,q} \eta_{k,q} (b_k + b_k^\dagger)(b_q - b_q^\dagger) + \eta_b (b^2 - b^{\dagger 2})\end{aligned}\quad (9.19)$$

such that the flowing Hamiltonian $H(B)$ is form invariant and retains the form of the initial Hamiltonian (9.14), with the function $\tilde{f}(\omega_k, B)$ chosen such that all the couplings λ_k decay in the limit $B \rightarrow \infty$. In the following, we omit the explicit dependence of coefficients on the parameter B . The coefficients in (9.19) are chosen as

$$\begin{aligned}\eta_k^{(1)} &= -\lambda_k \Delta \tilde{f}(\omega_k, B) \\ \eta_k^{(2)} &= \lambda_k \omega_k \tilde{f}(\omega_k, B) \\ \eta_{k,q} &= -\frac{2\lambda_k \lambda_q \Delta \omega_q}{\omega_k^2 - \omega_q^2} (\tilde{f}(\omega_k, B) + \tilde{f}(\omega_q, B)) \\ \eta_b &= -\frac{1}{4\Delta} \frac{d\Delta}{dB}.\end{aligned}\quad (9.20)$$

For numerical solutions of the flow equations, the choice $\tilde{f}(\omega_k, B) = -\frac{\omega_k - \Delta}{\omega_k + \Delta}$ leads to good convergence properties in the limit $B \rightarrow \infty$ (Kehrein and Mielke, 1997). Using this choice of generator, the flowing coupling constants of H are governed by the differential equations

$$\begin{aligned}\frac{d\Delta(B)}{dB} &= 4 \sum_k \eta_k^{(2)} \lambda_k \\ \frac{dE_0(B)}{dB} &= 2 \sum_k \eta_k^{(2)} \lambda_k + 2 \sum_k \eta_k^{(1)} \lambda_k \\ \frac{d\omega_k}{dB} &= \mathcal{O}\left(\frac{1}{N}\right) \\ \frac{d\lambda_k}{dB} &= \Delta \eta_k^{(1)} + \omega_k \eta_k^{(2)} \\ &+ 2 \sum_q \eta_{k,q} \lambda_q + 2\eta_b \lambda_k.\end{aligned}\quad (9.21)$$

Formally, a renormalization of the ω_k proportional to the inverse number of bosonic modes ($\frac{1}{N}$) occurs, which will drop out of the observable $\langle \hat{x}(t) \rangle$ in the thermodynamic limit $N \rightarrow \infty$. In the limit $B \rightarrow \infty$, the diagonal form of the Hamiltonian will be

$$\tilde{H} = \tilde{\Delta} b^\dagger b + \sum_k \omega_k b_k^\dagger b_k + \tilde{E}_0, \quad (9.22)$$

with a renormalized tunneling matrix element $\tilde{\Delta} < \Delta$. A construction of a solution to the transformed Heisenberg equation of motion $\frac{d\tilde{b}}{dt} = i[\tilde{H}, \tilde{b}]$ requires now to transform the bosonic operator b in analogy to the procedure we used to diagonalize the Hamiltonian H .

b) Flowing operators Using the generator $\eta(B)$ from Eq. (9.19) in the differential equation $\frac{db}{dB} = [\eta(B), b(B)]$, it is readily seen that the bosonic operator b flows according to

$$\begin{aligned} b(B) &= \beta(b + b^\dagger) + \bar{\beta}(b - b^\dagger) \\ &+ \sum_k \alpha_k(b_k + b_k^\dagger) + \bar{\alpha}_k(b_k - b_k^\dagger) \end{aligned} \quad (9.23)$$

with the flow equations

$$\begin{aligned} \frac{d\beta(B)}{dB} &= 2\eta_b\beta + 2 \sum_k \alpha_k\eta_k^{(2)} \\ \frac{d\bar{\beta}(B)}{dB} &= -2\eta_b\bar{\beta} - 2 \sum_k \bar{\alpha}_k\eta_k^{(1)} \\ \frac{d\alpha_k(B)}{dB} &= 2\eta_k^{(1)}\beta + 2 \sum_q \eta_{k,q}\alpha_q \\ \frac{d\bar{\alpha}_k(B)}{dB} &= -2\eta_k^{(2)}\bar{\beta} - 2 \sum_q \eta_{q,k}\bar{\alpha}_q. \end{aligned} \quad (9.24)$$

The initial conditions for the flow are given by $\beta(B=0) = \bar{\beta}(B=0) = 1/2$ and $\alpha_k(B=0) = \bar{\alpha}_k(B=0) = 0$, while in the limit of accomplished flow ($B \rightarrow \infty$), we will have $\beta(B \rightarrow \infty) = \bar{\beta}(B \rightarrow \infty) = 0$ and b will have decayed into a superposition of bath operators (Kehrein and Mielke, 1997).

c) Time evolution It is now straightforward to implement the remaining steps in order to solve the Heisenberg equation of motion $\frac{db}{dt} = i[H, b]$. Performing the time evolution of the transformed bosonic operator by solving the transformed Heisenberg equation of motion $\frac{d\tilde{b}}{dt} = i[\tilde{H}, \tilde{b}]$ endows the operator $\tilde{b}(t)$ with trivial phase factors

$$\begin{aligned} \tilde{\beta}(t) &= \tilde{\beta} \cos(\tilde{\Delta}t) - i\tilde{\beta} \sin(\tilde{\Delta}t) \\ \tilde{\bar{\beta}}(t) &= \tilde{\bar{\beta}} \cos(\tilde{\Delta}t) - i\tilde{\bar{\beta}} \sin(\tilde{\Delta}t) \\ \tilde{\alpha}_k(t) &= \tilde{\alpha}_k \cos(\omega_k t) - i\tilde{\alpha}_k \sin(\omega_k t) \\ \tilde{\bar{\alpha}}_k(t) &= \tilde{\bar{\alpha}}_k \cos(\omega_k t) - i\tilde{\bar{\alpha}}_k \sin(\omega_k t) \end{aligned} \quad (9.25)$$

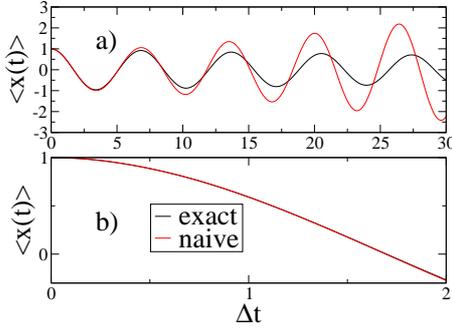


Figure 9.2: Comparison of the exact solution Eq. (9.33) against the naive perturbation theory of Eq. (9.32). The secular term occurring in the second-order perturbation expansion yields an error growing $\propto t$, see a). In the short time limit $t \ll 1$, naive perturbation theory becomes exact, see b). Parameters: $a = \frac{1}{\sqrt{2}}$, $\Delta = 1$; Ohmic bath: $J(\omega) = 2\alpha\omega\Theta(\omega_c - \omega)$ with $\alpha = 0.001$, $\omega_c = 10$.

and the time-evolved operator becomes

$$\begin{aligned} \tilde{b}(t) &= \tilde{\beta}(t)(b + b^\dagger) + \tilde{\bar{\beta}}(t)(b - b^\dagger) \\ &+ \sum_k \tilde{\alpha}_k(t)(b_k + b_k^\dagger) \\ &+ \sum_k \tilde{\bar{\alpha}}_k(t)(b_k - b_k^\dagger). \end{aligned} \quad (9.26)$$

d) Backward transformation The last step is to revert the unitary transformation used to diagonalize the Hamiltonian H to obtain the operator $b(t)$ from the operator $\tilde{b}(t)$. Since the operator $\tilde{b}(t)$ has the same formal structure than the flowing operator $b(B)$, the ansatz (9.23) needs just to be modified by an additional parameter t ,

$$\begin{aligned} b(B, t) &= \beta(B, t)(b + b^\dagger) + \bar{\beta}(B, t)(b - b^\dagger) \\ &+ \sum_k [\bar{\alpha}_k(B, t)(b_k - b_k^\dagger) \\ &+ \alpha_k(B, t)(b_k + b_k^\dagger)], \end{aligned} \quad (9.27)$$

in order to transform the operator $\tilde{b}(t)$ from the limit $B \rightarrow \infty$ to $B = 0$. The flow equations for the coefficients in Eq. (9.27) will therefore be equivalent to Eqs (9.24), with the initial condition for $B \rightarrow \infty$ posed by Eq. (9.26), from which it is seen that all coefficients in Eq. (9.27) will have both real and imaginary part. In conclusion, we presented an approach how to solve Heisenberg's equation of motion in a canonically transformed basis. All steps performed up to now do not depend on the initial state of the quantum system. E.g., it is possible to evaluate the operator $\hat{x}(t) = \frac{1}{\sqrt{2}}e^{iHt}(b + b^\dagger)e^{-iHt}$ with respect to arbitrary non-equilibrium initial states. In Fig. 9.3, we demonstrate how a numerical implementation of this approach compares against the exact analytical result of Eq. (9.33).

For all numerical calculations, we used an Ohmic spectral function defined by $J(\omega) = 2\alpha\omega\Theta(\omega_c - \omega)$ with a cutoff ω_c and damping strength α . A convenient work station allows to discretize the bosonic bath with $\mathcal{O}(10^3)$ states (using equal energy spacing of the bosonic modes) in order to integrate the resulting $\mathcal{O}(10^3) \times \mathcal{O}(10^3)$ coupled ordinary

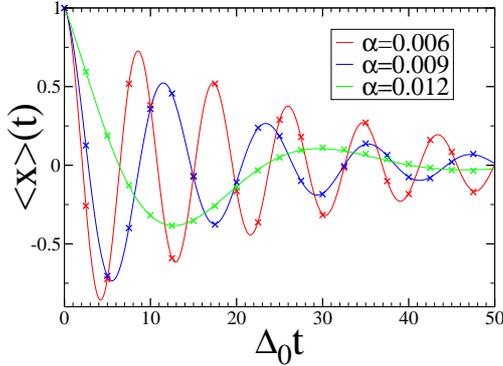


Figure 9.3: Comparison of the time-dependent displacement $\langle \hat{x} \rangle(t)$ of the dissipative harmonic oscillator, obtained from the analytical result of Eq. (9.33) (continuous lines) and numerical integration of the flow equations (9.24) (crosses). Different damping strengths α have been chosen, and the tunneling matrix element Δ is almost renormalized to zero at $\alpha = 0.012$, leading to a much slower oscillation period. The curve has been normalized to 1 by choosing $a = 1/\sqrt{2}$ in the initial state (9.17). The comparison demonstrates that a numerical solution using about 1000 bath states reproduces the analytical result already excellent with a relative error below 1%.

differential equations. Numerical solutions of these differential equations were obtained with a standard Runge Kutta algorithm from Press et al. (2007) that we implemented in the commonly used language “C”.

In order to numerically determine the initial condition (9.26), it is sufficient to integrate the flow equations (9.24) up to $B = \mathcal{O}(N^2/\omega_c^2)$, where only a fraction of $\mathcal{O}(1/N)$ of the couplings λ_k has not decayed exponentially yet. Flow equations with initial conditions given in the limit $B \rightarrow \infty$ usually cannot be integrated with a standard Runge Kutta algorithm, since the exponential smallness of the flowing couplings $\lambda_k(B)$ exceeds floating point precision and leads to ill-posed initial conditions. This problem was circumvented by storing the flow of the couplings $\lambda_k(B)$ from the diagonalization of the Hamiltonian and supplementing it to the integration procedure starting at a parameter value $B = \mathcal{O}(N^2/\omega_c^2)$.

Analytical results

a) Naive perturbation theory In analogy to classical perturbation theory (see section 9.1), we briefly illustrate the failure of perturbation theory in our simple quantum many body problem. The exact time evolution of the operator $\hat{x} = (b + b^\dagger)/\sqrt{2}$ is

$$\hat{x}(t) = e^{iHt} \hat{x} e^{-iHt} \quad (9.28)$$

where H is given by Eq. (9.14). It is convenient to perform a perturbative expansion of Eq. (9.28) in the *interaction picture*, in which we define the operators

$$\begin{aligned} \hat{x}_I(t) &= e^{-iH_0 t} \hat{x}(t) e^{iH_0 t} \\ H_{\text{int}}^I(t) &= e^{-iH_0 t} \left[\sum_k \lambda_k (b + b^\dagger) (b_k + b_k^\dagger) \right] e^{iH_0 t}. \end{aligned} \quad (9.29)$$

Here, $H_0 = \Delta b^\dagger b + \sum_k \omega_k b_k^\dagger b_k$ and $H_{\text{int}}^I(t)$ defines the interaction part of the Hamiltonian in the interaction picture. In the interaction picture, the equation of motion (9.28) is

readily rewritten as

$$\frac{\hat{x}^I(t)}{dt} = i[H_{\text{int}}^I(t), \hat{x}^I(t)] , \quad (9.30)$$

which can be expanded as

$$\begin{aligned} \hat{x}^I(t) &= \hat{x} + i \int_0^t d\tau_1 [H_{\text{int}}^I(\tau_1), \hat{x}] \\ &+ i^2 \int_0^t d\tau_1 \int_0^{\tau_1} d\tau_2 [H_{\text{int}}^I(\tau_1), [H_{\text{int}}^I(\tau_2), \hat{x}]] \\ &+ \mathcal{O}(H_{\text{int}}^I)^3 . \end{aligned} \quad (9.31)$$

This result is correct up to neglected terms of $\mathcal{O}(\lambda_k^3)$. Since the initial state $|\psi_i\rangle$ given in (9.17) is an eigenstate of H_0 , all odd orders of perturbation theory for $\hat{x}_I(t)$ will have vanishing expectation value with respect to $e^{-iH_0 t}|\psi_i\rangle$, and the expectation value $\langle \hat{x}(t) \rangle$ can be evaluated perturbatively as

$$\begin{aligned} \langle \hat{x}(t) \rangle &= \sqrt{2}a \cos(\Delta t) - \frac{a}{\sqrt{2}} \int_0^\infty d\omega \frac{4\Delta J(\omega)}{\Delta^2 - \omega^2} \\ &\times \left(-\frac{2\omega}{\Delta^2 - \omega^2} (\cos(\omega t) - \cos(\Delta t)) \right. \\ &\left. + \frac{\omega}{\Delta} \sin(\Delta t)t \right) + \mathcal{O}(\lambda_k^4) , \end{aligned} \quad (9.32)$$

where we made use of the spectral function $J(\omega)$ defined in Eq. (9.16). It can be seen that a secular term $\sim t$ occurs already in the first non-vanishing order of perturbation theory in λ_k and invalidates the perturbative result at large times, in analogy to the failure of perturbation theory in classical mechanics observed in section 9.1.

b) Exact result For an Ohmic bath with $J(\omega) = \alpha\omega\Theta(\omega_c - \omega)$, it is possible to evaluate the expectation value $\langle \hat{x}(t) \rangle$ with respect to the initial state (9.17) exactly by using the *equations-of-motion technique* (Hackl, 2006) with the result

$$\langle \hat{x}(t) \rangle = 2\sqrt{2}a \int_0^\infty \omega K(\omega) \cos(\omega t) d\omega \quad (9.33)$$

and the function $K(\omega)$ given by (Kehrein and Mielke, 1997)

$$K(\omega) = \frac{4\alpha\omega\Delta}{[\Delta^2 - \omega^2 + 8\alpha\Delta(-\omega_c + \frac{\omega}{2}\ln(\frac{\omega+\omega_c}{\omega_c-\omega}))]^2 + 16\pi^2\alpha^2\Delta^2\omega^2} . \quad (9.34)$$

In Fig. 9.2, we compare the perturbative result (9.31) with the exact result (9.33).

9.3 Conclusions

In this chapter, we motivated an analytical approach to real-time evolution in quantum many-body systems by an analogy to canonical perturbation theory in classical mechanics. We illustrated this approach by the application to a simple toy model and demonstrated its reliability by a fully numerical implementation of all flow equations. In the next chapter, we shall use this approach in the context of non-equilibrium magnetization dynamics in the ferromagnetic Kondo model by applying suitable approximations.

Chapter 10

Non-equilibrium spin dynamics in the ferromagnetic Kondo model

Our analysis of the ferromagnetic Kondo model under non-equilibrium initial conditions will use sophisticated analytical calculations that will require several approximations in order to extract asymptotic results. In order to motivate these calculations we illustrate several physical aspects on an exactly solvable toy model. Although the subsequent sections might be read independently, an improved understanding can be obtained from this simple example.

10.1 Toy model

A simple analogy to the ferromagnetic Kondo model is given by considering just two spin-1/2 fermionic levels coupled $SU(2)$ -symmetrically to a spin-1/2 impurity spin \vec{S} ,

$$H = \sum_{\alpha} \left(c_{\alpha}^{\dagger} c_{\alpha} - d_{\alpha}^{\dagger} d_{\alpha} \right) + \frac{g}{2} \vec{S} \cdot \sum_{\alpha, \beta} (c_{\alpha}^{\dagger} + d_{\alpha}^{\dagger}) \vec{\sigma}_{\alpha\beta} (c_{\beta} + d_{\beta}) . \quad (10.1)$$

The finite number of fermionic states makes this model tractable by *stationary* perturbation theory, irrespective of the sign of the coupling g . In this model, the energy levels are chosen particle-hole symmetrically, such that both occupied and unoccupied states are available in the non-interacting ground state of the fermionic system. Due to the $SU(2)$ -symmetric coupling in (10.1), the ground state of the interacting system (10.1) is twofold degenerate. Since we will be interested in the real-time evolution of the observable $\langle S^z(t) \rangle$ for a given non-equilibrium initial state of (10.1), it shall be advantageous to interpret this state as the ground state of a corresponding non-interacting Hamiltonian. An infinitesimal Zeeman splitting is sufficient to lift the degeneracy in the spin sector, such that the initial state can be chosen as the unique ground state of $\sum_{\alpha} \left(c_{\alpha}^{\dagger} c_{\alpha} - d_{\alpha}^{\dagger} d_{\alpha} \right) - B S^z$ with an infinitesimal positive value of B . We define this state as the initial state $|\psi(t=0)\rangle = |\psi_0\rangle$, denoted by

$$|\psi_0\rangle \stackrel{\text{def}}{=} |0\rangle \otimes |\uparrow\downarrow\rangle \otimes |\uparrow\rangle , \quad (10.2)$$

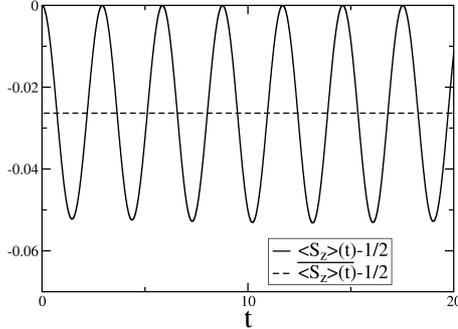


Figure 10.1: The time-dependence of the expectation value $\langle \psi_0 | S_z(t) - \frac{1}{2} | \psi_0 \rangle$ is shown for $g = -1/2$. In the oscillation spectrum, all Bohr frequencies $\tilde{E}_n - \tilde{E}_{n'}$ occur, with a nonzero average (dashed line) described by Eq. (10.5).

with an unoccupied c -electron level state $|0\rangle$, a doubly occupied d -electron level state $|\uparrow\downarrow\rangle$ and the spin-up state $|\uparrow\rangle$ of the impurity spin. Turning on the interaction at time $t = 0$ will induce spin flip processes, and the spin expectation value $\langle S^z \rangle$ will start to deviate from its initial value $\langle S^z(t=0) \rangle = 1/2$. We will analyze this deviation by calculating the time-dependence of the observable

$$\hat{O} = S^z - \frac{1}{2} \quad (10.3)$$

in the following. Particle number conservation and the $SU(2)$ -symmetric interaction will conserve particle number $N = 2$ and total spin $S = 1/2$ of the initial state $|\psi_0\rangle$ during time evolution, such that the full Hilbert space with 32 dimensions reduces to a five-dimensional subspace (denoted by $\mathcal{H}_{2, \frac{1}{2}}$ in the following) that contains all symmetry-allowed quantum states accessible for $|\psi(t)\rangle$. For a numerical calculation, it is convenient to expand the observable $\langle \psi_0 | \hat{O}(t) | \psi_0 \rangle$ in the set of eigenstates $|\tilde{\psi}_n\rangle$ of H (with eigenenergies \tilde{E}_n) lying in the subspace $\mathcal{H}_{2, \frac{1}{2}}$,

$$\begin{aligned} O(t) &= \langle \psi_0 | e^{iHt} \hat{O} e^{-iHt} | \psi_0 \rangle \\ &= \sum_{n, n'} u_n^* u_{n'} e^{-i(\tilde{E}_{n'} - \tilde{E}_n)t} \langle \tilde{\psi}_n | \hat{O} | \tilde{\psi}_{n'} \rangle. \end{aligned} \quad (10.4)$$

Here, we have used the decomposition $|\psi_0\rangle = \sum_n u_n |\tilde{\psi}_n\rangle$. An explicit construction of the coefficients u_n and eigenstates $|\tilde{\psi}_n\rangle$ requires a diagonalization of a suitable representation of the Hamiltonian matrix, and we relegated further details to appendix A.1. The eigenenergies \tilde{E}_n and coefficients u_n in Eq. (10.4) are easily obtained from a numerical diagonalization of the Hamiltonian matrix, for which we used the LAPACK routine `zgeev`, implemented with the commonly used language “C”. Fig. 10.1 shows the observable $O(t)$ for a particular choice of parameters, with oscillations around a nonzero average being visible.

In absence of a thermodynamic limit, the finite set of Bohr frequencies occurring in the expansion (10.4) will prohibit the existence of the limit $O(t \rightarrow \infty)$. However, the oscillations

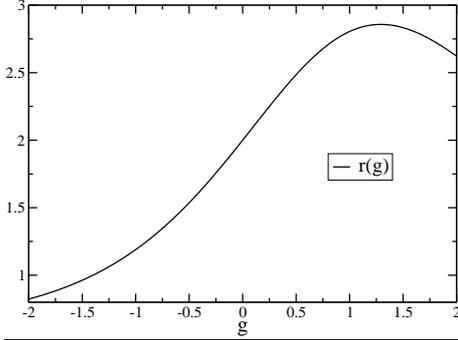


Figure 10.2: We depict the ratio $r(g) = \frac{\overline{\langle \psi_0 | S_z(t) - 1/2 | \psi_0 \rangle}}{\langle S_z - 1/2 \rangle_{eq}}$ as a function of the coupling strength g . In the weak-coupling limit one finds the universal ratio $r(0) = 2$, see text.

can be formally eliminated by averaging

$$\begin{aligned} \overline{O(t)} &= \lim_{T \rightarrow \infty} \frac{\int_0^T \langle \psi_0 | e^{iHt} \hat{O} e^{-iHt} | \psi_0 \rangle}{T} \\ &= \sum_n |u_n|^2 \langle \tilde{\psi}_n | \hat{O} | \tilde{\psi}_n \rangle \end{aligned} \quad (10.5)$$

in order to obtain the time-averaged expectation value $\overline{O(t)}$. It is interesting to compare this average with the expectation value in the ground state $|\tilde{\psi}_{eq}\rangle$ of the interacting Hamiltonian (10.1):

$$O_{eq} \stackrel{\text{def}}{=} \langle \tilde{\psi}_{eq} | \hat{O} | \tilde{\psi}_{eq} \rangle. \quad (10.6)$$

As depicted in Fig. 10.2, the ratio $\overline{O(t)}/O_{eq}$ as a function of coupling strength differs in general from one. A salient observation is the ratio of two reached in the weak-coupling limit $g \rightarrow 0$. This weak-coupling result for our particular problem can be generalized to a large class of weakly interacting discrete systems and to more general observables that fulfill the conditions of a theorem proven by Moeckel and Kehrein (2009):

consider a discrete quantum system described by $H = H_0 + gH_{int}$, with a weak perturbation gH_{int} for which non-degenerate perturbation theory is applicable. Let $|0\rangle$ be the ground state of H_0 and $|\tilde{0}\rangle$ be the ground state of H . Moreover, we assume a quantum mechanical observable \hat{O} which does not depend explicitly on time and obeys the following relations:

$$\begin{aligned} \hat{O} | 0 \rangle &= 0 \\ [\hat{O}, H_0] &= 0. \end{aligned} \quad (10.7)$$

Then, the long-time limit of the time-averaged expectation value of the time-evolved observable in the initial state equals two times the equilibrium expectation value of the observable in the interacting ground state,

$$r(g) \stackrel{\text{def}}{=} \frac{\overline{\langle 0 | e^{iHt} \hat{O} e^{-iHt} | 0 \rangle}}{\langle \tilde{0} | \hat{O} | \tilde{0} \rangle} = 2 + \mathcal{O}(g). \quad (10.8)$$

It is easy to show that these conditions are fulfilled in our particular toy model if we identify

$$\begin{aligned} H_0 &= \sum_{\alpha} \left(c_{\alpha}^{\dagger} c_{\alpha} - d_{\alpha}^{\dagger} d_{\alpha} \right) - B S^z \\ H_{int} &= \frac{1}{2} \vec{S} \cdot \sum_{\alpha, \beta} (c_{\alpha}^{\dagger} + d_{\alpha}^{\dagger}) \vec{\sigma}_{\alpha\beta} (c_{\beta} + d_{\beta}) . \end{aligned}$$

An explicit proof of this theorem formulated for our toy model is given in appendix A. One of the main results of this chapter shall be that this universal ratio of two between the time-averaged expectation value in the time-evolved initial state and the equilibrium ground state also holds in the weak-coupling limit of the ferromagnetic Kondo model.

10.2 Kondo model and flow equation transformation

In this section, we shall study the continuum version of the toy model discussed above, leading to the Kondo model described in Eq. (8.1). An extension of the non-equilibrium problem to this continuum model requires some more sophisticated approach than numerical diagonalization of a finite size system. We will apply the flow equation approach to diagonalize this model approximately before implementing the approach outlined in section 8.2. to calculate the magnetization $\langle S^z(t) \rangle$ for the non-equilibrium preparation discussed in the introductory chapter 8. The flow equation approach to the Kondo model has lead to several previous results (Kehrein, 2005, Lobaskin and Kehrein, 2005, Fritsch and Kehrein, 2009), and a derivation of the flow equations follows essentially the lines formulated in the book of Kehrein (2006). However, these works concentrated on the case of antiferromagnetic couplings, and we will comment on several aspects that make the case of ferromagnetic couplings different.

Flow equations for the Hamiltonian

The flowing Kondo Hamiltonian can be formally split up into the flowing interaction term $H_{int}(B)$ and the invariant non-interacting conduction electrons¹ $H_0 = \sum_{\mathbf{k}\sigma} \varepsilon_{\mathbf{k}} c_{\mathbf{k}\sigma}^{\dagger} c_{\mathbf{k}\sigma}$,

$$H(B) = H_0 + H_{int}(B) . \quad (10.9)$$

Within our calculation, the flowing interaction $H_{int}(B)$ will retain the form of a Kondo exchange interaction with the spin-1/2 degree of freedom \vec{S} , with the flow encoded in a change of coupling constants:

$$\begin{aligned} H_{int}(B) &= \sum_{\mathbf{k}'\mathbf{k}} J_{\mathbf{k}'\mathbf{k}}^{\parallel}(B) S^z : s_{\mathbf{k}'\mathbf{k}}^z : \\ &+ \sum_{\mathbf{k}'\mathbf{k}} J_{\mathbf{k}'\mathbf{k}}^{\perp}(B) (S^+ : s_{\mathbf{k}'\mathbf{k}}^- : + S^- : s_{\mathbf{k}'\mathbf{k}}^+ :) . \end{aligned} \quad (10.10)$$

¹Strictly spoken, the energy levels $\varepsilon_{\mathbf{k}}$ are renormalized by a contribution proportional to the inverse number of conduction electron states and are therefore unchanged in the thermodynamic limit.

Here, the electron spin density is normal ordered with respect to the Fermi sea in equilibrium. In several previous applications of the flow equation approach to the Kondo problem, the canonical generator obtained from $[H_0, H_{\text{int}}(B)]$ has been useful, given explicitly by

$$\begin{aligned}\eta(B) &= [H_0, H_{\text{int}}(B)] \\ &= \sum_{\mathbf{k}'\mathbf{k}} \left(\eta_{\mathbf{k}'\mathbf{k}}^{\parallel}(B) : S^z s_{\mathbf{k}'\mathbf{k}}^z : \right. \\ &\quad \left. + \eta_{\mathbf{k}'\mathbf{k}}^{\perp}(S^+ : s_{\mathbf{k}'\mathbf{k}}^- : + S^- : s_{\mathbf{k}'\mathbf{k}}^+ :) \right),\end{aligned}\quad (10.11)$$

with

$$\begin{aligned}\eta_{\mathbf{k}'\mathbf{k}}^{\parallel}(B) &\stackrel{\text{def}}{=} (\varepsilon_{\mathbf{k}'} - \varepsilon_{\mathbf{k}}) J_{\mathbf{k}'\mathbf{k}}^{\parallel}(B) \\ \eta_{\mathbf{k}'\mathbf{k}}^{\perp}(B) &\stackrel{\text{def}}{=} (\varepsilon_{\mathbf{k}'} - \varepsilon_{\mathbf{k}}) J_{\mathbf{k}'\mathbf{k}}^{\perp}(B).\end{aligned}\quad (10.12)$$

We shall use this generator in the following. By comparing coefficients in the differential equation $\frac{dH}{dB} = [\eta(B), H(B)]_-$, the system of differential equations for the flowing coupling constants is immediately obtained as

$$\begin{aligned}\frac{dJ_{\mathbf{k}'\mathbf{k}}^{\parallel}}{dB} &= -(\varepsilon_{\mathbf{k}'} - \varepsilon_{\mathbf{k}})^2 J_{\mathbf{k}'\mathbf{k}}^{\parallel}(B) \\ &\quad + \sum_{\mathbf{q}} (2\varepsilon_{\mathbf{q}} - \varepsilon_{\mathbf{k}'} - \varepsilon_{\mathbf{k}}) J_{\mathbf{k}'\mathbf{q}}^{\perp}(B) J_{\mathbf{q}\mathbf{k}}^{\perp}(B) \\ &\quad \times \left(\frac{1}{2} - n(\mathbf{q}) \right) + \mathcal{O}(J^3) \\ \frac{dJ_{\mathbf{k}'\mathbf{k}}^{\perp}}{dB} &= -(\varepsilon_{\mathbf{k}'} - \varepsilon_{\mathbf{k}})^2 J_{\mathbf{k}'\mathbf{k}}^{\perp}(B) \\ &\quad + \sum_{\mathbf{q}} (2\varepsilon_{\mathbf{q}} - \varepsilon_{\mathbf{k}'} - \varepsilon_{\mathbf{k}}) \\ &\quad \times \frac{1}{2} (J_{\mathbf{k}'\mathbf{q}}^{\parallel}(B) J_{\mathbf{q}\mathbf{k}}^{\perp}(B) + J_{\mathbf{k}'(B)\mathbf{q}}^{\perp}(B) J_{\mathbf{q}\mathbf{k}}^{\parallel}(B)) \left(\frac{1}{2} - n(\mathbf{q}) \right) \\ &\quad + \mathcal{O}(J^3),\end{aligned}\quad (10.13)$$

where we introduced the convention to label the couplings J^{\perp} and J^{\parallel} collectively by J in truncated terms characterized by the Landau symbol \mathcal{O} . Analytical solutions to this system of coupled differential equations are only possible in certain limits. Of particular importance are the couplings that connect states close to the Fermi surface (low-energy couplings). It is possible to approximately parametrize the flow of these couplings by the *infrared parameterization* (Kehrein, 2006)

$$J_{\mathbf{k}\mathbf{k}'}^{\perp, \parallel}(B) \stackrel{\text{def}}{=} \frac{J_{IR}^{\perp, \parallel}(B)}{N} e^{-B(\varepsilon_{\mathbf{k}} - \varepsilon_{\mathbf{k}'})^2}.\quad (10.14)$$

This approximation becomes asymptotically exact for energies $|\varepsilon_{\mathbf{k}}| \ll D, |\varepsilon_{\mathbf{k}'}| \ll D$, and it is possible to obtain the flow of the couplings at the Fermi surface in closed form by setting

$\epsilon_{\mathbf{k}} = \epsilon_{\mathbf{k}'} = 0$ for the flowing couplings $J_{\mathbf{k}\mathbf{k}'}^{\perp,\parallel}(B)$. This yields the flow equations

$$\begin{aligned}\frac{dJ^{\parallel}}{dB} &= -2J_{\perp}^2(B)\frac{1}{N}\sum_{\mathbf{q}}\epsilon_{\mathbf{q}}e^{-2B\epsilon_{\mathbf{q}}^2}\left[\frac{1}{2}-n(\mathbf{q})\right] \\ \frac{dJ^{\perp}}{dB} &= -2J_{\perp}(B)J_{\parallel}(B)\frac{1}{N}\sum_{\mathbf{q}}\epsilon_{\mathbf{q}}e^{-2B\epsilon_{\mathbf{q}}^2}\left[\frac{1}{2}-n(\mathbf{q})\right].\end{aligned}\quad (10.15)$$

At zero temperature, the momentum sum can be evaluated exactly by using the constant density of states ρ_F defined above

$$\begin{aligned}\frac{dj^{\parallel}}{dB} &= \frac{j_{\perp}^2}{2B}[1-e^{-2BD^2}] \\ \frac{dj^{\perp}}{dB} &= \frac{j_{\parallel}j_{\perp}}{2B}[1-e^{-2DB^2}].\end{aligned}\quad (10.16)$$

For $B \lesssim D^{-2}$, the change of the flowing coupling constants is of $\mathcal{O}(J^2)$ and it is justified to adjust the initial condition to $B = D^{-2}$ such that $J^{\parallel}(B = D^{-2}) = J^{\parallel}$ and $J^{\perp}(B = D^{-2}) = J^{\perp}$, with corrections that are only of $\mathcal{O}(J^2)$. Relating furthermore B in Eq. (10.16) with the flowing band cutoff Λ from a poor man's scaling approach by employing the relation $\Lambda = B^{-2}$ reproduces the well-known poor man's scaling equations (8.3).

We point out that a more sophisticated approximation to Eq. (10.13) can also parameterize the energy dependence of the couplings $J_{\mathbf{k},\mathbf{k}'}^{\perp}(B)$ and $J_{\mathbf{k},\mathbf{k}'}^{\parallel}(B)$ ($J_{IR}(B) \rightarrow J_{\mathbf{k}}(B)$ with $\epsilon_{\mathbf{k}}$ being the energy scale of the couplings $J_{\mathbf{k}}(B)$). A discussion of this more sophisticated approach is given in appendix A, and it is shown how it becomes asymptotically equivalent to the infrared parameterization in the limit $|\epsilon_{\mathbf{k}}| \ll D, |\epsilon_{\mathbf{k}'}| \ll D$.

Flow equations for the spin operator

Since the impurity spin operator \vec{S} and the diagonal Hamiltonian \tilde{H} are represented in different bases, we need to transform the impurity spin into the basis of the diagonal Hamiltonian in order to make use of this non-interacting form of the Hamiltonian for the procedure outlined in Fig. 8.4. This step is achieved by solving the differential equation

$$\frac{dS^a(B)}{dB} = [\eta(B), S^a(B)], \quad (10.17)$$

with $a = (x, y, z)$, the initial conditions $S^a(B = 0) = S^a$ and the generator $\eta(B)$ given by Eq. (10.11). Since the generator $\eta(B)$ is linear in the flowing coupling constants $J_{\mathbf{k}'\mathbf{k}}^{\perp}(B)$ and $J_{\mathbf{k}'\mathbf{k}}^{\parallel}(B)$, the flowing operators $S^a(B)$ can be expanded in powers of coupling strength. In the flowing Hamiltonian (10.13), we neglected terms of order $\mathcal{O}(J^2)$ that are generated during the flow. To this order in J , it is consistent to include newly generated terms in the flowing spin operator only to linear order in J , and it is therefore sufficient to consider the commutator $[\eta(B), S^a]$ in order to formulate the ansatz

$$S^a(B) = h(B)S^a + \sum_{\mathbf{k}',\mathbf{k}}\gamma_{\mathbf{k}'\mathbf{k}}(B) : (\vec{S} \times \vec{s}_{\mathbf{k}'\mathbf{k}})^a : , \quad (10.18)$$

for a solution to the flow equation (10.17). As an aside, we note that the operator $S^a(B, t) \stackrel{\text{def}}{=} e^{iH(B)t} S^z(B) e^{-iH(B)t}$ is given by the same formal ansatz (10.18) and coefficients $h(B, t)$ and $\gamma_{\mathbf{k}'\mathbf{k}}(B, t)$ that obtained a dependence on time, as will become clear in the next section. In order to clarify our notation for future purposes, we introduce here some appropriate notational conventions

$$h(B, t) =: \left\{ \begin{array}{l} h(t) \\ h(B) \\ \tilde{h}(t) \\ \tilde{h} \end{array} \right\} \text{ if } \left\{ \begin{array}{l} B = 0 \\ t = 0 \\ B \rightarrow \infty \\ B \rightarrow \infty, t = 0 \end{array} \right\}.$$

By comparing coefficients in the ansatz, the flowing operator is given by

$$\begin{aligned} \frac{dh}{dB} &= \sum_{\mathbf{k}'\mathbf{k}} (\varepsilon_{\mathbf{k}'} - \varepsilon_{\mathbf{k}}) J_{\mathbf{k}'\mathbf{k}}^\perp(B) \gamma_{\mathbf{k}\mathbf{k}'}(B) n(\mathbf{k}') (1 - n(\mathbf{k})) \\ \frac{d\gamma_{\mathbf{k}'\mathbf{k}}}{dB} &= h(B) (\varepsilon_{\mathbf{k}'} - \varepsilon_{\mathbf{k}}) J_{\mathbf{k}'\mathbf{k}}^\perp(B) \\ &\quad - \frac{1}{4} \sum_{\mathbf{u}} \left((\varepsilon_{\mathbf{k}'} - \varepsilon_{\mathbf{u}}) J_{\mathbf{k}'\mathbf{u}}^\parallel(B) \gamma_{\mathbf{u}\mathbf{k}}(B) + (\varepsilon_{\mathbf{k}} - \varepsilon_{\mathbf{u}}) J_{\mathbf{u}\mathbf{k}}^\parallel(B) \gamma_{\mathbf{k}'\mathbf{u}}(B) \right) \\ &\quad \times (1 - 2n(\mathbf{u})). \end{aligned} \tag{10.19}$$

A check of approximations is simplified by considering the sum rule

$$\begin{aligned} \langle S^z(B)^2 \rangle &= \frac{1}{4} (h^2(B) + \sum_{\mathbf{k}\mathbf{k}'} \gamma_{\mathbf{k}\mathbf{k}'}^2(B) n(\mathbf{k}') (1 - n(\mathbf{k}))) \\ &= \frac{1}{4}. \end{aligned} \tag{10.20}$$

This sum rule is easily verified by differentiating it with respect to the parameter B and inserting the flow equations (10.19). Since these neglect corrections of $\mathcal{O}(J^2)$ to (10.17), the sum rule is accurate to $\mathcal{O}(J^2)$.

10.3 Time-dependent magnetization

In this section we turn to a discussion of the time evolution of the observable $\langle S^z(t) \rangle$, evaluated in the initial state (10.21). Before turning to calculational details, we illustrate some fundamental aspects of the processes that lead to the dynamics of $\langle S^z(t) \rangle$. Part of the physics can be already understood from the equilibrium expectation value $\langle S^z \rangle$ for the coupled system in presence of an infinitesimal magnetic field, described by Eq. (8.6). In this case, weak spin-flip scattering mixes the fully polarized spin up state with the spin-down state of the impurity, such that the impurity magnetization is effectively reduced to $\langle S^z \rangle = \frac{1}{2}(1 + J/2)$. It is up to now unclear if the magnetization will be the same if a fully polarized spin is coupled instantaneously to a bath of conduction electrons, i.e. without allowing the full complex to equilibrate during coupling the systems. After turning

on the interaction, the impurity will react similarly to the ground state dynamics by dynamically flipping its orientation through the transverse coupling to the conduction electrons. However, it is not clear how the magnetization behaves asymptotically in the limit of long times.

In order to describe this behavior quantitatively, we assume in the following that the complex of impurity and conduction electrons is prepared in the product initial state

$$|\psi\rangle = |\uparrow\rangle \otimes |FS\rangle, \quad (10.21)$$

where $|FS\rangle$ is the non-interacting Fermi sea in equilibrium. We assume furthermore that impurity and conduction electrons become coupled instantaneously at time $t = 0$. Further aspects of this initial state were already motivated in chapter 8. Some insights into the initial process of magnetization reduction can be gained by expanding Heisenberg's equation of motion for the operator S^z , which we discuss along the lines given by Anders and Schiller (2006). This perturbation expansion is most conveniently performed in the interaction picture $S_I^z(t) = e^{-iH_0 t} S^z(t) e^{iH_0 t}$, with the non-interacting part $H_0 = \sum_{\mathbf{k}\sigma} \varepsilon_{\mathbf{k}} c_{\mathbf{k}\sigma}^\dagger c_{\mathbf{k}\sigma}$ and the interacting part H_{int} is given in the interaction picture by $H_{\text{int}}^I(t) = e^{-iH_0 t} H_{\text{int}} e^{iH_0 t}$. Then, the equation of motion for the operator $S_I^z(t)$ is given by

$$\frac{\partial S_I^z(t)}{\partial t} = i[H_{\text{int}}^I(t), S_I^z(t)], \quad (10.22)$$

which is integrated to

$$\begin{aligned} S_I^z(t) &= S^z + i \int_0^t d\tau_1 [H_{\text{int}}^I(\tau_1), S^z(0)] \\ &+ i^2 \int_0^t d\tau_1 \int_0^{\tau_1} d\tau_2 [H_{\text{int}}^I(\tau_1), [H_{\text{int}}^I(\tau_2), S^z(0)]] + \mathcal{O}(J^3), \end{aligned} \quad (10.23)$$

being perturbatively correct up to neglected operators of $\mathcal{O}(J^3)$. To evaluate $\langle S^z(t) \rangle$, all expectation values need to be evaluated with respect to Eq. (10.21), since $\langle S^z(t) \rangle = \langle S_I^z(t) \rangle$ in this case, with the result

$$\begin{aligned} \langle S^z(t) \rangle &= \langle S^z \rangle + \langle S^z \rangle (iJ^\perp)^2 \int_{-\infty}^{\infty} d\varepsilon \int_{-\infty}^{\infty} d\varepsilon' \rho(\varepsilon) \rho(\varepsilon') \\ &\times f(\varepsilon') (1 - f(\varepsilon)) \left[\frac{1 - \cos((\varepsilon - \varepsilon')t)}{(\varepsilon - \varepsilon')^2} \right] \\ &+ \mathcal{O}(J^3), \end{aligned} \quad (10.24)$$

using the Fermi function $f(\varepsilon)$ and evaluating $\langle S^z \rangle$ with respect to the initial state in Eq. (10.21). In our case, we use a flat band with density of states $\rho(\varepsilon) \equiv \rho_F = 1/(2D)$. This perturbative result contains no renormalization of the bare couplings J^\perp by J^z , since the coupling J^z enters the perturbative expansion only in $\mathcal{O}(J^3)$ or higher orders. These contributions will contribute to the observable $\langle S^z(t) \rangle$ once the low energy couplings contribute to the relaxation processes, which is expected to occur for sufficiently long times.

At $T = 0$, Eq. (10.24) can be rewritten as an integral over the variable $x = \epsilon - \epsilon'$,

$$\langle S^z(t) \rangle = \langle S^z \rangle - \langle S^z \rangle \int_0^{2D} \frac{k(x)}{x^2} J^2 (1 - \cos(xt)) dx, \quad (10.25)$$

where we introduced the function

$$k(x) = \begin{cases} x, & x \leq D \\ 2D - x, & x > D. \end{cases} \quad (10.26)$$

The integral (10.25) can be reexpressed as a series expansion, with the formal result

$$\langle S^z(t) \rangle = \langle S^z \rangle - \langle S^z \rangle (2J^\perp)^2 [G(2Dt) - 2G(Dt)] \quad (10.27)$$

and the function $G(x)$ given by the series expansion

$$G(x) = \sum_{l=1}^{\infty} \frac{(-1)^{l+1}}{(2l)! 2l(2l-1)} x^{2l}. \quad (10.28)$$

A comparison to a result for $\langle S^z(t) \rangle$ derived by the flow equation approach (which we derive in detail in the following sections) in Fig. 10.3 shows that the perturbative result (10.24) predicts a too large reduction of the magnetization $\langle S^z(t=0) \rangle$ by neglecting the renormalization of J^\perp contained in higher order terms of time-dependent perturbation theory. Once more, this example demonstrates the failure of a direct expansion of the Heisenberg equation of motion. However, it is our purpose to transform the spin operator first into the basis corresponding to the diagonal form of the Hamiltonian and then to expand the Heisenberg equation of motion $\tilde{S}^z(t) = e^{i\tilde{H}t} \tilde{S}^z e^{-i\tilde{H}t}$ in this basis, as illustrated in Fig. 8.4. It is straightforward to obtain the time-evolved form of the spin operators (10.18), since the time evolution is performed by multiplying the couplings $\gamma_{\mathbf{k}\mathbf{k}'}$ with the phase factors $e^{i(\epsilon_{\mathbf{k}} - \epsilon_{\mathbf{k}'})t}$,

$$\begin{aligned} \tilde{S}_z(t) &= \tilde{h} S^z \\ &+ \sum_{\mathbf{k}', \mathbf{k}} \tilde{\gamma}_{\mathbf{k}'\mathbf{k}}(t) : \left((S^+ s_{\mathbf{k}'\mathbf{k}}^- + S^- s_{\mathbf{k}\mathbf{k}'}^+) \right) : + \mathcal{O}(J^2) \\ \tilde{\gamma}_{\mathbf{k}'\mathbf{k}}(t) &= \tilde{\gamma}_{\mathbf{k}'\mathbf{k}} e^{it(\epsilon_{\mathbf{k}'} - \epsilon_{\mathbf{k}})}. \end{aligned} \quad (10.29)$$

Finally, this operator is transformed back into its initial basis representation, thereby providing an effective non-perturbative solution of Heisenberg's equation of motion $S^z(t) = e^{iHt} S^z e^{-iHt}$. Using the initial condition posed by the operator $\tilde{S}^z(t)$ and integrating the flow equations (10.19), the transformed operator will have the form

$$\begin{aligned} S^z(t) &= h(t) S^z + \sum_{\mathbf{k}', \mathbf{k}} \gamma_{\mathbf{k}'\mathbf{k}}(t) : \left((S^+ s_{\mathbf{k}'\mathbf{k}}^- + S^- s_{\mathbf{k}\mathbf{k}'}^+) \right) : \\ &+ \mathcal{O}(J^2). \end{aligned} \quad (10.30)$$

It remains to obtain the coefficients $h(t)$ and $\gamma_{\mathbf{k}'\mathbf{k}}(t)$ in (10.30). Those can be either obtained from a numerical solution of the flow equations (10.19), or by certain analytical approximations, which are the topic of the following section.

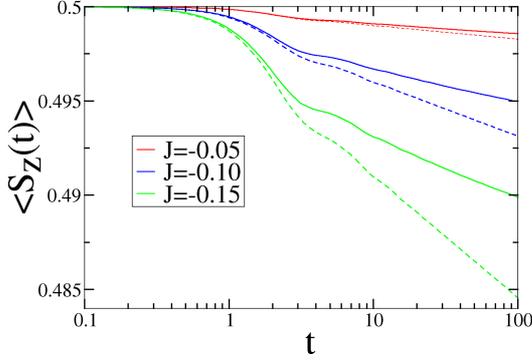


Figure 10.3: We show $\langle S^z(t) \rangle$ for isotropic coupling J and short times as compared to Fig. 10.4. For very short times $t \ll D^{-1}$, the perturbative result from Eq. (10.27) (dashed line) is asymptotically coinciding with the numerical solution of the flow equations (10.19) (full lines). The renormalization of J^\perp by J^\parallel sets in at energy scales $E < D$, leading to a reduction of spin-flip scattering. Beyond the short-time regime $t \ll D^{-1}$, the magnetization relaxes

therefore slower than predicted by the perturbative result.

10.4 Analytical results for the magnetization

An analytical solution of the full flow equations (10.13) is complicated by the large number of coupling constants. Only *two* flowing coupling constants remain if the infrared parameterization (10.14) of the flowing exchange couplings $J_{\mathbf{k}\mathbf{k}'}^{\perp,\parallel}(B)$ is utilized for an approximative solution, and an analytical solution of the flow equations (10.19) for the spin operator is tremendously simplified at the same time. We shall argue that this approximation will allow to analytically obtain the correct long-time asymptotics of the magnetization $\langle S^z(t) \rangle$, based on two arguments:

- (i) the low energy couplings $\gamma_{\mathbf{k}\mathbf{k}'}$ (with $|\epsilon_{\mathbf{k}}| \ll D$ and $|\epsilon_{\mathbf{k}'}| \ll D$) will dominate the long time behavior of the magnetization, since the phase factor $e^{it(\epsilon_{\mathbf{k}'} - \epsilon_{\mathbf{k}})}$ in Eq. (10.29) will average out all contributions with Bohr frequencies $(\epsilon_{\mathbf{k}'} - \epsilon_{\mathbf{k}}) \gtrsim t^{-1}$ in Eq. (10.41).
- (ii) obviously, the flow of the couplings $\gamma_{\mathbf{k}\mathbf{k}'}(B)$ at low energies $|\epsilon_{\mathbf{k}}| \ll D$ and $|\epsilon_{\mathbf{k}'}| \ll D$ is determined by the low-energy couplings $J_{\mathbf{k}'\mathbf{k}}^\perp(B)$, if the flow equation is approximated by

$$\frac{d\gamma_{\mathbf{k}'\mathbf{k}}}{dB} = h(B)(\epsilon_{\mathbf{k}'} - \epsilon_{\mathbf{k}})J_{\mathbf{k}'\mathbf{k}}^\perp(B) + \mathcal{O}((\epsilon_{\mathbf{k}'} - \epsilon_{\mathbf{k}})J^2), \quad (10.31)$$

since we can furthermore approximate $h(B) \equiv 1 + \mathcal{O}(J)$ and neglect the flow of $h(B)$ up to $\mathcal{O}(J^2)$. A formal justification of the approximation (10.31) is given in appendix A. It will therefore be useful to obtain the exact low-energy behavior of the couplings $\gamma_{\mathbf{k}'\mathbf{k}}$, which behaves qualitatively different for isotropic vs. anisotropic couplings.

As it will turn out (see Eq. (10.41)) that this qualitatively different behavior translates into different behavior of the magnetization dynamics, we discuss these cases separately in the following.

Isotropic regime

In order to proceed with an approximative solution of the flow equations (10.19), we recall that the flow of the exchange coupling $J_{\mathbf{k}\mathbf{k}'}$ at the Fermi surface ($\epsilon_{\mathbf{k}} = \epsilon_{\mathbf{k}'} = 0$) is described

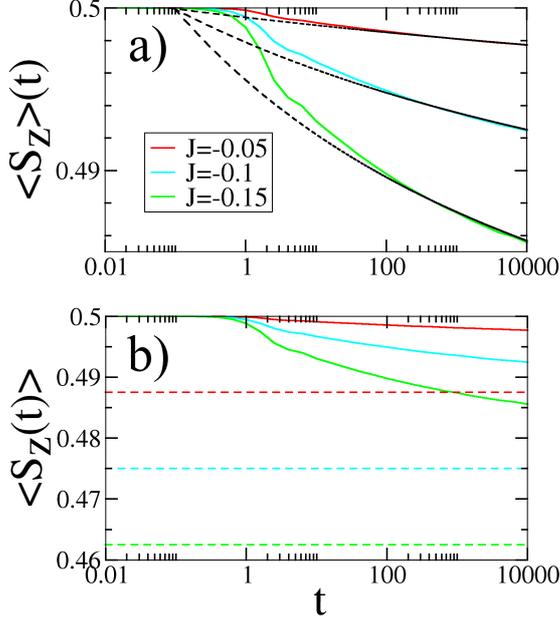


Figure 10.4: We show $\langle S^z(t) \rangle$ for different isotropic couplings j . In panel a) the full numerical solution of the flow equations (full lines in both panels) is compared to a fit to the asymptotic analytical behavior of Eq. (10.43) (dashed lines, fit parameters given in table 10.1). Beyond the perturbative short-time regime, described by unrenormalized spin-flip scattering according to Eq. (10.27), the logarithmic renormalization of the spin-flip scattering coupling J^\perp sets in. This leads to a logarithmically slow relaxation of the magnetization, and the asymptotic value $\langle S^z(t \rightarrow \infty) \rangle = 0.5 + \frac{j}{2} + \mathcal{O}(j^2)$ (dashed lines in panel b)) is reached extremely slowly.

by the scaling equation (see Eq. (8.5))

$$J(\Lambda) = \frac{J}{1 + j \ln\left(\frac{\Lambda}{D}\right)}. \quad (10.32)$$

By posing the initial condition $J(B = D^{-2}) = J_0$ and employing $\Lambda = B^{-1/2}$, the corresponding flow of the coupling J_{IR} defined in Eq. (10.14) is $J_{IR}(B) = J/(1 - \frac{1}{2}j \ln(BD^2))$. This behavior can now be employed for approximative solutions of the flow equations (10.19) for the spin operator S^z .

1. Flow of the spin operator

Our discussion of the flowing couplings of the spin operator begins by integrating the differential equation (10.31) of the coupling $\gamma_{\mathbf{k}\mathbf{k}'}(B)$, since it will turn out that this equation can be integrated independently of the flowing coupling $h(B)$. Since the equilibrium impurity magnetization (8.6) in the limit of infinitesimal magnetic field is $M = (1/2)g_i\mu_B\tilde{h}$ (Abrikosov and Migdal, 1970), the result for \tilde{h} will be $\tilde{h} = 1 + j$, with possible corrections of $\mathcal{O}(j^2)$. Therefore, we can set $h(B) \equiv 1$ in the flow equation (10.31) for $\gamma_{\mathbf{k}\mathbf{k}'}(B)$, with corrections that enter only to $\mathcal{O}(J^2)$ and will be neglected, leading to the approximated flow equation

$$\frac{d\gamma_{\mathbf{k}'\mathbf{k}}}{dB} = (\varepsilon_{\mathbf{k}'} - \varepsilon_{\mathbf{k}})J_{\mathbf{k}'\mathbf{k}}^\perp(B) + \mathcal{O}(J^2). \quad (10.33)$$

Considering now couplings which connect energies close to the Fermi surface ($|\varepsilon_{\mathbf{k}}| \ll$

Table 10.1: For large times, we fitted the full numerical solutions of the flow equations against the function $0.5(1 + aJ + 1/(\ln t + 1/(bJ)))$, as depicted in Fig. 10.4a. For couplings $-j < 0.1$, quantitative agreement with the analytical result $\langle S^z(t) \rangle = 0.5(1/(\ln t - 1/j) + 1/2 + j/2 + \mathcal{O}(j^2))$ is very good.

$j = j^\perp = j^\parallel$	-0.05	-0.1	-0.15
a	0.441	0.442	0.441
b	0.418	0.400	0.382

$D, |\epsilon_{\mathbf{k}'}| \ll D$), we employ the parameterization (10.14) in the differential equation (10.33)

$$\begin{aligned} \gamma_{\mathbf{k}\mathbf{k}'}(B) &= \int_0^B (\epsilon_{\mathbf{k}} - \epsilon_{\mathbf{k}'}) \frac{J_{IR}(B')}{N} e^{-B'(\epsilon_{\mathbf{k}} - \epsilon_{\mathbf{k}'})^2} dB' \\ &+ \mathcal{O}(J^2). \end{aligned} \quad (10.34)$$

This integral can be further simplified by noting that $J_{IR}(B)$ depends only logarithmically on the variable B . Up to corrections of $\mathcal{O}(J^2)$, it is therefore sufficient to evaluate $J_{IR}(B')$ at the scale $B = (\epsilon_{\mathbf{k}} - \epsilon_{\mathbf{k}'})^{-2}$, where the exponential decay of the integrand sets in, leading to the result

$$\begin{aligned} \gamma_{\mathbf{k}'\mathbf{k}}(B) &= \frac{J_{IR}(B = (\epsilon_{\mathbf{k}'} - \epsilon_{\mathbf{k}})^{-2})}{N(\epsilon_{\mathbf{k}'} - \epsilon_{\mathbf{k}})} (1 - e^{-B(\epsilon_{\mathbf{k}'} - \epsilon_{\mathbf{k}})^2}) \\ &+ \mathcal{O}(J^2) \\ \tilde{\gamma}_{\mathbf{k}'\mathbf{k}} &= \frac{J_{IR}(B = (\epsilon_{\mathbf{k}'} - \epsilon_{\mathbf{k}})^{-2})}{N(\epsilon_{\mathbf{k}'} - \epsilon_{\mathbf{k}})} + \mathcal{O}(J^2). \end{aligned} \quad (10.35)$$

Using the approximation (10.33) to the flowing couplings $\gamma_{\mathbf{k}'\mathbf{k}}(B)$ in the flow equations (10.19), the renormalized coupling \tilde{h} can be formally rewritten as

$$\begin{aligned} \tilde{h} - 1 &= -\frac{1}{2} \sum_{\mathbf{k}\mathbf{k}'} \int_0^\infty dB \frac{d}{dB} \gamma_{\mathbf{k}\mathbf{k}'}^2(B) n(\mathbf{k}') (1 - n(\mathbf{k})) \\ &= -\frac{1}{2} \sum_{\mathbf{k}\mathbf{k}'} \tilde{\gamma}_{\mathbf{k}\mathbf{k}'}^2 n(\mathbf{k}') (1 - n(\mathbf{k})). \end{aligned} \quad (10.36)$$

At zero temperature, this expression can be evaluated by inserting the low-energy approximation for the couplings $\tilde{\gamma}_{\mathbf{k},\mathbf{k}'}$ from Eq. (10.35) and rewriting the momentum summations as integrals over energy,

$$\tilde{h} = 1 - \frac{1}{2} \int_0^D \int_0^D d\epsilon d\epsilon' \frac{j^2}{1 + j \ln(\frac{\epsilon + \epsilon'}{D})^2} \frac{1}{[\epsilon + \epsilon']^2} + \mathcal{O}(j^2), \quad (10.37)$$

where we employed the explicit form $J_{IR}(B) = J/(1 - \frac{1}{2}j \ln(BD^2))$ for $J_{IR}(B)$. This integral is readily rewritten as an integral over the variable $x = \epsilon + \epsilon'$.

$$\tilde{h} - 1 = -\frac{1}{2} \int_0^{2D} dx \frac{k(x)}{x^2} \frac{j^2}{(1 + j \ln(\frac{x}{D}))^2} + \mathcal{O}(j^2), \quad (10.38)$$

where we made use of the function $k(x)$ defined in (10.26). We finally neglect the integration range \int_D^{2D} since it yields contributions of $\mathcal{O}(j^2)$ ($\int_0^{2D} dx = [\int_0^D dx \dots] + \mathcal{O}(j^2)$) and employ the indefinite integral $\int \frac{dx}{x[1+\ln(x)]^2} = -\frac{1}{1+\ln(x)} + C$, such that Eq. (10.38) reduces to

$$\tilde{h} = 1 + \frac{j}{2} + \mathcal{O}(j^2), \quad (10.39)$$

in agreement with the result (8.6) derived by Abrikosov and Migdal (1970).

2. Time-dependent magnetization

Since the magnetization $\langle S^z(t) \rangle$ follows from the coefficient $h(t)$, the flow equations (10.19) have to be integrated from $B \rightarrow \infty$ to $B = 0$ with the initial condition posed by Eq. (10.29). This in turn requires a solution to the flow equations (10.33) for the couplings $\gamma_{\mathbf{k}\mathbf{k}'}(B, t)$ using the initial condition from Eq. (10.29). Since the derivative of $\gamma_{\mathbf{k}\mathbf{k}'}(B, t)$ with respect to B is independent of time according to Eq. (10.35), we readily obtain

$$\begin{aligned} \gamma_{\mathbf{k}'\mathbf{k}}(B, t) &= \tilde{\gamma}_{\mathbf{k}'\mathbf{k}}(t) + \int_{\infty}^B (\varepsilon_{\mathbf{k}'} - \varepsilon_{\mathbf{k}}) J_{\mathbf{k}'\mathbf{k}}(B') dB' \\ &= \gamma_{\mathbf{k}'\mathbf{k}}(B) + \tilde{\gamma}_{\mathbf{k}'\mathbf{k}}(e^{it(\varepsilon_{\mathbf{k}'} - \varepsilon_{\mathbf{k}})} - 1) + \mathcal{O}(J^2). \end{aligned} \quad (10.40)$$

Employing this expression in the flow equation for the coupling $h(B)$, the formal result for the coupling $h(t)$ is

$$\begin{aligned} h(t) &= \tilde{h} + \sum_{\mathbf{k}\mathbf{k}'} \int_{\infty}^0 \frac{d\gamma_{\mathbf{k}'\mathbf{k}}}{dB} \tilde{\gamma}_{\mathbf{k}\mathbf{k}'}(e^{it(\varepsilon_{\mathbf{k}} - \varepsilon_{\mathbf{k}'})} - 1) dB \\ &\times n(\mathbf{k}')(1 - n(\mathbf{k})) \\ &+ \sum_{\mathbf{k}\mathbf{k}'} \int_{\infty}^0 \frac{d\gamma_{\mathbf{k}'\mathbf{k}}}{dB} \gamma_{\mathbf{k}\mathbf{k}'}(B) n(\mathbf{k}')(1 - n(\mathbf{k})) + \mathcal{O}(J^2) \\ &= \tilde{h} + \sum_{\mathbf{k}\mathbf{k}'} \tilde{\gamma}_{\mathbf{k}\mathbf{k}'}^2 (e^{it(\varepsilon_{\mathbf{k}} - \varepsilon_{\mathbf{k}'})} - \frac{1}{2}) \\ &\times n(\mathbf{k}')(1 - n(\mathbf{k})) + \mathcal{O}(J^2). \end{aligned} \quad (10.41)$$

This result is expected to be valid at all time scales, since approximations were only made in neglecting terms of $\mathcal{O}(J^2)$, and the perturbative expansion of the Heisenberg equation of motion in the canonically transformed basis is expected to remain controlled on all time scales, in analogy to canonical perturbation theory in classical mechanics (see chapter 9). Comparisons against an analytical short-time result and numerical results using the TD-NRG will justify these arguments later on. Finally, a different derivation of the same result Eq. (10.41) is given in appendix A by employing the sumrule (10.20), thereby further justifying all approximations.

In order to extract the long-time behavior of $\langle S^z(t) \rangle$ from Eq. (10.41), we plug in the

approximate low-energy couplings (10.35) and rewrite (10.41) as an integral over $x = \epsilon_{\mathbf{k}} - \epsilon_{\mathbf{k}'}$,

$$\langle S^z(t) \rangle = \frac{1}{2} + \frac{1}{2} \int_0^{2D} \frac{k(x)}{x^2} \frac{j^2}{(1 + j \ln(\frac{x}{D}))^2} (\cos(xt) - 1) dx , \quad (10.42)$$

where we used the same formal manipulations that lead to Eq. (10.38). The integral over $\cos(xt) \dots$ can be cut off at a scale of order the oscillation period of the cosine, such that $\int_0^\infty \cos(xt) dx \dots$ is replaced by $\int_0^{f(t)/t} dx \dots$ where $f(t)$ is some function with values of $\mathcal{O}(1)$. Once $\ln(t) \gg |\ln[f(t)]|$, this integral has the asymptotic behavior

$$\langle S^z(t) \rangle = 0.5 (1/(\ln(t) - 1/j) + 1/2 + j/2 + \mathcal{O}(j^2)) . \quad (10.43)$$

In turn, the asymptotic value of the magnetization is read off as

$$\langle S^z(t \rightarrow \infty) \rangle = 0.5(1 - j + \mathcal{O}(j^2)) . \quad (10.44)$$

Anisotropic regime

We turn to a discussion of the observable $\langle S^z(t) \rangle$ in the anisotropic parameter regime $J^\parallel \neq J^\perp$ by recalling some properties of the scaling equations (10.16). A stable fixed point of the scaling equations (8.3) exists not if $|J^\parallel| > |J^\perp|$, since J^\parallel will change sign during the flow and J^\perp eventually increases unboundedly. A stable fixed point exists if $|J^\parallel| < |J^\perp|$, with the couplings at the fixed point given by

$$\begin{aligned} \tilde{j}^\parallel &= -\sqrt{j^{\parallel 2} - j^{\perp 2}} \\ \tilde{j}^\perp &= 0 . \end{aligned} \quad (10.45)$$

Due to the finite value of the longitudinal coupling \tilde{j}^\parallel at the fixed point, a power-law decay

$$j^\perp(B) = \alpha B^{\tilde{j}^\parallel/2} \quad (10.46)$$

of the transverse coupling $j^\perp(B)$ is implied by the flow equations (10.16), where α is a non-universal number. We integrated the flow equations (10.16) numerically and obtained that $\alpha \simeq j^\perp$ as long as $|J^\parallel/J^\perp| \gtrsim 2$. This particular qualitative difference to the case of isotropic couplings will translate into qualitatively different dynamics of the magnetization. Our analysis of the magnetization curve $\langle S^z(t) \rangle$ will be completely analogous to the previous subsection, with the only modification being the modified flow of the transverse couplings $J_{\mathbf{k}\mathbf{k}'}^\perp(B)$.

1. Flow of the spin operator

We start by integrating the flow-equation (10.31) for $\gamma_{\mathbf{k}\mathbf{k}'}(B)$, for which we use again the infrared parameterization

$$J_{\mathbf{k}\mathbf{k}'}^\perp(B) = \frac{J^\perp(B)}{N} e^{-B(\epsilon_{\mathbf{k}} - \epsilon_{\mathbf{k}'})^2} . \quad (10.47)$$

Since the transverse coupling $J^\perp(B)$ decays faster upon increasing $|J^\parallel|$ above $|J^\perp|$, we can see from equation (10.35) that the couplings $\gamma_{\mathbf{k}\mathbf{k}'}$ will become smaller in magnitude upon increasing $|J^\parallel|$, hence formula (10.36) tells that \tilde{h} will be renormalized less than for isotropic couplings (where $J^\perp=J^\parallel$ and $\tilde{h} = 1 + \mathcal{O}(J)$). It is therefore furthermore possible to approximate $h(B) \equiv 1 + \mathcal{O}(J)$ in Eq. (10.31) and the flowing coupling is finally integrated as

$$\begin{aligned}\tilde{\gamma}_{\mathbf{k}\mathbf{k}'} &= \int_0^\infty (\varepsilon_{\mathbf{k}} - \varepsilon_{\mathbf{k}'}) e^{-B(\varepsilon_{\mathbf{k}} - \varepsilon_{\mathbf{k}'})^2} \frac{J^\perp(B)}{N} dB + \mathcal{O}(J^2) \\ &\simeq \frac{\alpha \Delta \varepsilon}{N \rho_F} \int_0^\infty e^{-B \Delta \varepsilon^2} B^{\frac{1}{2} \tilde{j}^\parallel} dB + \mathcal{O}(J^2) \\ &= \frac{\alpha \operatorname{sgn}(\Delta \varepsilon)}{N \rho_F |\Delta \varepsilon|^{1 + \tilde{j}^\parallel}} + \mathcal{O}(\alpha \tilde{j}^\parallel) + \mathcal{O}(J^2),\end{aligned}\quad (10.48)$$

where we defined $\Delta \varepsilon = \varepsilon_{\mathbf{k}} - \varepsilon_{\mathbf{k}'}$. In the second line of Eq. (10.48), we employed the asymptotic form (see Eq. (10.46)) $J^\perp(B) = (\alpha/\rho_F) B^{\frac{1}{2} \tilde{j}^\parallel}$ of the decay. The relative error made by this approximation can be made arbitrarily small by assuming a correspondingly small value for $|\Delta \varepsilon|$. Finally, in the third line we employed the series representation of the gamma function $\Gamma(1+x) = \int_0^\infty dt t^x \exp(-t) = \sum_{k=0}^\infty c_k x^k$ (Gradshteyn and Ryzhik, 2000).

Employing the final result for the couplings $\tilde{\gamma}_{\mathbf{k}\mathbf{k}'}$ in Eq. (10.36) and rewriting the resultant expression as an integral over the variable $x = \varepsilon_{\mathbf{k}} - \varepsilon_{\mathbf{k}'}$ allows to determine the renormalized coupling \tilde{h} as

$$\tilde{h} = 1 - \frac{1}{2} \int_0^{2D} dx \alpha^2 \frac{k(x)}{x^{2+2\tilde{j}^\parallel}} = 1 + \frac{\alpha^2}{4\tilde{j}^\parallel} + \mathcal{O}(J^2). \quad (10.49)$$

In conclusion, the equilibrium magnetization in presence of an infinitesimal magnetic field will be given by

$$\langle S^z \rangle = \frac{\tilde{h}}{2} = \frac{1}{2} + \frac{\alpha^2}{8\tilde{j}^\parallel} + \mathcal{O}(J^2). \quad (10.50)$$

2. Time-dependent magnetization

Using the low energy asymptotics of the couplings $\gamma_{\mathbf{k}\mathbf{k}'}$ in the formal expression (10.41), it is again possible to rewrite the magnetization $\langle S^z(t) \rangle$ as an integral over the variable $x = \varepsilon_{\mathbf{k}} - \varepsilon_{\mathbf{k}'}$,

$$\langle S^z(t) \rangle = \frac{1}{2} - \frac{1}{2} \int_0^{2D} k(x) \frac{\alpha^2}{x^{2+2\tilde{j}^\parallel}} (1 - \cos(xt)) dx. \quad (10.51)$$

Using the approximation $\alpha \approx j^\perp$ valid for $J^\perp \gtrsim -2J^\parallel$, this expression will asymptotically become equivalent to the short-time limit of Eq. (10.25). This can be seen by expanding $\cos(xt)$ to $\mathcal{O}((xt)^2)$ and approximating $D^{1+\tilde{j}^\parallel} = D + \mathcal{O}(\tilde{j}^\parallel)$. Based on the exact low energy asymptotics used to formulate Eq. (10.48), this expression is expected to become equivalent to Eq. (10.41) in the limit of asymptotically large times, which we can now extract analytically by replacing the integral $\int_0^\infty \cos(xt) dx \dots$ by $\int_0^{f(t)/t} dx \dots$ where $f(t)$ is an unknown function with values of $\mathcal{O}(1)$. The long-time tail is then easily obtained as

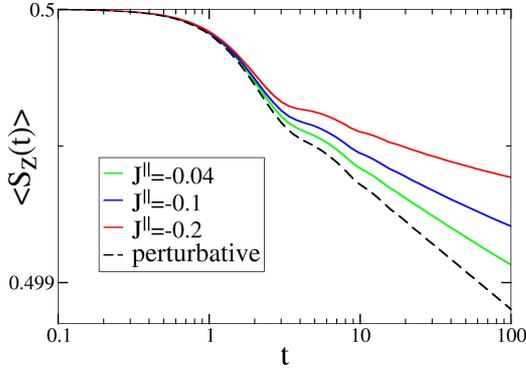


Figure 10.5: Short-time behavior of the magnetization for anisotropic couplings in comparison with the perturbative result from Eq. (10.27) (dashed line). The perpendicular coupling is fixed to $J^{\perp} = -0.04$, the curve with $J^{\parallel} = -0.04$ corresponds to the isotropic case. For increasing $|J^{\parallel}|$, the transverse coupling J^{\perp} is stronger renormalized, and the magnetization tends to decay slower than predicted by the unrenormalized perturbative result.

$$\langle S^z(t) \rangle = 0.5 \left(1 - \frac{\alpha^2}{2\tilde{j}^{\parallel}} t^{2\tilde{j}^{\parallel}} + \frac{\alpha^2}{2\tilde{j}^{\parallel}} + \mathcal{O}(j^2) \right), \quad (10.52)$$

with the asymptotic result $\langle S^z(t \rightarrow \infty) \rangle = 1/2 + \alpha^2/(4\tilde{j}^{\parallel}) + \mathcal{O}(j^2)$. We depict the qualitative difference in the observable $\langle S^z(t) \rangle$ between the cases of isotropic and anisotropic couplings in Fig 10.6. Anisotropy leads to clearly faster relaxation of the magnetization to its steady state limit.

10.5 Conclusions

In this chapter, we discussed the real time evolution of the ferromagnetic Kondo model initially prepared in the product state

$$|\psi\rangle = |\uparrow\rangle \otimes |FS\rangle \quad (10.53)$$

where $|FS\rangle$ is the non-interacting Fermi sea. An important result is the fact that the asymptotic value $\langle S^z(t \rightarrow \infty) \rangle_{\psi}$ of the time-dependent magnetization $\langle S^z(t) \rangle_{\psi}$ differs from the equilibrium value $\langle S^z \rangle_{eq}$ for infinitesimal positive magnetic field. Obviously, the system memorizes its initial preparation for all times. Interestingly, this property appears already in the equilibrium model, as can be seen from an adiabatic preparation of the equilibrium ground state: If the system is prepared in the initial state $|\psi\rangle$ and the ferromagnetic coupling to the leads is then switched on adiabatically, according to the adiabatic theorem (Born and Fock, 1928) the system will evolve to the equilibrium ground state with magnetization $\langle S^z \rangle_{eq}$. In contrary, the asymptotic magnetization would be inverted if the initial state were

$$|\downarrow\rangle \otimes |FS\rangle. \quad (10.54)$$

By preparing the spin state in an eigenstate $|\uparrow\rangle$ or $|\downarrow\rangle$ and adiabatically turning on the interaction to the conduction electrons, the system is not ergodic, e.g., the impurity states $|\uparrow\rangle$ or $|\downarrow\rangle$ are not equally likely measured during the adiabatic preparation process, since

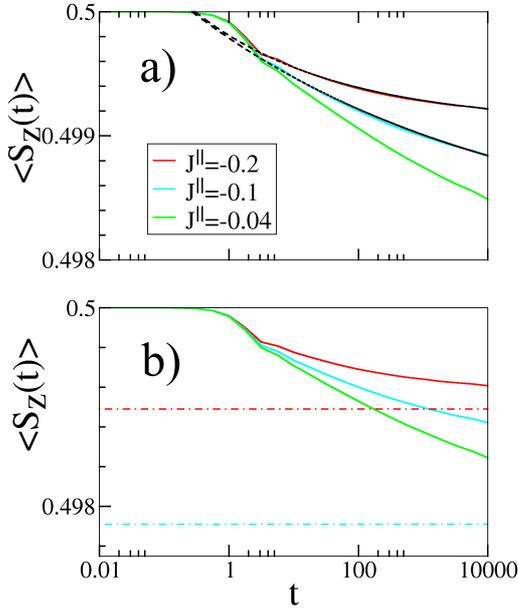


Figure 10.6: Long-time result of the magnetization relaxation for anisotropic couplings and comparison with a long-time fit. All parameters are equivalent to those from Fig. 10.5. In panel a), the full numerical solution of the flow equations (full lines in both panels) is fitted against the analytical power law behavior stated in Eq. (10.52) (dashed lines). At time scales where renormalization of J^{\perp} by J^{\parallel} becomes significant and leads to a deviation from the perturbative result, again the asymptotic fit describes the relaxation process very well. In panel b), a comparison with the saturation value $\langle S^z(t \rightarrow \infty) \rangle = 1/2 + \alpha^2/(4\tilde{j}^{\parallel})$ (dashed lines) is given. Clearly, anisotropic couplings $J^{\parallel} < J^{\perp}$ lead to much faster saturation of the

magnetization than isotropic couplings. Fitting parameters are given in table 10.2.

the impurity magnetization $\langle S^z \rangle$ remains finite at any stage of the adiabatic preparation. In the weak-coupling limit, we were able to prove that asymptotic non-equilibrium magnetization vs. equilibrium magnetization differ by a factor of two:

$$\left(\langle S^z(t \rightarrow \infty) \rangle_{\psi} - \frac{1}{2} \right) = 2 \left(\langle S^z \rangle_{\text{eq}} - \frac{1}{2} \right). \quad (10.55)$$

We were able to confirm this factor of two for a simple exactly solvable toy model with two lead levels and obtained the corrections to this result beyond the weak coupling limit. In the ferromagnetic Kondo model, our perturbative analytical flow equation results become asymptotically exact in the weak-coupling limit, since ferromagnetic couplings flow to a non-interacting or weak-coupling fixed point for the coupling parameters we considered. This aspect allowed us also to describe the approach to the asymptotic non-equilibrium magnetization, where we identified two asymptotically exact regimes in the weak-coupling limit.

(i) Unrenormalized perturbation theory describes an initial short-time regime governed by spin-flip scattering with an amplitude $\propto J^{\perp 2}$. (ii) At long times, the low-energy conduction electrons dominate the relaxation process and the relaxation is slowed down by the renormalized effective low energy couplings. Correspondingly, we found that the magnetization $\langle S^z(t) \rangle_{\psi}$ approaches the asymptotic expectation value logarithmically (with a power law) in time if the model is isotropic (anisotropic). These findings are supported by numerical results using time-dependent NRG which shows excellent agreement with the flow equation results for weak ferromagnetic coupling. Interestingly, our results have been recently confirmed analytically by the real-time RG method in frequency-space (Pletyukhov et al.,

Table 10.2: For large times, we fitted the full numerical solutions of the flow equations against the function $at^{-\sqrt{J_{\parallel}^2 - J_{\perp}^2}} + b$, as depicted in Fig. 10.6a. For couplings $-j^{\parallel} < 0.1$, quantitative agreement with the analytical result $\langle S^z(t) \rangle = 0.5(1 - \alpha^2/(2\tilde{j}^{\parallel}))t^{2\tilde{j}^{\parallel}} + \alpha^2/(2\tilde{j}^{\parallel}) + \mathcal{O}(j^2)$ is very good.

$\langle S^z(t) \rangle = at^{-\sqrt{J_{\parallel}^2 - J_{\perp}^2}} + b$	$j^{\parallel} = -0.05$	$j^{\parallel} = -0.1$
a	$1.66 \cdot 10^{-3}$	$7.07 \cdot 10^{-4}$
b	0.4981	0.4991

2009).

An explicit realization of the ferromagnetic Kondo model in molecular quantum dots is likely feasible in future (Roch et al., 2008), and techniques for preparing and measuring single spin or charge degrees of freedom by ultrafast optical (Braun et al., 2005, Atature et al., 2007) or electrical field pulses (Nowack et al., 2007) are under rapid development. These aspects hint towards a relevance of our results for future experiments.

On the methodological side, we have presented a rarely possible example for an analytical description of non-equilibrium phenomena in an interacting quantum system. Further applications of our approach to real-time evolution in quantum many-body systems may explore new phenomena in non-equilibrium physics.

In particular, non-equilibrium dynamics near impurity quantum phase transitions might be studied. One particular interesting example is the $SU(2)$ invariant Bose-Fermi fixed point in the Bose-Fermi Kondo model (Zarand and Demler, 2002) that has important relations to magnetic quantum phase transitions in metals. By quenching the coupling parameters between two phases separated by this quantum critical point, it might be studied how the quantum critical regime connected to the quantum critical point affects non-equilibrium dynamics.

Appendix A

Details to part III

A.1 Matrix representation of the toy model

In this section, we discuss a matrix representation of the model Hamiltonian

$$H = \sum_{\alpha} (c_{\alpha}^{\dagger} c_{\alpha} - d_{\alpha}^{\dagger} d_{\alpha}) + \frac{g}{2} \vec{S} \cdot \sum_{\alpha, \beta} (c_{\alpha}^{\dagger} + d_{\alpha}^{\dagger}) \vec{\sigma}_{\alpha\beta} (c_{\beta} + d_{\beta}) \quad (\text{A.1})$$

introduced in section 10.1. The full Hilbert space of this model Hamiltonian is spanned by two spin-1/2 fermionic levels and the spin-1/2 impurity spin. The five basis states with total spin $S = 1/2$, $S^z = 1/2$ and two fermions in the electronic levels are given by

$$\begin{aligned} |\psi_0\rangle &= |0\rangle \otimes |\uparrow\downarrow\rangle \otimes |\uparrow\rangle \\ |\psi_1\rangle &= |\uparrow\rangle \otimes |\uparrow\rangle \otimes |\downarrow\rangle \\ |\psi_2\rangle &= |\downarrow\rangle \otimes |\uparrow\rangle \otimes |\uparrow\rangle \\ |\psi_3\rangle &= |\uparrow\downarrow\rangle \otimes |0\rangle \otimes |\uparrow\rangle \\ |\psi_4\rangle &= |\uparrow\rangle \otimes |\downarrow\rangle \otimes |\uparrow\rangle, \end{aligned} \quad (\text{A.2})$$

where the first bra in the tensor product corresponds to the c -electron in our toy model, the second bra corresponds to the d -electron and the third bra corresponds to the impurity spin. The subspace spanned by these five states is denoted by $\mathcal{H}_{2, \frac{1}{2}}$. Due to the $SU(2)$ -symmetric interaction of the toy model Hamiltonian (10.1), the time-evolved initial state as well as the interacting ground state of the Hamiltonian (10.1) in the presence of an infinitesimal positive magnetic field lie in $\mathcal{H}_{2, \frac{1}{2}}$.

In the subspace $\mathcal{H}_{2, \frac{1}{2}}$ spanned by these states, we represent the Hamiltonian (10.1) of the toy model by the matrix $H = H_0 + g H_{int}$, $H_{i+1, j+1} \stackrel{\text{def}}{=} \langle \psi_i | H | \psi_j \rangle$ for $i, j = 0, 1, 2, 3, 4$:

$$H_0 = \begin{pmatrix} -2 & 0 & 0 & 0 & 0 \\ 0 & 2 & 0 & 0 & 0 \\ 0 & 0 & 0 & 0 & 0 \\ 0 & 0 & 0 & 0 & 0 \\ 0 & 0 & 0 & 0 & 0 \end{pmatrix} \quad (\text{A.3})$$

$$H_{int} = \begin{pmatrix} 0 & \frac{1}{2} & \frac{1}{2} & 0 & 0 \\ \frac{1}{2} & 0 & 0 & 0 & 0 \\ \frac{1}{2} & 0 & -\frac{1}{4} & 0 & 0 \\ 0 & 0 & 0 & 0 & 0 \\ 0 & 0 & 0 & 0 & 0 \end{pmatrix}. \quad (\text{A.4})$$

The states $|\psi_3\rangle$ and $|\psi_4\rangle$ decouple, so that one effectively only has to diagonalize a 3×3 -matrix to i) solve the dynamics of the toy model exactly and to ii) determine the ground state magnetization $g_i \mu_B \langle S^z \rangle$. Since the diagonalization is a trivial step with lengthy expressions, we will not give details here.

However, it is interesting to see explicitly how the factor 2 in the ratio $r(g)$ from (10.8) comes about in the weak-coupling limit. In perturbation theory the interacting eigenstates are given by

$$|\tilde{\psi}_j\rangle = |\psi_j\rangle + g \sum_{i \neq j} |\psi_i\rangle \frac{\langle \psi_i | H_{int} | \psi_j \rangle}{E_j - E_i} + \mathcal{O}(g^2), \quad (\text{A.5})$$

where $E_0 = -2, E_1 = 2, E_2 = 0$ are just the eigenvalues of H_0 . For the observable $\hat{O} = S^z - 1/2$ one has $\langle \psi_0 | \hat{O} | \psi_0 \rangle = \langle \psi_1 | \hat{O} | \psi_1 \rangle = 0$ and therefore the ground state expectation value

$$\begin{aligned} O_{eq} &= \langle \tilde{\psi}_0 | \hat{O} | \tilde{\psi}_0 \rangle \\ &= g^2 \langle \psi_2 | \hat{O} | \psi_2 \rangle \frac{|\langle \psi_2 | H_{int} | \psi_0 \rangle|^2}{(E_2 - E_0)^2} + \mathcal{O}(g^3). \end{aligned}$$

The time-averaged expectation value starting from the initial state $|\psi_0\rangle$ is according to Eq. (10.5)

$$\overline{O(t)} = \sum_j |\langle \tilde{\psi}_j | \psi_0 \rangle|^2 \langle \tilde{\psi}_j | \hat{O} | \tilde{\psi}_j \rangle \quad (\text{A.6})$$

and one can easily verify that only the terms $j = 0, 2$ contribute plus corrections in order g^3 . Each of these terms is identical to O_{eq} plus again corrections in order g^3 , which proves

$$r(g) = \frac{\overline{O(t)}}{O_{eq}} = 2 + \mathcal{O}(g). \quad (\text{A.7})$$

The general proof by Moeckel and Kehrein (2009) is a generalization of this argument. The universal factor 2 in the weak-coupling limit plays, e.g., a key role in the thermalization of a Fermi liquid after an interaction quench (Moeckel and Kehrein, 2008), that is the opposite limit of the adiabatic Landau Fermi-liquid paradigm.

A.2 Flow equations for general spin S

Impurity spins often have a total spin quantum number higher than $S = 1/2$, and accordingly, the magnetization curve $\langle S^z(t) \rangle$ will be modified. Here, we provide an analysis of

the modified flow equations for a spin S that shows that the magnetization $\langle S^z(t) \rangle$ fulfills the scaling relation

$$\langle S^z(t) \rangle = S \langle S^z(t) \rangle_{S=1/2} + \mathcal{O}(J^2 S^2). \quad (\text{A.8})$$

The prove starts with the observation that the commutation relation

$$[S^i, S^j]_- = i\epsilon_{ijk} S^k \quad (\text{A.9})$$

is independent of S . We illustrate all further steps only for isotropic couplings, since anisotropic couplings require only small modifications.

In the flow equations for $S^a(B)$ (determined via the commutator $[\eta(B), S^a(B)]$), the parameter S can only enter via the commutator

$$[: \vec{S} \cdot \vec{s}_{\mathbf{t}\mathbf{t}'} :, : (\vec{S} \times \vec{s}_{\mathbf{u}'\mathbf{u}})^a :]_- , \quad (\text{A.10})$$

where the relation (A.9) cannot be directly applied. In general, the operator product $S^i S^j$ will have the form

$$S^i S^j = x_{ij} + \frac{i}{2} \sum_k \epsilon_{ijk} S^k , \quad (\text{A.11})$$

where $\frac{i}{2} \sum_k \epsilon_{ijk} S^k$ is the operator obtained by projecting the operator $S^i S^j$ on the operator $\frac{i}{2} \sum_k \epsilon_{ijk} S^k$ as a basis operator in spin Hilbert space and the operator x_{ij} is defined by Eq. (A.11). Employing this decomposition in Eq. (A.11), we obtain

$$\begin{aligned} &[: \mathbf{S} \cdot \mathbf{s}_{\mathbf{t}\mathbf{t}'} :, : (\vec{S} \times \vec{s}_{\mathbf{u}'\mathbf{u}})^a :]_- = \\ &\sum_{ijk\alpha\beta\mu\nu} \left(\frac{1}{4} x_{ij} [\sigma_{\alpha\beta}^i \sigma_{\mu\nu}^k \epsilon_{ajk} [: c_{\mathbf{t}'\alpha}^\dagger c_{\mathbf{t}\beta}^\dagger :, : c_{\mathbf{u}'\mu}^\dagger c_{\mathbf{u}\nu} :]_-] \right. \\ &\left. + \frac{1}{4} \frac{i}{2} \sum_{k'} \sigma_{\alpha\beta}^i \sigma_{\mu\nu}^k \epsilon_{ajk} \epsilon_{ijk'} S^{k'} [: c_{\mathbf{t}'\alpha}^\dagger c_{\mathbf{t}\beta}^\dagger :, : c_{\mathbf{u}'\mu}^\dagger c_{\mathbf{u}\nu} :]_+ \right) . \end{aligned} \quad (\text{A.12})$$

Modifications to the flow equations can now only arise from the term in (A.12) that contains the operators x_{ij} . We rewrite this term as

$$\frac{i}{8} \sum_{ijkl} x_{ij} \epsilon_{ajk} \epsilon_{lik} [s_{\mathbf{t}'\mathbf{u}}^l \delta_{\mathbf{t}\mathbf{u}'} + \delta_{\mathbf{t}'\mathbf{u}} s_{\mathbf{u}'\mathbf{t}}^l] \quad (\text{A.13})$$

in order to show that this term has a vanishing projection on the operator $:(\mathbf{S} \times \mathbf{s}_{\mathbf{u}'\mathbf{u}})^a :$, due to the decomposition (A.11). In conclusion, we showed that the relation

$$\langle S^z(t) \rangle = S \langle S^z(t) \rangle_{S=1/2} + \mathcal{O}(J^2 S^2) \quad (\text{A.14})$$

is fulfilled for isotropic exchange couplings, and it can be proven analogously for anisotropic couplings.

A.3 Validity of tree-level approximation

In many calculations in chapter 10, we made use of the approximative form

$$\frac{d\gamma_{\mathbf{k}'\mathbf{k}}}{dB} = (\varepsilon_{\mathbf{k}'} - \varepsilon_{\mathbf{k}})J_{\mathbf{k}'\mathbf{k}}^\perp(B) + \mathcal{O}((\varepsilon_{\mathbf{k}'} - \varepsilon_{\mathbf{k}})J^2) \quad (\text{A.15})$$

of the derivative $\frac{d\gamma_{\mathbf{k}'\mathbf{k}}}{dB}$, which neglects terms of $\mathcal{O}(J^2)$. This approximation is not trivial if the couplings J^\perp and J^\parallel take anisotropic values with $|J^\perp| < |J^\parallel|$ and $J^\parallel < 0$, since the terms of $\mathcal{O}(J^2)$ contain the couplings $J_{\mathbf{k},\mathbf{k}'}^\parallel$ that flow to a finite value at the Fermi surface (given by $\varepsilon_{\mathbf{k}} = 0$ and $\varepsilon_{\mathbf{k}'} = 0$), while the leading order term is proportional to the coupling $J_{\mathbf{k}'\mathbf{k}}^\perp$ that flows to zero. Here, we give a detailed justification of this approximation, starting with the derivative including all terms up to $\mathcal{O}(J^2)$:

$$\begin{aligned} \frac{d\gamma_{\mathbf{k}\mathbf{k}'}}{dB} &= \Delta\varepsilon \frac{J^\perp(B)}{N} e^{-B(\Delta\varepsilon)^2} \\ &- \frac{1}{4} \int_{-D}^D d\varepsilon \operatorname{sgn}(\varepsilon) \left[(\Delta\varepsilon + \varepsilon_{\mathbf{k}'} - \varepsilon) J^\parallel(B) e^{-B(\Delta\varepsilon + \varepsilon_{\mathbf{k}'} - \varepsilon)^2} \right. \\ &\times \int_0^B dB' (\varepsilon - \varepsilon_{\mathbf{k}'}) \frac{\rho_F J^\perp(B')}{N} e^{-B'(\varepsilon - \varepsilon_{\mathbf{k}'})^2} + (\varepsilon_{\mathbf{k}'} - \varepsilon) J^\parallel(B) e^{-B(\varepsilon - \varepsilon_{\mathbf{k}'})^2} \\ &\left. \times \int_0^B dB' (\Delta\varepsilon + \varepsilon_{\mathbf{k}'} - \varepsilon) J^\perp(B') e^{-B'(\varepsilon - \Delta\varepsilon - \varepsilon_{\mathbf{k}'})^2} \right]. \end{aligned} \quad (\text{A.16})$$

Above, we made use of the abbreviation $\Delta\varepsilon = \varepsilon_{\mathbf{k}} - \varepsilon_{\mathbf{k}'}$, for which we assume $\Delta\varepsilon > 0$ and $\varepsilon_{\mathbf{k}'} > 0$ in the following. In the integral occurring in Eq. (A.16), the integrand vanishes except in small energy ranges of width $\Delta\varepsilon \ll D$, leading to the simplified expression

$$\begin{aligned} \frac{d\gamma_{\mathbf{k}'\mathbf{k}}}{dB} &= \Delta\varepsilon \frac{J^\perp(B)}{N} e^{-B(\Delta\varepsilon)^2} \\ &+ \frac{1}{2} \int_{-\Delta\varepsilon}^0 d\varepsilon [(\Delta\varepsilon + \varepsilon_{\mathbf{k}'} - \varepsilon) \rho_F \frac{J^\parallel(B)}{N} e^{-B(\Delta\varepsilon + \varepsilon_{\mathbf{k}'} - \varepsilon)^2} \\ &\times \int_0^B dB' (\varepsilon - \varepsilon_{\mathbf{k}'}) J^\perp(B') e^{-B'(\varepsilon - \varepsilon_{\mathbf{k}'})^2}] + \mathcal{O}(e^{-BD^2}), \end{aligned} \quad (\text{A.17})$$

with the correction of $\mathcal{O}(e^{-BD^2})$ arising from integration ranges close to the band edges. Using the asymptotic decay $J^\perp(B) = \frac{\alpha}{\rho_F} B^{\tilde{j}^\perp/2}$ ¹ of the coupling $J^\perp(B)$ derived in Eq. (10.46), a lower boundary for the first line in Eq. (A.16) is

$$\frac{\Delta\varepsilon}{N} \frac{\alpha}{\rho_F} B^{\tilde{j}^\perp/2} e^{-B(\Delta\varepsilon)^2}, \quad (\text{A.18})$$

¹A cautious reader might worry about our usage of dimensions in this asymptotic formula. We note that the parameter B is here formally used as a dimensionless number, and the expression $\frac{\alpha}{\rho_F} B^{\tilde{j}^\perp/2}$ has therefore the expected dimension of an energy.

and an upper boundary for the $\mathcal{O}(J^2)$ contribution to Eq. (A.17) is (valid for $B \lesssim (\Delta\epsilon)^{-2}$)

$$BJ^\perp J^\parallel \mathcal{O}(\Delta\epsilon)^3, \quad (\text{A.19})$$

where we used the inequality $|J^\perp(B)| \leq |J^\perp|$. From these two boundaries, we conclude that in the derivative (A.16) the first line will dominate the remaining contributions if

$$\Delta\epsilon^2 B^{1-\tilde{j}^\parallel/2} \ll \frac{1}{j^\parallel}. \quad (\text{A.20})$$

Hence, $\frac{d\gamma_{\mathbf{k}'\mathbf{k}}}{dB} \approx \Delta\epsilon \frac{J^\perp(B)}{N} e^{-B(\Delta\epsilon)^2}$ in the considered parameter regime $B \lesssim (\Delta\epsilon)^{-2}$. In the remaining parameter regime $B \gtrsim (\Delta\epsilon)^{-2}$ the derivative $\frac{d\gamma_{\mathbf{k}'\mathbf{k}}}{dB}$ decays exponentially as a function of B and is negligible. Hence, we conclude that the approximation $\frac{d\gamma_{\mathbf{k}'\mathbf{k}}}{dB} \approx (\varepsilon_{\mathbf{k}'} - \varepsilon_{\mathbf{k}}) J_{\mathbf{k}'\mathbf{k}}^\perp(B)$ is valid up to corrections of either relative size $\mathcal{O}(j^\parallel)$ or absolute size $\propto e^{-B(\Delta\epsilon)^2}$ once $B(\Delta\epsilon)^2 \gtrsim 1$.

A.4 Alternative way of calculating magnetization

In section (10.4), we derived an analytical approximation for the magnetization $\langle S^z(t) \rangle$, using several approximations to expression (10.41). In order to circumvent and thereby further justify some of these approximations we provide here a different way of obtaining the same result. The basic idea is to formulate the sum rule $\langle S^z(B)^2 \rangle = \frac{1}{4} + \mathcal{O}(J^2)$ (see Eq. (10.20)) independently for each of the unitary equivalent operators $S^z(t)$ and $\tilde{S}^z(t)$. Then, it is possible to make use of the identity

$$\langle S^z(t)^2 \rangle - \langle \tilde{S}^z(t)^2 \rangle = \mathcal{O}(J^2). \quad (\text{A.21})$$

Employing the explicit representations of the operators $S^z(t)$ and $\tilde{S}^z(t)$ stated in Eqs (10.29) and (10.30), this relation takes the explicit form

$$\begin{aligned} h^2(t) &= \tilde{h}^2 + \sum_{\mathbf{k}\mathbf{k}'} (|\tilde{\gamma}_{\mathbf{k}'\mathbf{k}}(t)|^2 - |\gamma_{\mathbf{k}'\mathbf{k}}(t)|^2) \\ &\times n(\mathbf{k}')(1 - n(\mathbf{k})) + \mathcal{O}(J^2). \end{aligned} \quad (\text{A.22})$$

Now it is possible to employ the approximate analytical solutions (10.29) and (10.40) for the coefficients $\tilde{\gamma}_{\mathbf{k}\mathbf{k}'}$ and $\tilde{\gamma}_{\mathbf{k}\mathbf{k}'}(t)$ in Eq. (A.22), with the result

$$\begin{aligned} h^2(t) &= \tilde{h}^2 + \sum_{\mathbf{k}\mathbf{k}'} |\tilde{\gamma}_{\mathbf{k}\mathbf{k}'}|^2 \left(-1 + 2 \cos[(\varepsilon_{\mathbf{k}} - \varepsilon_{\mathbf{k}'})t] \right) \\ &\times n(\mathbf{k}')(1 - n(\mathbf{k})) + \mathcal{O}(J^2). \end{aligned} \quad (\text{A.23})$$

Since the coefficient \tilde{h} obeys $\tilde{h} = 1 + \mathcal{O}(J)$ (see Eq. (10.39) and the subsection ‘‘anisotropic couplings’’), it is easily seen that the right hand side of Eq. (A.23) is of the form $1 + \mathcal{O}(J)$, and an expansion of $h(t)$ to first order in J immediately yields

$$\begin{aligned} h(t) &= \tilde{h} + \sum_{\mathbf{k}\mathbf{k}'} |\tilde{\gamma}_{\mathbf{k}\mathbf{k}'}|^2 \left(\cos((\varepsilon_{\mathbf{k}} - \varepsilon_{\mathbf{k}'}t) - \frac{1}{2}) \right) \\ &\times n(\mathbf{k}')(1 - n(\mathbf{k})) + \mathcal{O}(J^2). \end{aligned} \quad (\text{A.24})$$

Thereby, we were able to confirm the result in Eq. (10.41) without explicitly solving the flow equation for the coupling $h(B)$.

A.5 Diagonal parameterization of isotropic couplings

In explicit evaluations of the coupling constants $\tilde{\gamma}_{\mathbf{k}\mathbf{k}'}$, we integrated the flow equation

$$\frac{d\gamma_{\mathbf{k}\mathbf{k}'}}{dB} = (\epsilon_{\mathbf{k}} - \epsilon_{\mathbf{k}'})J_{\mathbf{k}\mathbf{k}'}^{\perp}(B) + \mathcal{O}(J^2(\epsilon_{\mathbf{k}} - \epsilon_{\mathbf{k}'})) . \quad (\text{A.25})$$

by using the infrared parameterization $J_{\mathbf{k}\mathbf{k}'}^{\perp}(B) = \frac{J^{\perp}(B)}{N}e^{-B(\epsilon_{\mathbf{k}} - \epsilon_{\mathbf{k}'})^2}$, assuming isotropic couplings $J_{\mathbf{k}\mathbf{k}'}^{\perp}(B) \equiv J_{\mathbf{k}\mathbf{k}'}^{\parallel}(B)$ here and in the following. This parameterization is only suitable for low energy couplings with $|\epsilon_{\mathbf{k}}| \ll D, |\epsilon_{\mathbf{k}'}| \ll D$. Here, we provide an approximation to the couplings $J_{\mathbf{k}\mathbf{k}'}(B)$ by an ansatz that also describes couplings above this low energy limit appropriately. Thereby, it is also possible to provide a more precise criterion for the validity of the infrared parameterization. One makes the ansatz (Kehrein, 2006)

$$J_{\mathbf{k}'\mathbf{k}}(B) = J_{\overline{\mathbf{k}'\mathbf{k}}}(B)e^{-B(\epsilon_{\mathbf{k}'} - \epsilon_{\mathbf{k}})^2} , \quad (\text{A.26})$$

with $J_{\overline{\mathbf{k}'\mathbf{k}}}(B=0) = J/N < 0$, where $\overline{\mathbf{k}'\mathbf{k}}$ is a label for the energy median

$$\epsilon_{\overline{\mathbf{k}'\mathbf{k}}} \stackrel{\text{def}}{=} \frac{\epsilon_{\mathbf{k}} + \epsilon_{\mathbf{k}'}}{2} . \quad (\text{A.27})$$

Note that the couplings $J_{\overline{\mathbf{k}'\mathbf{k}}}(B)$ therefore depend only on the energy $\epsilon_{\overline{\mathbf{k}'\mathbf{k}'}}$ but not explicitly on any momentum. Using this ansatz in the flow equations (10.13) leads to a reduced system of N flow equations

$$\begin{aligned} \frac{dJ_{\mathbf{k}}(B)}{dB} &= \sum_{\mu} 2(\epsilon_{\mathbf{k}} - \epsilon_{\mu})J_{\mathbf{k}\mu}J_{\mu\mathbf{k}}(n(\mu) - \frac{1}{2}) \\ &\approx -\frac{J_{\mathbf{k}}^2(B)N\rho_F}{2B}e^{-2B\epsilon_{\mathbf{k}}^2} . \end{aligned} \quad (\text{A.28})$$

In the second line, we replaced $J_{\mu\mathbf{k}}$ by $J_{\mathbf{k}}(B) := J_{\overline{\mathbf{k}\mathbf{k}}}(B)$ and evaluated the momentum sum at $T=0$. This approximation is justified by a weak dependence of $J_{\mu\mathbf{k}}(B)$ on momentum μ at scales B where these couplings will not be suppressed by the exponential $e^{-B(\epsilon_{\mathbf{k}} - \epsilon_{\mu})^2}$ anyway (Kehrein (2006), chapter 2). Using the initial condition $J_{\mathbf{k}}(B=D^{-2}) = J$,² the differential equation (A.28) can be integrated exactly, leading to

$$J_{\mathbf{k}}(B) = \frac{J}{N} \left(1 - J\frac{\rho_F}{2} \int_{D^{-2}}^B dB' \frac{\exp(-2B'\epsilon_{\mathbf{k}}^2)}{B'} \right)^{-1} . \quad (\text{A.29})$$

These couplings depend logarithmically or weaker on the parameter B , and it is possible to integrate Eq. (A.25) by evaluating them on the energy scale $(\epsilon_{\mathbf{k}} - \epsilon_{\mathbf{k}'})$, $\tilde{\gamma}_{\mathbf{k}\mathbf{k}'} =$

²In comparison to the exact initial condition $J_{\mathbf{k}}(B=0) = J$, this initial condition neglects only corrections of $\mathcal{O}(J^2)$, as argued in the context of Eq. (10.16).

$\frac{J_{\mathbf{k}}(B=(\varepsilon_{\mathbf{k}}-\varepsilon_{\mathbf{k}'}^{-2})}{\varepsilon_{\mathbf{k}}-\varepsilon_{\mathbf{k}'}}$, with an error of order $J_{\mathbf{k}}(B=(\varepsilon_{\mathbf{k}}-\varepsilon_{\mathbf{k}'}^{-2})^2)$. Now, we evaluate the coupling $J_{\mathbf{k}}(B=(\varepsilon_{\mathbf{k}}-\varepsilon_{\mathbf{k}'}^{-2})$ by approximating (A.29) in several steps:

$$\begin{aligned} \int_{D^{-2}}^{(\varepsilon_{\mathbf{k}}-\varepsilon_{\mathbf{k}'})^{-2}} dB' \frac{\exp(-2B'\varepsilon_{\mathbf{k}}^2)}{B'} &= \int_{D^{-2}}^{(\varepsilon_{\mathbf{k}}-\varepsilon_{\mathbf{k}'})^{-2}} dB' \frac{\exp(-2B'(\varepsilon_{\mathbf{k}}-\varepsilon_{\mathbf{k}'})^2)}{B'} + \mathcal{O}(1) \\ &= \int_{D^{-2}}^{\infty} dB' \frac{\exp(-2B'(\varepsilon_{\mathbf{k}}-\varepsilon_{\mathbf{k}'})^{-2})}{B'} + \mathcal{O}(1) \\ &= -\gamma - \ln\left(\frac{2(\varepsilon_{\mathbf{k}}-\varepsilon_{\mathbf{k}'})^2}{D^2}\right) + \mathcal{O}\left(\frac{2(\varepsilon_{\mathbf{k}}-\varepsilon_{\mathbf{k}'})^2}{D^2}\right) + \mathcal{O}(1). \end{aligned} \quad (\text{A.30})$$

In the first line we assumed that $\varepsilon_{\mathbf{k}}$ and $\varepsilon_{\mathbf{k}} - \varepsilon_{\mathbf{k}'}$ are of the same order. This assumption is justified in momentum sums $\sum_{\mathbf{k}\mathbf{k}'}$ weighted by the occupation factors $n(\varepsilon_{\mathbf{k}})(1-n(\varepsilon_{\mathbf{k}'}))$, since the phase space of the summation where $\varepsilon_{\mathbf{k}}$ and $\varepsilon_{\mathbf{k}} - \varepsilon_{\mathbf{k}'}$ are not of the same order has a relative size $\ll 1$ compared to the Brillouin zone. In the last line, we used the asymptotic expansion of the exponential integral

$$Ei(1, x) = \int_x^{\infty} \frac{e^{-t}}{t} dt = -\gamma - \ln(x) + \mathcal{O}(x)$$

with $\gamma \approx 0.5772$, being justified in the limit $|\ln\left(\frac{(\varepsilon_{\mathbf{k}}-\varepsilon_{\mathbf{k}'})^2}{D^2}\right)| \gg 1$.

Altogether, in the limit $|\ln\left(\frac{(\varepsilon_{\mathbf{k}}-\varepsilon_{\mathbf{k}'})^2}{D^2}\right)| \gg 1$ we were able to justify the approximation $\tilde{\gamma}_{\mathbf{k}\mathbf{k}'} \approx \frac{J_{IR}(B=(\varepsilon_{\mathbf{k}}-\varepsilon_{\mathbf{k}'})^{-2})}{\varepsilon_{\mathbf{k}}-\varepsilon_{\mathbf{k}'}}$, agreeing in this case with the more accurate diagonal parameterization $\tilde{\gamma}_{\mathbf{k}\mathbf{k}'} \approx \frac{J_{\mathbf{k}}(B=(\varepsilon_{\mathbf{k}}-\varepsilon_{\mathbf{k}'})^{-2})}{\varepsilon_{\mathbf{k}}-\varepsilon_{\mathbf{k}'}}$.

A.6 Normal ordering

Within the flow equation approach, fermionic operators occurring in transformed observables are usually normal-ordered in order to separate the various interaction terms generated during the flow into irreducible objects in the spirit of a diagrammatic expansion using Wick's theorem (Fritsch (2009), chapter 1; Kehrein (2006), chapter 4). In practice, this procedure is implemented with respect to a given reference state or density matrix, such that normal ordering of a product $c_{\mathbf{k}\sigma}^{\dagger}c_{\mathbf{k}'\sigma'}$ of fermionic operators amounts to subtracting the expectation value with respect to the given reference state or density matrix,

$$: c_{\mathbf{k}\sigma}^{\dagger}c_{\mathbf{k}'\sigma'} := c_{\mathbf{k}\sigma}^{\dagger}c_{\mathbf{k}'\sigma'} - \langle c_{\mathbf{k}\sigma}^{\dagger}c_{\mathbf{k}'\sigma'} \rangle. \quad (\text{A.31})$$

In our particular problem, we used the initial state $|\psi_i\rangle$ defined in Eq. (10.21) as reference state for the normal ordering procedure, such that $\langle c_{\mathbf{k}\sigma}^{\dagger}c_{\mathbf{k}'\sigma'} \rangle = \langle \psi_i | c_{\mathbf{k}\sigma}^{\dagger}c_{\mathbf{k}'\sigma'} | \psi_i \rangle$. However, this reference state will look very different at some finite time t or if it is transformed into the representation of the flowing operator $c_{\mathbf{k}}(B)$ by the unitary transformation

$$U(B) = T_B e^{\int_0^B \eta(B') dB'} \quad (\text{A.32})$$

induced by the generator $\eta(B)$, where the operator T_B causes B -ordering. In order to use a normal-ordering prescription with respect to the same quantum state for all values of B , we need to define normal ordering with respect to the time-evolved initial state in the basis for a given value of B ,

$$|\psi(B, t)\rangle \stackrel{\text{def}}{=} e^{-iHt} U^\dagger(B) |\psi_i\rangle . \quad (\text{A.33})$$

The contraction of fermionic operators then depends both on B and on time t ,

$$\begin{aligned} n_{ll'}(B, t) &\stackrel{\text{def}}{=} \langle \psi_i | U(B) e^{iHt} c_l^\dagger c_{l'} e^{-iHt} U^\dagger(B) | \psi_i \rangle \\ &= \langle \psi_i | c_l^\dagger(B, t) c_{l'}(B, t) | \psi_i \rangle , \end{aligned} \quad (\text{A.34})$$

where we introduced a general multiindex l comprising both spin and momentum label. Since a calculation of the full dependence of $n_{ll'}(B, t)$ on the parameters B and t turns out to be a very complicated problem of its own, we show here that the difference $n_{ll'}(B, t) - n_{ll'}(B = 0, t = 0)$ enters the flow equations for spin operators (the Hamiltonian) only to $\mathcal{O}(J^2)$ (to $\mathcal{O}(J^3)$), having no influence on the leading order of our calculation, which is $\mathcal{O}(J)$ ($\mathcal{O}(J^2)$).

In order to reduce (A.34) to the form $n_{ll'}(B, t) = n_{ll'}(B = 0, t = 0) + \mathcal{O}(J)$, we write the transformed operators $c_l(B, t) = U(B) e^{iHt} c_l e^{-iHt} U^\dagger(B)$ in the general form

$$c_l(B, t) = f_l(B, t) c_l + J \times \text{composite operator} + \mathcal{O}(J^2) , \quad (\text{A.35})$$

with a flowing coupling parameter $f_l(B, t)$ and the unitary transformation $U(B)$ generated by the generator (10.11). The time-evolved fermionic operator $c_l(B, t)$ can now be formally calculated in the forward-backwards transformation scheme depicted in Fig. (8.4), which guarantees that $f_l(B, t)$ behaves as $1 + \mathcal{O}(J)$ once the flow of this operator is expanded in powers of J . In this expansion, terms proportional to higher powers in J are expected to remain smaller by at least a factor of J than the linear order in J for *arbitrary* t due to the arguments given in chapter 9. Now the contractions can be written as

$$n_{ll'}(B, t) = \langle \psi(B, t) | c_l^\dagger c_{l'} | \psi(B, t) \rangle = \langle \psi_i | c_l^\dagger c_{l'} | \psi_i \rangle + \mathcal{O}(J) . \quad (\text{A.36})$$

Since $n_{ll'}(B, t)$ enters our flow equations only in terms of highest considered order in J , the correction of $\mathcal{O}(J)$ occurring in (A.36) enters our calculation only to subleading power in J . Therefore, it is sufficient in our calculation to use the simplified contractions $n_{ll'} = \langle \psi_i | c_l^\dagger c_{l'} | \psi_i \rangle$ for normal ordering.

Part IV

Normal-state Nernst effect in the Cuprates

Chapter 11

Introduction: Cuprates and the Nernst effect

11.1 The cuprates

More than twenty years ago, Bednorz and Müller (1986) announced the discovery of superconductivity in a ceramic copper oxide material at a temperature of about 30 K . Subsequently, several other superconducting ceramic copper oxides were discovered, with the uncommon property that they are insulators in the undoped state and become superconducting upon doping either holes or electrons into the copper-oxygen planes of these materials. The detailed investigation of their phase diagram revealed that the macroscopic properties of the copper oxides are profoundly influenced by strong electron-electron correlations (i.e., large Coulomb repulsion U). After many years of theoretical efforts, an explanation of the superconducting phase in the cuprates is still lacking. In the last few years, a series of new discoveries in the underdoped cuprates have been a breath of fresh air in that regard, including the observation of de Haas-van Alphen and Shubnikov-de Haas effects (LeBoeuf et al., 2007). Among other proposed explanations, these findings were subsequently interpreted as resulting from translational symmetry breaking induced by density wave order (Millis and Norman, 2007, Harrison, 2009, Dimov et al., 2008). Observations of a large normal state Nernst signal (Choinière et al., 2009) in samples with different types of density wave order provide an interesting probe for the *normal state* of the cuprates. In the following, we discuss general properties of the cuprates that will be important for our analysis of the normal state Nernst effect in the cuprates. In-depth details beyond our discussion can be found in the review articles by Dagotto (1994), Damascelli et al. (2003), Lee et al. (2006). On the example of two typical materials, the doping phase diagram of the cuprates (Damascelli et al., 2003) is sketched in Fig. 11.1, showing an asymmetry between the electron-doped cuprate $\text{Nd}_{2-x}\text{Ce}_x\text{CuO}_{4-\delta}$ and the hole-doped cuprate $\text{La}_{2-x}\text{Sr}_x\text{CuO}_4$.

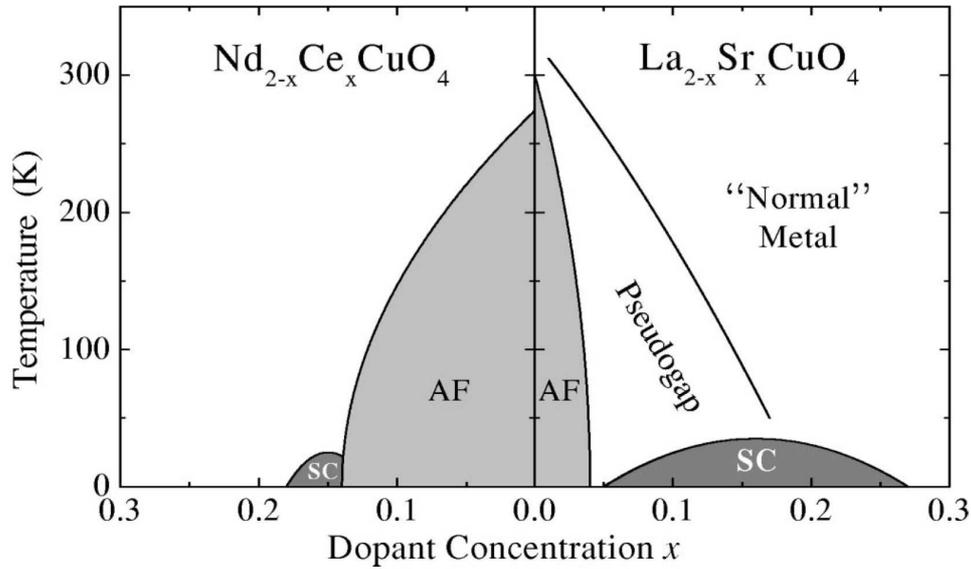


Figure 11.1: Phase diagram of cuprate materials doped with electron-like carriers (left) and hole-like carriers (right). Both materials show antiferromagnetism (AF) and superconductivity (SC), with an asymmetry caused, e.g., by the extended pseudogap phase observed in the hole doped cuprate. The “normal” metal phase shows an unusual T -linear resistivity. Figure from Damascelli et al. (2003).

Phase diagram

We concentrate first on the more prominent hole-doped cuprates, before commenting on the electron-doped part of the phase diagram later on.

With increasing hole-doping x , the materials go from being antiferromagnetic insulators at zero doping to more or less conventional metals at high doping. This metallic state shows a single hole-like Fermi surface with a volume containing $1 + x$ holes per Cu atom (Hussey et al., 2003). Between the insulator and the metal, a superconducting region intervenes, terminating at a critical temperature T_c with a maximum value at the so called *optimal doping*. Near optimal doping and above T_c , the normal state shows a resistivity which is linear in temperature and is conveniently called a “strange metal”. Upon raising temperature in an underdoped material, a crossover temperature T^* is found at which several physical properties undergo a rapid change (Timusk and Statt, 1999). Photoemission experiments on $\text{Bi}_2\text{Sr}_2\text{CaCu}_2\text{O}_{8+\delta}$ show a partially gapped Fermi surface, with Fermi arcs remaining near the Brillouin zone diagonals (Kanigel et al., 2006). In additional presence of stripe order, only nodal points appear to survive as low-energy excitations below the stripe-ordering temperature in $\text{La}_{2-x}\text{Ba}_x\text{CuO}_4$ (Valla et al., 2006, He et al., 2009). Although many theories have been proposed to explain the pseudogap

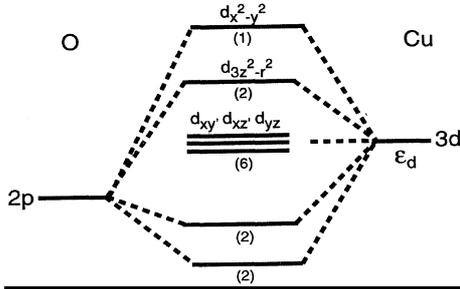


Figure 11.2: Bonding between a Cu^{2+} and two O^{2-} ions. Only the d electrons of Cu and the p_x and p_y orbitals of the oxygens are considered. The numbers in parentheses indicate the occupation of the different levels in the undoped compound. Figure from Fulde (1991).

regime – ranging from phase-fluctuating preformed Cooper pairs over competing orders to Mott physics and strong short-range antiferromagnetic fluctuations – its origin is still unclear.

Electronic properties

A Hamiltonian for high- T_c superconductors is usually derived by restricting electrons to move inside the CuO_2 planes, justified by the very strong Cu–O bonds. The construction of model Hamiltonians for the cuprates has been discussed at length by Dagotto (1994), Lee et al. (2006). Both Cu and O atoms of the CuO_2 planes contribute to the electronic structure, the copper ions Cu^{2+} having nine electrons in the five d orbitals, while O^{2-} has the three p orbitals occupied. The degeneracy of these d and p orbitals is removed by lattice structure, such that the state with the highest energy has mainly $d_{x^2-y^2}$ character and carries the missing electron of the Cu^{2+} d -orbitals (Fig. 11.2). Upon doping holes into the CuO planes, the strong Coulomb repulsion between holes in the same orbital has to be taken into account. These aspects lead to a description in terms of a three-band extended Hubbard model (Emery, 1987), in which Cu $3d_{x^2-y^2}$ as well as O $2p_x$ and $2p_y$ orbitals are explicitly considered. The three band model has several parameters and can be reduced to a simpler one band model due to an argument by Zhang and Rice (1988).

They argued that a hole on a neighboring oxygen atom forms a spin singlet with the central hole on the copper, such that the holes in the oxygen can be replaced by a spin singlet state centered at the copper. This is the basis to formulate an effective one-band Hamiltonian, the so-called *t-J model*

$$\begin{aligned}
 H &= J \sum_{\langle ij \rangle} [\mathbf{S}_i \cdot \mathbf{S}_j - \frac{1}{4} n_i n_j] \\
 &- t \sum_{\langle ij \rangle \sigma} [c_{i\sigma}^\dagger (1 - n_{i-\sigma}) (1 - n_{j-\sigma}) c_{j\sigma} + \text{H.c.}] , \quad (11.1)
 \end{aligned}$$

where \mathbf{S}_i ($n_{i\sigma}$) are spin- $\frac{1}{2}$ (fermionic occupation) operators at the sites i of a two-dimensional square lattice, and J is the antiferromagnetic coupling between nearest neighbor sites $\langle ij \rangle$. Since the early days of superconductivity, people have also been studying the one-band

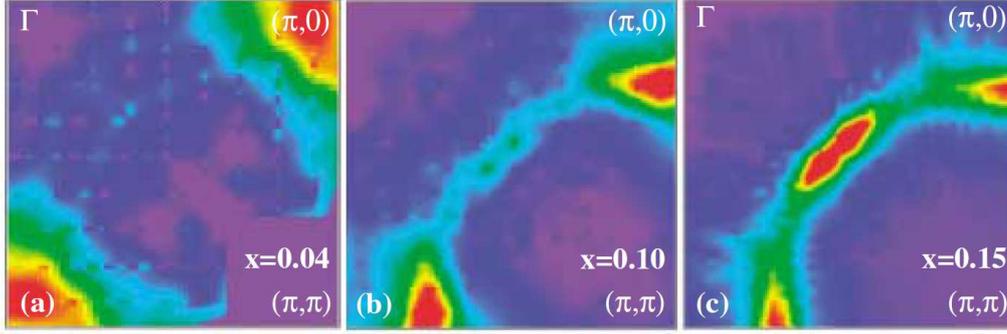


Figure 11.3: Fermi surface plots in NCCO obtained from angle-resolved photoemission spectroscopy (ARPES) for different electron dopings: (a) $x = 0.04$, (b) $x = 0.10$, and (c) $x = 0.15$. Energy distribution curves were integrated in a 60 meV window (-40 meV, $+20$ meV) plotted as a function of k . For small doping $x = 0.04$ intensity is only visible near $(\pi, 0)$ and $(0, \pi)$. From $x = 0.10$ to $x = 0.15$, spectral weight along the zone diagonal successively increases, until intensity remains only suppressed near $(0.65\pi, 0.3\pi)$ (and its symmetry related points) at the intersection of the Fermi surface with the antiferromagnetic Brillouin zone boundary. Figure taken from (Armitage et al., 2002).

Hubbard model (Hubbard, 1963). This model is defined as

$$H = -t \sum_{\langle ij \rangle, \sigma} [c_{i\sigma}^\dagger c_{j\sigma} + c_{j\sigma}^\dagger c_{i\sigma}] + U \sum_i (n_{i\uparrow} - \frac{1}{2})(n_{i\downarrow} - \frac{1}{2}), \quad (11.2)$$

where, as usual, U is the on-site repulsive interaction and t the hopping amplitude. At present, it remains an open question how much of the cuprate physics is captured by one-band models of Hubbard or $t - J$ type. While numerical methods have partly reproduced features of the cuprate phase diagram, recent results question even the validity of these numerical findings (Aomi and Imada, 2007). Remarkably, early mean field studies of the Hubbard model *predicted* the formation of inhomogeneous states at small doping (Zaanen and Gunnarson, 1989). Such states of matter break translational symmetry, and this aspect has invoked thoughts about reconstruction of the Fermi surface in presence of modulations in the charge or spin distributions (Millis and Norman, 2007, Harrison, 2009).

Fermi surface reconstruction in high T_c superconductors

a) electron-doped cuprates Photoemission experiments on NCCO show salient changes in the Fermi surface geometry in dependence of electron doping as depicted in Fig. 11.3. At low doping, the Fermi surface is an electron-pocket (with volume $\sim x$) centered at $(\pi, 0)$. Further doping leads to the creation of a new hole-like Fermi surface (volume $\sim 1 + x$) centered at (π, π) . It is apparent that these features are related to the evolution of magnetic order in this material.

Commensurate (π, π) spin density wave order in this cuprate family has been detected by muon spin rotation (μ SR) (Luke et al., 1990) and neutron scattering measurements (Motoyama et al., 2006) in different materials. In these measurements, long-ranged magnetic order is found over a wide range of dopings and is suggested to vanish at a critical doping x_c by μ SR measurements (Luke et al., 1990). Ambiguities about the value of this critical doping arise from elastic neutron scattering measurements on NCCO that report short-ranged antiferromagnetism for dopings between $x = 0.134$ and $x = 0.154$ (Motoyama et al., 2006). It has also to be considered that this behavior might change in strong magnetic fields, where the tendency to SDW order might be significantly enhanced (Matsuura et al., 2003). Indeed, quantum oscillations in the magnetoresistance of NCCO at magnetic field strengths around 50 T have revealed a drastic change in the oscillation frequency from doping $x = 0.16$ to $x = 0.17$, what has been interpreted as a Fermi surface reconstruction induced by long-range magnetic order above optimal doping (Helm et al., 2009). Whether these findings are confirmed also with other probes and in other electron-doped materials has still to be investigated.

The occurrence of changes in Fermi surface properties near optimal doping have also been analyzed by transport measurements (Dagan et al., 2004). Measurements of the Hall coefficient and the in-plane resistivity in the normal state show rapidly changing transport properties upon tuning the electron doping through the critical value $x_c \simeq 0.165$. These measurements have been interpreted as evidence for a quantum phase transition already significantly above optimal doping, although this interpretation has still to be unified with measurements of magnetic order.

b) hole-doped cuprates At low hole doping, high T_c superconductors may be characterized as doped insulators (Lee et al., 2006), with a Hall number $V/eR_H \equiv x$ equal to the number of holes (Ando et al., 2004), where R_H is the Hall coefficient, e is the electron charge and V is the volume per Cu atom. The overdoped metallic state is characterized by a single large hole Fermi surface whose volume contains $1 + x$ holes per Cu atom, as determined by ARPES and angle-dependent magnetoresistance measurements (Taillefer et al., 2009). What has remained unclear so far is how these materials evolve from one state to the other, i.e., what happens to the Fermi surface upon increasing doping from the underdoped to the overdoped side. Since two years ago, the debate about Fermi surface reconstruction in the underdoped cuprates attracted much interest by the observation of quantum oscillations in $\text{YBa}_2\text{Cu}_3\text{O}_y$ in very strong magnetic fields of up to 50 T or more (LeBoeuf et al., 2007).

An interpretation of these discoveries in terms of a semiclassical picture assuming a Landau quantization of states in a magnetic field leads to the interpretation of the oscillation frequency F in terms of a closed Fermi surface area enclosing a carrier density n , such that $F = n\Phi_0$, with the flux quantum Φ_0 (Taillefer et al., 2009). It is still under discussion whether these oscillations have to be interpreted as closed electron orbits, although several forms of density wave order have been proposed that might account for the formation of closed electron orbits in the underdoped cuprates (Millis and Norman, 2007, Harrison,

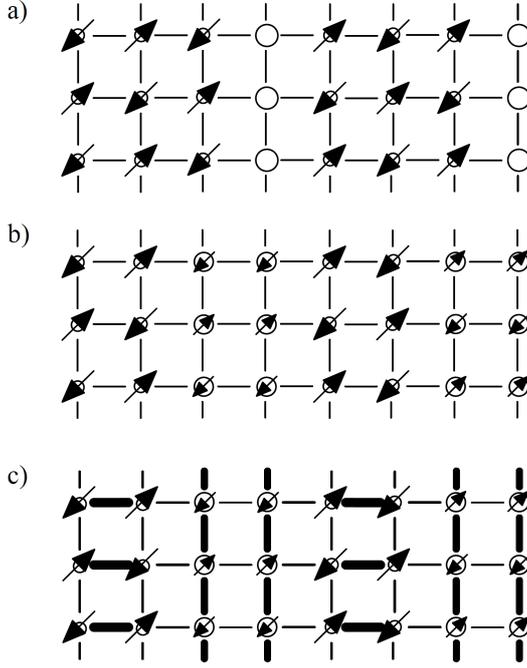


Figure 11.4: Real-space structure of a) site-centered and b),c) bond-centered stripes with period-4 (period-8) order in the charge (spin) sector. Shown are spin and charge distributions, with the circle radii corresponding to on-site hole densities. In panel c), showing “valence-bond” stripes, (Vojta, 2008b) the structure of spin-singlet bond modulations is shown as well which has a dominant d -wave form factor.

2009, Dimov et al., 2008). One particular proposal is Fermi surface reconstruction by static spin density wave (SDW) order (Millis and Norman, 2007, Harrison, 2009), which has indeed been confirmed in underdoped $\text{YBa}_2\text{Cu}_3\text{O}_y$ (Haug et al., 2009), with a local moment size growing strongly in applied magnetic fields. In some other cuprate materials, static order of spin or charge density has been observed as well (Vojta, 2009), and stripe order has been proposed to be of particular importance for the pseudogap phase and the normal state Nernst effect in cuprates (Choinière et al., 2009). In order to prepare our subsequent theoretical considerations, we review some of the fundamental aspects of stripe order in the cuprates in the following.

Stripe order

a) Definitions Stripe order occurs in a variety of different materials and manifestations, and its basic component is unidirectional order of charge or spin density, for which we synonymously use the term “stripe”. A description of stripe order requires the definition of two different order parameters which describe unidirectional modulations of the charge and spin degrees of freedom, respectively. We will characterize a spin density wave by a vector order parameter $\phi_{s\alpha}(\vec{r}, \tau)$, $\alpha = x, y, z$, with the spin density modulation given by

$$\langle S_\alpha(\vec{R}, \tau) \rangle = \text{Re} [e^{i\vec{Q}_s \cdot \vec{R}} \phi_{s\alpha}(\vec{R}, \tau)] \quad (11.3)$$

with an ordering wave vector \vec{Q}_s . A description of charge density wave order thus requires a scalar order parameter $\phi_c(\vec{r}, \tau)$, such that

$$\langle \rho(\vec{R}, \tau) \rangle = \rho_0 + \text{Re} [e^{i\vec{Q}_c \cdot \vec{R}} \phi_c(\vec{R}, \tau)] , \quad (11.4)$$

with a background density ρ_0 . In a Landau-Ginzburg-Wilson theory, a coupling $\lambda(\phi_c^* \phi_s^2 + h.c.)$ is symmetry-allowed if the ordering wavevectors fulfill $\vec{Q}_c = 2\vec{Q}_s$ (Zachar et al., 1998, Vojta, 2009). A collinear spin density wave therefore has an associated spin-singlet order parameter that describes a charge density wave of the general type (11.4) with a doubled ordering wave vector $2\vec{Q}_s$.

b) Experiments Stripe-order was first detected by Tranquada et al. (1995) in neutron scattering experiments on $\text{La}_{1.6-x}\text{Nd}_{0.4}\text{Sr}_x\text{CuO}_4$. Those experiments detected static spin correlations with an onset temperature of about 55K, which were peaked at wave vectors $\vec{Q}_{sx} = 2\pi(0.5 \pm \epsilon_s, 0.5)$ and $\vec{Q}_{sy} = 2\pi(0.5, 0.5 \pm \epsilon_s)$. At the same time both neutron and X-ray scattering found another set of superlattice peaks at $\mathbf{Q}_{cx} = 2\pi(\pm\epsilon_c, 0)$ and $\mathbf{Q}_{cy} = 2\pi(0, \pm\epsilon_c)$ with $\epsilon_s = 2\epsilon_c$. Meanwhile, such spin and charge orders have also been confirmed to exist in $\text{La}_{1.8-x}\text{Eu}_{0.2}\text{Sr}_x\text{CuO}_4$ and $\text{La}_{2-x}\text{Ba}_x\text{CuO}_4$ (LBCO). In $\text{La}_{1.8-x}\text{Eu}_{0.2}\text{Sr}_x\text{CuO}_4$ and $\text{La}_{1.6-x}\text{Nd}_{0.4}\text{Sr}_x\text{CuO}_4$, stripe order remains stable up to $x = 0.20$ (Vojta, 2009), while in LBCO, stripe order is confined to a small region near $x = 1/8$. At this particular doping stripe order is most stable and has the ordering pattern shown in Fig. 11.4a if the modulation is centered at the lattice sites, or the pattern depicted in Fig. 11.4b if the modulation pattern is centered on the bonds.

In other cuprate families, static incommensurate spin order is rarely detected, with the exception of strongly underdoped $\text{YBa}_2\text{Cu}_3\text{O}_y$ (Haug et al., unpublished). Strong magnetic fields enhance the local moment size measured by neutron scattering, while reports of charge order in $\text{YBa}_2\text{Cu}_3\text{O}_y$ by Mook et al. (2002) remained inconclusive.

Charge order has also been detected using scanning tunneling microscopy (STM) techniques, including the detection of static short range modulations in the charge sector on the surface of $\text{Bi}_2\text{Sr}_2\text{CaCu}_2\text{O}_{8+\delta}$ (Howald et al., 2003) and $\text{Ca}_{2-x}\text{Na}_x\text{CuO}_2\text{Cl}_2$ (Kohsaka et al., 2007) samples. A bond-centered nature of these modulations is apparent in this data, and a description in terms of a d -wave like modulation of the kinetic energy compares well with experiment (Vojta, 2008b) – the resulting ordering pattern is sketched in Fig. 11.4c. These two materials provide furthermore examples for the existence of charge order without coexisting long-range magnetic order, although spin-glass-like magnetism has been reported to exist in $\text{Ca}_{2-x}\text{Na}_x\text{CuO}_2\text{Cl}_2$ (Ohishi et al., 2005).

11.2 Nernst effect and pseudogap

The Nernst effect is the generation of a transverse voltage arising in response to an applied thermal gradient in the presence of a perpendicular magnetic field. A key indication that the normal state of the cuprate superconductors is aberrant came from the pioneering measurements of the Nernst effect by Ong and co-workers (Xu et al., 2000). Before this discovery, the Nernst effect had been studied in both conventional and high- T_c superconductors (Behnia, 2009). Since then, the Nernst effect has become an important probe for an improved understanding of pseudogap physics. Below, we give a separated discussion of some important experimental results for electron- and hole-doped cuprate materials.

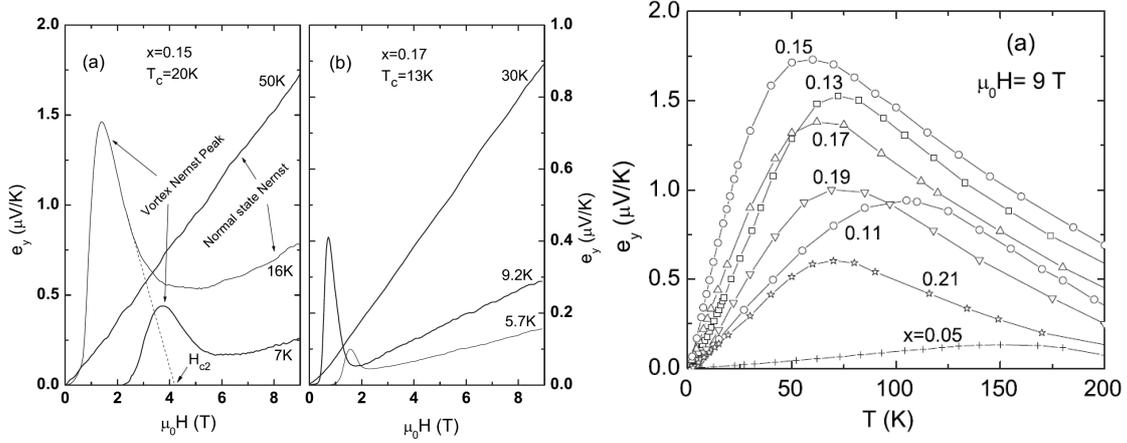


Figure 11.5: left panel: Nernst signal as a function of magnetic field in an optimally doped ($x = 0.15$) and an overdoped ($x = 0.17$) PCCO film. For temperatures corresponding to the normal state, the signal is linear in the applied field. Below the superconducting transition temperature T_c , a peak structure as function of magnetic field emerges that is usually interpreted as a Nernst signal caused by vortex movement. right panel: Temperature dependence of the Nernst signal for samples with different Ce doping x , measured in $B = 9$ T. At low temperatures, the signal is linear in T as in a Fermi liquid. The maximal value of the signal is largest near optimal doping $x \simeq 0.15$. Figures taken from Li and Greene (2007b).

a) electron-doped cuprates Among the cuprates, the electron-doped materials offer the unique possibility to suppress vortex contributions to the Nernst signal by external magnetic fields of less than 10 T. Very detailed measurements of the normal state Nernst signal in dependence of temperature, magnetic field and doping have been performed in thin PCCO films (Li and Greene, 2007b). Some results of these experiments are shown in Fig. 11.5. These show that the Nernst signal is linear in magnetic field up to the highest measured fields of $\mathcal{O}(10)$ T, as well as linear in temperature up to around $T \approx 50$ K, as expected for a Nernst signal resulting from charged fermionic quasiparticles (Behnia, 2009). Close to optimal doping, the signal at $B = 9$ T has the same sign and order of magnitude than the maximal vortex Nernst signal at the same temperature and lower magnetic field strength. It is apparent that the normal state Nernst signal is significantly enhanced near optimal doping, similar to the rapid change of the Hall effect and the in-plane electrical resistivity observed in this doping region (Dagan et al., 2004).

b) hole-doped cuprates Vortex movement caused by the application of a thermal gradient is a well known source for a large positive Nernst signal in type-II superconductors.

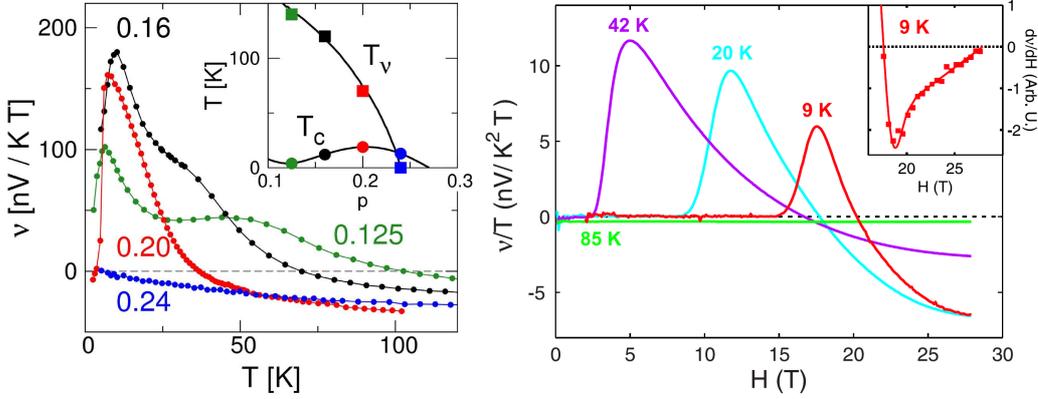


Figure 11.6: Left panel: Temperature dependence of the Nernst coefficient $\nu(T)$ for different dopings in Eu-LSCO [$x=1/8$ in green; $x=0.16$ in black] and Nd-LSCO [$x=0.20$ in red; $x=0.24$ in blue] at $B = 10 \text{ T}$. At doping $x = 1/8$, two different contributions to the Nernst signal are clearly visible as two different peak structures. These peaks merge gradually upon increasing doping towards the critical value $x = 0.24$, where the charge- and spin-density wave ordering temperatures extrapolate to zero (Taillefer et al., 2009). Figure from Choinière et al. (2009). Right panel: Nernst coefficient in $\text{YBa}_2\text{Cu}_3\text{O}_y$ plotted as ν/T vs H , for temperatures as indicated. The inset shows the derivative $d\nu/dH$ of the 9-K isotherm, showing that $d\nu/dH \rightarrow 0$ at $H \rightarrow 28 \text{ T}$. Figure from Chang et al. (2009).

In conventional superconductors, fluctuations in the phase $\theta(r)$ of the superconducting wavefunction $\psi \exp[i\theta(r)]$ incur a sizable cost in energy (the phase stiffness energy is large). Hence $\theta(r)$ is uniform in the absence of field and currents. In the underdoped copper oxides, however, the small superfluid density n_s implies a small phase stiffness energy. The Meissner state is readily destroyed by strong phase fluctuations. This enables a diffusion of vortices, and a common interpretation of Nernst effect measurements in this regime is that diffusing vortices cause a comparatively large Nernst signal (Xu et al., 2000). Theoretical treatments have interpreted the large positive Nernst signal well above the superconducting T_c in terms of a liquid of vortices in the superconducting order. *Amplitude fluctuations* (i.e. in Gaussian approximation) (Ussishkin et al., 2002) of the pairing have been considered as a source of an enhanced Nernst signal as well. Interestingly, the onset temperature of the Nernst signal seems to lie below the T^* line marking the boundary of the pseudogap phase (Johannsen et al., 2007). Recent experiments in different hole-doped cuprate materials have revealed an additional peak in the temperature dependence of the Nernst signal near hole doping $x = 1/8$ which seems to have a different origin than fluctuating superconductivity, see left panel in Fig. 11.6. In $\text{La}_{1.8-x}\text{Eu}_{0.2}\text{Sr}_x\text{CuO}_4$, an enhanced positive Nernst signal has been measured far above the superconducting ordering temperature, with an onset temperature that seems to follow the onset of charge order observed in this material (Choinière et al., 2009). A similar result has been obtained for the higher hole doping

$x = 0.2$ in $\text{La}_{1.6-x}\text{Nd}_{0.4}\text{Sr}_x\text{CuO}_4$, showing a positively enhanced Nernst signal at elevated temperatures, being small and negative at $x = 0.24$ where static stripe order is absent. Again, static stripe order exists in the sample with $x = 0.20$ and was argued to be related to the origin of the enhanced Nernst signal.

Subsequent experiments by Chang et al. (2009) demonstrated similar behavior also in $\text{YBa}_2\text{Cu}_3\text{O}_y$ in strong external magnetic fields. As depicted in the left panel of Fig. 11.6, upon increasing magnetic field strength up to 28 T, a large negative Nernst signal has been observed at temperatures down to 9 K. The observed saturation of the Nernst coefficient in high magnetic fields has been interpreted as a suppression of superconducting fluctuations, such that the Nernst signal results purely from the field-induced normal state. The fact that these measurements were performed at $x = 0.12$ have led to the suggestion that field-induced spin-density wave order might be responsible for the negative and enhanced Nernst signal. Furthermore, the Seebeck coefficient in $x = 0.12$ $\text{YBa}_2\text{Cu}_3\text{O}_y$ has a salient zero crossing at nearly the same temperature $T \simeq 50$ K than the 124 cuprate family has, and it has been proposed that the Fermi surfaces in $\text{YBa}_2\text{Cu}_3\text{O}_y$ and the 124 cuprates reconstruct due to similar mechanisms (Chang et al., 2009).

11.3 Outline

In the introduction to this chapter, we motivated that translational symmetry breaking in form of density wave order is of timely interest in order to investigate various observations of Fermi surface reconstruction in recent experiments on cuprate materials. On the other hand, we noted that recent observations of a strongly enhanced Nernst effect in cuprate materials in parameter regimes where stripe order or SDW order have been observed are unlikely to be explained by fluctuations of superconducting order. We will merge these aspects in the following chapters by considering quasiparticle models for stripe and SDW order in cuprates and analyzing the resultant quasiparticle Nernst effect.

In the next chapter, we will analyze the normal state Nernst effect in the electron-doped cuprates in terms of a quasiparticle model for commensurate (π, π) spin-density wave order. This analysis will be performed within a semiclassical Boltzmann approach. In chapter 13, we will investigate the influence of incommensurate SDW and stripe order, as appropriate for the hole-doped cuprates. After formulating mean-field models for incommensurate SDW and stripe order, we discuss the Fermi surface reconstruction induced by these types of orders, before concluding with their influences on the Nernst signal.

Chapter 12

Normal-state Nernst effect in the electron-doped cuprates

12.1 Model

In cuprate materials, it is convenient to approximate the electronic dispersion by electrons moving on a square lattice with the tight-binding dispersion

$$\varepsilon_{\mathbf{k}} = -2t_1(\cos k_x + \cos k_y) + 4t_2 \cos k_x \cos k_y - 2t_3(\cos 2k_x + \cos 2k_y) , \quad (12.1)$$

with a corresponding non-interacting Hamiltonian $H_0 = \sum_{\mathbf{k}\sigma} \varepsilon_{\mathbf{k}} c_{\mathbf{k}\sigma}^\dagger c_{\mathbf{k}\sigma}$. This dispersion fits well Fermi surfaces measured in photoemission experiments, which are well reproduced by the parameters $t_1 = 0.38$ eV, $t_2 = 0.32 t_1$, and $t_3 = 0.5 t_2$ (Andersen et al., 1995). Important modifications to the Fermi liquid ground state can arise due to local Coulomb repulsion between the conduction electrons, which is minimally described by the Hubbard interaction

$$H_{el-el} = \frac{U}{N} \sum_{\mathbf{k}, \mathbf{k}', \mathbf{q}, \sigma} c_{\mathbf{k}, \sigma}^\dagger c_{\mathbf{k}+\mathbf{q}, \sigma} c_{\mathbf{k}', -\sigma}^\dagger c_{\mathbf{k}'-\mathbf{q}, -\sigma} , \quad (12.2)$$

where U is the on-site Coulomb interaction and N is the number of conduction electrons per unit volume. The full Hamiltonian is given by the Hubbard Hamiltonian $H = H_0 + H_{el-el}$, and the local repulsion between electrons of opposite spin leads to an enhanced response to an external magnetic field, which we describe in random phase approximation (RPA) by the susceptibility (Grüner, 1994)

$$\chi_{\mathbf{q}} = \frac{\chi_0(\mathbf{q})}{1 - U \chi_0(\mathbf{q}) / 2\mu_B^2} , \quad (12.3)$$

where $\chi_0(\mathbf{q})$ is the susceptibility in absence of Coulomb interactions and μ_B is the Bohr magneton. Depending on the dispersion $\varepsilon_{\mathbf{k}}$, $\chi_0(\mathbf{q})$ might be strongly peaked at a wave vector $\mathbf{q} = \mathbf{Q}$, leading to the formation of a spin-density wave with modulation wave vector \mathbf{Q} . Such a type of ground state can be described within a mean-field theory for the

Hubbard model. Spin-density wave order is described by the complex order parameter

$$\Delta = \frac{U}{N} \frac{1}{V} \sum_{\mathbf{k}} \langle c_{\mathbf{k}\uparrow}^\dagger c_{\mathbf{k}+\mathbf{Q},\uparrow} \rangle = \frac{U}{N} \frac{1}{V} \sum_{\mathbf{k}} \langle c_{\mathbf{k}\downarrow}^\dagger c_{\mathbf{k}+\mathbf{Q},\downarrow} \rangle, \quad (12.4)$$

which can be easily used for a mean-field decoupling of the Hubbard-interaction. Here, $\langle \cdot \rangle$ denotes averaging with respect to the equilibrium density matrix $e^{-\beta H}$ of the Hubbard model. By replacing $c_{\mathbf{k},\sigma}^\dagger c_{\mathbf{k}+\mathbf{q},\sigma} \rightarrow \langle c_{\mathbf{k}\sigma}^\dagger c_{\mathbf{k}+\mathbf{Q},\sigma} \rangle \delta_{\mathbf{Q},\mathbf{q}}$ in Eq. (12.2), the mean-field amplitude Δ can be determined self-consistently by minimizing the free energy $-\ln[\text{tr}\{e^{-\beta H}\}]/\beta$ with respect to Δ . The resulting mean-field Hamiltonian becomes

$$\begin{aligned} H_{MF} &= \sum_{\mathbf{k}\sigma} \epsilon_{\mathbf{k}} c_{\mathbf{k}\sigma}^\dagger c_{\mathbf{k}\sigma} + \frac{2N}{U} |\Delta|^2 \\ &+ \sum_{\mathbf{k}\sigma} \Delta [c_{\mathbf{k}+\mathbf{Q},\uparrow}^\dagger c_{\mathbf{k},\uparrow} + c_{\mathbf{k}+\mathbf{Q},\downarrow}^\dagger c_{\mathbf{k},\downarrow} + \text{h.c.}]. \end{aligned} \quad (12.5)$$

Using the unitary transformation $\gamma_{\mathbf{k}\sigma}^+ = u_{\mathbf{k}} c_{\mathbf{k}\sigma} + v_{\mathbf{k}} c_{\mathbf{k}+\mathbf{Q}\sigma}$ and $\gamma_{\mathbf{k}\sigma}^- = u_{\mathbf{k}} c_{\mathbf{k}\sigma} - v_{\mathbf{k}} c_{\mathbf{k}+\mathbf{Q}\sigma}$, with real coefficients $v_{\mathbf{k}}$ and $u_{\mathbf{k}}$ fulfilling $v_{\mathbf{k}}^2 + u_{\mathbf{k}}^2 \equiv 1$, the resulting quasiparticle Hamiltonian becomes

$$H_{MF} = \sum_{\mathbf{k}\sigma, \alpha=\pm} E_{\mathbf{k}}^\alpha \gamma_{\mathbf{k}\sigma}^{\alpha\dagger} \gamma_{\mathbf{k}\sigma}^\alpha, \quad (12.6)$$

with the quasiparticle dispersion given by

$$E_{\mathbf{k}}^\pm = \frac{1}{2} \left(\epsilon_{\mathbf{k}} + \epsilon_{\mathbf{k}+\mathbf{Q}} \pm \sqrt{(\epsilon_{\mathbf{k}} - \epsilon_{\mathbf{k}+\mathbf{Q}})^2 + 4|\Delta|^2} \right). \quad (12.7)$$

For commensurate $\mathbf{Q} = (\pi, \pi)$ SDW order, the allowed wave vectors \mathbf{k} are in the reduced antiferromagnetic Brillouin zone defined by $|k_x + k_y| \leq \pi$, in analogy to the discussion given in Fig. 5.5. This mean-field model can be readily applied to theoretically describe a SDW transition in electron-doped cuprates as a function of electron doping. For the analysis of transport equations, it is important to define the quasiparticle velocities

$$v_{\mathbf{k}}^\pm = \frac{1}{\hbar} \nabla_{\mathbf{k}} E_{\mathbf{k}} / \hbar. \quad (12.8)$$

Experimentally, the order parameter amplitude Δ is tuned by the concentration of electron carriers, and we will assume the mean-field dependence

$$\Delta(x)[\text{eV}] = 0.7 \sqrt{1 - \frac{x}{x_c}}. \quad (12.9)$$

This modeling leads to a rapid opening of the SDW gap at $x = x_c$, leading to the Fermi surface reconstruction shown in Fig. 12.1, which is in qualitative agreement with ARPES data (Armitage et al., 2002). Our modeling can be further justified by previous experimental and theoretical analyses of the Hall effect. Hall measurements by Onose et al. (2001) indicate that hole pockets in the Fermi surface are present for Ce doping $0.1 < x < x_c$. Moreover, qualitative consistency with our particular mean-field model has been achieved by choosing an amplitude $\Delta = 0.7 \text{ eV}$ that explains to some extent the evolution of the Hall coefficient upon Ce doping (Lin and Millis, 2005).

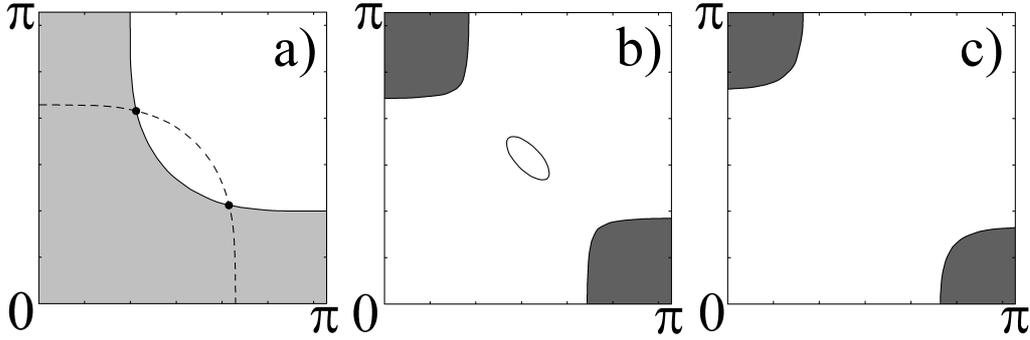


Figure 12.1: Evolution of the Fermi surface upon decreasing electron doping x . To distinguish holes from electrons, electrons from the upper band $E_{\mathbf{k}}^+$ are dark shaded, light shading contains all electrons from both bands. At $x = x_c = 0.165$, a gap opens at the points where the dispersion crosses its translation by the wave vector (π, π) , see a). A hole pocket centered at $(\pi/2, \pi/2)$ is present for $x_1 < x < x_c$ (with $x_1 = 0.145$), as shown in b) for $x = 0.15$. For $x < x_1$, only electron-like pockets remain, as shown in c) for $x = 0.12$.

12.2 Semiclassical approach

In presence of external electric and magnetic fields $\mathbf{E}(\mathbf{r}, t)$ and $\mathbf{B}(\mathbf{r}, t)$, under certain assumptions a Bloch electron with dispersion $\epsilon_n(\mathbf{k})$ and band label n evolves according to the equations of motion (Ashcroft and Mermin (1976), chapter 12)

$$\begin{aligned}\dot{\mathbf{r}} &= \mathbf{v}_n(\mathbf{k}) = \frac{1}{\hbar} \frac{\partial \epsilon_n(\mathbf{k})}{\partial \mathbf{k}} \\ \hbar \dot{\mathbf{k}} &= -e \left[\mathbf{E}(\mathbf{r}, t) + \frac{1}{c} \mathbf{v}_n(\mathbf{k}) \times \mathbf{H}(\mathbf{r}, t) \right].\end{aligned}$$

E.g., these equations of motion are strictly valid only in absence of translational symmetry breaking of the crystal, caused by impurities, e.g..

Range of validity

We will assume in the following that effects of translational symmetry breaking cause scattering processes that are described by a relaxation time $\tau_{\mathbf{k}}$ that measures the mean time between two scattering events of a Bloch electron with wave vector \mathbf{k} . At asymptotically low temperatures, phonons or other thermally excited degrees of freedom are assumed to have negligible influence on the relaxation time $\tau_{\mathbf{k}}$. It is then sensible to assume that the relaxation time is dominated by randomly distributed impurities.¹ In the experimentally accessible normal state regime of $\text{Bi}_2\text{Sr}_2\text{CaCu}_2\text{O}_{8+\delta}$, a scattering rate proportional to temperature has been reported for most parts of the Brillouin zone, excluding a regime of low

¹We will comment on possible shortcomings of these assumptions later on when comparing our results to experiments.

temperatures where the normal state is masked by superconductivity. At lowest temperatures, we will assume that the scattering rate is independent of temperature, unless noted otherwise.

Besides from scattering on impurities, also Bragg scattering on incommensurate SDW order has a characteristic scattering length, given by the inverse of the momentum scale $p_\Delta = \Delta/v_F$. Coherent backscattering of the conduction electrons is expected to interfere with impurity scattering if the mean free path l drops below the scattering length p_Δ^{-1} , such that $p_\Delta l \lesssim 1$. In analogy, the interference of multiple scattering processes caused by *the same type of scattering mechanism* is negligible if the characteristic Fermi momentum scale k_F of the quasiparticles is large enough, described by the relations $k_F l \gtrsim 1$ and $k_F p_\Delta^{-1} \gtrsim 1$. Analogous to Zener tunneling, magnetic fields may lead to tunneling through bandgaps, assuming that the band structure itself is not modified by the magnetic field. The transmission amplitude for this process is then given by (Blount, 1962)

$$\alpha = \exp\left(-\frac{\pi}{2} \frac{\Delta^2}{e\hbar B |v_x v_y|}\right), \quad (12.10)$$

with the Fermi velocities $v_x, v_y \approx v_F$ evaluated at the opening of the SDW gap. It has been shown by Lin and Millis (2005) that the condition for absence of the magnetic breakdown is, in order of magnitude, that the inverse magnetic length $p_B = 2\pi(\pi B/\Phi_0)^{1/2}$ be less than the gap momentum scale p_Δ , $p_B < p_\Delta$, with the superconducting flux quantum $\Phi_0 = \frac{hc}{2e}$

Interband transitions may be explicitly contained in the definition of the current operator. In terms of the quasiparticle spinor

$$\psi_{\mathbf{k}\sigma} = (\gamma_{\mathbf{k}\sigma}^+, \gamma_{\mathbf{k}\sigma}^-)^T \quad (12.11)$$

a compact formulation of the current operator is given by

$$\mathbf{j} = -e \sum_{\sigma} \int_{RBZ} \frac{d^2\mathbf{k}}{(2\pi)^2} \psi_{\mathbf{k},\sigma}^\dagger \begin{pmatrix} \nabla_{\mathbf{k}} E_{\mathbf{k}}^+ / \hbar & v_{\mathbf{k}}^{inter} \\ v_{\mathbf{k}}^{inter} & \nabla_{\mathbf{k}} E_{\mathbf{k}}^- / \hbar \end{pmatrix} \psi_{\mathbf{k},\sigma}. \quad (12.12)$$

For a Boltzmann transport description, the semiclassical equations of motion have to be fulfilled, requiring the absence of interband transitions. Those are mediated by the off-diagonal elements (Oganesyan and Ussishkin, 2004)

$$v_{\mathbf{k}}^{inter} = -\frac{1}{\hbar} \frac{[\nabla_{\mathbf{k}} \epsilon_{\mathbf{k}} - \nabla_{\mathbf{k}} \epsilon_{\mathbf{k}+\mathbf{Q}}] \Delta}{\sqrt{(\epsilon_{\mathbf{k}} - \epsilon_{\mathbf{k}+\mathbf{Q}})^2 + 4\Delta^2}}. \quad (12.13)$$

In absence of external fields, scattering events between bands are mediated either by thermal excitations or scattering from disorder, being negligible if the spin-density wave gap 2Δ is larger than $k_B T$ and \hbar/τ , respectively. However, the spin density wave gap itself will be destroyed already at the ordering temperature $T_{SDW} \ll \hbar\Delta/k_B$, as can be seen by comparing the respective temperatures $T_{SDW} \approx 250\text{K}$ (Yu et al., 2007) and $\hbar\Delta/k_B \approx 16000\text{K}$ occurring in the far underdoped region. Within our description, only close to the QCP, the gap might be small enough to make such inter-band processes important, and we give

estimates for the conditions for the importance of magnetic breakdown in the following. Using the mean-field dependence (12.9) of the SDW order parameter and considering the exponent of the transmission amplitude to be equal -1 , magnetic breakdown is estimated to be important in the doping range

$$\Delta x \approx e\hbar v_F^2 B / (0.7eV)^2 x_c \approx 7.1 \times 10^{-5} B x_c . \quad (12.14)$$

Here we assumed an isotropic Fermi velocity equal to the *universal Fermi velocity* $v_F = 2.3 \times 10^7$ cm/s (Zhou et al., 2003). Moreover, inter-band transitions due to impurity scattering are estimated to be of importance for $\Delta \lesssim \frac{\hbar}{\tau}$, being fulfilled in the doping range

$$\Delta x \approx \left(\frac{\hbar}{\tau}\right)^2 \frac{x_c}{(0.7eV)^2} \approx 8.6 \times 10^{-3} \left(\frac{10^{-14}s}{\tau}\right)^2 x_c . \quad (12.15)$$

Finally, thermal excitations will destroy the spin density wave gap at an ordering temperature for which we assume the mean-field dependence

$$T_{\text{SDW}} = T_0 \sqrt{1 - \frac{x}{x_c}} . \quad (12.16)$$

Upon equating $T = T_{\text{SDW}}$, it is readily seen that below doping x_c the gap will be destroyed by thermal excitations in a doping range of width

$$\Delta x \simeq x_c (T/T_0)^2 . \quad (12.17)$$

Boltzmann equation approach

After our discussion of the validity of semiclassical transport theory within the relaxation-time approximation, we proceed with a description of our transport theory for the Nernst effect.

The Nernst effect is measured as a transverse electrical response to a thermal gradient $\vec{\nabla}T$ in presence of a perpendicular magnetic field. The applied fields are assumed to be weak, such that the electrical field can be understood as a weak spatial dependence of the chemical potential μ , defining the electrochemical potential by the relation

$$2e\vec{E} = -\vec{\nabla}\mu , \quad (12.18)$$

while the temperature gradient describes a similar weak spatial dependence in T . Even in linear response, electrical and thermal effects imply the existence of each other, and a proper description of a linear response of the system needs to include an electrical current \vec{J} and a thermal current \vec{Q} into the transport equations, described by the matrix equation

$$\begin{pmatrix} \vec{J} \\ \vec{Q} \end{pmatrix} \begin{pmatrix} \hat{\sigma} & \hat{\alpha} \\ T\hat{\alpha} & \hat{\kappa} \end{pmatrix} = \begin{pmatrix} \vec{E} \\ -\vec{\nabla}T \end{pmatrix} . \quad (12.19)$$

Appropriate boundary conditions have to be applied to the transport equation 12.19 in order to solve for the Nernst response defining the relation between electrical field and thermal gradient in the sample,

$$\vec{E} = -\hat{\partial}\vec{\nabla}T . \quad (12.20)$$

This thermally induced electrical field is measured in absence of charge current ($\vec{J} = 0$), and Eq. (12.19) yields then the relation

$$\hat{\vartheta} = -\hat{\sigma}^{-1}\hat{\alpha} \quad (12.21)$$

between Nernst response and electrical / thermoelectrical response. For a thermal gradient $\vec{\nabla}T$ along the x -axis, the Nernst signal is readily obtained as the transverse response coefficient

$$\vartheta_{yx} = -\frac{\sigma_{xx}\alpha_{yx} - \sigma_{yx}\alpha_{xx}}{\sigma_{xx}\sigma_{yy} - \sigma_{xy}\sigma_{yx}}, \quad (12.22)$$

while the diagonal entry ϑ_{xx} describes the thermopower

$$\vartheta_{xx} = \frac{\alpha_{xx}}{\sigma_{xx}}. \quad (12.23)$$

This expression can be further simplified in presence of small magnetic fields or certain symmetries of the unit cell.

a) Transport equation The derivation of a Boltzmann transport equation assumes the existence of a distribution function $f_{\mathbf{k}}(\mathbf{r})$ which measures the number of carriers with momentum \mathbf{k} near the coordinate \mathbf{r} . This distribution function can change in time due to diffusion processes $\dot{f}_{\mathbf{k}}|_{\text{diff}} = -\mathbf{v}_{\mathbf{k}} \cdot \frac{\partial f_{\mathbf{k}}}{\partial \mathbf{r}}$, external fields $\dot{f}_{\mathbf{k}}|_{\text{field}} = -\frac{e}{\hbar} [\mathbf{E} + \frac{1}{c}\mathbf{v}_{\mathbf{k}} \times \mathbf{H}] \cdot \frac{\partial f_{\mathbf{k}}}{\partial \mathbf{k}}$ (Ashcroft and Mermin, 1976) that change momentum according to Eq. (12.10), and the rate $\dot{f}_{\mathbf{k}}|_{\text{coll}}$ that is due to collisions caused by lattice defects. In a steady state all these contributions add up to a vanishing total rate of change $\dot{f}_{\mathbf{k}}|_{\text{tot}}$ and we have

$$\dot{f}_{\mathbf{k}}|_{\text{tot}} = \dot{f}_{\mathbf{k}}|_{\text{diff}} + \dot{f}_{\mathbf{k}}|_{\text{field}} + \dot{f}_{\mathbf{k}}|_{\text{coll}} = 0. \quad (12.24)$$

We shall assume that the deviation from equilibrium is small such that the rate equation (12.24) can be linearized in the driving fields \mathbf{E} and \mathbf{B} . Furthermore, we assume a weak uniform temperature gradient, such that $\mathbf{v}_{\mathbf{k}} \cdot \frac{\partial f_{\mathbf{k}}}{\partial \mathbf{r}} \simeq \mathbf{v}_{\mathbf{k}} \cdot \frac{\partial f_{\mathbf{k}}^0}{\partial T} \vec{\nabla}T$. Finally, we will make use of the relaxation time approximation

$$\dot{f}_{\mathbf{k}}|_{\text{coll}} = -\frac{f(\mathbf{k}) - f_0(\mathbf{k})}{\tau_{\mathbf{k}}}, \quad (12.25)$$

where $f_0(\mathbf{k})$ is the equilibrium distribution function, given by the Fermi function $f_0(\mathbf{k}) = 1/(1 + \exp(-\beta\varepsilon_{\mathbf{k}}))$. This approximation becomes exact either for isotropic scattering or for elastic scattering in weak fields (Lundstrom, 2000) and is therefore appropriate for the impurity scattering dominated regime we defined above. The general form of the relaxation time is (Ashcroft and Mermin, 1976)

$$\frac{1}{\tau_{\mathbf{k}}} = \int \frac{d^d \mathbf{k}'}{(2\pi)^d} W_{\mathbf{k},\mathbf{k}'} [1 - f_{\mathbf{k}}] \quad (12.26)$$

For a weak scattering potential \hat{U} , the transition rate $W_{\mathbf{k},\mathbf{k}'}$ ² can be obtained by applying Fermi's "Golden Rule"

$$W_{\mathbf{k},\mathbf{k}'} = \frac{2\pi}{\hbar} \delta(\epsilon_{\mathbf{k}} - \epsilon_{\mathbf{k}'}) |\langle \mathbf{k} | \hat{U} | \mathbf{k}' \rangle|^2, \quad (12.27)$$

where $|\mathbf{k}\rangle$ is a Bloch state. For isotropic dispersion $\epsilon_{\mathbf{k}} \sim k^2$, $|\langle \mathbf{k} | \hat{U} | \mathbf{k}' \rangle|^2$ will not depend on \mathbf{k} after averaging a random distribution of impurities. Then, the relaxation time is only a function of the dispersion, $\tau(\epsilon_{\mathbf{k}})$, describing pure *s*-wave scattering. We will assume this case in the following. Altogether, the rate equation (12.24) simplifies to the Boltzmann equation

$$\left[-\frac{e}{\hbar c} (\mathbf{v}_{\mathbf{k}} \times \mathbf{B}) \cdot \nabla_{\mathbf{k}} + \frac{1}{\tau(\epsilon_{\mathbf{k}})} \right] g_{\mathbf{k}} = \left[-e \mathbf{v}_{\mathbf{k}} \mathbf{E} - (\epsilon_{\mathbf{k}} - \mu) \mathbf{v}_{\mathbf{k}} \frac{\nabla_{\mathbf{r}} T}{T} \right] \left(-\frac{\partial f_{\mathbf{k}}^0}{\partial \epsilon_{\mathbf{k}}} \right), \quad (12.28)$$

where we introduced the deviation from the equilibrium distribution function, $g(\mathbf{k}) = f(\mathbf{k}) - f_0(\mathbf{k})$. The non-equilibrium distribution function $g(\mathbf{k})$ is now obtained as

$$g_{\mathbf{k}} = A_{\mathbf{k}}^{-1} \left[-e \mathbf{v}_{\mathbf{k}} \mathbf{E} - (\epsilon_{\mathbf{k}} - \mu) \mathbf{v}_{\mathbf{k}} \frac{\nabla_{\mathbf{r}} T}{T} \right] \left(-\frac{\partial f_{\mathbf{k}}^0}{\partial \epsilon_{\mathbf{k}}} \right) \quad (12.29)$$

where the operator

$$A_{\mathbf{k}} = \left[-\frac{e}{\hbar c} (\mathbf{v}_{\mathbf{k}} \times \mathbf{B}) \cdot \nabla_{\mathbf{k}} + \frac{1}{\tau_{\mathbf{k}}} \right] \quad (12.30)$$

has been defined.

b) Transport coefficients Using the function $g(\mathbf{k})$ – obtained as a solution to the Boltzmann equation (12.28) – the electrical and thermal currents \mathbf{J} and \mathbf{Q} are given by

$$\begin{aligned} \mathbf{J} &= -e \sum_{\mathbf{k}} \mathbf{v}_{\mathbf{k}} g_{\mathbf{k}} \\ \mathbf{Q} &= \sum_{\mathbf{k}} \mathbf{v}_{\mathbf{k}} (\epsilon_{\mathbf{k}} - \mu) g_{\mathbf{k}}. \end{aligned} \quad (12.31)$$

According to Eq. (12.19), the transport tensors are then obtained from

$$\begin{aligned} \sigma_{\mu\nu} &= 2e^2 \sum_{\mathbf{k}} v_{\mathbf{k}}^{\mu} A_{\mathbf{k}}^{-1} v_{\mathbf{k}}^{\nu} \left(-\frac{\partial f_{\mathbf{k}}^0}{\partial \epsilon_{\mathbf{k}}} \right) \\ \alpha_{\mu\nu} &= -\frac{2e}{T} \sum_{\mathbf{k}} v_{\mathbf{k}}^{\mu} (\epsilon_{\mathbf{k}} - \mu) A_{\mathbf{k}}^{-1} v_{\mathbf{k}}^{\nu} \left(-\frac{\partial f_{\mathbf{k}}^0}{\partial \epsilon_{\mathbf{k}}} \right) \end{aligned} \quad (12.32)$$

Now $A_{\mathbf{k}}^{-1}$ can be arranged as a perturbative expansion in the magnetic field \mathbf{B} (Ziman, 1960) in order to obtain transport coefficients that do not depend on \mathbf{B} . Define $A_{\mathbf{k}} = K_{\mathbf{k}} + M_{\mathbf{k}}^B$ where $K_{\mathbf{k}} = \tau_{\mathbf{k}}^{-1}$ and $M_{\mathbf{k}}^B$ the rest. Then

$$A_{\mathbf{k}}^{-1} = K_{\mathbf{k}}^{-1} - K_{\mathbf{k}}^{-1} M_{\mathbf{k}}^B K_{\mathbf{k}}^{-1} + K_{\mathbf{k}}^{-1} M_{\mathbf{k}}^B K_{\mathbf{k}}^{-1} M_{\mathbf{k}}^B K_{\mathbf{k}}^{-1} + \mathcal{O}(B^3). \quad (12.33)$$

² $\frac{dt d\mathbf{k}'}{(2\pi)^d} W_{\mathbf{k},\mathbf{k}'}$ describes the probability for a transition into a volume element $d\mathbf{k}'$ of wave vectors around \mathbf{k}' during the differential time dt .

The first term in this expansion defines the zero-field longitudinal thermal and electrical DC conductivities, while the off-diagonal components σ_{yx} and α_{yx} vanish to zeroth order in B . The thermal and electrical Hall conductivities σ_{yx} and α_{yx} are therefore obtained from the second term in (12.33), which is proportional to B . A justification of this expansion is given if the momentum scale $a = \frac{\pi l B}{\Phi_0}$ is smaller than all other momentum scales l^{-1} , p_B , p_Δ and p_0 , as detailed by Lin and Millis (2005). Considering our assumptions $p_\Delta l \lesssim 1$ and $p_B < p_\Delta$ requires then only one additional condition $a < p_\Delta$ for the validity of the Zener-Jones expansion. Using the expansion (12.33) and neglecting all terms of $\mathcal{O}(B^2)$, the transport tensors are

$$\begin{aligned}
\alpha_{xx} &= \frac{2e}{T} \sum_{\mathbf{k}, \alpha=\pm} \frac{\partial f_{\mathbf{k}}^0}{\partial E_{\mathbf{k}}^\alpha} (E_{\mathbf{k}}^\alpha - \mu) \tau_{\varepsilon_{\mathbf{k}}} (\mathbf{v}_{\mathbf{k}}^x)^2 \\
\alpha_{xy} &= \frac{2e^2 B}{T \hbar c} \sum_{\mathbf{k}, \pm} \frac{\partial f_{\mathbf{k}}^0}{\partial E_{\mathbf{k}}^\alpha} (E_{\mathbf{k}}^\alpha - \mu) \tau_{\varepsilon_{\mathbf{k}}}^2 v_{\mathbf{k}}^x \left[\mathbf{v}_{\mathbf{k}}^y \frac{\partial \mathbf{v}_{\mathbf{k}}^y}{\partial k_x} - v_{\mathbf{k}}^x \frac{\partial \mathbf{v}_{\mathbf{k}}^y}{\partial k_y} \right] \\
\sigma_{xx} &= -2e^2 \sum_{\mathbf{k}, \pm} \frac{\partial f_{\mathbf{k}}^0}{\partial E_{\mathbf{k}}^\alpha} \tau_{\varepsilon_{\mathbf{k}}} (v_{\mathbf{k}}^x)^2 \\
\sigma_{xy} &= -2 \frac{e^3 B}{\hbar c} \sum_{\mathbf{k}, \pm} \frac{\partial f_{\mathbf{k}}^0}{\partial E_{\mathbf{k}}^\alpha} \tau_{\varepsilon_{\mathbf{k}}}^2 v_{\mathbf{k}}^x \left[\mathbf{v}_{\mathbf{k}}^y \frac{\partial \mathbf{v}_{\mathbf{k}}^y}{\partial k_x} - v_{\mathbf{k}}^x \frac{\partial \mathbf{v}_{\mathbf{k}}^y}{\partial k_y} \right].
\end{aligned} \tag{12.34}$$

These equations can be further simplified at temperatures $k_B T \ll E_F$, where the thermoelectrical conductivities can be simplified by a Sommerfeld expansion (Ashcroft and Mermin, 1976), yielding the Mott relation

$$\alpha_{ij} = -\frac{\pi^2 k_B^2 T}{3 e} \frac{\partial \sigma_{ij}}{\partial \mu} \Big|_{E_F}. \tag{12.35}$$

Comparison to experiment

For a comparison to experiment, it is important to discuss contributions to the Nernst signal arising from an energy dependency of the relaxation time, measured by the derivative $\frac{\partial \tau}{\partial \mu} \Big|_{E_F}$. Usually, it is expected that the energy-dependence of τ behaves as $\tau \propto E^p$, with $p \in [-1/2, 3/2]$ (Barnard, 1972). For temperatures around or above the Debye temperature ($T \gtrsim \Theta_D$), scattering processes with phonons dominate the relaxation time, for which $p = 3/2$. At asymptotically low temperatures, Fermi's golden rule shows $\tau \propto 1/N(E)$, such that $p = 0$ for the two-dimensional Fermi gas. Corrections to the Nernst coefficient due to energy dependency of the relaxation time can be expressed as

$$-\frac{\pi^2 k_B^2 T}{3 e} \frac{\partial \tau}{\partial \epsilon} \frac{1}{\tau} \frac{\sigma_{xx} \sigma_{yy}^2 - \sigma_{yx} \sigma_{xx}}{\sigma_{xx} \sigma_{yy} - \sigma_{xy} \sigma_{yx}}, \tag{12.36}$$

e.g., the correction to the first term in the Nernst signal ($-\frac{\alpha_{yx}}{\sigma_{yy}}$) is twice the correction to the second term $-\frac{\sigma_{yx} \alpha_{xx}}{\sigma_{xx} \sigma_{yy}}$. If the contribution to the Nernst signal due to energy dependence of the relaxation time is therefore of comparable size to the total Nernst signal ϑ_{yx} , we would

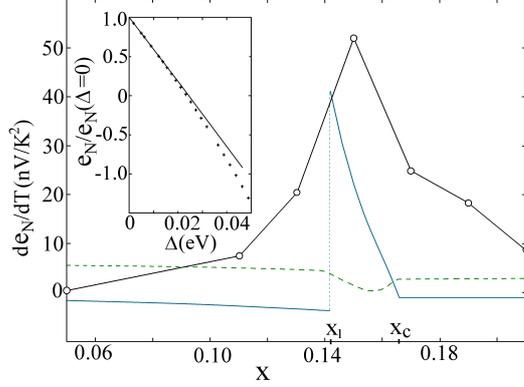


Figure 12.2: Dependence of the ratio ν/T on electron doping in the limit $T \rightarrow 0$. With decreasing x , the coefficient has an onset near $x = x_c$, where SDW order sets in; the discontinuity at $x = x_1$ is due to the opening of hole pockets (blue curve). The magnitude of our estimate of contributions due to energy dependence of the relaxation time has negligible size in the peak region (dashed line), as compared to the experimental values (black curve). Ex-

perimental data points from Li and Greene (2007b) correspond to the small circles, the line is a guide to the eye. The inset shows the quantum critical contribution to ϑ_{yx} , which becomes large already at small gap energies Δ . Numerical data points in the inset correspond to the crosses, which asymptotically behave as a linear function of gap amplitude, as given by the black line.

have necessarily $\vartheta_{xx} \tan(\Theta_H) = \mathcal{O}(\vartheta_{yx})$. In contrast, Nernst measurements on PCCO clearly show that $\vartheta_{xx} \tan(\Theta_H) \ll \vartheta_{yx}$ for all Ce concentrations $x > 0.05$ (Li and Greene, 2007b), implying that corrections due to an energy dependence of the relaxation time are small.

A quantitative comparison to experimental results requires an estimate of the relaxation time τ , which can be obtained from the Drude formula for the residual conductivity,

$$\sigma_D = \frac{n\tau}{m} e^2. \quad (12.37)$$

The unknown carrier density n and carrier effective mass m can be inferred from the plasma frequency

$$\omega_p^2 = \frac{n\tau}{m} e^2 \quad (12.38)$$

as typically obtained from optical conductivity measurements. Particular values are $\rho = 57 \mu\Omega \text{ cm}$ (Dagan et al., 2004) for the residual conductivity and the wave number $\omega_p = 13000 \text{ cm}^{-1}$ (Homes et al., 2006) for the plasma frequency, both measured at optimal doping, from which we obtain $\tau = 3.30 \times 10^{-14} \text{ s}$. For a numerical evaluation of the Nernst coefficient $\nu = \vartheta_{xy}/B$, we consider only the universal low temperature regime where $\nu \propto T$ by virtue of Eq. (12.35), such that the ratio ν/T becomes independent of T . Numerical results for ν/T are discussed in Fig. 12.2, using a discretization of the Brillouin zone with $\mathcal{O}(10^8)$ equally spaced datapoints. The summation procedure was implemented using the language ‘‘C’’ and temperature lowered until convergence in ν/T was observed within 1% error at around $T = 10^{-3} \text{ eV}$. In a certain range above optimal doping, the experimental peak structure is comparable to our theory, albeit from a shift of about $\Delta x \approx 0.02$ on the doping axis. This doping discrepancy might be explained by a more rapid opening of the spin density wave gap then described by the mean-field dependency $\delta \sim \sqrt{x - x_c}$. Overall,

a quantitative description of electron doping is complicated by an uncertainty in the carrier concentration in terms of nominal electron content. Quantitatively, this uncertainty might be quite large as indicated by a comparison of Hall effect and ARPES measurements with theoretical results of Lin and Millis (2005) and Millis et al. (2005), although a shift of the doping axis would not change the relative distance of SDW transition and optimal doping. Away from optimal doping, the experimentally observed Nernst signal (Li and Greene, 2007b) deviates significantly from our theoretical result. In these regions, influences due to anisotropy of the relaxation time can become important, while near the singular doping x_1 , our result suggests that the dominant contribution to the signal arises from the non-analyticity in the electronic density of states. Close to the quantum critical point, scattering of order parameter fluctuations can also lead to important corrections. However, it remains questionable whether such effects can be treated within the relaxation-time approximation (RTA), since the mutual interaction-induced track of the quasiparticles cannot be described by a single particle relaxation time. E.g., this leads to the neglect of current vertex corrections $\Delta J_{\mathbf{k}}$ that have to be added to the quasiparticle current $J_{\mathbf{k}} = -ev_{\mathbf{k}}$ obtained within the RTA in order to maintain a conserving approximation in the sense of Baym and Kadanoff (Kontani and Yamada, 2005).

Nernst effect near singular doping

The singular doping x_1 associated with the jump in the Nernst signal has a further interesting property: precisely at this doping hole-like carriers emerge in the Fermi volume (see Fig. 12.1). In experiment, this singularity will be smeared out by several effects until the energy distance of the local maximum of the quasiparticle band to the Fermi surface has become sufficiently large. This distance can be formally expanded as $\Delta E = (d\mu/dx)_{x_1}(x - x_1) + \mathcal{O}(x - x_1)^2$ (Bazaliy et al., 2004). The applicability of a Sommerfeld expansion to linear order in temperature is restricted to the temperature regime $k_B T \ll |\Delta E|$ and thus, thermal excitations will smear out the singularity in the Nernst signal over a finite doping range $\Delta x \approx (k_B T)/|d\mu/dx|_{x_1}$ with $|d\mu/dx|_{x_1} \simeq 1.52$ eV obtained from a numerical calculation. In analogy, magnetic breakdown processes will smear out the hole Fermi surface until the transmission amplitude (given by Eq. (12.10)) for tunneling through an energy gap of size $|\Delta E|$ has become negligible, $\alpha \ll 1$. The relevant range for such processes is

$$\Delta x \approx \frac{v_F}{|d\mu/dx|_{x_1}} \sqrt{\frac{2\hbar e}{\pi}} B \approx 5 \times 10^{-3} \sqrt{B}, \quad (12.39)$$

where we used $\Delta = |\Delta E|$ and $v_x = v_y \simeq 2.3 \times 10^7$ cm/s (Zhou et al., 2003). For experimentally relevant field strengths of $\mathcal{O}(10$ T), the Nernst signal is therefore expected to become sharply enhanced already for dopings of about 1 – 2% below x_1 , consistent with the experimental result shown in Fig. 12.2

It is possible to approximate the dispersion near the opening of the hole pocket by the quadratic form $\epsilon_h(\mathbf{k}) = \sum_{i=x,y} \delta k_i^2/m_i - \mu_h$. In two dimensions, the hole density of states $N_h \equiv \frac{1}{N} \sum_{\mathbf{k}} \delta(\epsilon - \epsilon_h(\mathbf{k}))$ takes a constant value and transport can be simplified by introducing the reduced hole mass $\bar{m}_h = m_1 m_2 / (m_1 + m_2)$. In the following, we formally

distinguish scattering rates of electrons (τ_e^{-1}) and holes (τ_h^{-1}) in order to decompose the transport tensors into electron and hole contributions, $\sigma_{ij} = \sigma_{ij}^e + \sigma_{ij}^h$ and $\alpha_{ij} = \alpha_{ij}^e + \alpha_{ij}^h$. At $T = 0$, we can readily evaluate the transport integrals (12.34) by integrating just over the hole dispersion –considering $\mu_h > 0$ to account for a finite density of holes– and obtain the result

$$\begin{aligned}\sigma_{xx}^h(\mu_h) &= \frac{2}{3}\mu_h\tau_h(\mu_h)e^2\frac{N_h}{\bar{m}_h} \\ \sigma_{xy}^h(\mu_h) &= \frac{2}{3}\mu_h\tau_h^2(\mu_h)\frac{e^3B}{c}\frac{N_h}{\bar{m}_h}.\end{aligned}\quad (12.40)$$

Although changing continuously with μ_h , at zero temperature these conductivities have a non-analyticity at $\mu_h = 0$, since they vanish for all $\mu_h \leq 0$. This non-analyticity renders the derivatives $d\sigma_{xx}/d\mu$ and $d\sigma_{xy}/d\mu$ discontinuous at $\mu_h = 0$ and will translate into a discontinuity of the thermoelectric conductivities α_{ij} via the Mott relation (12.35). In the limit of weak dilute disorder considered in our analysis, the impurity scattering rate is energy independent, since it can be obtained from Fermi's golden rule and follows therefore $1/\tau_h \propto N_h$. At temperatures much smaller than the Fermi temperature $T_F = E_F/k_B$, the hole contributions to the thermoelectric conductivities will therefore jump–neglecting a continuous contribution of $\mathcal{O}(T^2)$ – from zero to the finite constant values

$$\begin{aligned}\alpha_{xx}^h &= \frac{2\pi}{9}ek_B^2T\tau(\mu_h)\frac{N_h}{\bar{m}_h} \\ \alpha_{xy}^h &= \frac{\pi^2}{9}\frac{k_B^2T}{e}\tau(\mu_h)^2\frac{e^3B}{c}\frac{N_h}{\bar{m}_h}\end{aligned}\quad (12.41)$$

upon increasing μ_h above $\mu_h = 0$. Altogether, this non-analyticity leads to discontinuities of Nernst signal and thermopower described by

$$\begin{aligned}\Delta\vartheta_{yx} &= \left[\frac{\sigma_{xx}^e\alpha_{xy}^h - \sigma_{xy}^e\alpha_{xx}^h}{(\sigma_{xx}^e)^2} \right]_{\mu_h=0^+} \\ \Delta\vartheta_{xx} &= \left[\frac{\alpha_{xx}^h}{\sigma_{xx}^e} \right]_{\mu_h=0^+},\end{aligned}\quad (12.42)$$

where $\vartheta_{yx}|_{\mu_h=0^-}$ and $\vartheta_{xx}|_{\mu_h=0^-}$ are evaluated without contributions of hole carriers. Expanding also the electron dispersion as $\epsilon_{\mathbf{k}} = \sum_{i=x,y} \delta k_i^2/m_i - \mu$, these changes can be analyzed in relation to the absolute quantities

$$\begin{aligned}\frac{\Delta\vartheta_{yx}}{\vartheta_{yx}|_{\mu_h=0^-}} &= -\frac{N_h\bar{m}_e\tau_h}{N_e\bar{m}_h\tau_e} \left[\frac{\tau_h + \tau_e}{\tau_e'\mu_e} \right] \\ \frac{\Delta\vartheta_{xx}}{\vartheta_{xx}|_{\mu_h=0^-}} &= -\frac{\tau_h N_h \bar{m}_e}{\tau_e N_e \bar{m}_h}.\end{aligned}\quad (12.43)$$

Assuming that $\frac{N_h\bar{m}_e\tau_h}{N_e\bar{m}_h\tau_e} = \mathcal{O}(1)$, and $\tau_e'\mu_e = \mathcal{O}(\tau_e)$, the relative sizes of the discontinuities in both Nernst signal and thermopower are expected to be of the same order than the

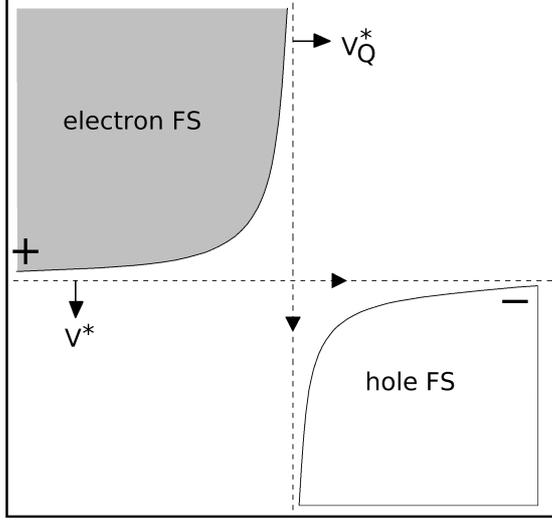


Figure 12.3: To leading order in the gap amplitude Δ , opening of the SDW gap modifies the Fermi surface only near the crossing points in momentum space where $\varepsilon_{\mathbf{p}} = \varepsilon_{\mathbf{p}+\mathbf{Q}} = \mu$. As shown in this sketch, a crossing point is coinciding with the crossing point as long as curvature of the Fermi surfaces is neglected near the crossing point. The vertical dashed line is the Fermi line for the normal state which is parallel to the vector $(0, \pi)$. The horizontal dashed line is the normal state Fermi line shifted by $\mathbf{Q} = (\pi, \pi)$, thus directing parallel to $(\pi, 0)$. The reconstructed Fermi surface contains electron pockets, denoted by +, and hole pockets, denoted by -.

values of the transport coefficients in the limit $\mu_h \rightarrow 0^-$.

We can make our analysis more general by assuming a general system of two types of carriers with elliptical dispersions and an arbitrary combination of effective charge, e.g. two identically charged pockets of carriers might be considered. Again, the transport coefficients will be the sum of partial contributions of carrier type 1 and 2, $\sigma_{ij} = \sigma_{ij}^{(1)} + \sigma_{ij}^{(2)}$ and $\alpha_{ij} = \alpha_{ij}^{(1)} + \alpha_{ij}^{(2)}$. Assuming that the band bottom of carrier type 2 equals the chemical potential, a discontinuous change in the coefficient of the T-linear behavior of the Nernst coefficient occurs upon raising the chemical potential. In this case, the change of the Nernst signal will be $\Delta\vartheta_{yx} = (\sigma_{xx}^{(1)}\alpha_{xy}^{(2)} - \sigma_{xy}^{(1)}\alpha_{xx}^{(2)})/(\sigma_{xx}^{(1)})^2$, in complete analogy to the special case of coexisting electron and hole carriers discussed previously. Considering a positive sign of the magnetic field B in the following, $\alpha_{xy}^{(2)}$ is restricted to positive values within our assumption of a constant relaxation time for carrier type 2. This is seen from the Mott relation (12.35), since $\frac{\partial\sigma_{xy}}{\partial\mu}|_{E_F}$ is negative (positive) for electrons (holes) and the charge $-e$ is conjugate (e) for holes. Since the electrical conductivity rises upon increasing the density of carriers, $\frac{\partial\sigma_{xx}}{\partial\mu}|_{E_F}$ is always positive, and via Eq. (12.35) the sign of $\alpha_{xy}^{(2)}$ is therefore equal to the sign of the charge carried by the carrier type 2. Overall, $\sigma_{xx}^{(1)}\alpha_{xy}^{(2)}$ is therefore positive and the sign of $\sigma_{xy}^{(1)}\alpha_{xx}^{(2)}$ is given by the product of the signs of carriers 1 and 2. If these charges have opposite sign, $\Delta\vartheta_{yx}$ will be positive, while $\Delta\vartheta_{yx}$ can be both positive or negative if carriers 1 and 2 are oppositely charged. Whether carriers 1 and 2 have the same charge or not can be decided from a measurement of the Hall angle $\tan(\Theta_H^{(1)}) \stackrel{\text{def}}{=} \sigma_{xy}^{(1)}/\sigma_{xx}^{(1)}$ and the discontinuity in the thermopower $\Delta\vartheta_{xx}$ and using the relationship $\Delta\vartheta_{xx} \tan(\Theta_H) = \sigma_{xy}^{(1)}\alpha_{xx}^{(2)}/(\sigma_{xx}^{(1)})^2$.

Behavior near quantum critical point

We now analyze the onset of the Nernst signal at the $x = x_c$ QCP where Δ becomes non-zero with decreasing x . The reconstruction of the Fermi surface due to opening of a spin density wave gap is important to understand the changes in the Nernst signal close to the QCP. Importantly, away from momenta where the bare dispersion $\epsilon_{\mathbf{k}}$ and its shifted version $\epsilon_{\mathbf{k}+\mathbf{Q}}$ cross or touch each other, the new Fermi surface will be close to one of the two original Fermi surfaces. The corresponding quantitative condition reads (for definiteness, we specify it here for one branch of the Fermi surface)

$$|E^+(\mathbf{k}) - \epsilon(\mathbf{k})| \ll |\epsilon_{\mathbf{k}} - \epsilon_{\mathbf{k}+\mathbf{Q}}| ,$$

which, using Eq. (12.7), can be reexpressed as

$$|\epsilon_{\mathbf{k}} - \epsilon_{\mathbf{k}+\mathbf{Q}}| \gg \Delta .$$

Therefore, the crossover from large to small deviation of the reconstructed Fermi surface from the old Fermi surface takes place at

$$|\epsilon_{\mathbf{k}} - \epsilon_{\mathbf{k}+\mathbf{Q}}| \sim \Delta .$$

Above, the variation of the chemical potential upon onset of ordering is neglected. A simple justification is that $\mu(x)$ will depend linearly on doping, while the SDW gap has the standard mean-field dependence $\Delta(x) \sim \sqrt{x_c - x}$. Hence, in the immediate vicinity of the transition, the leading dependence of the transport coefficients on doping is defined implicitly by the dependence on $\Delta(x)$, and can be found neglecting the variation of μ . To leading order in Δ , changes in transport coefficients originate therefore from regions near the crossing points depicted in Fig. 12.3. It is therefore possible to evaluate changes in transport quantities near the QCP due to opening of the SDW gap only to leading order in Δ . We now turn to finding this dependence.

Since to leading order in Δ , changes in the dispersion $\epsilon_{\mathbf{p}}$ occur around momenta \mathbf{p} with $\epsilon_{\mathbf{p}+\mathbf{Q}} = \epsilon_{\mathbf{p}} = \mu$, it is sufficient to discuss modifications of the old dispersion $\epsilon_{\mathbf{p}}$ near the crossing points in Fig. 12.1a and their symmetry related counterparts. To calculate the changes in the conductivity tensor due to opening of the SDW gap, it is advantageous to rewrite its entries as integral over the Fermi arc (Lin and Millis, 2005)

$$\begin{aligned} \sigma_{xx} &= \sigma_Q \frac{1}{4\pi^2} \oint ds l(s) \\ \sigma_{xy} &= \sigma_Q \frac{B}{\Phi_0} \frac{1}{2\pi} \oint d\vec{l} \times \vec{l} \cdot \hat{\mathbf{z}}/2 , \end{aligned} \quad (12.44)$$

where we used the conductance quantum $\sigma_Q = \frac{e^2}{h}$ and the flux quantum $\Phi_0 = \frac{hc}{2e}$. The formula for the Hall conductivity allows for a geometrical interpretation of the Hall conductivity in terms of the total area swept out by the mean free path $\vec{l}_{\mathbf{k}} = \mathbf{v}_{\mathbf{k}}\tau_{\mathbf{k}}$ as \mathbf{k} circumscribes the Fermi surface (Ong, 1991). The basic ideas of the following analytical calculations have been used by Bazaliy et al. (2004) and Lin and Millis (2005).

An analytical calculation is straightforward by parameterizing the momentum \mathbf{p} by the energies $\varepsilon_{\mathbf{p}}$ and $\varepsilon_{\mathbf{p}+\mathbf{Q}}$, what is possible in the vicinity of any crossing point \mathbf{p}^* defined by $\varepsilon_{\mathbf{p}^*+\mathbf{Q}} = \varepsilon_{\mathbf{p}^*} = \mu$. This can be achieved by expanding the dispersions

$$\begin{aligned}\varepsilon_{\mathbf{p}} - \mu &= \mathbf{v}^* \cdot \delta\mathbf{p} + \frac{m_{ij}}{2} \delta p_i \delta p_j \\ &+ \frac{y_{ijk}}{6} \delta p_i \delta p_j \delta p_k + \mathcal{O}(\delta p^4) \\ \varepsilon_{\mathbf{p}+\mathbf{Q}} - \mu &= \mathbf{v}_{\mathbf{Q}}^* \cdot \delta\mathbf{p} + \frac{n_{ij}}{2} \delta p_i \delta p_j \\ &+ \frac{z_{ijk}}{6} \delta p_i \delta p_j \delta p_k + \mathcal{O}(\delta p^4),\end{aligned}\quad (12.45)$$

where

$$\begin{aligned}\delta\mathbf{p} &= \mathbf{p} - \mathbf{p}^* \\ \mathbf{v}^* &= \mathbf{v}(\mathbf{p}^*), \quad \mathbf{v}_{\mathbf{Q}}^* = \mathbf{v}(\mathbf{p}^* + \mathbf{Q}) \\ m_{ij} &= (\partial^2 \varepsilon_{\mathbf{p}} / \partial p_i \partial p_j)|_{\mathbf{p}^*} \\ n_{ij} &= (\partial^2 \varepsilon_{\mathbf{p}} / \partial p_i \partial p_j)|_{\mathbf{p}^*+\mathbf{Q}} \\ y_{ijk} &= (\partial^3 \varepsilon_{\mathbf{p}} / \partial p_i \partial p_j \partial p_k)|_{\mathbf{p}^*} \\ z_{ijk} &= (\partial^3 \varepsilon_{\mathbf{p}} / \partial p_i \partial p_j \partial p_k)|_{\mathbf{p}^*+\mathbf{Q}}.\end{aligned}\quad (12.46)$$

Equation (12.45) can be inverted in order to reexpress the momentum coordinate,

$$\delta\mathbf{p} = \mathbf{u}_1 \varepsilon_{\mathbf{p}} + \mathbf{u}_2 \varepsilon_{\mathbf{p}+\mathbf{Q}} = \left(\mathbf{u}_1 + \frac{\Delta^2}{\varepsilon_{\mathbf{p}}^2} \mathbf{u}_2 \right) \varepsilon_{\mathbf{p}}, \quad (12.47)$$

where the second equality holds only on the SDW Fermi surface. The two reciprocal vectors \mathbf{u}_1 and \mathbf{u}_2 of the Fermi velocities at the crossing point have been defined as:

$$\begin{aligned}\mathbf{u}_1 &= \frac{\mathbf{v}_{\mathbf{Q}}^* \times [\mathbf{v}^* \times \mathbf{v}_{\mathbf{Q}}^*]}{(\mathbf{v}^* \times \mathbf{v}_{\mathbf{Q}}^*)^2} \\ \mathbf{u}_2 &= \frac{\mathbf{v}^* \times [\mathbf{v}_{\mathbf{Q}}^* \times \mathbf{v}^*]}{(\mathbf{v}^* \times \mathbf{v}_{\mathbf{Q}}^*)^2}.\end{aligned}\quad (12.48)$$

From Eq. (12.47), we find the differential equation

$$d\mathbf{p} = \mathbf{u}_1 d\varepsilon_{\mathbf{p}} + \mathbf{u}_2 d\varepsilon_{\mathbf{p}+\mathbf{Q}} = \left(\mathbf{u}_1 - \frac{\Delta^2}{\varepsilon_{\mathbf{p}}^2} \mathbf{u}_2 \right) d\varepsilon_{\mathbf{p}}. \quad (12.49)$$

Considering a constant relaxation time τ , the integral over mean free path in (12.44) is obtained by an integration over velocity, which can be simplified by defining the vectors

$$\begin{aligned}\eta_1^{\mathbf{p}} &= (m_{11}u_{1x} + m_{12}u_{1y})\hat{\mathbf{x}} + (m_{21}u_{1x} + m_{22}u_{1y})\hat{\mathbf{y}} \\ \eta_2^{\mathbf{p}} &= (m_{11}u_{2x} + m_{12}u_{2y})\hat{\mathbf{x}} + (m_{21}u_{1x} + m_{22}u_{2y})\hat{\mathbf{y}} \\ \eta_1^{\mathbf{p}+\mathbf{Q}} &= (n_{11}u_{1x} + n_{12}u_{1y})\hat{\mathbf{x}} + (n_{21}u_{1x} + n_{22}u_{1y})\hat{\mathbf{y}} \\ \eta_2^{\mathbf{p}+\mathbf{Q}} &= (n_{11}u_{2x} + n_{12}u_{2y})\hat{\mathbf{x}} + (n_{21}u_{1x} + n_{22}u_{2y})\hat{\mathbf{y}}.\end{aligned}\quad (12.50)$$

Then, the differential velocity change close to the crossing point is obtained as (Lin and Millis, 2005)

$$\begin{aligned}\mathbf{v}^b &= \mathbf{v}^{b*} + \delta\mathbf{v}^b = \mathbf{v}^{b*} + [\bar{\eta}_1^b + \bar{\eta}_2^b(\Delta/\epsilon_{\mathbf{p}})^2]\epsilon_{\mathbf{p}} \\ d\mathbf{v}^b &= [\bar{\eta}_1^b - \bar{\eta}_2^b(\Delta/\epsilon_{\mathbf{p}})^2]d\epsilon_b.\end{aligned}\quad (12.51)$$

Using this result in Eq. (12.44), the linearized $T = 0$ change in the Hall conductivity near the crossing point is obtained as

$$\delta\sigma_{xy} = \sigma_Q \tau^2 \frac{B\Delta}{\Phi_0} \hat{\mathbf{z}} \cdot [\eta_1^{\mathbf{p}} + \eta_2^{\mathbf{sp}} + 3\eta_2^{\mathbf{p}} + 3\eta_1^{\mathbf{sp}}] \times (\mathbf{v}_{\mathbf{Q}}^* - \mathbf{v}^*). \quad (12.52)$$

We note that the total change in the Hall conductivity is obtained by summing over the two symmetry inequivalent crossing points depicted in Fig. (12.1) and accounting for the symmetry equivalent quarters of the Brillouin zone by multiplying the result with a factor of four. The weak-field longitudinal electrical conductivity is discussed by using the differential change ds in the Fermi arc obtained by combining Eqs (12.48) and (12.47).

$$\left| \frac{ds}{d\epsilon_{\mathbf{p}}} \right| = \frac{1}{|\mathbf{v}^{\mathbf{p}} \times \mathbf{v}^{\mathbf{sp}}|} \left[(v^{\mathbf{sp}})^2 + (v^{\mathbf{p}})^2 \left(\frac{\Delta^2}{\epsilon_{\mathbf{p}}^2} \right)^2 + 2 \left(\frac{\Delta^2}{\epsilon_{\mathbf{p}}^2} \right) \mathbf{v}^{\mathbf{p}} \cdot \mathbf{v}^{\mathbf{sp}} \right]^{1/2}. \quad (12.53)$$

Using this relation, the integration over the Fermi arc in Eq. (12.44) can be replaced by an energy integral that can be evaluated to leading order in Δ . This calculation has been performed in detail by Bazaliy et al. (2004) for the three-dimensional SDW transition in Cr, and the result in two-dimensions as obtained by Lin and Millis (2005) is

$$\delta\sigma_{xx} = -\sigma_Q \frac{\tau}{\pi} \frac{(\mathbf{v}^* - \mathbf{v}_{\mathbf{Q}}^*)^2}{|\mathbf{v}_{\mathbf{Q}}^* \times \mathbf{v}_{\mathbf{Q}}^*|} \Delta. \quad (12.54)$$

It remains to calculate the change in the thermoelectric conductivities α_{ij} to finally obtain the change $\vartheta_{yx}(\Delta) - \vartheta_{yx}(\Delta = 0)$ in the Nernst signal. This problem is simplified at low temperatures, where changes in the thermoelectric conductivities are obtained from the derivatives $\frac{d\delta\sigma_{ij}}{d\mu}|_{EF}$ due to the Mott relation (12.35). These derivatives of Eqs (12.52) and (12.54) are obtained from the relations

$$\begin{aligned}\frac{dv_i^*}{d\mu} &= \sum_j m_{ij}(u_1^j + u_2^j) \\ \frac{dm_{ij}}{d\mu} &= \sum_k v_{ijk}(u_1^k + u_2^k),\end{aligned}\quad (12.55)$$

Linearizing Eq. (12.22) in Δ in this way yields $\delta\vartheta_{xx}$ and $\delta\vartheta_{yx}$ to linear order in Δ . From a numerical calculation of ϑ_{xx} and ϑ_{yx} , we obtain the values $\delta\vartheta_{xx}/\vartheta_{xx} = 47.4\Delta/\text{eV}$ and $\delta\vartheta_{yx}/\vartheta_{yx} = -39.8\Delta/\text{eV}$, see also Fig. 12.2. Very close to $x_c = 0.165$ it might be difficult to measure the quantum critical contributions $\delta\vartheta_{yx}$ and $\delta\vartheta_{xx}$ experimentally due to other contributions to the signal which we could not specify.

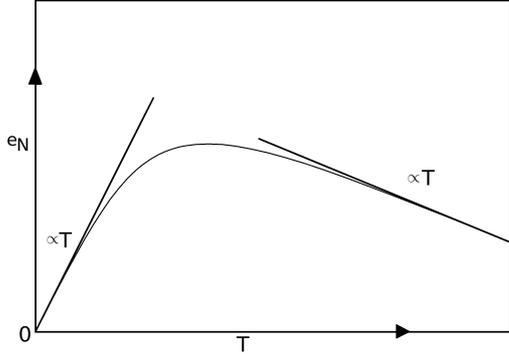


Figure 12.4: Sketch of the normal state Nernst signal dependence on temperature as observed in experiments in electron doped cuprates near optimal doping by Li and Greene (2007b). The linear temperature dependence at lowest T turns over in a maximum, which is at roughly $50K$ for optimal doping. Above the peak temperature, the signal vanishes proportional to temperature.

Finite temperatures

Although we justified our previous analysis only at low temperatures with impurity dominated scattering and long-range SDW order, it is possible to make some further statements about changes in the Nernst effect upon increasing temperature to allow for changes in the scattering processes and the spin density wave gap. Below the ordering temperature T_{SDW} , the spin density wave gap is finite and fluctuations of the SDW order parameter are gapped. In this temperature regime, the original Fermi surface will still remain gapped near crossing points with $\epsilon_{\mathbf{p}+\mathbf{Q}} = \epsilon_{\mathbf{p}} = \mu$, whereas the temperature dependence of the quasiparticle scattering rate will be of importance. In cuprates, the normal state quasiparticle scattering rate is linear in temperature in most parts of the Brillouin zone (Valla et al., 2000). The situation becomes far more complicated at temperatures above T_{SDW} , where a sizable Nernst signal is still observed in experiment. Fluctuations of the order parameter are an important and complicated source of scattering in this regime, and it has been shown that these fluctuations enhance the normal state Nernst signal in a finite temperature range above T_{SDW} (Kontani and Yamada, 2005). These effects are certainly not described by a relaxation time approximation, since this approach neglects interaction induced drag between quasiparticles. Above T_{SDW} , the Fermi surface is described by the bare dispersion $\epsilon_{\mathbf{k}}$ and is therefore hole-like and almost circular, see Fig. 12.1a. This situation comes close to the isotropic Fermi surface of a Fermi gas, where the Nernst signal vanishes for a constant relaxation time (Sondheimer, 1948). The RTA predicts therefore a small Nernst signal.

12.3 Antiferromagnetic fluctuations

Our theoretical description requires that the SDW gap vanishes at a quantum critical point tuned by electron doping. Here, we consider modifications to the *position* of the quantum critical point and to the *mean-field description* near the quantum critical point.

Substantial disagreement over the position of the quantum critical point arose due to inconsistent results using different experimental probes. Elastic neutron-scattering experiments on $\text{Nd}_{2-x}\text{Ce}_x\text{CuO}_{4-\delta}$ in zero magnetic field suggest short-ranged antiferromagnetic order between $x = 0.145$ and $x = 0.154$, and it has been proposed that short-ranged order might even occur at $x = 0.134$ (Motoyama et al., 2006). These findings are contrasted by trans-

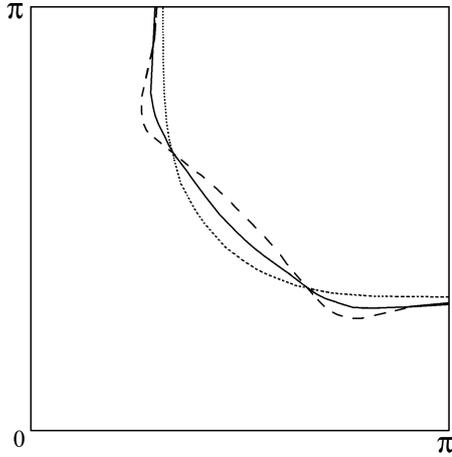


Figure 12.5: Fermi surface changes due to finite spin correlation lengths corresponding to electron dopings somewhat above the SDW quantum critical point. The Fermi surface without any influences of spin fluctuations is shown as the dotted line. The dashed line shows a renormalized Fermi surface for a large coupling to spin fluctuations ($\lambda = 0.4$) and a small distance $r = 0.001$ to the quantum critical point. Renormalization effects become weaker for a smaller coupling $\lambda = 0.2$ and $r = 0.1$ (continuous line). At the crossing

points with $\epsilon(\mathbf{p} + \mathbf{Q}) = \epsilon(\mathbf{p}) = \mu$, the Fermi surface remains unchanged by spin fluctuations. The cutoff energy is $E_0 = 0.88$ eV .

port measurements on $\text{Pr}_{2-x}\text{Ce}_x\text{CuO}_{4-\delta}$ which show rapidly changing transport properties at dopings below $x = 0.165$, hinting towards Fermi surface reconstruction already slightly above optimal doping $x \simeq 0.15$. Recently, a proposal to resolve these discrepancies has been given by suggesting that the QCP is shifted by strong magnetic fields (Moon and Sachdev, 2009). This argument is substantiated by recent experiments of Helm et al. (2009) that observe the onset of quantum oscillations in the magnetoresistance at a doping between $x = 0.16$ and $x = 0.17$ in NCCO, making it plausible that magnetic fields of 50 T or more shift the quantum critical point towards the doping value $x = 0.165$ obtained from transport measurements (Dagan et al., 2004).

Even way above optimal doping, experiments show a strong doping dependence of Hall and Nernst effect (Dagan et al., 2004, Li and Greene, 2007b), where long-ranged spin order is clearly absent. Such effects are not captured by our mean-field theory description, whose band-structure is insensitive to doping changes above critical doping x_c . One important issue in this parameter regime are antiferromagnetic spin-fluctuations, leading to self-energy corrections not captured by mean-field theory.

In addition, it is important to clarify whether these fluctuation effects are also of importance close to optimal doping, e.g., whether they can account for the experimentally observed Fermi surface or the enhancement of the Nernst signal at low temperatures. A full treatment of spin fluctuations certainly exceeds the limitations of a relaxation-time approximation, e.g., due to the current vertex corrections discussed in section 12.2. Therefore, we will assume that impurity scattering dominates the electronic transport at lowest energies and neglect the imaginary part of the self-energy due to spin-fluctuations. It remains to analyze the real part of the self-energy that describes changes in the Fermi surface properties. These changes have been discussed by Lin and Millis (2005), and we

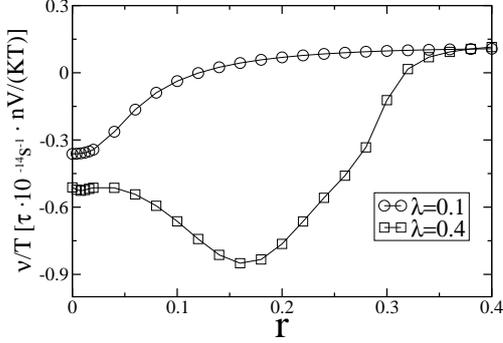


Figure 12.6: Nernst coefficient ν/T as resulting from the dispersion (12.58) for different couplings λ as a function of the control parameter r . Neither for a small coupling ($\lambda = 0.1$) nor for a large coupling ($\lambda = 0.4$), an enhanced and positive Nernst signal results close to the QCP. Instead, close to the quantum critical point ($r \simeq 0$) the signal is strongly negative. Far from the quantum critical point ($r = \mathcal{O}(1)$) the signal turns positive but is rather small. Electron doping has been adjusted to $x = 0.24$.

give a brief account of these results in the context of the normal state Nernst effect. A general discussion of low energy fermions interacting with their own collective spin fluctuations near an antiferromagnetic quantum phase transition can be found in the review of Abanov et al. (2003). The leading approximation to the electronic self-energy due to spin fluctuations is

$$\Sigma(\mathbf{k}, i\omega) = -g^2 T \int d^2\mathbf{q} \sum_{i\Omega_n} G(\mathbf{k} + \mathbf{q}, i\omega + i\Omega_n) D(\mathbf{q}, i\Omega_n), \quad (12.56)$$

where G and D are Matsubara Green's functions for electrons and spin-fluctuations, respectively and g is the spin-fermion coupling. The evaluation of this self-energy is performed with the bare electron propagator $G(\mathbf{p}, i\omega) = (i\omega - \zeta_{\mathbf{p}})^{-1}$ and the spin fluctuation propagator – renormalized by particle-hole excitations – $D(\mathbf{q}, i\Omega_n) = -(\Gamma_{\mathbf{q}} + |\Omega_n|)^{-1}$, with $\zeta_{\mathbf{p}} = \varepsilon_{\mathbf{p}} - \mu$ and $\Gamma_{\mathbf{q}} = \omega_{sp}(r + \xi^2(\mathbf{q} - \mathbf{Q})^2)$, where ω_{sp} is the energy scale characteristic of spin fluctuations and ξ the correlation length of magnetic order. We will assume a finite distance r to the QCP where SDW order at wave vector $\mathbf{Q} = (\pi, \pi)$ sets in. In order to obtain the renormalized quasiparticle dispersion, the self-energy (12.56) can be integrated at $T = 0$ and $i\omega = 0$ by assuming that r and $\zeta_{\mathbf{k}+\mathbf{Q}}/E_0$ are small, where E_0 is introduced as a cutoff of order the normal state bandwidth, with the result (Lin and Millis, 2005)

$$\Sigma(\mathbf{k}, i\omega = 0) \simeq 0.5\lambda\zeta_{\mathbf{k}+\mathbf{Q}} \ln(r^2 + (\zeta_{\mathbf{k}+\mathbf{Q}}/E_0)^4). \quad (12.57)$$

We can define an energy scale $\bar{g} = (g\xi)^2$, such that λ describes the dimensionless ratio

$$\lambda = \frac{\bar{g}}{v_F \xi^{-1}}.$$

Physically, λ measures the ratio of the effective coupling constant \bar{g} and a fermionic energy at a typical fermionic $|k - k_F| \sim \xi^{-1}$, which sets the momentum range for spin-fermion coupling. When λ is small (Abanov et al., 2003) ($\lambda \ll 1$), fermions are nearly decoupled from spin fluctuations and behave as an almost ideal Fermi gas. On the contrary, when λ is large ($\lambda > 1$), the bare fermionic dispersion is almost completely overshadowed by the interaction, and this may give rise to a non-Fermi liquid behavior. Somewhat above the

critical doping where the correlation length ξ diverges, λ will be small enough to allow for perturbation theory. The new electronic dispersion is then described by

$$\epsilon_{\mathbf{p}} + \Sigma(\mathbf{p}, i\omega = 0) . \quad (12.58)$$

In Fig. 12.6, we evaluate the resulting Nernst signal for a parameter range $r \in [0, 0.4]$ and $\lambda \in [0, 0.4]$. For small values of r , the Nernst signal is strongly negative and gets slightly positive once the mass gap for the spin fluctuations becomes of order $\omega_{\text{sp}} \leftrightarrow r = \mathcal{O}(1)$. We conclude that Fermi surface changes induced by antiferromagnetic spin-fluctuations are insufficient to explain a positively enhanced Nernst signal at optimal doping and below. The origin of this failure might be (at least) twofold:

(i) Our neglect of scattering on spin-fluctuations might be wrong and this additional scattering mechanism might lead to important corrections to our quasiparticle calculation of the Nernst effect. In this case, it might be possible that the Nernst signal is enhanced by spin fluctuations even *at optimal doping or below*. (ii) Long-range magnetic order might persist up to and slightly above optimal doping, as assumed in our theoretical description. The second point of view is supported by Fermi surfaces as obtained from ARPES experiments at optimal doping $x \simeq 0.15$ (see Fig. 11.3), which show a significant suppression – as compared to the Fermi surface of an overdoped sample – of photoemission intensity near $(0.65\pi, 0.3\pi)$ (and at three symmetry equivalent points). These points are positioned at the intersection of the unreconstructed Fermi surface (given by $\epsilon(\mathbf{p}) \equiv \mu$) with the antiferromagnetic Brillouin zone boundary, where the leading order self-energy correction (12.57) will cancel since the relation $\epsilon(\mathbf{p} + \mathbf{Q}) = \epsilon(\mathbf{p}) = \mu$ is fulfilled. Thus, it is more convincing that a spin density wave gap originating from long-range magnetic order is responsible for the Fermi surface reconstruction setting in slightly above optimal doping $x = 0.15$.

12.4 Conclusions

In this chapter, we demonstrated that SDW order in the electron doped cuprates has profound implications for the normal state Nernst signal and the thermopower in these materials. The fundamental origin of these implications is a singularity in the quasiparticle density of states occurring at the emergence of hole like orbits in the Fermi surface, induced by a critical value of the SDW gap. At low temperatures, both Nernst signal and thermopower are proportional to temperature, and the proportionality coefficient is expected to show a large discontinuous change in the Nernst signal and also the thermopower, where in addition a sign change will occur. The discontinuity in these transport quantities will be smeared out by scattering processes across the SDW gap, which can be mediated by magnetic field, impurity scattering and thermal excitations.

It is important to note that the singularity in the electronic density of states is the primary origin of an enhanced Nernst signal, while the signal gets smaller upon increasing carrier concentration of the holes. The presence of oppositely charged carriers in the Fermi volume is therefore a necessary, but not a sufficient condition in order to obtain an enhanced Nernst signal. This is to some extent contrary to the widespread explanation of an enhanced normal-state Nernst signal by the existence of two oppositely charged and current

carrying quasiparticles (Behnia, 2009). Our results require a more subtle explanation, and stay in direct contrast to an *ambipolar* Nernst effect predicting a maximal Nernst signal when hole- and electron-like carrier densities exactly compensate each other (Oganesyan and Ussishkin, 2004). This argument has been used to explain the large normal-state Nernst signal in PCCO Li and Greene (2007b), although our analysis predicts instead a maximal Nernst signal when the hole pocket just touches the Fermi surface. Our findings establish therefore a direct relation between the peak in the normal-state Nernst signal at optimal doping and SDW order. We expect only slight modifications to our result due to energy dependence of the relaxation time, although a more detailed understanding of the scattering mechanism seems necessary for a quantitative explanation of the persistence of a large normal state Nernst signal into the underdoped and overdoped regimes.

We close this chapter with an outlook on the normal state Nernst effect in *hole-doped* cuprates that will be the topic of the next chapter. The evolution from a “large” to a “small” Fermi surface with decreasing doping (Daou et al., 2009a) could have a similar influence on the Nernst signal by the opening/closing of hole or electron pockets. The observed large normal state Nernst signals in the stripe ordered phase of $\text{La}_{1.6-x}\text{Nd}_{0.4}\text{Sr}_x\text{CuO}_4$ (Choinière et al., 2009) are therefore of particular interest in order to analyze the influence of stripe order on the normal state Nernst effect.

Chapter 13

Normal-state Nernst effect in the presence of stripe order

13.1 Model and formalism

Mean-field theory

The crucial aspect of density wave order is translational symmetry breaking, i.e. momentum is no longer a conserved quantity. The new spatial periodicity causes a scattering potential that scatters quasiparticles with dispersion (12.1) by transferring momentum of multiples $n\mathbf{Q}$ for integer n . Alternatively, these scattering potentials can be considered as periodic modulations in the site chemical potential or bond kinetic energy, arising from a mean-field treatment of interactions in a $t - J$ or Hubbard model. We will not determine these modulations self-consistently but treat them in form of scattering potentials added to non-interacting quasiparticles with the dispersion given by Eq. (12.1).

These scattering potentials \hat{V} have to be added to the non-interacting electrons such that the total Hamiltonian has the form $H = \sum_{\mathbf{k}\sigma} \varepsilon_{\mathbf{k}} c_{\mathbf{k}\sigma}^\dagger c_{\mathbf{k}\sigma} + \hat{V}$. In this way, a charge density wave can be described by the scattering potential

$$\hat{V}_1 = \sum_{\mathbf{k},\sigma} (V_c(\mathbf{k}) c_{\mathbf{k}+\mathbf{Q}_c\sigma}^\dagger c_{\mathbf{k}\sigma} + h.c.) , \quad (13.1)$$

where $V_c(\mathbf{k})$ can be complex. The complex potential $V_c(\mathbf{k})$ describes phase and amplitude of the modulation, while the period is set by $\mathbf{Q}_c = (Q_c, 0)$. In case of a real constant $V_c(\mathbf{k}) = -V_c$, the maxima/minima of the modulation are located on the lattice sites, and we refer to this case as a *site-centered* charge density wave. The maxima of the modulation may also be positioned between two neighboring sites if $V_c(\mathbf{k}) = -V_c e^{-iQ_c/2}$, what we call a *bond-centered* CDW. $V_c(\mathbf{k})$ can also lead to a modulation of the kinetic energy term. We will chose a *d-wave* form factor for this modulation such that $V_c(\mathbf{k}) = -\delta t (\cos(k_x + \frac{Q_c}{2}) - \cos(k_y)) e^{-iQ_c/2}$; these three different cases are illustrated in Fig. 11.4. Order in the spin density wave sector is similarly described by a complex valued scattering potential, such that the modulation of the spins might either be collinear or form a spiral. We exclude here spiral order, since its realization in $\text{YBa}_2\text{Cu}_3\text{O}_y$ is still under discussion,

e.g., Haug et al. (2009) report difficulties to identify it by neutron scattering techniques. Collinear spin order with spin quantization axis in z -direction is generally described by the scattering potential

$$\hat{V}_2 = \sum_{\mathbf{k}, \sigma} \sigma (V_s(\mathbf{k}) c_{\mathbf{k}+\mathbf{Q}_s \sigma}^\dagger c_{\mathbf{k} \sigma} + h.c.) . \quad (13.2)$$

Again we will make use both of a site-centered SDW (with $V_s(\mathbf{k}) = V_s$) and a bond-centered SDW (with $V_s(\mathbf{k}) = -V_s(1 + e^{-iQ_c/2})/(2 \cos(Q_c/4))$) with $\mathbf{Q}_s = (Q_s, \pi)$. Considering symmetry arguments, a Landau free energy for coupled spin and charge density wave order parameters ϕ_c and ϕ_s is minimized if ϕ_c and ϕ_s^2 are in phase (Zachar et al., 1998), which is fulfilled in our case since V_s^2 and V_c have the same phase. In addition, the sign of V_c has to be chosen in accordance with the stripe patterns shown in Fig. 11.4 and will be specified later on.

As has been discussed for Cr (Fawcett, 1988), the Fermi surface reconstruction due to collinear SDW order is caused by a hierarchy of gaps of order $2\Delta_m \sim 2V_s^m/t^{m-1}$ opening at the crossing points of bands $\epsilon_{\mathbf{k}+n\mathbf{Q}}$ and $\epsilon_{\mathbf{k}+(n\pm m)\mathbf{Q}}$, where V_s is the amplitude of the spin potential. An analogous hierarchy of gaps is also caused by charge order with wave vector \mathbf{Q}_c and scattering potential V_c . This situation can be simplified if $V_s, V_c \ll t$, since then gaps with $m > 1$ can be neglected since they are broken through in presence of external fields or disorder or by thermal fluctuations.

It is important to emphasize that different types of density wave order may imply each other, e.g., may not exist independently. One reason is the broken 90° rotation symmetry of the underlying square lattice in presence of uni-directional density wave order. In this case, the s -wave and $d_{x^2-y^2}$ representations of the point group mix. In this sense, the solution of a mean-field Hamiltonian with d -wave bond modulations will display a finite on-site charge density modulation (which may be interpreted as s -wave component) and vice versa, the solution of a mean-field Hamiltonian with modulated on-site potentials will include inequivalent modulations of horizontal and vertical bonds, including a d -wave component. In addition, a mean field Hamiltonian with a collinear SDW modulation only will also lead to a CDW with $\mathbf{Q}_c = 2\mathbf{Q}_s$ (Zachar et al., 1998), as discussed in section 11.1.

Semiclassical transport

In order to obtain the transport coefficients contained in the expression (12.22) for the Nernst signal, we shall use the same semiclassical approach that we described already in section 12.2. In particular, we will make use of the transport equations (12.34) and shall assume the same conditions of validity. E.g., we will again consider an isotropic relaxation time τ that originates from s -wave scattering on weak and dilute impurities. As already discussed in chapter 12 for the electron-doped cuprates, the relaxation time approximation fails in presence of antiferromagnetic fluctuations (Kontani and Yamada, 2005), and the validity of our approach is restricted therefore below the spin and – in analogy – charge ordering temperatures.

In contrast to commensurate spin density wave order at wave vector (π, π) , unidirectional stripe order breaks square lattice symmetry and transport properties are anisotropic within a single CuO layer. It has to be noted that on general grounds, not all of the quanti-

ties entering the expression (12.22) can show anisotropies. The Hall conductivity obeys $\sigma_{xy} = -\sigma_{yx}$ independent of crystal symmetry for a fixed orientation $\vec{B} \parallel \hat{z}$, what can be shown from the Kubo formula using $\langle [j_x, j_y]_- \rangle = -\langle [j_y, j_x]_- \rangle$. At low temperatures, this identity follows also from the geometric interpretation of the Hall conductivity. (Ong, 1991) From the Mott relation (12.35), it follows then that also $\alpha_{xy} = -\alpha_{yx}$ at low temperatures. Importantly, these relations imply that for a C_4 -symmetric situation, according to Eqs. (12.22) and (12.19) $\vartheta_{xy} = -\vartheta_{yx}$ for a fixed magnetic field $\vec{B} \parallel \hat{z}$. Here we adopt the experimentally used convention that the three vectors \vec{E} , $\vec{\nabla}T$ and \vec{B} form a right-handed system for the measurements of both ϑ_{xy} and ϑ_{yx} , which may be achieved by switching the sign of the magnetic field. Then $\vartheta_{xy} = \vartheta_{yx}$ for C_4 -symmetry. In this sign convention, the vortex Nernst coefficient is always positive.

In $\text{YBa}_2\text{Cu}_3\text{O}_y$ compounds, the presence of CuO chains marks a preferred direction of stripe orientation, and rotation symmetry breaking can be expected to have the same orientation in all layers. The situation is different in 214 cuprates with a low temperature tetragonal (LTT) structure – like $\text{La}_{1.6-x}\text{Nd}_{0.4}\text{Sr}_x\text{CuO}_4$ –, where the stripe ordering pattern alternates from layer to layer and is believed to follow the distorted in-plane pattern (Vojta, 2009). This effect is accounted for by averaging macroscopic transport properties over neighboring layers, which is easily achieved by symmetrizing the in-plane matrix elements of the transport coefficients, e.g., the layer-averaged *Nernst signal* will be $(\vartheta_{xy} + \vartheta_{yx})/2$. In the following, we define the *Nernst coefficient* as $\nu = (\vartheta_{xy} + \vartheta_{yx})/(2B)$ if the signal is averaged over layers and as $\nu = \vartheta_{yx}/B$ if the signal is calculated for a *single* layer.

It remains to define the quasiparticle bands that enter the transport equations (12.34), which are obtained from a numerical diagonalization of the Hamiltonian matrix. We obtained these eigenvalues by implementing the LAPACK routine “zgeev” in the commonly used language “C”. From these numerically obtained eigenvalues and eigenvectors, we obtained the first and second derivatives of the eigenvalues by implementing an algorithm devised by Andrew and Tan (1999), requiring the iteration of a coupled set of matrix equations. In order to integrate the transport equations (12.34), we discretized the Brillouin zone integrals with an equidistant mesh around the Fermi surface of an energy width proportional to temperature and extrapolated the result to zero temperature, such that the ratio ϑ_{yx}/T becomes independent of temperature.

13.2 Nernst effect from stripe order for $x \geq 1/8$

Stripe order is most stable at $x = 1/8$, and it is furthermore useful that the related spin modulation observed in 214 cuprates has a constant ordering wave vector \mathbf{Q}_s^* if $x \geq 1/8$ (Vojta, 2009). This aspect simplifies a discussion of Fermi surface reconstruction due to stripe order and its impact on the Nernst signal, which shall be the subject of this section. Hole concentrations $x < 1/8$ with correspondingly longer stripe modulation periods will be the subject of section 13.3.

For a semiclassical description of transport properties, we require knowledge of the quasiparticle dispersions that enter Eq. (12.34), which are obtained as eigenmodes of the bare dispersion $\epsilon_{\mathbf{k}}$ subject to the scattering potentials defined above. This calculation is further

simplified by the spin degeneracy of the quasiparticle bands, because the paramagnetic (antiferromagnetic) stripe-states shown in Fig. 11.4 are invariant under global spin-flips (global spin-flips plus a translation by one lattice spacing along the stripe direction). According to the doping dependencies of the ordering wave vector \mathbf{Q}_s^* introduced in section 11.1, we have $\mathbf{Q}_s^* = \pi(3/4, 1)$ if $x \geq 1/8$. This ordering wave vector induces period eight stripe order, and the reduced Brillouin zone in the ordered state is given by the wavevectors $\mathbf{k} \in [-\frac{\pi}{4}, \frac{\pi}{4}] \times [-\frac{\pi}{2}, \frac{\pi}{2}]$. The scattering potential \hat{V}_2 defined in Eq. 13.2 connects therefore the momentum state \mathbf{k} with all momentum states $\mathbf{k} + n\mathbf{Q}_s^*$, $n = 1 \dots 8$. In presence of charge and spin potentials (Eqs (13.1) and (13.2)), the quasiparticle dispersions can therefore be obtained from a 8×8 matrix, given by (Millis and Norman, 2007)

$$\begin{bmatrix} \varepsilon_{\mathbf{k}} & V_c & 0 & V_c^* & 0 & V_s & V_s^* & 0 \\ V_c^* & \varepsilon_{\mathbf{k}+(\frac{\pi}{2},0)} & V_c & 0 & 0 & 0 & V_s & V_s^* \\ 0 & V_c^* & \varepsilon_{\mathbf{k}+(\pi,0)} & V_c & V_s^* & 0 & 0 & V_s \\ V_c & 0 & V_c^* & \varepsilon_{\mathbf{k}+(\frac{3\pi}{2},0)} & V_s & V_s^* & 0 & 0 \\ 0 & 0 & V_s & V_s^* & \varepsilon_{\mathbf{k}+(\frac{\pi}{4},\pi)} & V_c & 0 & V_c^* \\ V_s^* & 0 & 0 & V_s & V_c^* & \varepsilon_{\mathbf{k}+(\frac{3\pi}{4},\pi)} & V_c & 0 \\ V_s & V_s^* & 0 & 0 & 0 & V_c^* & \varepsilon_{\mathbf{k}+(\frac{5\pi}{4},\pi)} & V_c \\ 0 & V_s & V_s^* & 0 & V_c & 0 & V_c^* & \varepsilon_{\mathbf{k}+(\frac{7\pi}{4},\pi)} \end{bmatrix} . \quad (13.3)$$

For readability, in this matrix we dropped the momentum dependence in the scattering potentials. Of course, these potentials in some cases depend on momentum, and this dependence is easily obtained by labeling a potential connecting energies with momenta $\mathbf{k} + \mathbf{q}$ and $\mathbf{k} + \mathbf{q} + \mathbf{Q}_{c/s}^*$ with the momentum $\mathbf{k} + \mathbf{q}$ in the matrix (13.3). The general form of this matrix is further restricted by the particular spin and charge patterns we shall analyze in the following. Those are classified in Fig. 11.4 as “site centered”, “bond centered” and “valence bond stripes”. An interpretation of the charge and spin modulations induced by the scattering potentials is simplified by analyzing the real space form of the potentials (13.1) and (13.2). For this purpose, we introduce the Fourier transform

$$c_{\mathbf{k}\sigma} = \frac{1}{\sqrt{\mathcal{N}}} \sum_i e^{i\mathbf{k}\mathbf{r}_i} c_{i\sigma} , \quad (13.4)$$

defined in the Brillouin zone $[-\pi, \pi] \times [-\pi, \pi]$, such that the real space representation is now given by

$$\begin{aligned} \hat{V}_1 &= V_c \sum_{i\sigma} \cos(\mathbf{Q}_c \mathbf{r}_i + \frac{Q_c}{2}) c_{i\sigma}^\dagger c_{i\sigma} \\ &\quad - \delta t \sum_{i\sigma} \left(\cos(Q_c x_i) c_{i+(1,0)\sigma}^\dagger c_{i\sigma} - \cos(Q_c [x_i - 1/2]) c_{i+(0,1)\sigma}^\dagger c_{i\sigma} + \text{h. c.} \right) \\ \hat{V}_2 &= V_s \sum_{i\sigma} (\cos(\mathbf{Q}_s \mathbf{r}_i) + \cos(\mathbf{Q}_s \mathbf{r}_i + \frac{Q_c}{2})) c_{i\sigma}^\dagger c_{i\sigma} . \end{aligned} \quad (13.5)$$

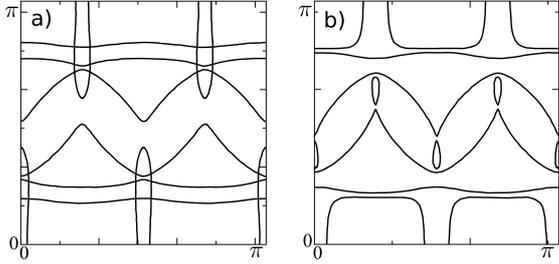


Figure 13.1: Fermi surfaces for the bond-centered period-8 stripe states with a) pure bond modulation, $\delta t = 0.05$ eV, and b) pure spin modulation, $V_s = 0.09$ eV, plotted in the first quadrant of the Brillouin zone of the underlying square lattice. The Fermi surfaces are qualitatively equivalent to those obtained from site-centered spin or charge potentials (not shown). Without

spin order (case a), besides open orbits only small hole-like closed orbits with a large aspect ratio are present. Additional spin order (case b) induces both hole-like and electron-like closed orbits. The electron-like pockets correspond to the structures at the Brillouin zone boundary. We checked the effective charge of the pockets numerically by the analyzing the curvature of the band structure.

for bond-centered stripe patterns and

$$\begin{aligned}\hat{V}_1 &= V_c \sum_{i\sigma} \cos(\mathbf{Q}_c \mathbf{r}_i) c_{i\sigma}^\dagger c_{i\sigma} \\ \hat{V}_2 &= V_s \sum_{i\sigma} \cos(\mathbf{Q}_s \mathbf{r}_i) c_{i\sigma}^\dagger c_{i\sigma}\end{aligned}\quad (13.6)$$

for site-centered stripe patterns, according to the definitions used in the context of Eqs (13.1) and (13.2). We will chose the d -wave part of the bond modulation in Eq. (13.5) such that sites with large spin density are connected by stronger bonds, implying $\delta t > 0$. Consistent with Fig. 11.4, the charge potential is chosen such that sites or bonds with maximal spin density have higher electron density than sites or bonds with minimal spin density, implying $V_c > 0$ in (13.6) for either sign of V_s . As can be especially seen from Eq. (13.6), spin stripe potentials act as a periodically modulated spin-dependent chemical potential. Therefore, the local moment size will not be equal on all sites. For comparison with experimental values we calculated the zero-temperature expectation values $\langle S_z(r_i) \rangle = \frac{1}{2} \langle \hat{n}_{i\uparrow} - \hat{n}_{i\downarrow} \rangle$ and $\langle \hat{n}_i \rangle = \langle \hat{n}_{i\uparrow} + \hat{n}_{i\downarrow} \rangle$, with $\hat{n}_{i\sigma} = c_{i\sigma}^\dagger c_{i\sigma}$. These quantities are easily obtained numerically from the eigenvalues and eigenvectors of the matrix (13.3), in analogy to the calculation for the pnictides detailed in appendix A.

Fermi-surface reconstruction

Fermi surface geometry has a particular strong influence on the Nernst signal (Behnia, 2009). The dominant contribution typically derives from closed electron orbits, since open orbits restrict the electronic motion mostly along one spatial direction and do not allow for a transverse flow of carriers. This can be understood from the formulas for the Hall conductivity and the thermoelectrical Hall conductivity in Eq. (12.34). Their size is proportional to mass terms that measure the band curvature, which tends to be small for open

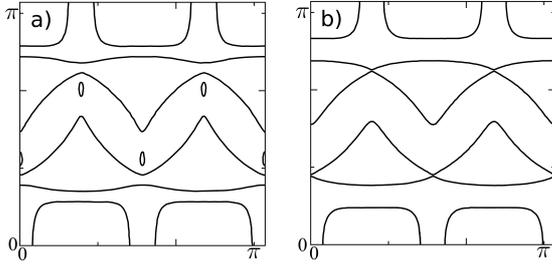


Figure 13.2: Fermi surfaces for the bond-centered period-8 stripe states with combined spin and charge modulation, plotted in the first quadrant of the Brillouin zone of the underlying square lattice. a) $V_s = 0.09$ eV, $\delta t = 0.02$ eV. b) $V_s = 0.09$ eV, $\delta t = 0.055$ eV. With increasing bond modulation, the small hole-like pockets shrink (case a) and disappear (case b).

orbits as compared to closed orbits.

Closed carrier orbits can contribute in different ways to the Nernst signal, with a vanishing Nernst signal in case of a single isotropic Fermi surface and an energy-independent relaxation time (Sondheimer, 1948). Similar to this ideal case, in absence of stripe order a single hole-like cylindrical Fermi surface is present (Daou et al., 2009a), and the experimentally observed in-plane Nernst signal is indeed very small. A natural way to avoid an almost canceled Nernst signal is the emergence of a second type of oppositely charged carriers in the Fermi surface (Behnia, 2009).

It has been suggested that electron-like orbits cause the negative sign of the high-field Hall coefficient measured by LeBoeuf et al. (2007). Soon after, it has been proposed that electron pockets might also be of relevance for the observed quantum oscillations in underdoped cuprates (Millis and Norman, 2007). In the context of period-8 stripe order, Millis and Norman (2007) concluded that a formation of closed electron-like orbits requires a finite spin-stripe potential, as illustrated in Fig. 13.1. Charge stripe order can only result in closed hole-like orbits, which eventually vanish in the limit of large charge stripe potential (Fig. 13.1a). Finite spin stripe order separates electron-like pockets at the zone boundary (Figs 13.1, 13.1), with decreasing size upon increasing spin-stripe order. These arguments point towards a fundamental role of spin-stripe order in enhancing the Nernst signal, motivating us to concentrate on the case of pure spin stripe order in the following. The impact of charge order on Fermi surfaces as resulting from pure spin stripes is illustrated in Fig. 13.2. We will discuss the impact of charge order on the Nernst effect afterwards.

Nernst effect from spin modulations

After motivating the importance of spin stripe order for the formation of closed electron orbits, we analyze the influence of spin-driven stripe order on the quasiparticle Nernst effect in the following. Spin stripe order is most stable near $x = 1/8$ doping, and a strong positive enhancement of the normal state Nernst effect has been observed in $\text{La}_{1.6-x}\text{Nd}_{0.4}\text{Sr}_x\text{CuO}_4$ near this doping as well (Choinière et al., 2009). Formally we will consider a pure spin stripe potential of the form (13.2) with modulation period 8, which will induce weak charge order with period 4. In this case, the eigenvalues of the Hamiltonian matrix (13.3) can be

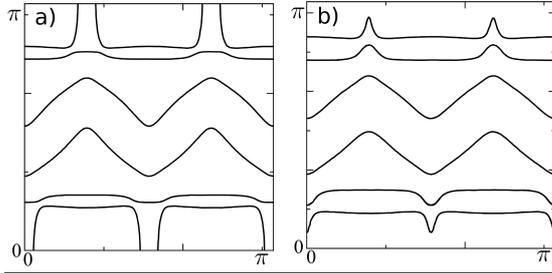


Figure 13.3: As in Fig. 13.2, but for site-centered period eight stripe order. a) $V_s = 0.1$ eV, $V_c = 0.10$ eV. b) $V_s = 0.1$ eV, $V_c = 0.15$ eV. As above, with increasing charge modulation the Fermi pockets disappear in favor of open one-dimensional orbits.

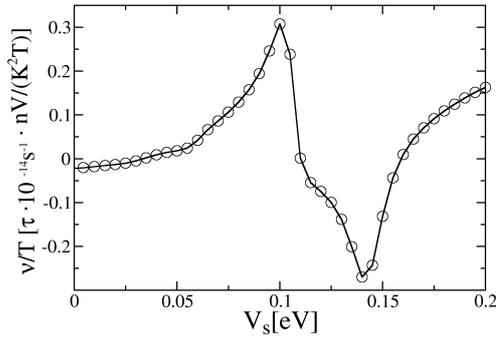


Figure 13.4: Nernst effect for period-8 anti-ferromagnetic stripes at doping $x = 1/8$ as function of the spin modulation; the results are identical for the site-centered and bond-centered spin stripe order. In a restricted range of potential strength, the signal is negative. The Nernst coefficient becomes negative at $V_s \simeq 0.1$ eV, corresponding to maximal local moments of $2\mu_B \langle S_z \rangle \simeq 0.3\mu_B$, staying negative up to an unrealistically large maximal moment size of $2\mu_B \langle S_z \rangle \simeq 0.5\mu_B$.

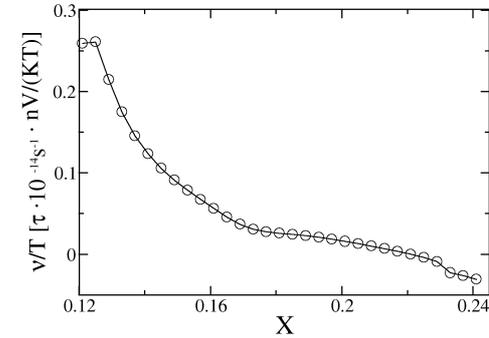


Figure 13.5: Doping dependence of the Nernst coefficient for period-8 antiferromagnetic stripes, assuming a doping dependence of the stripe order described by Eq. (13.8) and $V_0 = 0.14$. It can be seen that the Nernst coefficient is significantly enhanced and positive near $x = 1/8$.

equivalently obtained from the matrix

$$\begin{bmatrix} \epsilon_{\mathbf{k}} & V_s^*(\mathbf{k}) \\ V_s(\mathbf{k}) & \epsilon_{\mathbf{k}+\mathbf{Q}_s} \end{bmatrix} \quad (13.7)$$

if \mathbf{k} is in the full Brillouin zone $\mathbf{k} \in [-\pi, \pi] \times [-\pi, \pi]$. The phase of a complex valued potential $V_s^*(\mathbf{k})$ does therefore not enter the eigenvalues of (13.7), such that bond and site centered spin stripe order will yield the same Nernst signal. As we will see later on, a finite charge stripe potential will distinguish bond and site centered stripe order.

In Fig. 13.4, we depict our numerical solution for the coefficient ν/T as a function of increasing V_s . For small spin stripe potential, the coefficient becomes positively enhanced, while a sign change occurs above $V_s \simeq 0.1$ eV, with a second sign change at even higher spin stripe potential. Stripe-induced changes of Fermi pockets are responsible for these changes:

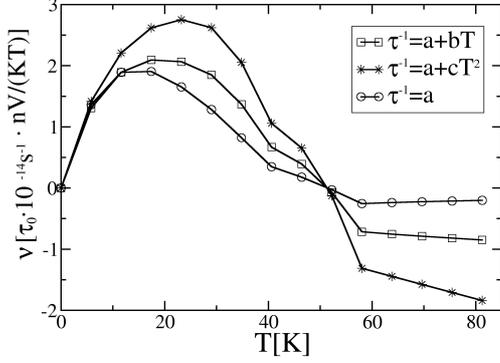


Figure 13.6: Temperature dependence of the Nernst coefficient for period-8 antiferromagnetic stripes with a temperature-dependent spin stripe potential $V_0\sqrt{1 - T/T_{\text{sp}}}$. Upon increasing temperature, the Nernst coefficient increases strongly to a large positive value which becomes maximal at around 20 K. Slightly below the ordering temperature $T_{\text{sp}} \simeq 60$ K, the coefficient becomes negative, as observed in experiment. The different scattering rates have been parameterized with $a = \tau_0^{-1}$, $b = a/70$ K and $c = a/800$ K², and we set $V_0 = 0.1$ eV.

Increasing V_s eliminates the small hole pockets in Fig. 13.1 near the local maximum of ν/T in Fig. 13.4, at even higher V_s , these orbits split and form pockets at the local minimum of ν/T (not shown, see Millis and Norman (2007)).

The parameter V_s needs to be determined from experimental observables, and a suitable quantity is the ordered magnetic moment as obtained in several experiments (Nachumi et al., 1998, Vojta, 2009). While neutron scattering determines the average local moment, μSR measurements are sensitive to the maximal local moment which at 1/8 doping is roughly $0.3\mu_B$ in 214 compounds (Nachumi et al., 1998, Vojta, 2009), or half that of the undoped parent compound, implying $\langle S_z \rangle = 0.15$. Our mean-field model produces a maximal ordered moment $\langle S_z \rangle_{\text{max}} = 0.15$ for a stripe potential $V_s \simeq 0.10$ eV, being close to the maximum in the Nernst coefficient shown in Fig. 13.4, and values of V_s beyond this maximum correspond to unrealistically strong magnetic order. Ordered magnetism in $\text{YBa}_2\text{Cu}_3\text{O}_y$ in zero magnetic field is only observed for $y \leq 0.45$, with a moment of $0.05\mu_B$ at zero field and $0.07\mu_B$ at 15 T measured by neutron scattering (Haug et al., 2009). Stripe order becomes less stable at dopings above $x \geq 1/8$ and the magnetic ordering temperature in $\text{La}_{1.6-x}\text{Nd}_{0.4}\text{Sr}_x\text{CuO}_4$ extrapolates to zero at $x = 0.24$ (Taillefer et al., 2009), while the ordering wave vector \mathbf{Q}_s is constant in this doping range (Vojta, 2009). We account for this behavior by using a mean-field dependence of the spin-stripe order parameter,

$$V_s(x) = V_0\sqrt{1 - x/x_c} \quad (13.8)$$

for x below x_c and setting $V_s = 0$ elsewhere. This mean-field field dependency of the gap in principle has to be determined self-consistently, together with the doping-dependence $\mu(x)$ and $\mathbf{Q}(x)$. The doping dependence of the gap is indeed self-consistently described by (13.8), see the discussion of Bazaliy et al. (2004) and references therein. Near $x \simeq x_c$, the SDW gaps can become arbitrarily small and the semiclassical equations of motion will be invalidated by interband transitions, mediated by magnetic breakdown, impurity scattering or thermal excitations. For these effects, we can apply the estimates we made in section 12.2 by replacing $V_0 = 0.7$ eV with $V_0 = 0.15$ eV and adjusting the SDW ordering

temperature T_0 to about 90 K (Ichikawa et al., 2000) in Eqs. (12.14), (12.15) and (12.17), leading to reasonable small corrections due to interband transitions at sufficiently low temperatures $T < T_0$.

We now turn to a discussion of finite temperatures, which will influence both spin stripe potential and the relaxation time. The latter effect on spin stripe order is captured by a temperature-dependent spin stripe potential with the mean-field dependence $V_0\sqrt{1 - T/T_{\text{sp}}}$, with $T_{\text{sp}} \simeq 60$ K at $x = 1/8$ in $\text{La}_{1.6-x}\text{Nd}_{0.4}\text{Sr}_x\text{CuO}_4$ (Ichikawa et al., 2000). Since the Nernst coefficient is proportional to the relaxation time, the overall temperature dependence of the relaxation time will only multiply the result obtained by assuming a constant relaxation time. For completeness, we use various parameterizations to model the temperature dependence of the relaxation time, e.g., including the linear behavior $\tau^{-1} = a + bT$, with $b = a/70$ K accounting for the relation $\tau^{-1}(T=0) \simeq 2\tau_0^{-1}(T=70$ K) – as qualitatively consistent with the experimental results of Valla et al. (2000) – and $a \equiv \tau_0^{-1}$ remaining as a free parameter.

Our numerical results – depicted in Fig. 13.6 – show a peak in the Nernst coefficient at around $T = 20$ K. Comparing this peak with the peak structure of height $50\text{nV}/(\text{KT})$ observed in Nernst measurements in $\text{La}_{1.8-x}\text{Eu}_{0.2}\text{Sr}_x\text{CuO}_4$ our calculation requires a reasonable relaxation time $\tau \simeq 0.5\hbar/(k_B T)$ to reproduce this peak height if the scattering rate is assumed to be proportional to temperature, as observed experimentally in most parts of the Brillouin zone (Valla et al., 2000). It is important to note that experimentally, a positive rise in the Nernst coefficient is already observed at twice the charge ordering temperature, $T = 2T_{\text{ch}}$ (Choinière et al., 2009), likely due to fluctuating order which is not captured by our description.

Nernst effect from charge modulations

In this section, we analyze how pure charge modulations effect the Nernst coefficient. This is motivated by the fact that on theoretical grounds, charge order may exist without spin order, even at zero temperature (Zachar et al., 1998). Between $T_{\text{ch}} \simeq 80$ K and $T_{\text{sp}} \simeq 45$ K, this has been clearly confirmed in experiments on $\text{La}_{1.8-x}\text{Eu}_{0.2}\text{Sr}_x\text{CuO}_4$ near doping $x = 1/8$ (Vojta, 2009). Although long-range static charge order has been detected in several 214 cuprates, reliable information about the amplitude of charge modulation is lacking, since most scattering experiments are not directly sensitive to the charge modulation, with the exception of resonant soft x-ray scattering (Vojta, 2009). We shall not make use of these experimental results, because a quantitative analysis of them turns out to be model-dependent. Instead, it is possible to infer a rough order of magnitude estimate from STM data of Kohsaka et al. (2007), which shows a contrast in the tunneling asymmetry that might be interpreted as charge density modulation, leading to a modulation amplitude in the charge sector of $\pm 20 \dots 30\%$ (Kohsaka et al., 2007).

We introduced two variants for charge order in the beginning, modulated on-site potentials or a spatially modulated hopping amplitude which is only realized for bond-centered stripe order. For an interpretation of transport properties in presence of charge order, it is important to note that period eight charge order with bond or electron density modulation below a reasonable value of 30% cannot produce closed electron-like orbits, and only hole-

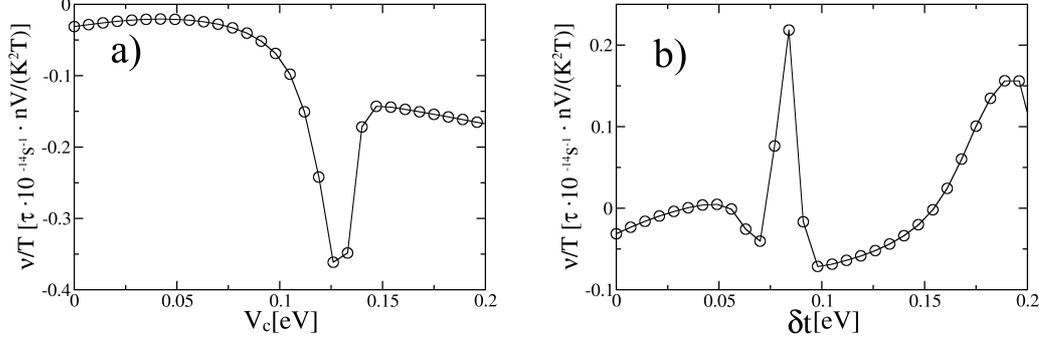


Figure 13.7: Nernst effect for period-4 charge-only stripes at doping $x = 1/8$ as function of a) site-centered chemical-potential modulation and b) bond-centered bond modulation. The Nernst coefficient is clearly either negative or much less enhanced than for pure spin stripe order for both types of charge order. In addition, it remains much less enhanced than for pure spin stripe order *everywhere where modulation in the charge channel does not exceed 30%*, corresponding to $\delta t \lesssim 0.06$ eV and $V_c \lesssim 0.1$ eV.

orbits as depicted in Fig. 13.1 can emerge. Overall, we found little qualitative difference in the Fermi surfaces between site-centered and bond-centered charge order, and it has been already pointed out by Millis and Norman (2007) that site-centered stripes produce closed electron orbits only in presence of finite spin stripe potential. Our numerical results for the Nernst coefficient in presence of pure charge order are depicted in Fig. 13.7 and show a negative or very small Nernst coefficient in presence of site-centered charge order and a negative Nernst coefficient for bond-centered order. Site-centered charge stripes with $V_c = 0.1$ eV lead to 30% modulation amplitude, while $\delta t = 0.055$ eV leads to 20% (30%) modulation of vertical (horizontal) bond density, and reasonable potential strengths thus cannot account for the positively enhanced Nernst signal which has been measured in presence of stripe order (Choinière et al., 2009).

Combined spin and charge modulations

It remains to discuss the influence of explicitly adding a charge stripe potential on top of spin stripe order. As can be seen from Fig. 13.2, adding charge order on top of spin stripe order has the effect of breaking up closed electron orbits into open orbits for sufficiently strong charge order. Transport properties resulting from pure spin stripe order are therefore expected to change qualitatively if charge stripe order becomes too strong. As a quantitative orientation for the strength of on-site modulations, we obtain a modulation of 20% in the mean conduction electron density for a charge potential of $V_c = 0.07$ eV.

Adding a charge stripe potential to a finite spin stripe potential of $V_s = 0.1$ eV leads to a very small or negative Nernst coefficient for charge potentials stronger than 0.05 eV, see

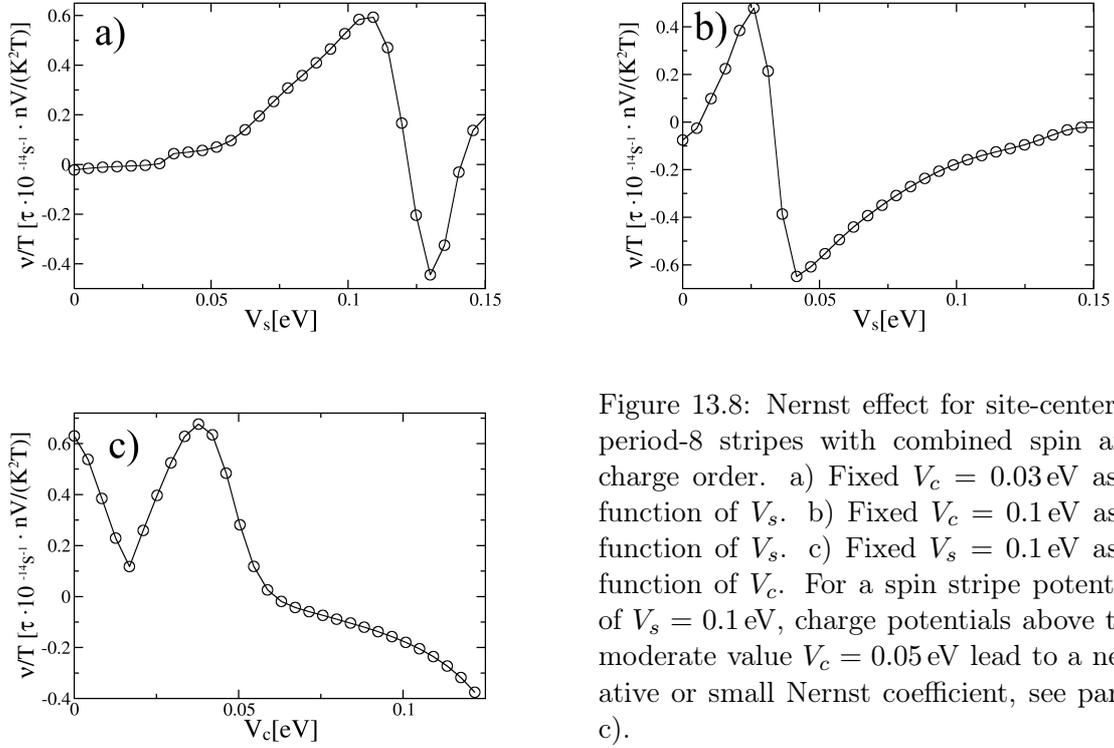


Figure 13.8: Nernst effect for site-centered period-8 stripes with combined spin and charge order. a) Fixed $V_c = 0.03 \text{ eV}$ as a function of V_s . b) Fixed $V_c = 0.1 \text{ eV}$ as a function of V_s . c) Fixed $V_s = 0.1 \text{ eV}$ as a function of V_c . For a spin stripe potential of $V_s = 0.1 \text{ eV}$, charge potentials above the moderate value $V_c = 0.05 \text{ eV}$ lead to a negative or small Nernst coefficient, see panel c).

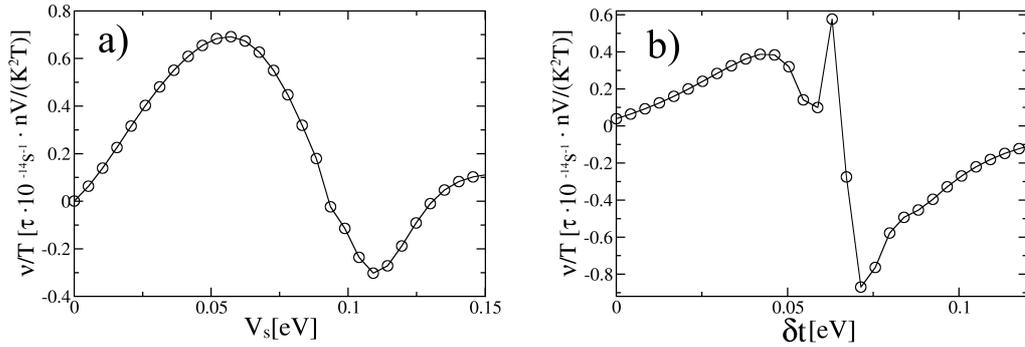


Figure 13.9: Similar to Fig. 13.8, but for bond-centered period-8 stripes. a) Fixed $\delta t = 0.055 \text{ eV}$ as a function of V_s . b) Fixed $V_s = 0.09 \text{ eV}$ as a function of δt . As is depicted in panel a), for a wide range of spin stripe potentials below $V_s \simeq 0.09 \text{ eV}$ the Nernst coefficient is positively enhanced. ($V_s = 0.1 \text{ eV}$ corresponds to an ordered moment of $\simeq 0.3 \mu_B$). For bond modulations $\delta t \lesssim 0.05 \text{ eV}$, the Nernst coefficient can remain positive, see panel b).

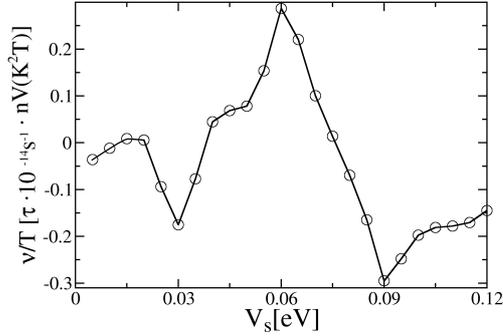


Figure 13.10: Nernst effect for a period-16 SDW order as a function of V_s with $x = 0.1$. For $V_s \gtrsim 0.07$ eV (corresponding to a maximal local moment of $2\mu_B \langle S_z \rangle \gtrsim 0.20\mu_B$) the Nernst coefficient turns negative with an enhanced amplitude in comparison to the non-ordered state.

Fig. 13.8c). This behavior would therefore be compatible with the normal state Nernst coefficient in $\text{La}_{1.6-x}\text{Nd}_{0.4}\text{Sr}_x\text{CuO}_4$ if charge order leads only to less than 15% modulations in the charge sector.

In case of bond-centered spin stripes with additional bond modulations, the Nernst signal in presence of a spin stripe potential of $V_s = 0.09$ eV remains positively enhanced even for a large bond modulation of $\delta t = 0.05$ eV with a kinetic energy modulation of between 20 – 30%, see Fig. 13.9b. At a fixed bond modulation of $\delta t = 0.055$ eV, the Nernst coefficient is negative only in a range of spin stripe potentials $V_s \gtrsim 0.1$ eV. Charge modulations exceeding 10% would therefore suggest rather a bond-centered nature of charge order in $\text{La}_{1.6-x}\text{Nd}_{0.4}\text{Sr}_x\text{CuO}_4$ if the modulation in the charge sector exceeds 15% (corresponding to $V_c \simeq 0.05$ eV).

13.3 Nernst effect below doping $x = 1/8$

The underdoped regime of the cuprates is of particular interest for our analysis, since below doping $x = 1/8$, the incommensurability ϵ_s in $\text{La}_{1.6-x}\text{Nd}_{0.4}\text{Sr}_x\text{CuO}_4$ and $\text{La}_{2-x}\text{Sr}_x\text{CuO}_4$ follows the doping level, $\epsilon_s \approx x$ (Vojta, 2009). The ordering wave vector is therefore not independent of doping, and it is of interest to analyze possible changes in the quasiparticle Nernst effect as compared to period eight stripe order occurring above doping $x = 1/8$. Our interest in this doping range is also motivated by the observation of quantum oscillations in recent high magnetic field experiments on underdoped $\text{YBa}_2\text{Cu}_3\text{O}_y$ at hole doping $x \simeq 0.1$ (LeBoeuf et al., 2007). Theoretical work has interpreted these oscillations in terms of multiple small Fermi pockets induced by incommensurate SDW order (Harrison, 2009). Interestingly, these experiments were followed by the observation of an enhanced negative Nernst coefficient saturating in strong magnetic fields (Choinière et al., 2009).

In the underdoped region of $\text{La}_{1.6-x}\text{Nd}_{0.4}\text{Sr}_x\text{CuO}_4$ and $\text{La}_{1.8-x}\text{Eu}_{0.2}\text{Sr}_x\text{CuO}_4$, period-10 spin order corresponds to a doping level $x = 0.1$, whereas period-16 spin order is motivated by recent neutron scattering work on $\text{YBa}_2\text{Cu}_3\text{O}_y$ with $y = 6.45$, where incommensurate correlations at $\mathbf{Q}_s = 2\pi(0.5, 0.5 \pm \epsilon_s)$ with $\epsilon_s \simeq 0.06$ were detected (Haug et al., 2009). In this section, we consider stripe order with collinear spin order of periods 10 and 16 (and

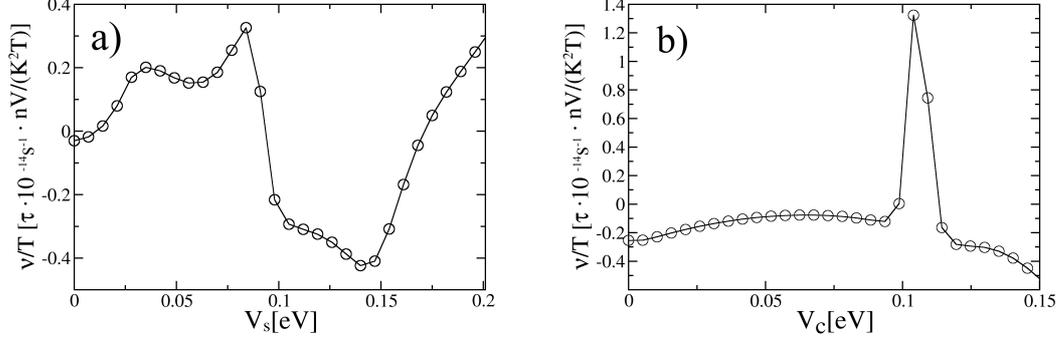


Figure 13.11: Nernst effect for site-centered period-10 stripe order. Spin only stripe order (a) leads to a negative Nernst coefficient for spin potentials of $V_s = 0.09 \dots 0.17$ eV. Adding additional charge order to a spin potential of $V_s = 0.1$ eV does not change the sign of the Nernst coefficient for charge potentials $V_c \leq 0.1$ eV, which correspond to realistic charge modulations of up to 30% (b).

corresponding charge order with period 5 and 8), which are adequate to analyze the normal state Nernst effect of underdoped cuprate samples.

Period-16 stripe order

In underdoped cuprates, long-ranged antiferromagnetic order at wave vector $\mathbf{Q}_s = (\pi, \pi[1 \pm 2\delta])$ with $\delta \approx 0.055$ has been confirmed recently in magnetic-field dependent elastic scattering experiments in $B = 14.9$ T (Haug et al., 2009). Using inelastic neutron scattering, incommensurate magnetic excitations have been found in $\text{YBa}_2\text{Cu}_3\text{O}_y$ samples with $y \approx 6.5$ and $\delta \approx 0.6$ in absence of an applied field (Stock et al., 2004). It is convenient to approximate the experimentally observed incommensurability by the rational value $\delta = \frac{1}{16} = 0.0625$ in order to model the reconstructed band structure by the 16×16 matrix

$$H = \begin{pmatrix} \varepsilon_{\mathbf{k}} & V_s^* & V_c^* & \dots & V_c & V_s \\ V_s & \varepsilon_{\mathbf{k}+\mathbf{Q}_s} & V_s^* & \dots & 0 & V_c \\ V_c & V_s & \varepsilon_{\mathbf{k}+2\mathbf{Q}_s} & \dots & 0 & 0 \\ \vdots & \vdots & \vdots & \ddots & \vdots & \vdots \\ V_c^* & 0 & 0 & \dots & \varepsilon_{\mathbf{k}+14\mathbf{Q}_s} & V_s^* \\ V_s^* & V_c^* & 0 & \dots & V_s & \varepsilon_{\mathbf{k}+15\mathbf{Q}_s} \end{pmatrix}. \quad (13.9)$$

In this matrix, the momenta \mathbf{k} are defined to lie in the reduced Brillouin zone $\mathbf{k} \in [-\frac{\pi}{8}, \frac{\pi}{8}] \times [-\frac{\pi}{2}, \frac{\pi}{2}]$. Again, momentum dependence of the scattering potentials has been dropped in Eq. (13.9) and can be restored by labeling a potential connecting energies with momenta $\mathbf{k} + \mathbf{q}$ and $\mathbf{k} + \mathbf{q} + \mathbf{Q}_{c/s}^*$ with the momentum $\mathbf{k} + \mathbf{q}$. As motivated in the beginning of this chapter, incommensurate collinear spin order leads to the opening of gaps at the crossing

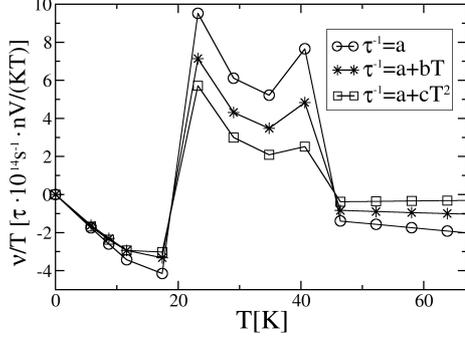


Figure 13.12: Nernst effect for period-10 stripe order at finite temperatures. Upon decreasing temperature to below about 25 K, the Nernst coefficient changes sign and becomes negative. Upon increasing temperature above about 25 K, the coefficient becomes positive and significantly enhanced. Slightly below the ordering temperature $T_{\text{sp}} \simeq 50$ K, the coefficient becomes negative again. The different scattering rates have been parameterized with $a = \tau_0^{-1}$, $b = a/70$ K and $c = a/800$ K², and we set $V_0 = 0.12$ eV.

points of bands $\varepsilon_{\mathbf{k}+n\mathbf{Q}_s}$ and $\varepsilon_{\mathbf{k}+n\pm m\mathbf{Q}_s}$. The approximation of the incommensurability by a rational value certainly does not describe gaps opening at the crossing of bands with $m \geq 16$. However, these gaps will be of order $2\Delta_m \sim 2V_s^m/t^{m-1}$ and will not be of importance if $V_s \ll t \sim t_1$ (Harrison, 2009). If we consider the value $V_s = t_1/6$ used by Harrison (2009), the transmission amplitude through the $m = 3$ gap in $B = 20$ T is $\approx 94.1\%$, using formula (12.10) together with the universal Fermi velocity $v_F = 2.3 \times 10^7$ cm/s (Zhou et al., 2003). An estimate for the size of V_s can be inferred from the magnitude of ordered moment, which increases from $0.05\mu_B$ to $0.07\mu_B$ at 15 T, as measured by neutron scattering (Haug et al., 2009). In this context, it is important to note again that the maximal local moment in a collinear stripe structure is larger than the one inferred from neutron scattering which averages over the oscillation period. As depicted in Fig. 13.10, values of $V_s \gtrsim 0.07$ eV lead to a negative Nernst signal, with $V_s = 0.07$ eV corresponding to a maximum ordered moment of $\simeq 0.2\mu_B$. Experimental results from Chang et al. (2009) report that field strengths of above 20 T are sufficient to produce a large negative normal state Nernst coefficient in underdoped $\text{YBa}_2\text{Cu}_3\text{O}_y$. Assuming that effects of Landau quantization are negligible in this regime, our result of a negative Nernst coefficient for $V_s \gtrsim 0.07$ eV is potentially compatible with these experimental results.

Period-10 stripe order

In underdoped cuprates of the 124 family, the stripe ordering wave vector $\mathbf{Q}_s = 2\pi(0.5, 0.5 \pm \epsilon_s)$ follows $\epsilon_s = x$ for $x < 1/8$, such that the period of order increases with decreasing doping. A doping of $x = 0.1$ causes therefore ordering with $\mathbf{Q}_s = \pi(4/5, 1)$, and is associated with period-10 spin stripe order. For this period, it is impossible that both charge and spin modulation have extrema positioned on the bond centers, and we are lead to assume a site-centered stripe geometry in the following. Then, the Hamiltonian matrix formulated in Eq. (13.9) can be used by replacing the wave vector with $\mathbf{Q}_s = \pi(4/5, 1)$ and using a 10×10 matrix with analogous structure.

A moderate spin stripe potential of $V_s = 0.08$ eV produces typically both electron and

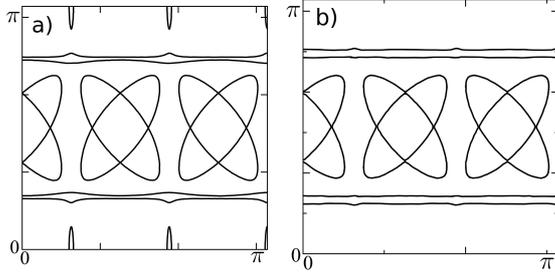


Figure 13.13: Fermi surfaces as resulting from period-10 stripe order, plotted in the first quadrant of the Brillouin zone of the underlying square lattice. Pure spin stripe order with $V_s = 0.08$ eV produces both electron-like and hole-like closed orbits, see a). Adding additional charge stripe order with $V_c = 0.07$ eV eliminates the small electron-like orbits and the remaining closed orbits are all hole-like, see b).

hole-pockets, while adding sufficiently strong charge order finally eliminates the electron like orbits and the remaining closed orbits are all hole-like, see Fig. 13.13.¹ Likewise, the electron-like orbits shrink upon increasing V_s above $V_s = 0.1$ eV (not shown), and the hole-orbits start dominating transport properties. These Fermi surface changes are related to a sign change in the Nernst signal at a spin potential strength of $V_s \simeq 0.09$ eV, as shown in Fig. 13.11a. The negative sign is explained by the dominant contribution of the closed hole-like orbits (see Fig. 13.13b) to the Nernst coefficient. Numerical checks show that $|\alpha_{xx}\sigma_{xy}| \gg |\alpha_{xy}\sigma_{xx}|$ and analogously $|\alpha_{yy}\sigma_{yx}| \gg |\alpha_{yx}\sigma_{yy}|$ for these orbits, and the resulting Nernst coefficient is negative since both α_{xx} and σ_{xy} are positive for hole-like carriers, as we also checked numerically. Adding charge order to a spin potential of $V_s = 0.1$ eV maintains a negative Nernst coefficient for charge potentials corresponding to realistic values of up to 30% charge density modulation (Fig. 13.11b), which is probably below the value realized in charge-ordered samples.

Analogous to period eight stripe order, we can discuss finite temperature properties of the Nernst coefficient by assuming a mean-field dependence $V_s(T) = V_0\sqrt{1 - T/T_{sp}}$ with $V_0 = 0.12$ eV and $T_{sp} = 50$ K taken from neutron scattering experiments Ichikawa et al. (2000). As depicted in Fig. 13.12, successive lowering of temperature below the ordering temperature T_{sp} leads to two successive sign changes in the Nernst coefficient with a negative Nernst coefficient resulting below $\simeq 20$ K. Upon variation of the temperature dependence of the relaxation time, the overall shape of the signal is qualitatively similar. Our results lead to the conclusion that incommensurate spin-stripe order in underdoped cuprates of the 124 family can lead to an observable negative peak in the Nernst coefficient as a function of temperature. In order to observe this peak, eventually large magnetic fields have to be applied in order to increase spin stripe potential and to decrease vortex contributions to the Nernst coefficient.

¹We checked the effective charge of the closed orbits by numerically analyzing the curvature of the dispersion in the vicinity of these orbits.

13.4 Influence of pseudogap and local pairing

So far, our model calculations have assumed the existence of metallic quasiparticles with a large Fermi surface in the symmetry-unbroken state. In underdoped cuprates at zero field, these assumptions might be invalidated by the pseudogap phenomenon, showing a partially gapped Fermi surface with Fermi arcs remaining near the Brillouin zone diagonals in photoemission experiments on $\text{Bi}_2\text{Sr}_2\text{CaCu}_2\text{O}_{8+\delta}$ (Kanigel et al., 2006). Furthermore, in stripe-ordered $\text{La}_{2-x}\text{Ba}_x\text{CuO}_4$, only nodal points appear to survive as low-energy excitations below the stripe-ordering temperature (Valla et al., 2006, He et al., 2009). These phenomena are restricted to the temperature range $T_c < T < T^*$, where T^* is the pseudogap temperature. This situation might invalidate our approach if pseudogap and enhanced Nernst coefficient are caused by the same phenomena, as might be concluded from the relation between the onset of the enhanced Nernst coefficient and the pseudogap temperature in underdoped $\text{La}_{2-x}\text{Sr}_x\text{CuO}_4$ (Xu et al., 2000). Recent observations by Choinière et al. (2009) do not agree with this point of view, since a second positive peak in the Nernst signal emerges near doping $x = 1/8$ in $\text{La}_{1.6-x}\text{Nd}_{0.4}\text{Sr}_x\text{CuO}_4$, while the resistively defined pseudogap temperature still decreases below doping $x = 1/8$ and cannot follow the onset temperature of the additional peak structure. Therefore, we will concentrate on the effect of translational symmetry breaking on the Nernst coefficient, without accounting for other possible sources of pseudogap phenomena in full detail. Instead, we will briefly discuss corrections to this quasiparticle picture based on a recent discussion by Senthil and Lee (2009).

The resistive transition in underdoped cuprates happens at a modest field of about 40 T. However, it is questionable how this modest field can close the large antinodal gap and be responsible for the quantum oscillations seen in experiment. A way out of this problem is to consider the influence of phase decoherence of the superconducting order parameter, which we will consider as the dominating corrections to the quasiparticle picture. Such a scenario has been argued recently to account for a large part of the phenomenology of the underdoped cuprates (Senthil and Lee, 2009). The self-energy correction due to phase incoherence can be derived from a BCS Hamiltonian in second order perturbation theory in the pairing gap Δ_0 (Senthil and Lee, 2009),

$$\Sigma(\mathbf{k}, \omega) = \Delta_{0\mathbf{k}}^2 \frac{-i\omega + \varepsilon_{\mathbf{k}}}{\omega^2 + \varepsilon_{\mathbf{k}}^2 + \pi\Gamma^2}, \quad (13.10)$$

where Γ is the Cooper pair phase decay rate and the pairing gap follows $\Delta_{0\mathbf{k}} = \frac{\Delta_0}{2}(\cos(k_x) - \cos(k_y))$. This self-energy correction describes scattering of quasiparticles on a fluctuating d -wave order parameter. It is readily seen that the renormalized quasiparticle dispersion is given by $E(\mathbf{k}) = \varepsilon(\mathbf{k}) + \text{Re}\Sigma(\mathbf{k}, \omega = 0)$, which is explicitly given by

$$E(\mathbf{k}) = \varepsilon_{\mathbf{k}} \left(1 + \frac{\Delta_{0\mathbf{k}}^2}{\varepsilon_{\mathbf{k}}^2 + \pi\Gamma^2} \right). \quad (13.11)$$

Remarkably, the original Fermi surface remains unchanged, and only renormalization of band masses and quasiparticle velocities by a factor $(1 + (\Delta_{0\mathbf{k}}^2/(\pi\Gamma^2)))$ occurs. Since Γ is

of the order Δ_0^{-1} near H_{c2} , we may expect no qualitative change of transport properties due to phase incoherent pairing at magnetic fields of the order H_{c2} .

13.5 Summary and relation to experiments

In this chapter, we calculated the normal-state Nernst coefficient in the presence of translational symmetry breaking caused by stripe order. These calculations were based on a simple quasiparticle picture, combined with a Boltzmann equation approach.

For a large quasiparticle Nernst coefficient, the role of Fermi pockets turned out to be crucial. In our results, the existence of Fermi pockets plays an important role for a large quasiparticle Nernst coefficient. In particular, charge order does not generate combinations of electron and hole pockets, but spin order is required. Both positive and negative Nernst coefficients can be generated, depending on both spatial period and amplitude of the stripe order. As a function of the stripe amplitude, sign changes occur which can be traced back to topological changes of the Fermi surface. A robust positive Nernst signal was mainly found for period-8 modulated antiferromagnetic order with $\mathbf{Q}_s = \pi(3/4, 1)$, appropriate for cuprates with doping levels $x \geq 1/8$, as long as the magnetic order is not assumed to be unrealistically strong. For small charge modulation, there is little qualitative difference between bond-centered and site-centered stripes; for larger charge modulation, site-centered stripes tend to destroy hole-like orbits and induce a negative Nernst coefficient. Charge order alone generates a small and typically negative Nernst coefficient.

Experimental results bear several qualitative aspects of our theoretical analysis. One feature that is certainly absent in our theory is a pairing-induced positive peak at low T near the superconducting T_c , as studied theoretically before by several authors, e.g., Ussishkin et al. (2002), Podolsky et al. (2007). In experiments on $\text{La}_{1.6-x}\text{Nd}_{0.4}\text{Sr}_x\text{CuO}_4$, an extra piece has been identified at elevated temperatures. Our positive quasiparticle Nernst coefficient for period-8 stripes is in qualitative agreement with these experimental results, see Figs 13.5 and 13.6. As function of temperature, the quasiparticle Nernst signal peaks below the charge ordering temperature T_{ch} , vanishes linearly as $T \rightarrow 0$ and becomes negative at high T , Fig. 13.6. Experimentally, the temperature maximum of the extra piece in the Nernst signal appears to be above T_{ch} , which may be explained in terms of strong precursor stripe fluctuations not captured by our mean-field theory. The doping dependence of the quasiparticle Nernst signal in the doping range $0.12 < x < 0.24$ is in qualitative agreement with experiment as well, Fig. 13.5.

Our analysis of magnetic modulation periods larger than 8 sites yields sign changes of the quasiparticle Nernst signal as a function of the modulation amplitude. Therefore, we predict sign changes in the Nernst signal in compounds with well-established stripe order, or as a function of applied field if the order is primarily field-induced. The latter situation indeed occurred in a recent experiment on $\text{YBa}_2\text{Cu}_3\text{O}_y$ at $y = 6.67$ (Chang et al., 2009), corresponding to a doping level of 0.12. While the Nernst coefficient showed substantial field-dependence at small fields, it turns negative at high fields > 10 T and becomes essentially field-independent at fields above 25 T. These findings could be consistent with our theoretical results under the assumption that such fields induce sizable SDW order with

a modulation period larger than 8. In order to clarify the sign structure of the Nernst coefficient in the underdoped region further, more experiments in underdoped $\text{YBa}_2\text{Cu}_3\text{O}_y$ samples are needed.

A further very important aspect might be the spatial anisotropy in the Nernst signal caused by unidirectional stripe order. Especially, such anisotropies cannot be measured by the Hall effect, since the Hall conductivity is constrained by the relation $\langle [j_x, j_y]_- \rangle = -\langle [j_y, j_x]_- \rangle$ obeyed by the correlation functions of the current operators j_x and j_y . In a recent publication by Hackl and Vojta (2009b), it has been shown that rotational symmetry breaking (extensively discussed theoretically in form of *nematic order* in the cuprates) can lead to large anisotropies in the Nernst effect of metals. A sizable anisotropy ratio of up to $\simeq 8$ in the normal state Nernst signal has been observed in a recent experiment on underdoped $\text{YBa}_2\text{Cu}_3\text{O}_y$, and it has been suggested that the maximum in the signal anisotropy keeps track of a nematic phase boundary (Daou et al., 2009b). It is therefore of particular interest to theoretically analyze the influence of other exotic order parameters breaking C_4 -symmetry on the Nernst effect.

Bibliography

- Abanov, A., and A. Chubukov, 2004, Phys. Rev. Lett. **93**, 255702.
- Abanov, A., A. Chubukov, and J. Schmalian, 2003, Adv. Phys. **52**, 119.
- Abrikosov, A., 1965, Physics **2**, 5.
- Abrikosov, A., and A. A. Migdal, 1970, J. Low Temperature Physics **3**, 519.
- Allen, J. W., and R. M. Martin, 1982, Phys. Rev. Lett. **49**, 1106.
- Anders, F. B., and A. Schiller, 2006, Phys. Rev. B **74**, 245113.
- Andersen, O. K., A. I. Liechtenstein, O. Jepsen, and F. Paulsen, 1995, J. Phys. Chem. Solids **56**, 1573.
- Anderson, P., 1961, Phys. Rev. **124**, 41.
- Anderson, P., and G. Yuval, 1969, Phys. Rev. Lett. **23**, 89.
- Anderson, P., G. Yuval, and D. Hamann, 1970, Phys. Rev. B **1**, 4464.
- Anderson, P., 1970, J. Phys. C **3**, 2436.
- Ando, S., Y. Kurita, S. Kondya, S. Ono, and K. Segawa, 2004, Phys. Rev. Lett. **92**, 197001.
- Andres, K., J. E. Graebner, and H. R. Ott, 1975, Phys. Rev. Lett. **35**, 1779.
- Andrew, A. L., and R. C. E. Tan, Commun. Numer. Meth. Eng. **15**, 641 (1999).
- Anisimov, V., I. Nekrasov, D. Kondakov, T. Rice, and M. Sigrist, 2002, Eur. Phys. J. B **25**, 191.
- Aomi, T., and M. Imada, 2007, J. Phys. Soc. Jpn. **76**, 113708.
- Armitage, N. P., F. Ronning, D. H. Lu, C. Kim, A. Damascelli, K. M. Shen, D. L. Feng, H. Eisaki, and Z.-X. Shen, 2002, Phys. Rev. Lett. **88**, 257001.
- Ashcroft, N. W., and N. D. Mermin, 1976, *Solid State Physics*, Holt, Ribehart and Winston, New York.

- Atature, M., J. Dreiser, A. Badolato, and A. Imamoglu, 2007, *Nat. Phys.* **3**, 101.
- Barnard, R. D., 1972, *Thermoelectricity in Metals and Alloys*, (Taylor & Francis, London).
- Baym, G., and L. P. Kadanoff, 1961, *Phys. Rev.* **124**, 287.
- Bazaliy, Y. B., R. Ramazashvili, Q. Si, and M. R. Norman, 2004, *Phys. Rev. B* **69**, 144423.
- Bednorz, J. G., and K. A. Müller, 1986, *Z. Phys. B: Condensed Matter* **64**, 189.
- Behnia, K., 2009, *J. Phys.: Condens. Matter* **21**, 113101.
- Belashchenko, K. D., and V. P. Antropov, 2008, *Phys. Rev. B* **78**, 212515.
- Biermann, S., L. de Medici, and A. Georges, 2005, *Phys. Rev. Lett.* **95**, 206401.
- Blount, E. I., 1962, *Phys. Rev.* **126**, 5.
- Born, M., and V. A. Fock, 1928, *Zeitschrift für Physik* **51**, 165.
- Braun, P.-F. et al., 2005, *Phys. Rev. Lett.* **94**, 116601.
- Bronstein, I. N., and Semendjajew, K. A., 1987, *Taschenbuch der Mathematik*, Verlag Harri Deutsch, Thun.
- Burdin, S., A. Georges, and D. R. Grempel, 2000, *Phys. Rev. Lett.* **85**, 1048.
- Burdin, S., 2001, *Le réseau Kondo à basse température: du liquide de Fermi au liquide de spin*, PhD thesis, Université Grenoble 1.
- Burdin, S., D. R. Grempel, and A. Georges, 2002, *Phys. Rev. B* **66**, 045111.
- Canfield, P. C., S. L. Bud'ko, N. Ni, A. Kreyssig, A. I. Goldman, R. J. McQueeney, M. S. Torikachvili, D. N. Argyriou, G. Luke, and W. Yu, 2009, preprint arXiv:0901.4672.
- Chaikin, P. M., and Lubensky, T. C., 1995, *Principles of Condensed Matter Physics*, (Cambridge University Press, Cambridge).
- Chandra, P., and B. Doucot, 1988, *Phys. Rev. B* **38**, 9335.
- Chandra, P., P. Coleman, and A. I. Larkin, 1990, *Phys. Rev. Lett.* **64**, 88.
- Chang, J. et al., 2009, preprint arXiv:0907.5839.
- Chattopadhyay, T., H. v. Löhneysen, T. Trappmann, and M. Loewenhaupt, 1990, *Z. Phys. B* **80**, 159.
- Chen, T. Y. et al., 2008, *Nature* **453**, 1224.
- Chen, L. Y., and Z. B. Su, *Phys. Rev. B.* **40**, 9309 (1987).
- Chen, L. Y., and Z. B. Su, *Int. J. Mod. Phys.* **4**, 293 (1990).

- Cyr-Choinière et al., 2009, *Nature* **458**, 743.
- Coleman, P., C. Pépin, Q. Si, and R. Ramazashvili, 2001, *J. Phys: Condens. Matt.* **13**, R723.
- Coleman, P., J. B. Marston, and A. J. Schofield, 2005, *Phys. Rev. B* **72**, 245111.
- Coleman, P., 2007, in *Handbook of Magnetism and Advanced Magnetic Materials*, eds. H. Kronmüller and S. Parkin, Vol. **1**, 95, John Wiley and Sons, Hoboken.
- Colombier, E., S. L. Bud'ko, N. Ni, and P. C. Canfield, 2009, preprint arXiv:0904.4488.
- Coqblin, B., and Blandin, A., 1968, *Adv. Phys.* **17**, 281.
- Coqblin, B., and Schrieffer, J. R., 1969, *Phys. Rev.* **185**, 847.
- Cowley, R. A., 1976, *Phys. Rev. B* **13**, 4877.
- Coqblin, B., C. Lacroix, M. A. Gusmao, and J. R. Iglesias, 2003, *Phys. Rev. B* **67**, 064417.
- Craco, L., M. S. Laad, S. Leoni, and H. Rosner, 2008, *Phys. Rev. B* **78**, 134511.
- Cruz, C. de la et al., 2008, *Nature* **453**, 899.
- Custers, J., P. Gegenwart, H. Wilhelm, K. Neumaier, Y. Tokiwa, O. Trovarelli, C. Geibel, F. Steglich, C. Pépin, and P. Coleman, 2003, *Nature* **424**, 524.
- Dagan, Y., M. M. Qazilbash, C. P. Hill, V. N. Kulkarni, and R. L. Greene, 2004, *Phys. Rev. Lett.* **92**, 167001.
- Dagotto, E., 1994, *Rev. Mod. Phys.*, **66**, 763.
- Dai, J., Q. Si, J.-X. Zhu, and E. Abrahams, 2009, *PNAS* **106**, 4118.
- Dai, J., G. Cao, H.-H. Wen, and Z. Xu, 2009, preprint arXiv:0901.2787.
- Damascelli, A., Z. Hussain, and Z.-X. Shen, 2003, *Rev. Mod. Phys.* **75**, 473.
- Daou, R. et al., 2009, *Nature Phys.* **5**, 31.
- Daou, R. et al., 2009, preprint arXiv:0909.4430.
- de Haas, W. J, J. de Boer, and van den Berg, 1934, *Physica*, **1**, 1115.
- Dimov, I., P. Goswami, X. Jia, and S. Chakravarty, 2008, *Phys. Rev. B* **78**, 134529.
- Ding, H. et al., 2008, *Europhys. Lett.* **83**, 47001.
- Doniach, S., 1977, *Physica B* **91**, 231.
- Dzero, M., M. R. Norman, I. Paul, C. Pépin, and J. Schmalian, 2006, *Phys. Rev. Lett.* **97**, 185701.

- Emery, V. J., 1987, Phys. Rev. Lett. **58**, 2794.
- Fang, C., H. Yao, W.-F. Tsai, J.-P. Hu, and S. A. Kivelson, Phys. Rev. B **77**, 2008, 224509.
- Fawcett, E., 1988, Rev. Mod. Phys., **60**, 209.
- Forster, D., 1990, *Hydrodynamic Fluctuations, Broken Symmetry and Correlation Functions*, Addison-Wesley Publishing, Reading, Massachusetts.
- Fournier, P., X. Jiang, W. Jiang, S. N. Mao, T. Venkatesan, C. J. Lobb, and R. L. Greene, 1997, Phys. Rev. B **56**, 14149.
- Friedemann, S., N. Oeschler, S. Wirth, C. Krellner, C. Geibel, F. Steglich, S. MaQuilon, Z. Fisk, S. Paschen, G. Zwicknagl, 2008, preprint arXiv:0808.1425.
- Friedemann, S., T. Westerkamp, M. Brando, N. Oeschler, S. Wirth, P. Gegenwart, C. Krellner, C. Geibel, and F. Steglich, 2009, Nature Physics **5**, 465.
- Friedemann, S. 2009, *Elektrischer Transport und Quantenkritikalität in reinem und substituiertem YbRh_2Si_2* , PhD thesis, TU Dresden.
- Fritsch, P., 2009, *Non-Equilibrium Scaling Analysis of Quantum Dots in the Kondo Regime*, PhD thesis, LMU München.
- Fritsch, P., and Kehrein, S., 2009, Ann. Phys. **324**, 1105.
- Fulde, P., 1991, *Electron Correlations in Molecules and Solids*, Springer Series in Solid state Sciences Vol. **100**, Springer, Berlin, Heidelberg, New York.
- Gan, J., and E. Wong, 1993, Phys. Rev. Lett **71**, 4226.
- Gebhardt, F., 1997, *The Mott Metal-Insulator Transition- Models and Methods*, Springer, Heidelberg.
- Gegenwart, P., J. Custers, C. Geibel, K. Neumaier, T. Tayama, K. Tenya, O. Trovarelli, and F. Steglich, 2002, Phys. Rev. Lett. **89**, 056402.
- Gegenwart, P., T. Westerkamp, C. Krellner, Y. Tokiwa, S. Paschen, C. Geibel, F. Steglich, E. Abrahams, and Q. Si, 2007, Science **315**, 5814.
- Gegenwart, P. Q. Si, and F. Steglich, 2008, Nature Physics **4**, 186.
- Georges, A., Parcollet, O., and Sachdev, S., 2001 Phys. Rev. B **63**, 134406.
- Giovannetti, G., S. Kumar, and J. van den Brink, 2008, Physica B **403**, 3653.
- Głazek, S. D., and K.G. Wilson, 1993, Phys. Rev. D **48**, 5863.
- Głazek, S. D., and K. G. Wilson, 1994, Phys. Rev. D **49**, 4214.
- Goldman, A. I. et al., 2009, Phys. Rev. B **79**, 024513.

- Goldstein, H., Ch. P. Poole, and J. L. Safko, 2002, *Classical Mechanics*, Addison-Wesley, Third edition.
- Goko, T. et al., 2008, preprint arXiv:0808.1425.
- Gonzalez, G., M. N. Leuenberger, and E. R. Mucciolo, 2008, Phys. Rev. B **78**, 054445.
- Gradshteyn, I. S., and Ryzhik, I. M., 2000, *Table of integrals, series and products* Academic Press, San Diego.
- Grepel, D. R., and Q. Si, 2003, Phys. Rev. Lett. **91**, 026401.
- Grüner, G., 1994, Rev. Mod. Phys. **66**, 1.
- Hackl, A., 2006, *Flow equations for dissipative quantum systems under non-equilibrium conditions*, diploma thesis, Universität Augsburg.
- Hackl, A., and M. Vojta, 2008, Phys. Rev. B **77**, 134439.
- Hackl, A., and S. Kehrein, 2008, Phys. Rev. B **78**, 092303.
- Hackl, A., and S. Kehrein, 2009, J. Phys. C **21**, 015601.
- Hackl, A., and M. Vojta, 2009, New J. Phys. **11**, 055064.
- Hackl, A., D. Roosen, S. Kehrein, and W. Hofstetter, 2009, Phys. Rev. Lett. **102**, 196601.
- Hackl, A., and S. Sachdev, 2009, Phys. Rev. B **79**, 235124.
- Hackl, A., S. Kehrein, and M. Vojta, 2009, preprint arXiv:0908.3647.
- Hackl, A., M. Vojta, and S. Sachdev, 2009, preprint arXiv:0908.1088.
- Hackl, A., and M. Vojta, 2009, preprint arXiv:0909.4534.
- Hänsch, W., and Mahan, G. D., 1983, Phys. Rev. B **28**, 4.
- Harrison, N., 2009, Phys. Rev. Lett. **102**, 206405.
- Haug, D., et al., 2009, Phys. Rev. Lett. **103**, 017001.
- Haug, D. et al., unpublished.
- He, R.-H. et al., 2009, Nature Phys. **5**, 119.
- H. B. Heersche, Z. de Groot, J. A. Folk, H. S. J. van der Zant, C. Romeike, M. R. Wegewijs, L. Zobbi, P. Barreca, E. Tondello, and A. Cornia, 2006, Phys. Rev. Lett. **96**, 206801.
- Held, K., A. K. McMahan, and R. T. Scalettar, 2001, Phys. Rev. Lett. **87**, 276404.
- Helm, T., M. V. Katsovnik, M. Bartkowiak, N. Bittner, M. Lambacher, A. Erb, J. Wasnitza, and R. Gross, 2009, arXiv:0906.1431.

- Henley, C. L., 1989, Phys. Rev. Lett. **62**, 2056.
- Herbut, I. F., Seradjeh, B. H., Sachdev, S., and Murthy, G., 2003, Phys. Rev. B **68**, 195110.
- Hertz, J. A., 1976, Phys. Rev. B, **14**, 1165.
- Hewson, A. C., 1997, *The Kondo Problem to Heavy Fermions*, Cambridge University Press, Cambridge.
- Hicks, C. W., T. M. Lippman, M. E. Huber, Z. A. Ren, Z. X. Zhao, and K. A. Moler, 2009, J. Phys. Soc. Jpn. **78**, 013708.
- Holstein, T., R. Norton, and P. Pincus, 1973, Phys. Rev. B **8**, 2649.
- Homes, C. C., R. P. S. M. Lobo, P. Fournier, A. Zimmers, and R. L. Greene, 2006, Phys. Rev. B **74**, 214515.
- Howald, C., H. Eisaki, N. Kaneko, M. Greven, and A. Kapitulnik, 2003, Phys. Rev. B **67**, 014533.
- Huang, Q., Y. Qiu, W. Bao, J. W. Lynn, M. A. Green, Y. Chen, T. Wu, G. Wu, and X. H. Chen, 2008, Phys. Rev. Lett. **101**, 257003.
- Hubbard, J., 1963, Proc. R. Soc. London, Ser. A **276**, 238.
- Hussey, N. E., M. Abdel-Juvad, A. Carrington, A. P. Mackenzie and L. Balicas, 2003, Nature, **425**, 814.
- Ichikawa, N., S. Uchida, J. M. Tranquada, T. Niemöller, P. M. Gehring, S.-H. Lee, and J. R. Schneider, 2000, Phys. Rev. Lett. **85**, 1738.
- Imry, Y., Phys. Rev. Lett., 1974, **33**, 1304.
- Ioffe, L. B., and G. Kotliar, 1990, Phys. Rev. B **42** 10348.
- Ioffe, L. B., and A. I. Larkin, Phys. Rev. B, 1989, **39**, 8988.
- Johannsen, N., T. Wolf, A. V. Sologubenko, T. Lorenz, A. Freimuth, and J. A. Mydosh, 2007, Phys. Rev. B **76**, 020512(R).
- Johansson, B., 1974, Philos. Mag. **30**, 469.
- Kamihara, Y., T. Watanabe, M. Hirano, and H. Hosono, 2008, J. Am. Chem. Soc. **130**, 3296.
- Kang, H. J., P. Dai, H. A. Mook, D. N. Argyriou, V. Sikolenko, J. W. Lynn, Y. Kurita, S. Komiyama, and Y. Ando, 2005, Phys. Rev. B **71**, 214512.
- Kanigel, A. et al., 2006, Nature Phys. **5**, 119.
- Kasuya, T., 1956, Prog. Theor. Phys. **16**, 45.

- Kehrein, S., and A. Mielke, 1997, *Ann. Phys. (Leipzig)* **6**, 90.
- Kehrein, S., 2005, *Phys. Rev. Lett.* **95**, 056602.
- Kehrein, S., 2006, *The Flow Equation Approach to Many-Particle Systems*, Springer, Berlin Heidelberg New York.
- Kehrein, S., 2008, private communication.
- Kinoshita, T., T. Wenger, and D. S. Weiss, 2006, *Nature* **440**, 900.
- Klauss, H.-H. et al., 2008, *Phys. Rev. Lett.* **101**, 077005.
- Klingeler, R., N. Leps, I. Hellmann, A. Popa, C. Hess, A. Kondrat, J. Hamann-Borrero, G. Behr, V. Kataev, and B. Büchner, 2008, preprint arXiv:0808.0708.
- Kondo, J., 1964, *Prog. Theor. Phys.* **32**, 37.
- Kondo, T. et al, 2008, *Phys. Rev. Lett.* **101**, 147003.
- Kohsaka, Y. et al., 2007, *Science* **315**, 1380.
- Kontani, H., and K. Yamada, 2005, *J. Phy. Soc. Jpn.* **74**, 155.
- Kou, S.-P., T. Li, and Z.-Y. Weng, 2008, preprint arXiv:0811.4111.
- Krellner, C., N. Caroca-Canales, A. Jesche, H. Rosner, A. Ormeci, and C. Geibel, 2008, *Phys. Rev. B* **78**, 100504(R).
- Kreyssig, A. et al., 2008, *Phys. Rev. B* **78**, 184517.
- Küchler, R. et al., 2003, *Phys. Rev. Lett.* **91**, 066405.
- Kuroki, K., S. Onari, R. Arita, H. Usui, Y. Tanaka, H. Kontani, and H. Aoki, 2008, *Phys. Rev. Lett.* **101**, 0807004.
- Kusminskiy, S. Viola, K. S. D. Beach, A. H. Castro Neto, and D. K. Campbell, 2008, preprint arXiv:0711.2074.
- Landau, L. D., 1957a, *Sov. Phys. JETP* **3**, 920.
- Landau, L. D., 1957b, *Sov. Phys. JETP* **5**, 101.
- Landau, L. D., 1959, *Sov. Phys. JETP* **8**, 70.
- Landau, L. D., and I. M. Lifshitz, 1986, *Theory of Elasticity, Theoretical Physics*, vol. 7, Butterworth-Heinemann, Oxford.
- Lavagna, M., C. Lacroix, and M. Cyrot, 1982, *Phys. Lett.* **90A**, 210.
- Lavagna, M., C. Lacroix, and M. Cyrot, 1983, *J. Phys. F:Met. Phys.* **13**, 1007.

- LeBoeuf, D. et al., 2007, Nature **450**, 533.
- Lee, P. A., and Nagaosa, N., Phys. Rev. B **46**, 5621, (1992).
- Lee, P. A., and Nagaosa, N., and Wen, X.-G., 2006, Rev. Mod. Phys. **78**, 17.
- Leggett, A. J., S. Chakravarty, A. T. Dorsey, and M. P. A. Fisher, 1987, Rev. Mod. Phys. **59**, 1.
- Leuenberger, M. N., and D. Loss, Nature **410**, 789 (2001).
- Li, P., K. Behnia, and R. L. Greene, 2007, Phys. Rev. B **75**, 020506.
- Li, P., and R. L. Greene, 2007, Phys. Rev. B **76**, 174512.
- Lifshitz, I. M., 1960a, Sov. Phys. -JETP **11**, 1130.
- Lifshitz, I. M., 1960b, J. Exptl. Theoret. Phys. (U.S.S.R) **38**, 1569.
- Lin, J., and A. J. Millis, 2005, Phys. Rev. B **72**, 214506.
- Lin, J., and A. J. Millis, 2008, Phys. Rev. B, **78**, 115108.
- Liu, C. et al., 2008, Phys. Rev. Lett. **101**, 177005.
- Livanov, D. V., 1999, Phys. Rev. B **60**, 13439.
- Lobaskin, D., and S. Kehrein, 2005, Phys. Rev. B **71**, 193303.
- Lobaskin, D., and S. Kehrein, 2006, J. Stat. Phys. **123**, 301.
- Löhneysen, H. v., T. Pietrus, G. Portisch, H. G. Schlager, A. Schroeder, M. Sieck, and T. Trappmann, 1994, Phys. Rev. Lett. **72**, 3262.
- Löhneysen, H. v., M. Sieck, O. Stockert, and M. Waffenschmidt, 1996, Physica B **223-224**, 471.
- Löhneysen, H. v., S. Mock, A. Neubert, T. Pietrus, A. Schröder, O. Stockert, U. Tutsch, M. Lowenhaupt, A. Rosch, and P. Wölfle, 1998, Eur. Phys. J. B **5**, 447.
- Löhneysen, H. v., A. Rosch, M. Vojta, and P. Wölfle, 2007, Rev. Mod. Phys. **79**, 1015.
- Luetkens, H. et al., 2008, Nature Mat. **8**, 305.
- Luke, G. M. et al., 1990, Phys. Rev. B **42**, 7981.
- Lumsden, M. D. et al., 2009, Phys. Rev. Lett. **102**, 107005.
- Lundstrom, M., 2000, *Fundamentals of carrier transport*, Cambridge University Press, Cambridge.
- Luttinger, J. M., 1960, Phys. Rev. **119**, 1153.

- Ma, F., Z. Lu, and T. Xiang, 2008, Phys. Rev. B **78**, 224517.
- Mahan, G. D., 1990, *Many Particle Physics*, Plenum Press, New York.
- Malaeb, W., et al., 2009, preprint arXiv:0906.1846.
- Mang, P. K., O. P. Vajk, A. Arvanitaki, J. W. Lynn, and M. Greven, 2004, Phys. Rev. Lett. **93**, 027002.
- Marston, J. B., and Affleck, I., 1989, Phys. Rev. B. **39**, 11538.
- Martin, C. et al., 2009, Phys. Rev. Lett. **102**, 247002.
- Matsui, H., T. Takahashi, T. Sato, K. Terashima, H. Ding, T. Uefuji, and K. Yamada, 2007, Phys. Rev. B **75**, 224514.
- Matsuura, M., P. Dai, H. J. Kang, J. W. Lynn, D. N. Argyriou, K. Prokes, Y. Onose, and Y. Tokura, 2003, Phys. Rev. B **68**, 144503.
- Mazin, I. I., M. D. Johannes, L. Boeri, K. Koepernik, and D. J. Singh, 2008, Phys. Rev. B **78**, 085104.
- Mazin, I. I., D. J. Singh, M. D. Johannes, and M. H. Du 2008, Phys. Rev. Lett. **101**, 057003 (2008).
- Mazin, I. I., and J. Schmalian, 2009, preprint arXiv:0901.4790.
- McGuire, M. A. et al., 2008, Phys. Rev. B **78**, 094517.
- McMahan, A. K., C. Hushcroft, R. T. Scalettar, and E. L. Pollock, 1998, J. of Comp.-Aided Mat. Design **5**, 131.
- McMahan, A. K., K. Held, and R. T. Scalettar, 2003, Phys. Rev. B **67**, 075108.
- McQueeney, R. J. et al., 2008, Phys. Rev. Lett. **101**, 227205.
- Mermin, N D., and H. Wagner, Phys. Rev. Lett. **17**, 1133 (1966).
- Millis, A. J., 1993, Phys. Rev. B **48**, 7183.
- Millis, A. J., A. Zimmers, R. P. S. M. Lobo, N. Bontemps, and C. C. Homes, 2005, Phys. Rev. B **72**, 224517.
- Millis, A. J., and M. R. Norman, 2007, Phys. Rev. B **76**, 220503(R).
- Moeckel, M. and S. Kehrein, 2008, Phys. Rev. Lett. **100**, 175702.
- Moeckel, M., and S. Kehrein, 2009, preprint arXiv:0903.1561.
- Mook, H. A., P. Dai, F. Doğan, Phys. Rev. Lett. **88**, 097004.
- Moon, E. G., and S. Sachdev, 2009, Phys. Rev. B **80**, 035117.

- Motoyama, E. M., G. Yu, I. M. Vishik, O. P. Vajk, P. K. Mang, and M. Greven, 2006, *Nature* **445**, 186.
- Mukerjee, S., and D. A. Huse, 2004, *Phys. Rev. B* **70**, 014506.
- Nachumi, B. et al., 1998, *Phys. Rev. B* **58**, 8760.
- Nolting, W., 2005, *Grundkurs theoretische Physik 4*, Springer, Berlin, Heidelberg, New York.
- Norman, M. R., *Physics*, **1**, 21 (2008).
- Nowack, K. C., F. H. L. Koppens, Y. V. Nazarov, and L. M. K. Vandersypen, 2007, *Science* **318**, 1430.
- Nozières, P., 1974, *J. Low Temp. Phys.* **17**, 31.
- Nozières, P., and Blandin, 1980, *J. Phys.* **41**, 193.
- Nozières, P., 1985, *Ann. Phys. (Paris)* **10**, 19.
- Nozières, P., 2005, *J. Phys. Soc. Jpn.* **74**, 4.
- Oganesyan, V., and I. Ussishkin, 2004, *Phys. Rev. B* **70**, 054503.
- Ohishi, K., I. Yamada, A. Koda, W. Higemoto, S. R. Saha, R. Kadono, K. M. Kojima, M. Azuma, and M. Takano, 2005, *J. Phys. Soc. Jpn.* **74**, 2408.
- Oitmaa, J., and W. H. Zheng, 1996, *Phys. Rev. B* **54**, 3022.
- Ong, N. P., 1991, *Phys. Rev. B* **43**, 193.
- Onose, Y., Y. Taguchi, K. Ishizaka, and Y. Tokura, 2001, *Phys. Rev. Lett.* **87**, 217001.
- Oshikawa, M., 2000, *Phys. Rev. Lett.* **84**, 3370.
- Palma, G. M., K.-A. Suominen, and A. K. Ekert, 1996, *Proc. R. Soc. Lond. A* **452**, 567.
- Paschen, S., T. Lühmann, S. Wirth, P. Gegenwart, O. Trovarelli, C. Geibel, F. Steglich, P. Coleman, and Q. Si, 2004, *Nature* **432**, 881.
- Paul, I., C. Pépin, and M. R. Norman, 2007, *Phys. Rev. Lett.* **98**, 026402.
- Paul, I., C. Pépin, and M. R. Norman, 2008, *Phys. Rev. B* **78**, 035109.
- Pépin, C., 2005, *Phys. Rev. Lett.* **94**, 066402.
- Pépin, C., 2007, *Phys. Rev. Lett.* **98**, 206401.
- Pépin, C., 2008, *Phys. Rev. B* **77**, 245129.
- Pletyukhov, M., D. Schuricht, and H. Schoeller, 2009, preprint arXiv:0910.0119.

- Podolsky, D., S. Raghu, and A. Vishwanath, 2007, Phys. Rev. Lett. **99**, 117004.
- Polyakov, A. M., 1977, Nucl. Phys. B **120**, 429.
- Pratt, D. K., Y. Zhao, S. A. J. Kimber, A. Hiess, D. N. Argyriou, C. Broholm, A. Kreyssig, and S. Nandi, 2009, Phys. Rev. B **79**, 060510(R).
- Press, W. H., S. A. Teukolsky, W. T. Vetterling, and B. P. Flannery, 2007, *Numerical Recipes (Third Edition)*, Cambridge University Press, Cambridge.
- Pruschke, T., R. Bulla, and M. Jarrell, 2000, Phys. Rev. B **61**, 12799.
- Qi, Y., and C. Xu, 2008, preprint arXiv:0812.0016.
- Rammer, J., and H. Smith, 1986, Rev. Mod. Phys. **58**, 323.
- Ritter, S., A. Öttl, T. Donner, T. Bourdel, M. Köhl, and T. Esslinger, 2007, Phys. Rev. Lett. **98**, 090402.
- Roch, N., S. Florens, V. Bouchiat, W. Wernsdorfer, and F. Balestro, Nature **453**, 633 (2008).
- Roosen, D., M. R. Wegewijs, and W. Hofstetter, 2008, Phys. Rev. Lett. **100**, 087201.
- Rosch, A., A. Schröder, O. Stockert, and H. v. Löhneysen, 1997, Phys. Rev. Lett. **79**, 159.
- Rotter, M., M. Tegel, and D. Johrendt, 2008, Phys. Rev. Lett. **101**, 107006.
- Ruderman, M. A., and C. Kittel, 1954, Phys. Rev. **96**, 99.
- Sachdev, S., *Quantum Phase Transitions*, 1999, Cambridge University Press, Cambridge.
- Sachdev, S., 2002, Physica A **313**, 252.
- Samolyuk, G. D., and V. P. Antropov, 2009, Phys. Rev. B **79**, 052505.
- Schrieffer, J. R., and P. Wolff, 1966, Phys. Rev. **149**, 491.
- Schröder, A., G. Aeppli, R. Coldea, M. Adams, O. Stockert, H. v. Löhneysen, E. Bucher, R. Ramazashvili, and P. Coleman, 2000, Nature (London) **407**, 351.
- Sebastian, S. E., J. Gillett, N. Harrison, P. H. C. Lau, C. H. Mielke, and G. G. Lonzarich, 2008, J. Phys.: Condens. Matter **20** 422203.
- Senthil, T., S. Sachdev, and M. Vojta, 2003, Phys. Rev. Lett. **90**, 216403.
- Senthil, T., M. Vojta, and S. Sachdev, 2004, Phys. Rev. B **69**, 035111.
- Senthil, T., S. Sachdev, and M. Vojta, 2005, Physica B **359-361**, 9.
- Senthil, T., 2006, preprint arXiv:0604240.

- Senthil, T., and P. A. Lee, 2009, Phys. Rev. B **79**, 245116.
- Shapiro, S. M., J. D. Axe, R. J. Birgenau, J. M. Lawrence, and R. D. Parks, Phys. Rev. B **16**, 2225.
- Shim, J. H., K. Haule, and G. Kotliar, 2008, preprint arXiv:0809.0041.
- Si, Q., J. L. Smith, and K. Ingersent, 1999, Int. J. Mod. Phys. B **13**, 2331.
- Si, Q., S. Rabello, K. Ingersent, and J. L. Smith, 2001, Nature (London) **413**, 804.
- Si, Q., S. Rabello, K. Ingersent, and J. L. Smith, 2003, Phys. Rev. B **68**, 115103.
- Si, Q., and E. Abrahams, 2008, Phys. Rev. Lett. **101**, 076401.
- Singh, D. J., and M.-H. Du, 2008, Phys. Rev. Lett. **100**, 237003.
- Singh, D. J., 2008, Phys. Rev. B **78**, 094511.
- Smith, J. L., and Q. Si, 2000, Phys. Rev. B **61**, 5184.
- Sondheimer, E. H., 1948, Proc. R. Soc. London, Ser. A **193**, 484.
- Steglich, F., J. Aarts, C. D. Bredl, W. Lieke, D. Meschede, W. Franz, and H. Schäfer, 1979, Phys. Rev. Lett. **43**, 1892.
- Stewart, G. R., 1984, Rev. Mod. Phys. **56**, 755.
- Stewart, G. R., 2001, Rev. Mod. Phys. **73**, 797.
- Stock, C., W. J. L. Buyers, R. Liang, D. Peets, Z. Tun, D. Bonn, W. N. Hardy, and R. J. Birgeneau, 2004, Phys. Rev. B **69**, 014502.
- Stockert, O., H. v. Löhneysen, A. Rosch, N. Pyka, and M. Loewenhaupt, 1998, Phys. Rev. Lett. **80**, 5627.
- Subedi, A., L. Zhang, D. J. Singh, M. H. Du, 2008, preprint arXiv:0807.4312.
- Taillefer, L., 2009, Journal of Physics: Condensed Matter **21**, 164212.
- Takahashi, H., K. Igawa, K. Arii, Y. Kamihara, M. Hirano, and H. Hosono, 2008, Nature **453**, 376.
- Thalmeier, P., and B. Lüthi, 1991, in *Handbook of the Physics and Chemistry of the Rare Earths*, eds. K. A. Gschneidner and L. Eyring, Vol. **14**, Chap. 96, North-Holland, Amsterdam.
- Timusk, T., and B. Statt, 1999, Rep. Prog. Phys. **62**, 61.
- Torikachvili, M. S., S. L. Bud'ko, N. Ni, and P. C. Canfield, 2008, Phys. Rev. Lett. **101**, 057006.

- Tranquada, J. M., B. J. Sternlieb, J. D. Axe, Y. Nakamura, and S. Uchida, 1995, *Nature* **375**, 561.
- Trovarelli, O., C. Geibel, S. Mederle, C. Langhammer, F. M. Grosche, P. Gegenwart, M. Lang, G. Sparn, and F. Steglich, 2000, *Phys. Rev. Lett.* **85**, 626.
- Tsunegutsu, H., Sigrist, M., and Ueda, K. 1997, *Rev. Mod. Phys.* **69**, 809.
- Ussishkin, I. S. L. Sondhi, and D. A. Huse, 2002, *Phys. Rev. Lett.* **89**, 287001.
- Valla, T., A. V. Fedorov, P. D. Johnson, Q. Li, G. D. Gu, and N. Koshizuka, 2000, *Phys. Rev. Lett.* **85**, 828.
- Valla, T., A. V. Fedorov, J. Lee, J. C. Davis, and G. D. Gu, 2006, *Science* **314**, 1914.
- Vojta, M., 2003, *Rep. Prog. Phys.* **66**, 2069.
- Vojta, M., 2008, *Phys. Rev. B* **78**, 125109.
- Vojta, M., and O. Rösch, 2008, *Phys. Rev. B* **77**, 094504.
- Vojta, M., 2009, preprint arXiv:0901.3145.
- Wang, Y., L. Li, and N. P. Ong, 2006, *Phys. Rev. B* **73**, 024510.
- Wang, C. et al., 2008, *Europhys. Lett.* **83**, 67006.
- Watanabe, H., and M. Ogata, 2007, *Phys. Rev. Lett.* **99**, 136401.
- Wegner, F., 1994, *Ann. Phys. (Leipzig)* **3**, 77.
- Wick, G. C., 1950, *Phys. Rev.* **80**, 268.
- Wiegmann, P. B., 1980, *Phys. Lett.* **80A**, 163.
- Wieliczka, D., J. H. Weaver, D. W. Lynch, C. G. Olson, 1982, *Phys. Rev. B* **26**, 7056.
- Wilson, K. G., 1975, *Rev. Mod. Phys.* **47**, 773.
- Wu, J., P. Phillips, and A. H. Castro Neto, 2008, *Phys. Rev. Lett.* **101**, 126401.
- Xu, Z. A., N. P. Ong, Y. Wang, T. Kakeshita, and S. Uchida, 2000, *Nature* **406**, 486.
- Yang, J. et al., 2008, *Supercond. Sci. Technol.* **21**, 082001.
- Yaresko, A. N., G.-Q. Liu, V. N. Antonov, and O. K. Andersen, 2009, *Phys. Rev. B* **79**, 144421.
- Yamaji, Y., T. Misawa, and M. Imada, 2006, *J. Phys. Soc. Jpn.* **75**, 094719.
- Yildirim, T., 2008, *Phys. Rev. Lett.* **101**, 057010.

- Yildirim, T., 2009, Phys. Rev. Lett., **102**, 037003.
- Yildirim, T., 2009, preprint arXiv:0902.3462.
- Yu, W., J. S. Higgins, P. Bach, and R. L. Greene, 2007, Phys. Rev. B **76**, 020503(R).
- Yu, W., A. A. Aczel, T. J. Williams, S. L. Bud'ko, N. Ni, P. C. Canfield, and G. M. Luke, 2008, preprint arXiv:0811.2554.
- Zaanen, J., and Gunnarson, O., 1989, Phys. Rev. B, **40**, 7391.
- Zachar, O., S. A. Kivelson, and V. J. Emery, 1998, Phys. Rev. B **57**, 1422.
- Zarand, G., and E. Demler, 2002, Phys. Rev. B **66**, 024427.
- Zener, C., 1951, Phys. Rev. **81**, 440.
- Zhang, F. C., and T. M. Rice, 1988, Phys. Rev. B **37**, 3759.
- Zhao, L. et al., 2008, Chin. Phys. Lett. **25**, 4402.
- Zhou, X. J. et al., 2003, Nature **423**, 398.
- Zhu, J.-X., D. R. Grempel, and Q. Si, 2003, Phys. Rev. Lett. **91**, 156404.
- Ziman, J. M., 1960, *Electrons and Phonons* (Oxford University Press, Oxford).

Acknowledgements

After the end of three years of hard work, I like to note some final remarks on various people's contributions to this thesis. Without any doubt, it was Matthias Vojta who gave me all the financial and scientific possibilities I ever demanded during the last three years. Especially the second half of this thesis profited a lot from very intense collaboration and a very competitive scientific attitude that helped speed up our scientific output. That is like physics should be. His care especially exceeded my own expectations during the very exhausting last months. Thank you Matthias.

It is indispensable to name also two other "good spirits" on my scientific journey, Stefan Kehrein and Subir Sachdev. It was Stefan Kehrein who always was open-minded to support my scientific ideas since my time as a diploma student and he has been a companion on numerous occasions since then. I am indebted to Subir Sachdev for his many ideas and hints towards "hot" scientific topics that in the end were worth enough several publications. I also very much appreciate his hospitality at Harvard and a very entertaining collaboration during that time. Thank you Stefan and Subir.

I thank all these three people for initiating many of the topics contained in this thesis, giving me the opportunity to work on a great variety of modern topics in condensed matter physics. I have to name these people also as the most influential teachers during my scientific education, providing me a basis for further independent research.

A very nice collaboration with Walter Hofstetter and David Roosen won't be forgotten. After all formulas have been written down, I have to thank Ralf Bulla, Markus Grüninger, Achim Rosch and Herbert Schoeller for their participation in the final examination procedures. A big thank goes also to Andreas Sindermann, who does an outstanding job in managing the IT resources. Many institutes of theoretical physics would urgently need his professionalism. I also thank the people who are much responsible for the everyday life, e.g., my officemates Ricardo Doretto, Lars Fritz, Etienne Gärtner, Eun-Gook Moon, Tanja Rindler-Daller, Oliver Rösch, and Heidrun Weber. Finally, I thank Sébastien Burdin, Ricardo Doretto, Lars Fritz, Markus Garst, Walter Hofstetter, Eun-Gook Moon, Michael Norman, Indranil Paul, Yang Qi, Oliver Rösch, David Roosen, Achim Rosch, Louis Taillefer, Cenke Xu and Jan Zaanen for the many scientific discussions that helped me finding a faithful way to think about my scientific problems.

Anhänge gemäß Prüfungsordnung

Abstract

In this thesis, several cases of non-equilibrium phenomena and quantum phase transitions in strongly correlated electron systems are analyzed.

The unconventional critical behavior near magnetic quantum phase transitions in various heavy-fermion metals has triggered proposals on the breakdown of the Kondo effect at the critical point. In part I, we investigate, within one specific scenario, the fate of such a zero-temperature transition upon coupling of the electronic to lattice degrees of freedom. We study a Kondo-Heisenberg model with volume-dependent Kondo coupling – this model displays both Kondo volume collapse and Kondo-breakdown transitions. Within a large- N treatment, we find that the Kondo breakdown transition remains of second order except for very soft lattices. Finally, we relate our findings to current heavy-fermion experiments. Using non-equilibrium Green's functions, we derive transport equations for the degrees of freedom participating in the quantum critical region of the Kondo breakdown transition. We discuss conditions under which the transport of electrical charge is described by the independent motion of conduction electrons and auxiliary bosons. Under these conditions, we derive a semiclassical transport equation for the bosons and quantitatively discuss the electrical conductivity of the whole system.

Motivated by pressure experiments on FeAs-122 superconductors, in part II we propose a scenario based on local-moment physics to explain salient features at the magnetic phase boundary of CaFe_2As_2 . In this scenario, the low-pressure magnetic phase derives from Fe moments, which become screened in the paramagnetic high-pressure phase. The quantum phase transition can be described as an orbital-selective Mott transition, which is rendered first order by coupling to the lattice. These ideas are illustrated by a suitable mean-field analysis of an Anderson lattice model.

An analytical description of non-equilibrium phenomena in interacting quantum systems is rarely possible. In part III we present one example where such a description can be achieved, namely the ferromagnetic Kondo model. In equilibrium, this model is tractable via perturbative renormalization-group techniques. We employ a recently developed extension of the flow-equation method to calculate the non-equilibrium decay of the local magnetization at zero temperature. The flow equations admit analytical solutions which become exact at short and long times, in the latter case revealing that the system always retains a memory of its initial state.

Finally, in part IV we analyze the Nernst effect resulting from normal state quasiparticles in the cuprates in presence of various types of translational symmetry breaking. In the electron-doped cuprates, the Nernst signal resulting from a reconstruction of the Fermi surface due to spin density wave order is discussed. An order parameter consistent with the reconstruction of the Fermi surface detected in electron-doped materials is shown to

sharply enhance the Nernst signal close to optimal doping. Within a semiclassical treatment, the obtained magnitude and position of the enhanced Nernst signal agrees with Nernst measurements in electron-doped cuprates.

In the hole-doped cuprates, we discuss relations between the normal-state Nernst effect and stripe order. We find that Fermi pockets caused by translational symmetry breaking lead to a strongly enhanced Nernst signal with a sign depending on the modulation period of the ordered state and other details of the Fermi surface. This implies differences between antiferromagnetic and charge-only stripes. We compare our findings with recent data from $\text{La}_{1.6-x}\text{Nd}_{0.4}\text{Sr}_x\text{CuO}_4$ and $\text{YBa}_2\text{Cu}_3\text{O}_y$.

Kurzzusammenfassung

In dieser Dissertation werden verschiedene Nichtgleichgewichts-Phänomene und Quantenphasenübergänge in Systemen stark korrelierter Elektronen untersucht.

Das ungewöhnliche kritische Verhalten nahe magnetischer Quantenphasenübergänge in verschiedenen Schwerfermionen-Systemen verursachte mehrere Vorschläge bzgl. eines Zusammenbruchs des Kondoeffektes am quantenkritischen Punkt. Im ersten Teil dieser Arbeit werden innerhalb eines bestimmten Szenarios Veränderungen dieses Quantenphasenüberganges durch Kopplung der elektronischen Freiheitsgrade an die Gitterfreiheitsgrade untersucht. Wir untersuchen ein Kondo-Heisenberg-Modell mit volumenabhängiger Kondokopplung – dieses Modell zeigt sowohl sogenannte Kondo-Volumen-Kollaps als auch Kondo-Zusammenbruch-Übergänge. Innerhalb des Grenzfalles großer orbitaler Entartung N finden wir, dass der Kondo-Zusammenbruch-Übergang ein Phasenübergang zweiter Ordnung bleibt, ausser im Grenzfall weicher Gitter. Diese und weitere Ergebnisse werden schließlich in Beziehung zu aktuellen Experimenten an Schwerfermionen-Systemen gesetzt. Unter Verwendung von Nichtgleichgewichts-Greenschen Funktionen leiten wir Transportgleichungen für die an der quantenkritischen Region des Kondo-Zusammenbruch-Übergangs beteiligten Freiheitsgrade ab. Wir diskutieren Bedingungen, unter welchen der Transport elektrischer Ladung durch die unabhängige Bewegung von Leitungselektronen und bosonischen Hilfsteilchen beschreibbar ist. Unter diesen Bedingungen leiten wir eine semiklassische Transportgleichung für die Bosonen ab und diskutieren quantitativ die elektrische Leitfähigkeit des Gesamtsystems.

Motiviert durch Druckexperimente an Supraleitern der FeAs-122 Familie, schlagen wir in Teil II eine auf lokale-Momente-Magnetismus basierende Theorie vor, um auffällige Eigenschaften der magnetischen Phasengrenze von CaFe_2As_2 zu erklären. In diesem Szenario entsteht die magnetische Phase bei tiefen Drücken durch die lokalen Momente von Eisen, welche in der paramagnetischen Hochdruckphase abgeschirmt sind. Der Quantenphasenübergang kann als orbital-selektiver Mott-Übergang beschrieben werden, welcher durch die Gitterkopplung zu einem Phasenübergang erster Ordnung wird. Diese Ideen werden anhand

einer geeigneten mean-field Theorie eines Anderson-Gitter-Modells erörtert.

Eine analytische Beschreibung von Nichtgleichgewichtsphänomenen in wechselwirkenden Quantensystemen ist selten möglich. In Teil III dieser Arbeit präsentieren wir als Beispiel für solch eine Beschreibung das ferromagnetische Kondommodell. Im Gleichgewicht ist dieses Modell mittels perturbativer Renormierungsgruppen-Techniken behandelbar. Wir benutzen eine jüngst entwickelte Erweiterung der Flußgleichungsmethode, um den zeitlichen Zerfall der lokalen Magnetisierung am Temperaturnullpunkt zu berechnen. Die Flußgleichungen ermöglichen analytische Lösungen, welche im Grenzfall kurzer und langer Zeiten exakt werden. Im letzteren Fall offenbart sich, dass das System stets ein Gedächtnis von seinem Anfangszustand behält.

In Teil IV untersuchen wir den Nernsteffekt im normalleitenden Zustand von Kupraten unter Anwesenheit verschiedener Verletzungen der Translationssymmetrie des Gitters. In den elektrondotierten Kupraten untersuchen wir den Einfluss einer Fermiflächenrekonstruktion durch Spindichtewellenordnung auf das Nernstsignal. Es wird gezeigt, dass ein mit der in elektrondotierten Materialien beobachteten Fermiflächenrekonstruktion konsistenter Ordnungsparameter das Nernstsignal nahe optimaler Dotierung stark verstärkt. Innerhalb einer semiklassischen Beschreibung wird gezeigt, dass Position und Amplitude des verstärkten Nernstsignals mit experimentellen Messungen an elektrondotierten Kupraten übereinstimmt.

In den lochdotierten Kupraten diskutieren wir Beziehungen zwischen dem Nernsteffekt im normalleitenden Zustand und Streifenordnung. Wir zeigen, dass durch Brechung der Translationssymmetrie verursachte Taschen in der Fermifläche zu einem stark erhöhten Nernstsignal führen, mit einem Vorzeichen welches von der Modulationsperiode des geordneten Zustands und anderen Details der Fermifläche abhängt. Diese Eigenschaften lassen auf Unterschiede zwischen Spin-Streifenordnung und Ladungstreifenordnung schließen. Wir vergleichen unsere Befunde schließlich mit jüngsten Experimenten an $\text{La}_{1.6-x}\text{Nd}_{0.4}\text{Sr}_x\text{CuO}_4$ und $\text{YBa}_2\text{Cu}_3\text{O}_y$.

Erklärung

Ich versichere, dass ich die von mir vorgelegte Dissertation selbständig angefertigt, die benutzten Quellen und Hilfsmittel vollständig angegeben und die Stellen der Arbeit – einschliesslich Tabellen, Karten, und Abbildungen –, die anderen Werken im Wortlaut oder dem Sinn nach entnommen sind, in jedem Einzelfall als Entlehnung kenntlich gemacht habe; dass diese Dissertation noch keiner anderen Fakultät oder Universität zur Prüfung vorgelegen hat; dass sie – abgesehen von unten angegegebenen Teilpublikationen – noch nicht veröffentlicht worden ist sowie, dass ich eine solche Veröffentlichung vor Abschluss des Promotionsverfahrens nicht vornehmen werde. Die Bestimmungen der Promotionsordnung sind mir bekannt. Die von mir vorgelegte Dissertation ist von Herrn Prof. Dr. Matthias Vojta betreut worden.

Köln, den 15. Oktober 2009

Teilpublikationen

- A. Hackl and M. Vojta, “*Kondo volume collapse, Kondo breakdown, and Fermi surface transitions in heavy-fermion metals*”, Phys. Rev. B **77**, 134439 (2008).
- A. Hackl and S. Kehrein, “*Unitary perturbation theory approach to real-time evolution problems*”, J. Phys. C **21**, 015601 (2009).
- A. Hackl and M. Vojta, “*Pressure-induced magnetic transition and volume collapse in FeAs superconductors: An orbital-selective Mott scenario*”, New J. Phys. **11**, 055064 (2009).
- A. Hackl, D. Roosen, S. Kehrein, and W. Hofstetter, “*Nonequilibrium Spin Dynamics in the Ferromagnetic Kondo Model*”, Phys. Rev. Lett. **102**, 196601 (2009).
- A. Hackl and S. Sachdev, “*Nernst effect in the electron-doped cuprates*”, Phys. Rev. B **79**, 235124 (2009).
- A. Hackl, M. Vojta, and S. Sachdev, “*Quasiparticle Nernst effect in stripe-ordered cuprates*”, Phys. Rev. B **81**, 045102 (2010).
- A. Hackl, S. Kehrein, and M. Vojta, “*Non-equilibrium magnetization dynamics of ferromagnetically coupled Kondo spins*”, Phys. Rev. B **80**, 195117 (2009).
- A. Hackl, and M. Vojta, “*Nernst effect as a sensitive probe of nematic order*”, Phys. Rev. B **80**, 220514(R) (2009). (Editor’s suggestion)

Lebenslauf

Persönliche Daten

Name	Andreas Hackl
Geburtsdatum	16. Juli 1980
Geburtsort	Nördlingen
Familienstand	ledig
Staatsangehörigkeit	deutsch

Schulbildung

1987-1991	Grundschule Nördlingen
1991-2000	Theodor-Heuss-Gymnasium, Nördlingen
Juni 2000	Abitur

Wehrdienst

Nov. 2000 - August 2001	Wehrdienst im Fernmelderegiment 220, Donauwörth
-------------------------	--

Hochschulstudium

Oktober 2001	Immatrikulation an der Universität Augsburg Studiengang: Physik (Diplom)
Oktober 2003	Vordiplom, Physik, Augsburg
Oktober 2006	Diplom, Physik, Augsburg
seit Januar 2007	Anfertigung der vorliegenden Dissertation, Köln
Oktober 2008 - April 2009	Gastwissenschaftler, Harvard University, Cambridge, USA

Arbeitsverhältnisse

Juni 2005 -Juli 2006	studentische Hilfskraft am Lehrstuhl für Theoretische Physik III, Universität Augsburg
seit Januar 2007	wissenschaftlicher Mitarbeiter am Institut für Theoretische Physik, Universität zu Köln